The Dissertation Committee for HASAN JAVED KHAN certifies that this is the approved version of the following dissertation:

Particle straining in vuggy porous media

Committee:

Maša Prodanović, Co-Supervisor

David DiCarlo, Co-Supervisor

Kenneth E Gray

Mukul Sharma

Chadi El Mohtar

Particle straining in vuggy porous media

by

Hasan Javed Khan

Dissertation

Presented to the Faculty of the Graduate School of

The University of Texas at Austin

in Partial Fulfillment

of the Requirements

for the Degree of

Doctor of Philosophy

The University of Texas at Austin
December 2019

Acknowledgments

پڑھ پڑھ عالم فاضل ہو یا کدے اپنے آپ نوں پڑھیا نہیں۔۔۔
(بابا بھلے شاہ)

You read to become all knowledgeable but you never read yourself
(Baba Bulleh Shah)

First of all I would like to praise and thank ALLAH, the Almighty, without whose permission I could not have finished this research. I express my sincere gratitude to my advisors Dr. Maša Prodanović and Dr. David DiCarlo for offering me an opportunity to work in their research groups. Their constant guidance and encouragement within all aspects of this research, including down blind alleyways, is a major reason for this success. I would like to thank the Dr. Paul Bommer for his guidance and financial support in the form a teaching assistant position.

I would also like to thank all the people working in the Hildebrand Department of Petroleum and Geosysterms Engineering, particularly Glen Baum, Gary Miscoe and Daryl Nygaard for all their timely help and support. Sincere thanks to Amy Stewart, Leah Freeman, Leilani Swafford, and Gabby Banales for their support capabilities.

I am also very grateful to all the colleagues in our research group especially Dr. Maryam Mirabolghasemi for her support in reasoning out the science, Dr. Hongtao Yang for the ability to laugh at my jokes, Dr. Rahul Verma for the life lessons, Javier Santos for the constant disruption, Min Zhang for her persona, Joshua Bautista for the constant reality checks, Dr. Igor Shovkun for the hilarity, and Dr. Ayaz Mehmani for his technical guidance.

My sincere thanks to the band of friends, old and new, including Shiraz, Saqib, Mujtaba, Shivam, Abhishek, Imran, Faizan, Dr. Asad, and others for the their support and friendship.

My deepest and most sincere thanks to Fabio, Leo, Mayowa, Amir, and Yousef for my fledging football career and keeping my sanity in check.

Last, but not least, my deepest gratitude to my wife Asma. Her patience enabled me to power through the final stages of my degree and efficiently finish this write up. Here is to many moons together.

Abstract

PARTICLE STRAINING IN VUGGY POROUS MEDIA

Hasan Javed Khan, Ph.D.

The University of Texas at Austin, 2019

Supervisors: Maša Prodanović & David DiCarlo

Formation damage is the loss of inherent permeability of porous media and is of vital importance in petroleum engineering. One important mechanism of formation damage is particulate straining, where suspended solid particles jam the flow pathways and reduce its flow capability. Most studies of particulate transport have been performed in porous media of uniform pore size, such as sandstones and sandpacks. Carbonates often contain large openings, called vugs, which can affect the flow and transport properties (particle straining) of the porous medium.

In this study, particle straining experiments are performed on multiple configurations of synthetic vuggy media. A novel method is introduced to generate synthetic vuggy glass bead cores: glass beads, with dissolvable inclusions, are sintered in the presence of air in a muffle furnace and later dissolved with a core flood. Smaller-sized glass beads are injected at multiple flow rate and injection concentrations and changes in porosity, permeability, vug size, and particle effluent volume are monitored using continuous pressure measurements and computed tomography scanning. The results are combined with quasi-2D streamline simulations to understand the particle deposition patterns in these vuggy media.

Furthermore, spontaneous imbibition experiments are conducted on multiple configurations of these synthetic vuggy media and capillary rise is measured. Rudimentary vug-pore flow models are generated, and solved for spontaneous imbibition using a computational fluid dynamics solver, to better explain the behavior observed in the experiments.

The results can be summarized as follows: (i) particles penetrate and deposit at a deeper depth when a vug is present; (ii) the particles deposit on the vug-matrix boundary and result in a smaller and smoother vug; (iii) the maximum change in the vug is observed at the bottom of the vug; and (iv) more particle deposition occurs in the matrix around the vug. The high permeability vugs cause flow convergence, which increases the particle-particle and particle-matrix interaction, and results in an increased number of particles dropping out of the flow stream. Each vug has a sphere of influence within which it will affect the particle flow pathway; if the sphere of influence of two vugs overlap, the particle will be affected by both the vugs, with the dominance depending on the separation between the particle and the vug.

The results suggest that for the vug conditions studied, the vugs in series focus the flow and increase the depth of particle deposition and the total volume of particles deposited in the core. The vugs in parallel acts independently as separate vugs, with their separation greater than their individual sphere of influence, and do not dictate the deposition of injected particles.

In future, this study can be carried forward by conducting experiments inside a CT machine, to enable time-lapse particle deposition maps, on proxy vuggy media or real rocks. Coupled with real-time porosity, permeability, and possibly resistivity measurements, new near-wellbore interpretative models can be envisioned for improved formation evaluation of vuggy carbonates.

Table of Contents

List of Figures

Page

List of Tables

Chapter 1: Introduction

Formation damage is the loss of inherent permeability of a rock caused by the oilfield fluids, resulting in the formation of an internal filter cake in the near wellbore region, and an external filter cake at the rock face due to fines migration or the entrapment of solids present in the drilling mud or injection fluids. It is present throughout the lifecycle of a well in different forms: drilling mud has suspended solids which are pushed into the formation due to the overbalance pressure, sand moves in the near wellbore region due to high flowrate during production, solid fragments move due to dissolution and chipping of the rock matrix, proppant and perforation debris cause screenouts, and wettability alteration occurs during secondary and tertiary recovery.

Deep bed filtation is a type of formation damage that efficiently and quickly removes colloids and small particles from the fluid by straining and surface deposition. It has been extensively studied in different aspects of engineering and physical sciences [80, 84, 85, 87, 112, 138, 145]. Particle straining takes place by the process of size exclusion, where the size of the suspended particle is either greater than the orifice or multiple smaller sized particles approach the opening at the same time, leading to bridging and multi-particle blocking. Khilar and Fogler [115] proposed that straining (plugging and bridging) happens when the infiltrate particle is larger than 30% of the pore size while Herzig et al. [87] suggested straining is the dominant mechanism at infiltrate particle diameter greater than 30 μm. Surface deposition is prominent for smaller-sized infiltrate, where surface forces such as electrostatic and van der Waals forces become significant.

Numerous studies [21, 42, 80, 87, 147] have measured filtration in homogeneous sandstone media, while not much attention has been afforded to the carbonates. Formation damage in carbonates is a complex phenomenon due to the wide range of porosity and pore size distribution [37] and has not been studied comprehensively.

The aim of this work is to show the impact of pore heterogeneity, specifically the presence and placement of vugs in carbonates, on particle entrapment. Synthetic vuggy glass bead cores are fabricated with desired porosity and vug structures. Smaller sized glass beads are injected at different flow rates and injected particle concentrations; pressure drop, and therefore the permeability change, is measured across the cores. The cores are scanned using a computed tomography scanner ($\sim$250 μm) before and after injection and the change in porosity is measured.

This dissertation is outlined as follows:

- Chapter 2 provides a brief literature review on mechanisms of formation damage, complexity of carbonate pore structure, experimental and numerical studies in particle entrapment done in the literature. This section identifies the areas where the literature is lacking and serves as the stepping stone for the experimental design for the entire study.

- Chapter 3 focuses on a Guelph dolomite characterization study. Multi-scale imaging is performed on the sample and workflows are generated to identify the pore and vug structures present in the carbonates. The pore heterogeneity of the Guelph dolomite will be the basis of our rock matrix for entrapment experiments in the subsequent chapters.

- Chapter 4 presents a novel glass bead core fabrication techniques which results in a synthetic vuggy core. These cores are used in the subsequent chapters for particulate entrapment and capillary rise experiments.

- Chapter 5 shows an in-depth study on particle entrapment in presence of a single vug

with variation in flowrate and injected particle concentration.

- Chapter 6 extends the study to multiple configuration of vugs.
- Chapter 7 presents a capillary rise study in the presence of vug(s), and shows the interference of vugs on capillary-dominated flow.
- Chapter 8 summarizes the study, discusses the limitations of the work, and proposes work to be done in the future.

Chapters 4, 5, and 6 have been published in peer reviewed papers [110, 112, 113] and have been slightly modified here to fit the flow of the dissertation. Chapter 7 is being prepared for submission to a peer-reviewed journal. All the experimental datasets related to this dissertation are uploaded on the Digital Rocks Portal [106, 108, 109, 111].

Chapter 2: Background and literature review

This chapter starts with an introduction to the problem which relates to solid transport and retention in porous media and then talks about the different sources of solids that can be introduced in the porous media. It then sequently talks about the forces governing particle transport in the presence of a single grain, followed by a porous medium, and thereafter moves onto continuum scale models. Solid transport modeling approaches are discussed along with the prior work I have done on particle entrapment in synthetic porous media. It then briefly looks at the major differences between sandstone and carbonate rocks, and come up with the problem statement and the considerations for the experimental set up.

2.1 Excess water production problem and subsequent water re-injection troubles

Large volumes of water are produced during the life cycle of oil and gas wells [45]. Globally, an average of three barrels of water are produced for every barrel of oil [65], and this increases to more than seven barrels of water per barrel of oil in the United States [196]. Drilling waste, mature oil-fields with a high water cut, hydraulically fractured well kick-off, and coal-bed methane well dewatering are instances of operations with high amounts of produced water. This produced water contains in part oil , radioactive elements, dissolved solids, and suspended solids [11, 16, 35, 81, 213] (Table 2.1). It can be toxic, and dumping it without filtering and cleanup is an environmental hazard [74, 201].

Table 2.1: Mean concentration (mg/kg or parts per million) of several elements and inorganic ions in produced water compared with average concentrations in 3.5% seawater [49].

Element/Ion	**Seawater**	**Produced water**
Salinity	35,000	<500 – >300,000,000
Sodium	10,760	23,000 – 57,300
Chloride	19,353	46,100 – 141,000
Calcium	416	2,530 – 25,800
Magnesium	1,294	530 – 4,300
Potassium	387	130 – 3,100
Sulfate	2,712	210 – 1,170
Bromide	87	46 – 1,200
Strontium	0.008	7 – 1,000
Ammonium	–	23 – 300
Bicarbonate	142	77 – 560
Iodide	167	3 – 210
Boron	4.45	8 – 40
Carbonate	–	30 – 450
Lithium	0.17	3 – 50

Produced water re-injection is a cost-effective method to use this fluid for subsurface oil field operations [206], including but not limited to hydraulic fracturing [103] and water flooding [3, 16], and for disposal in depleted sandstone [120, 176] and carbonate reservoirs [17, 168]. A common problem with injection of unclean fluid is formation damage due to entrainment of solids in the porous media, causing a reduction in the permeability and porosity of the reservoir [154], that can severely shorten the life of the operation. This entrapment is the focus here.

2.2 Particulate flow and retention in porous media

Formation damage is defined as any process that causes a reduction in the natural inherent productivity of an oil or gas producing formation, or a reduction in the injectivity of a water or gas injection well [25, 42]. Common mechanisms causing formation damage, with examples, are listed below and are further classified in Figure 2.2.

1. Mechanical mechanism – e.g. movement and deposition of solids present in the drilling mud and injection fluids due to overburden [53].
2. Chemical mechanism – e.g. asphaltene precipitation during miscible and immiscible flooding [15].
3. Thermal mechanism – e.g. insitu mineral transformation during steam flooding [26].
4. Biological mechanism – e.g. polysaccharide generation by bacteria present in injected water for water flooding [186].

In this dissertation I study mechanical formation damage in single phase flow caused by the movement and deposition of solids inside the porous media.

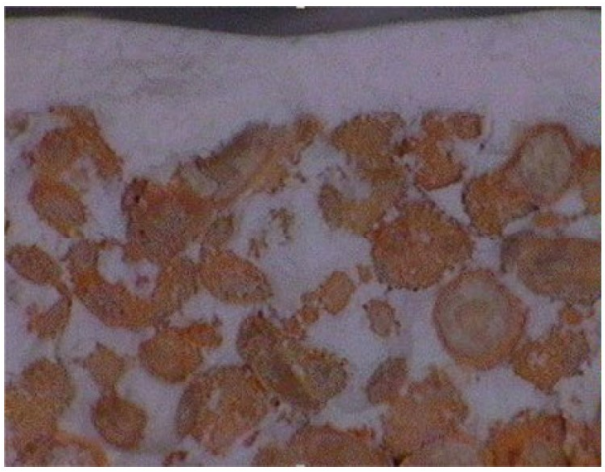

Figure 2.1: Invasion of mud solids on Ketton limestone [21]. Grain to fine ratio 125/1.

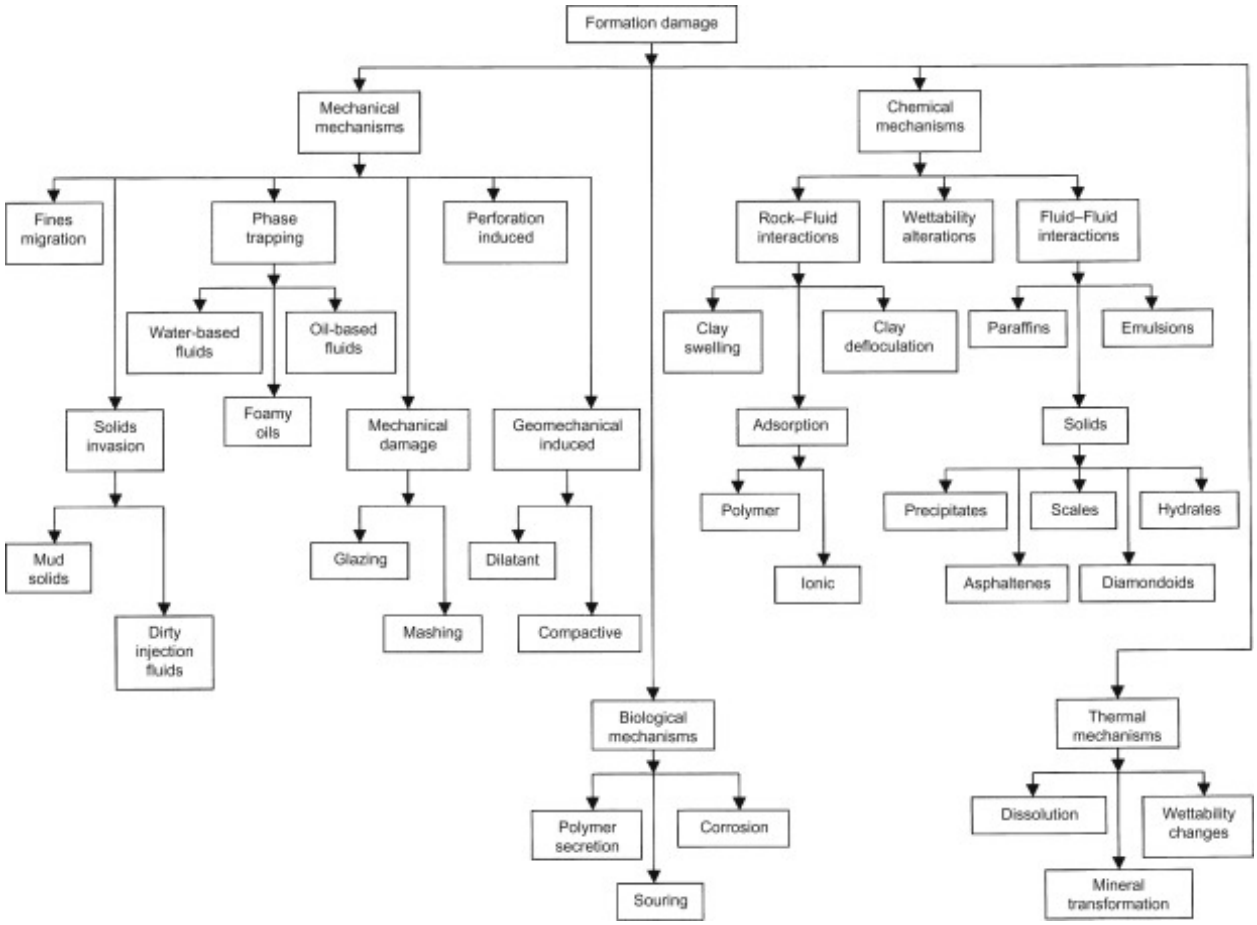

Figure 2.2: Common formation damage mechanisms. (Reproduced from Bennion [25])

2.2.1 Source of particulates

Particulates that deposit in porous medium can either be introduced via the injected fluid with high concentrations of dissolved solids or they can be generated in-situ by the rock-fluid interaction. In-situ generation of particulates can be further divided into either release of fines, which are small particles (< 63 μm) [90] present in all naturally occuring porous material [80] and have a diverse minerology [116, 150] (Figure 2.3), or biological/chemical production of a solid. Multiple processes can release fines including water salinity change and mineral replacement [75, 102], chemical dissolution [64, 165, 191, 203], and grain crushing [24, 38] while algal secretions [128] can generate aragonite in-situ.

In this dissertation, I have used the terms "infiltrate particles" and "fines" interchangeably to refer to the solids that are mobilized inside the porous medium and the term "grain" or "bed" to refer to the porous medium.

2.2.2 Single infiltrate particle transport in presence of a grain particle

Infiltrate particles are transported by multiple mechanisms [92] which combine to make the particle capture processes and are effected by the flow conditions [101, 140, 162], porous medium structure [114], surface chemistry of porous medium and invading particles [195], and size of the invading particles [28, 117, 153]. The most common ones are listed below and drawn in Figure 2.4:

Infiltrate particles are transported inside the porous media by multiple mechanisms [92] which combine to make the particle capture processes and are effected by the flow conditions [101, 140, 162], porous medium structure [114], surface chemistry of porous medium and invading particles [195], and size of the invading particles [28, 117, 153]. The most common ones are listed below and drawn in Figure 2.4:

1. Direct interception – If the infiltrate particles are within one radius of the grain surface, they will ultimately have a head on collision with the porous medium due to the surface

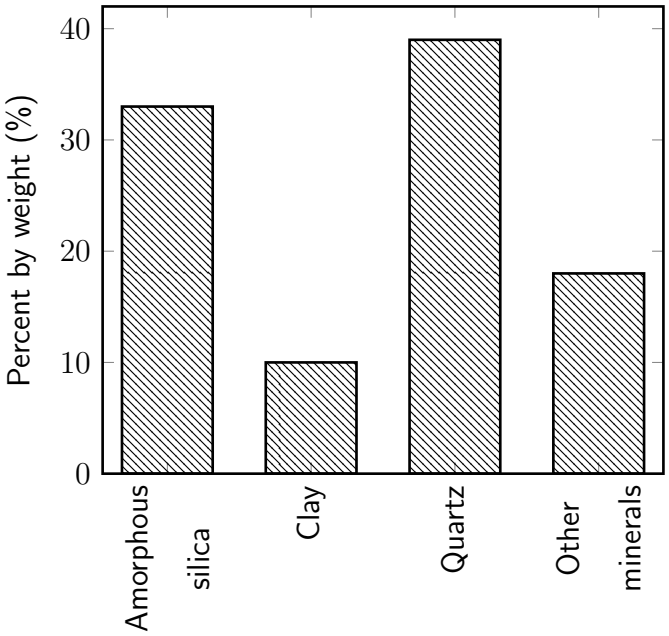

Figure 2.3: Average mineralogical content of fine particles present in five US Gulf Coast formations (reproduced from Muecke [150]).

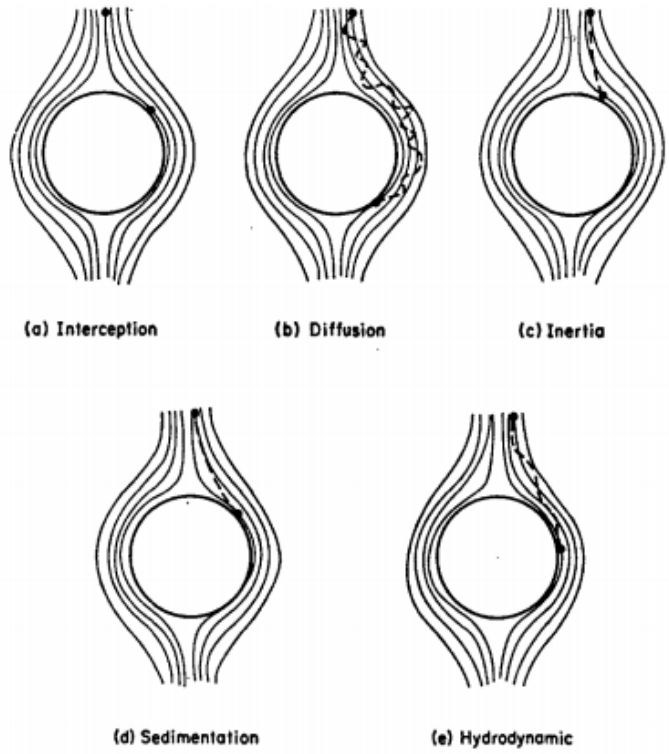

Figure 2.4: Transport mechanism principle (reproduced from Ives [92]).

attractive forces. This mechanism is governed by the invading particle (d_p) to grain diameter (d_g) ratio, with larger ratios having a larger attractive force.

2. Inertia – The infiltrate particles, mostly heavy ones, are not able to move along with the diverging streamlines at the grain surface due to inertia of the particles and fall out of the flow stream. For Darcy flow in porous media, this mechanism is governed by the dimensionless Stokes number (N_{st}):

$$N_{st} = \frac{\rho_p \ {d_p}^2 \cdot u_{fluid}}{18\mu d_g} \tag{2.1}$$

where ρ_p = infiltrate particle density, u_{fluid} = fluid approach velocity, and μ is the dynamic viscosity of the fluid. For large Stokes number, the particles are not influenced by the fluid flow and move with little deviation from their initial trajectory.

3. Sedimentation – If the particle density is greater than the density of the fluid, the gravity forces push the particle into the porous medium. This mechanism is governed by the gravitational parameter (N_g), which differs from inertial interaction by the inclusion of the fluid density and it only acts in the direction of the gravity:

$$N_g = \frac{(\rho_p - \rho_{fluid}) \cdot {d_p}^2 \ g}{18\mu \cdot u_{fluid}} \tag{2.2}$$

where g is the acceleration due to gravity and ρ_{fluid} is the fluid density. A larger density difference between the solid and fluid phase results in a large N_g, and therefore a larger force pushes the particles in the gravitation force direction.

4. Diffusion – Brownanian diffusion, the random movement of fluid particles, is observed for all fluids. This random movement is prominent for smaller particles (< 1 μm), and increases with decreasing particle size. This mechanism is governed by the dimensionless Peclet number (N_{Pe}), which is the ratio of advective transport rate to diffusive transport rate:

$$N_{Pc} = \frac{u_{fluid} \cdot d_g}{D} \tag{2.3}$$

where D is the mass diffusion coefficient and can be calculated as [141]:

$$D = \frac{kT}{3\pi\mu\ d_p} \tag{2.4}$$

where k = Boltzmann constant and T = temperature.

5. Hydrodynamic action – Infiltrate particles undergo rotation due to low sphericity and non-uniform shear forces in the porous medium [92]. This causes the particles to undergo an unpredictable random migration across the shear field which can cause collision with the grain surface.

2.2.3 Forces governing particle retention

Attachment and detachment of the infiltrate particles on the porous medium grain is governed by short and long-range forces [97, 171], which play an important role in particle deposition. The significance of their effect is based on the distance of the infiltrate particle from the grain surface.

1. Axial pressure force of the fluid – As mentioned before, the fluid pressure at the back of a constrained particle can hold it in place and prevent further movement in the porous medium.

2. Inertial force – The inertial force maintains the infiltrate particle motion in a straight line. It can be calculated as:

$$F_{intertial} = \pi \cdot \frac{d^3\ {u_{fluid}}^2 \cdot (\rho_p - \rho_{fluid})}{3{\phi_{bed}}^2\ d_g} \tag{2.5}$$

3. London-van der Waals force – Van der Waals (vdW) forces are the sum of all the weak intermolecular forces between two close surfaces and constitute of attractive or repulsive electrostatic interaction between dipoles, attractive interaction between an induced dipole and permanent multipole on one molecule, and attractive interaction between molecules because of instantaneous dipoles. These can be quantified [82] by:

$$F_g = \frac{h_H \; d_p}{12 \; r^2} \tag{2.6}$$

where h_H = Hamaker constant (5×10^{-13} J), d_p = infiltrate particle diameter, and r = separation between the infiltrate particle and matrix grain. The van der Waals force drops drastically after the first few nanometers (Figure 2.5) and scales with the infiltrate particle diameter (Figure 2.6).

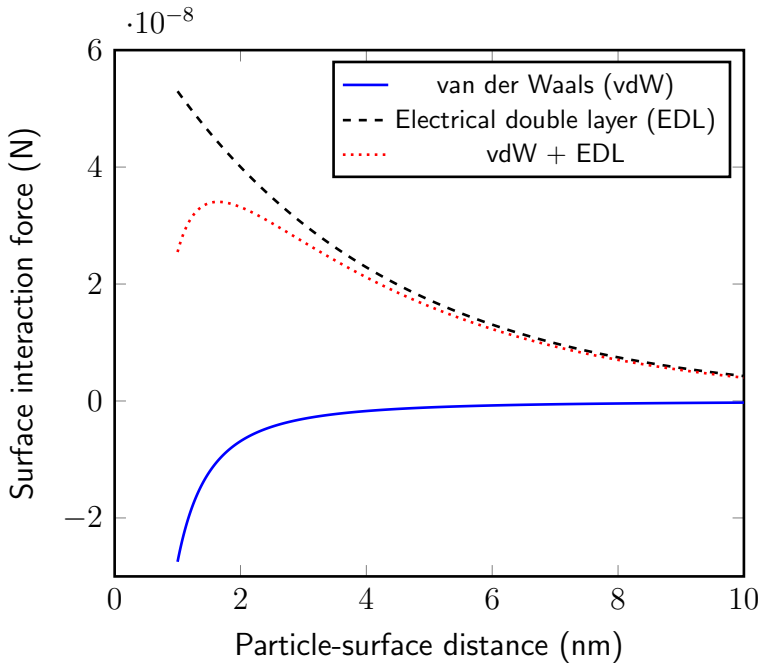

Figure 2.5: van der Waals force, electric double layer force, and the sum of the two forces plotted against the distance between infiltrate particle and grain surface for $d_p = 25$ μm.

4. Electrical double-layer (EDL) interactions – EDL forces are repulsice forces between two parallel layers of charge surrounding the grain due to the grain's surface charges interaction with the fluid ions and is explained by the DLVO (Derjaguin-Landau-Verwey-Overbeek) theory. The first layer consists of ions adsorbed onto the surface (chemical interactions) and the second layer consists of the counter-ions present in the solution. For grain and infiltrate particle of similar material (surface charge), Hogg et al. [88] calculates the EDL interactions as:

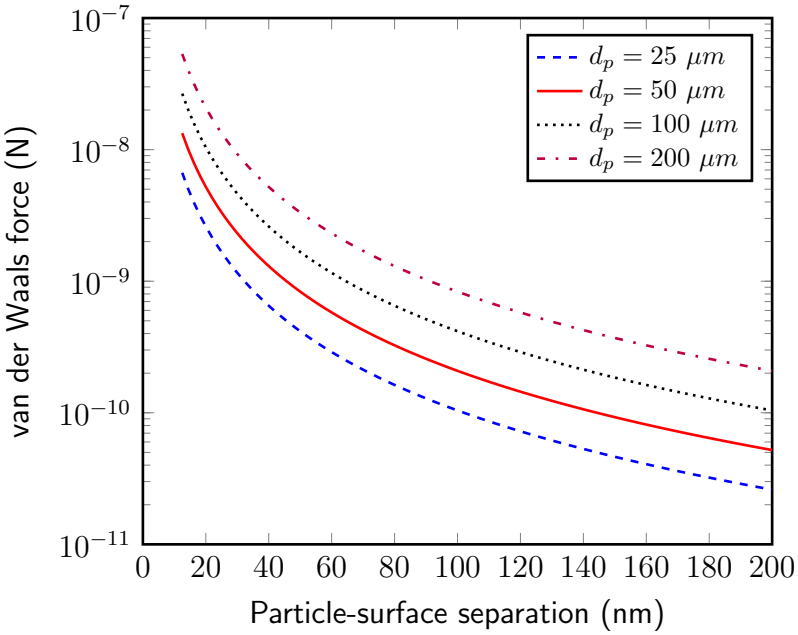

Figure 2.6: Spread of van der Waals force with respect to the infiltrate particle size

$$F_{DL} = \frac{\epsilon\ d_p\ d_g\ {\psi_0}^2}{2(d_p + d_g)}\ ln\Big(1 + e^{-\kappa r}\Big) \tag{2.7}$$

where ϵ = dielectric constant ($7.2 \times 10^{-10}\ F/m$), ψ_0 = surface potential, and κ = Debye-Hückel reciprocal length parameter ($2.8 \times 10^8\ m^{-1}$). Figure 2.5 shows the EDL interactions in comparison with the van der Waals force.

5. Gravitational force – This is the attractive force in the direction of the Earth acting on the particle due to the presence of Earth's gravity. It can be quantified by:

$$F_{gravity} = \frac{\pi {d_p}^3}{6}\ (\rho_p - \rho_{fluid}) \cdot g \tag{2.8}$$

where g = gravitational acceleration and ρ_p = infiltrate particle density. This force is prominent for larger particles. Particles flowing perpendicular to gravity are dragged down while particles in flow streams parallel to gravity get additional acceleration.

Figure 2.7 shows a comparison of the gravity and inertial forces over the injected size

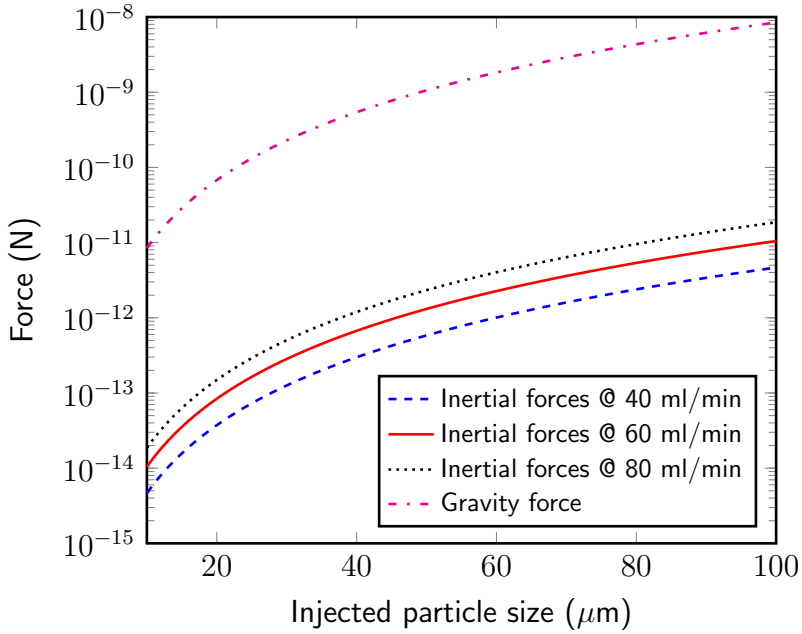

Figure 2.7: Comparison of inertial and gravity forces

of particles and Figure 2.8 shows the grain-surface separation required for the van der Waals force to be equal to the gravity forces. From the two figures it can be deduced that gravity plays a prominent role when the particle size is larger (on the order of tens of microns) while van der Waals forces play a prominent role for smaller-sized particles. The inertial force is consistently three orders of magnitude smaller than the gravity force, and therefore does not play an important role in the filtration.

6. Born repulsion force – These are short range repulsive forces generated between atoms with overlapping electron shells. This determines the closeness of the atom pair. It can be quantified by simplifying the twelfth-power law Lennard-Jones potential [171, 177]:

$$F_B = -\frac{h_H \; d_p \cdot {\delta_{col}}^6}{180 \; r^8} \tag{2.9}$$

where δ_{col} = collision diameter.

7. Hydration force – A monotonic or oscillatory repulsive interaction occurs when two particle with hydrated surfaces (hydration of the ionic surface groups) interact. Raveen-

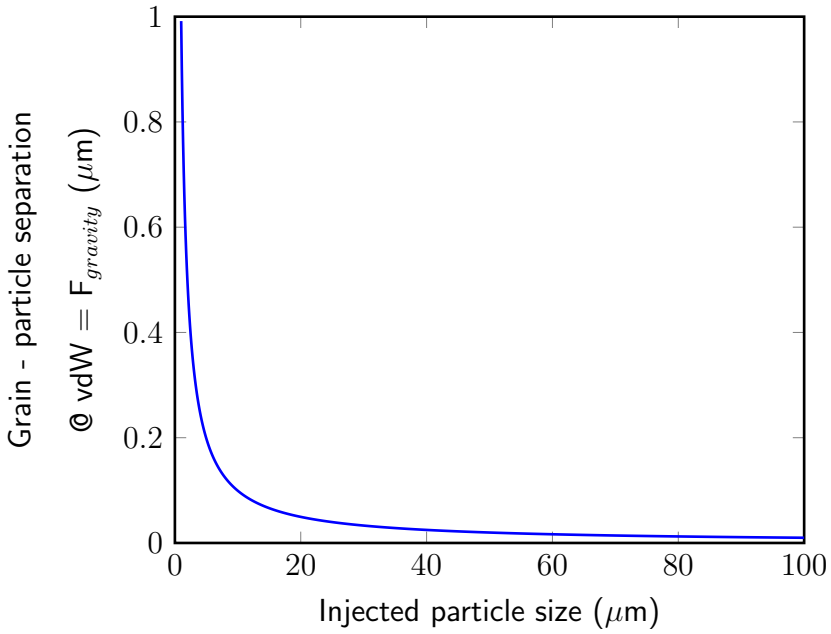

Figure 2.8: Grain-surface separation (in μm) when van der Waals forces are equal to gravity forces

dran and Amirtharajah [170, 171] calculate it by differentiating the total hydration energy (E_h) as:

$$F_h = -\frac{dE_h}{dr} = -2\pi d_p \; Kh \cdot e^{-r/h} \tag{2.10}$$

where K and h are empiral constants for hydration force calculation.

2.2.4 Infiltrate particle retention mechanisms in porous media retention

Combining the transport mechanism along a single medium grain with particle retention mechanisms and extrapolating for a collection of grains, Herzig et al. [87] distinguished four retention sites (surface sites, crevice sites, constriction sites, and cavern sites – Figure 2.9), and four retention forces (fluid pressure, surface forces, friction forces, and chemical forces) that contribute to the retention of infiltrate particles in porous beds. The two most significant retention mechanisms present in the literature, viz., straining and surface deposition, are

described below.

Straining The main process in straining is size exclusion and occurs if the size of the invading particle is larger than the entrance of the pore space or if multiple smaller-sized particles approach the pore opening at the same time causing multi-particle bridging. The particle(s), which are moving along the flow stream, can physically jam and block the pore. The fluid pressure on the back of these particles keeps them jammed.

The retention sites for this mechanism are constriction and crevice sites, and occur by the process of inertial capture and direct interception [56]. Researchers have suggested that the resulting deposits continually reduce the free passage and ultimately plug off the entry to these passages [28, 94, 95, 178, 195], by forming multi-particle bridges [101, 115] (Figure 2.10).

Surface deposition Surface deposition happens when the infiltrate particles are smaller than the pore size [115] and can get close to enough to the surface such that surface forces (e.g. electrostatic force and Van der Waals force) become significant. This happens predominantly for smaller-sized particles.

This mechanism can occur at any retention site, with direct interception [95, 158], diffusion,

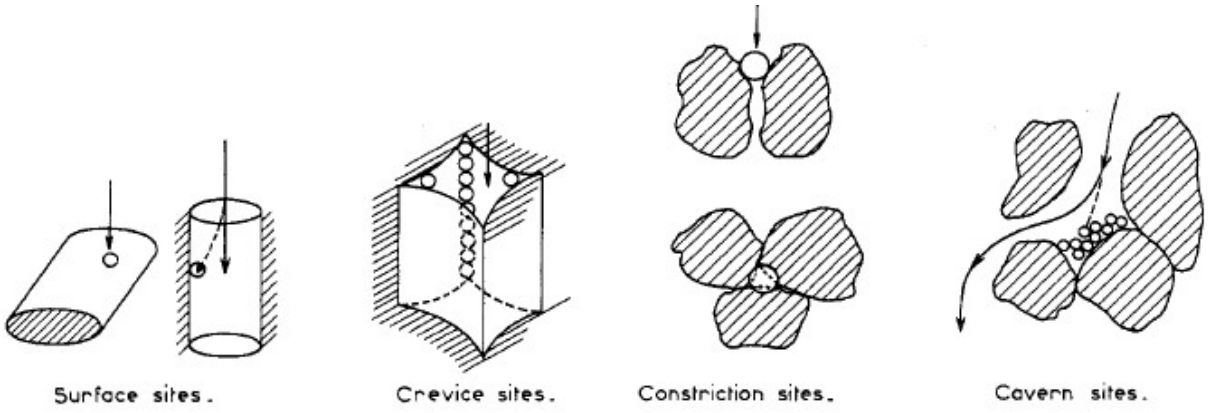

Figure 2.9: Retention sites (reproduced from Herzig et al. [87])

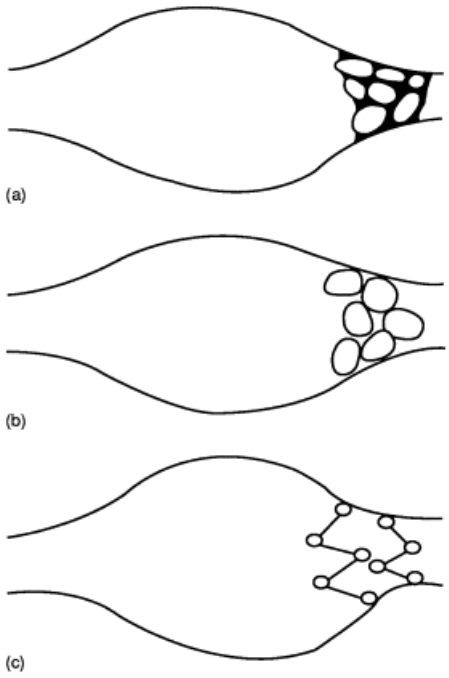

Figure 2.10: Pore blocking mechanism for straining: (a) plugging and sealing, (b) flow restriction, and (c) bridging (reproduced from Civan [43]).

and hydrodynamic action [140] processes contributing the most towards deposition. Surface roughness of the grain may contribute to the particle capture and attachment onto the grain surface [55, 184].

2.2.5 Continuum-scale models

Upscaling the particle retention in porous medium to the core scale results in continuum-scale filtration models, that allow for the estimation of spatial and temporal changes in porosity. It starts with the conservation of mass equation and assumes only convective flow with constant fluid velocity:

$$\frac{\partial(\sigma + \phi c_{sus})}{\partial t} + u_{fluid}\left(\frac{\partial c_{sus}}{\partial z}\right) = 0 \tag{2.11a}$$

$$\frac{\partial \sigma}{\partial t} = T_{wr}^{p} \tag{2.11b}$$

where c_{sus} = suspended particle concentration, ϕ = porosity, u_{fluid} = fluid velocity, t = time, z = length, T_{wr}^{p} = rate of transfer of particles from the fluid to the rock phase, and σ = trapped volume fraction. Different formulations of the term $\partial\sigma/\partial t$ have been suggested, and the two commonly found models are presented below.

Deep bed filtration (DBF) model Iwasaki et al. [96] studied the pollution trapping capacity of sand beds for filtration of municipal water by flowing raw water through a sand bed at a low velocity (3 - 12 m/day), and observing the size, quantity, and spatial location of the pollutant infiltrate using a microscope. He proposed a term *impediment modulus* or λ, which is a measure of the depth of penetration of the suspended particle and has units of inverse length, and the following relationship:

$$\frac{\partial c_{sus}}{\partial z} = -\lambda c_{sus} \tag{2.12a}$$

$$\frac{\partial \sigma}{\partial t} + \left(\frac{u_{fluid}}{\phi}\right)\frac{\partial c_{sus}}{\partial z} = 0 \tag{2.12b}$$

where λ = impediment modulus or filtration coefficient. The first equation shows that the removal of suspended particles from the fluid is proportional to the concentration of suspended particles. The second equation is mass conservation for an incompressible solid/fluid system, and shows that the mass (volume) of particles removed from the fluid would accumulate in the porous bed. The term ϕc_{sus} is small compared to the deposited particle volume fraction. From experimental measurements, he came up with a functional relationship for the impediment modulus:

$$\lambda = \lambda_o(1 + b\sigma) \tag{2.13}$$

where λ_o = filtration coefficient at initial time and b = empirical fitting parameter (which is a function of depth and time).

Different relationships for the impediment modulus have been determined experimentally and theoretically by different research groups, some of which are presented in Table 2.2. Ives and Gregory [95] considered the tortuosity and specific surface, caused by deposition of particles in the filter, to initially increase the bed efficiency (lower λ), before the deposition of the particles reduced it significantly. Heertjes and Lerk [86] neglected the electrokinetic forces and proposed that the decrease in λ is proportional to the increase in interstitial velocity. Sakthivadivel [178] modified the functional relationship by adding the suspended particle concentration term.

Table 2.2: Empirical and/or theoretical relationship for the impediment modulus [92].

Article	**Porous medium**	Impediment modulus [i]
Iwasaki et al. [96]	Sand	$\lambda_o(1 + b_1\ \sigma)$
Stein [190]	Perspex rods	$\lambda_c\left(\frac{1-b_1\ \sigma}{1-b_1\ \sigma_c}\right)^4$
Ives and Gregory [95]	Sand	$\lambda_o\left(1 + b_1\sigma - \frac{b_2\sigma^2}{\phi-\sigma}\right)$
Sakthivadivel [178]	Spherical plastic ball	$\lambda_o[1 + b_1(\sigma + \phi c_{sus})]$
Heertjes and Lerk [86]	Spherical grains	$\lambda_o\left(1 - \frac{\sigma(1-\phi)}{\phi}\right)$
Mackrle et al. [132]	Calcium carbonate	$\lambda_o\left(1 + \frac{\sigma b_1\sigma}{\phi}\right)^{b_2}\left(1 - \frac{\sigma}{\phi}\right)^{b_3}$
Maroudas and Eisenklam [138]	Glass spheres	$\lambda_c\left(1 - \frac{\sigma}{\sigma_u}\right)$

[i] where λ_o = filtration co-efficient at initial time; λ_c = maximum value of λ at $\sigma = \sigma_c$; and b_1, b_2, and b_3 are empirical fitting parameters;

Herzig et al. [87], alongwith [85, 91, 93], proposed a kinetic equation of clogging similar to chemical kinetics but written with time and space variable, and used it with the complete mass balance equation (Eq. 2.11a):

$$\frac{\partial \sigma}{\partial t} = -\lambda c_{sus} \cdot u_m \tag{2.14}$$

where u_m = suspension approach velocity and λ is not a constant and can be defined by a functional relationship similar to those in Table 2.2.

Bailey et al. [21] modified this formulation by adding a clogging efficiency term ($F(\sigma)$) that is a function of the deposited volume fraction. They assumed it to be linear function of deposited volume fraction, i.e. the deposited particles reduce the clogging efficiency of the porous bed. They used the functional relationship proposed by Iwasaki et al. [96] and chose $b_1 = 1$ and fit λ to the deposition profiles generated during their experiments in Ketton limestone.

$$\frac{\partial \sigma}{\partial t} = u_{fluid} \cdot c_{sus} \cdot \lambda \; F(\sigma) \tag{2.15a}$$

$$F(\sigma) = 1 - \sigma \tag{2.15b}$$

To quantify formation damage, pressure loss across the formation was calculated and combined with Darcy law to calculate the change in permeability. Maroudas [137] estimated it for larger-sized grains (2.0 mm) as:

$$\frac{\Delta P}{(\Delta P)_i} = \left(\frac{1-\phi}{1-\phi_i}\right)^{4/3} \left(\frac{\phi_i}{\phi}\right)^3 \tag{2.16}$$

where ΔP = pressure drop across a thickness and the subscript i is at initial conditions. Sakthivadivel [178] proposed a similar formulation:

$$\frac{\Delta P}{(\Delta P)_i} = \left(\frac{1-\phi}{1-\phi_i}\right)^{2} \left(\frac{\phi_i}{\phi}\right)^3 \tag{2.17}$$

Heertjes and Lerk [85] showed that the pressure drop can be estimated by:

$$\frac{\Delta P}{(\Delta P)_i} = 1 + c_1 c_2 \sigma \tag{2.18}$$

where c_1 and c_2 are constants.

Researchers have also calculated permeability from the porosity of the porous media based on fitting the Carmen-Kozeny formulation to experimental data [107, 139, 179]. Bailey et al. [21] assumed the permeability to be a function of σ and calculated it as:

$$k = k_i \left(1 - \frac{\sigma}{\phi_i}\right)^{n=3} \tag{2.19}$$

where k = permeability of rock and k_i = permeability of rock at initial conditions. Boek et al. [32] validated this model using core flood experiments followed by energy-dispersive x-ray diffraction tomography using a synchrotron source (synchrotron EDD-T) and scanning electron microscopy energy dispersive spectroscopy (SEM-EDS) profiling (Figure 2.11).

Parallel pathways partial differential model Gruesbeck and Collins [80] proposed a parallel pathway model which assumes two parallel fluid pathways: plugging (small pore size) and non-plugging (larger pore size). The plugging pathway is blocked by deposition of particles and does not allow any flow whereas the non-plugging pathway is never completely blocked by the particles deposited on the surface, but resulting in a reduction of the pore size (Figure 2.12). The fines are loosely deposited, the fines deposition rate is proportional to the fines concentration, and the fines can be re-entrained at a different position by the moving fluid. Particle exchange between these pathways is not allowed and same particle concentration is assumed in both tracks. They proposed:

$$\frac{\partial \sigma_{np}}{\partial t} = -\alpha(u_{np} - u_c) \cdot \sigma_{np} + \beta c_{sus} \tag{2.20a}$$

$$\frac{\partial \sigma_{pl}}{\partial t} = (\delta + \rho \sigma_{pl}) \cdot u_{pl} c_{sus} \tag{2.20b}$$

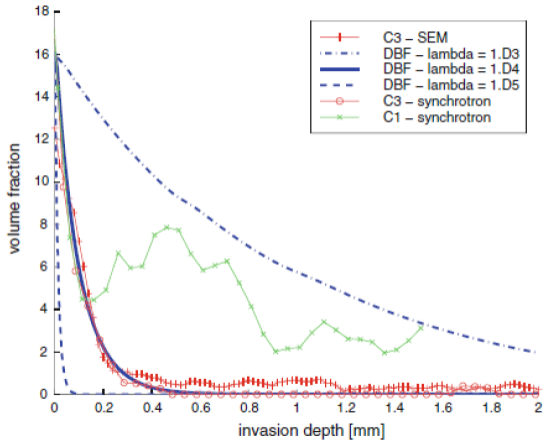

Figure 2.11: Comparison of synchrotron EDD-T and SEM-EDS analysis and DBF model profiling of solids invasion (reproduced from Boek et al. [32]).

where the subscripts np and pl stand for non-plugging and plugging pathways, σ = volume of fines deposited per unit initial pore volume, u = volumetric flux, u_c = critical volumetric flux, and α, δ, and β are constants. They assumed the approximate form of permeabilities, tuned from experiments, to be:

$$k_{np} \approx \frac{k_{np,i}}{1 + \epsilon\sigma_{np}} \tag{2.21a}$$

$$k_{pl} \approx k_{pl,i} \cdot e^{a(\sigma_{pl})^4} \tag{2.21b}$$

where ϵ, a, $k_{pl,i}$, and $k_{np,i}$ are empirically determined constants.

Civan and Nguyen [44] extended the model by introducing particle and fluid transfer between the two tubes (plugging and non-plugging pathways) with the aid of a cross-flow. Furthermore, the bulk fraction of the porous medium containing the plugging and non-plugging pathways were allowed to vary with progression of deposition, with allowance for remobilization of entrapped particles. Eqs. 2.20 were modified with different kinetic laws governing

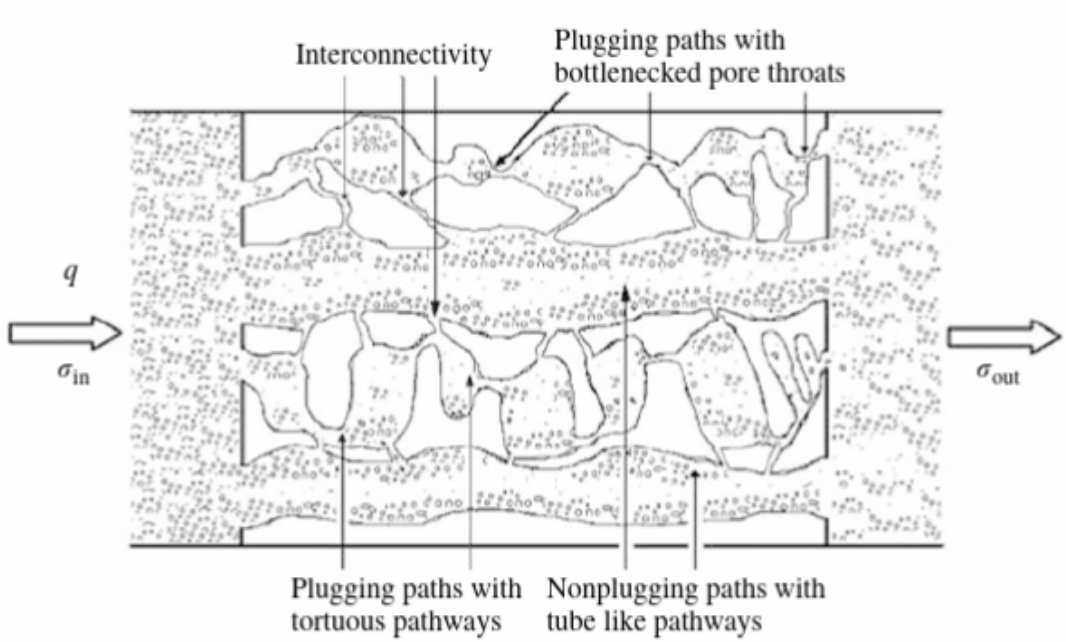

Figure 2.12: Plugging and non-plugging pathways with exchange for particle migration and deposition in porous media (reproduced from Civan and Nguyen [44]).

the rate of fines deposition in each pathway:

$$\frac{\partial \sigma_{np}}{\partial t} = K_d u_{np} {\phi_{np}}^{2/3} c_{sus,np} - K_e \sigma_{np} {\phi_{np}}^{2/3} \eta_e (\tau_{np} - \tau_{cr}) \tag{2.22a}$$

$$\frac{\partial \sigma_{pl}}{\partial t} = (\delta + K_{pl}\phi_{pl}) \cdot u_{pl} c_{sus,pl} \tag{2.22b}$$

where K = rate constant, η_e = fraction of uncovered deposits that can be mobilized from the pore surface, and τ = wall shear stress. The subscripts cr, d, and e stand for critical, surface deposition, and mobilization, respectively.

The permeability for the non-plugging pathway is calculated similar to Eq. 2.19:

$$k_{np} = k_{np,i} \cdot \left(1 - \frac{\sigma_{np}}{\phi_{np,i}}\right)^{n_1} \tag{2.23}$$

where n_1 is an empirical parameter. Plugging pathway permeability is calculated by Civan [41] as:

$$k_{pl} = k_{pl,i} \cdot e^{-\alpha {\sigma_{pl}}^{n_2}} \tag{2.24}$$

where α is a dimensionless constant and n_2 is an empirical parameter. The total permeability of the core can be calculated as a weighted sum of the plugging and non-plugging pathway permeabilities:

$$k = \theta_{pl} k_{pl} + \theta_{np} k_{np} \tag{2.25}$$

where θ = volume fraction of the individual pathway.

2.2.6 Experiments in literature

Deep bed filtration has been studied extensively in different aspects of engineering and physical sciences. Iwasaki et al. [96] studied the effects of pollution in sand filter beds and the different penetration depths of suspended matter. Maroudas and Eisenklam [138] measured the pressure loss in granular media by injecting dilute solutions. Gruesbeck and Collins [80] injected $CaCO_3$ particles suspended in 2% KCl solution in an unconsolidated sand pack and measured the effluent concentrations. Similar experiments were performed by [21, 100, 150, 193, 208].

Al-Abduwani et al. [9] performed the experiments while closely monitoring the flow rate and measured the pressure (converted to permeability), characterized the effluent sample by laser diffraction, and chemically quantified the injection/effluent concentrations. Bedrikovetsky et al. [23] suggested using three core points to determine the filtration coefficient λ. Recently researchers have combined computed tomography imaging [105, 107, 194, 214] and nuclear magnetic imaging [12] with pressure loss data to calculate formation damage.

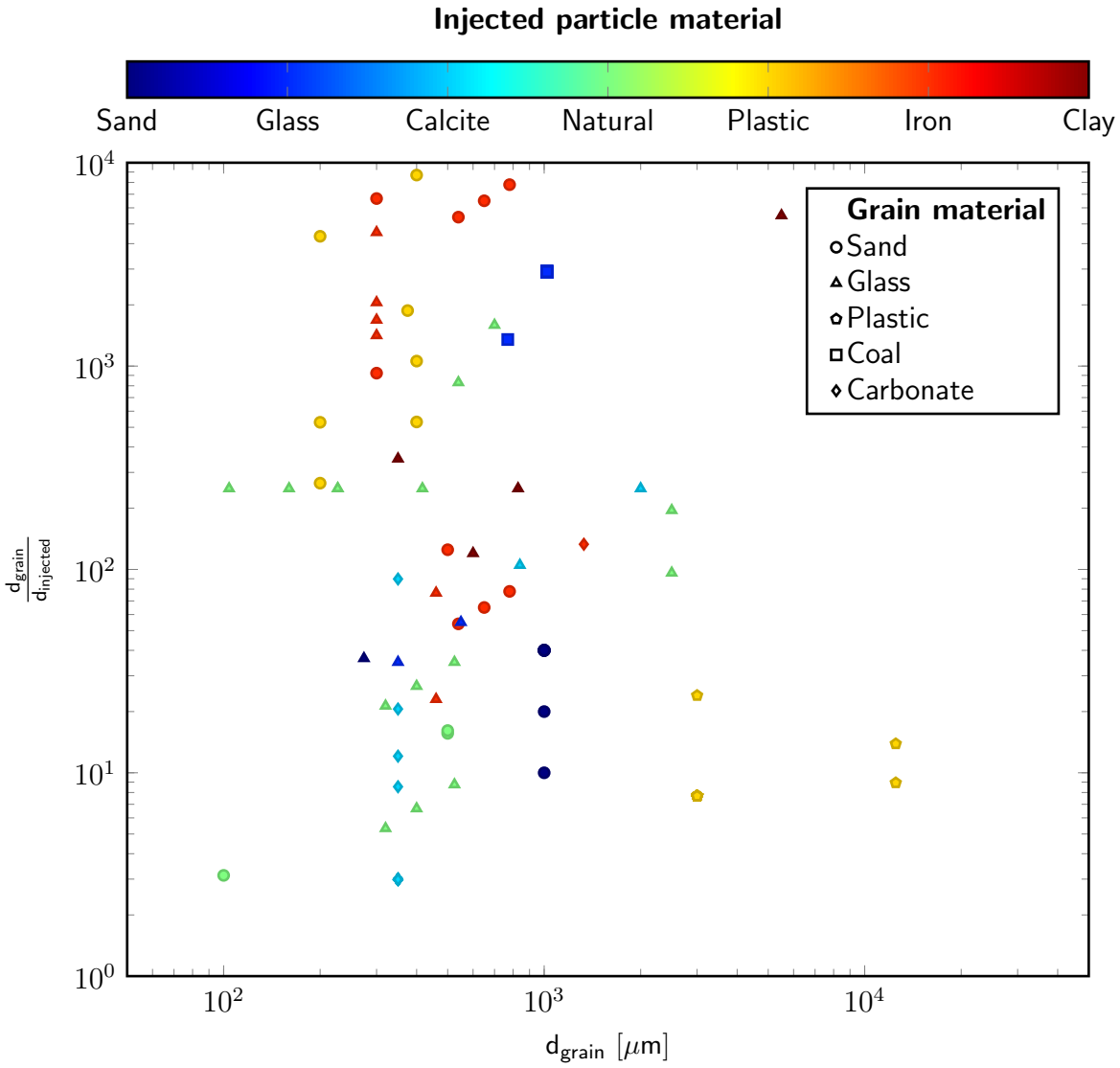

Figure 2.13: Ratio of porous medium grain diameter to injected particle diameter plotted against grain diameter of porous media [21, 80, 86, 87, 95, 96, 107, 112, 138, 145, 158, 178, 190]. The marker shape represents the grain material and the marker color represents the injected particle material.

Figure 2.13 shows a scatter of formation damage experiments present in the literature and plots the size ratio of grain particle to injected particles and the porous medium grain size. A comprehensive variety of sizes and types of injected particles and filtration medium are found throughout the literature, for example Heertjes and Lerk [85] injected $Fe(OH)_2$ in glass sphere packs, Ives and Gregory [95] injected Chlorella in sands, and Bailey et al. [21] injected $CaCO_3$ in Ketton limestone in their experiments. Most of the experiments have been performed in uniform porous media; some experiments have been conducted in carbonate media, but they have been performed in Ketton limestone, which consists of large connected uniform pore spaces [31]. The experiments presented in Figure 2.13 are not an exhaustive list, for which the readers are referenced to the excellent review papers by Herzig et al. [87] and Ives [92].

Researchers have suggested different size ratio limits based on studies of particle removal by straining and surface deposition. Herzig et al. [87] proposed that straining is dominant for suspended particles larger than 30 μm. Abrams [4] suggested that the particles are trivially affected by electrochemical surface force, and together with Barkman and Davidson [22] proposed that particles less than one-third and greater than one-seventh the pore diameter form an internal filter cake. van Oort et al. [193] further modified this range to one-third to one-fourteenth of the pore diameter for low velocities (< 0.033 cm/sec). Khilar and Fogler [115] suggested that surface deposition is only important when particles are less than one-tenth of the pore throat. Figure 2.14 shows the injected particle approach velocity plotted against the ratio of grain diameter to injected particle diameter for some of the experiments in Figure 2.13. The marker color denotes the porous medium grain size.

Imaging in formation damage Computed tomography (CT) imaging has been used in petroleum engineering to non-destructively observe porosity distributions, saturation distributions, and multiphase flow in rocks [8]. CT imaging scans, computes, and combines 2D x-ray scans of the sample from different angles. Electrons produced in a cathode are directed at a metallic target to generate x-rays, which are then transmitted towards the sample and

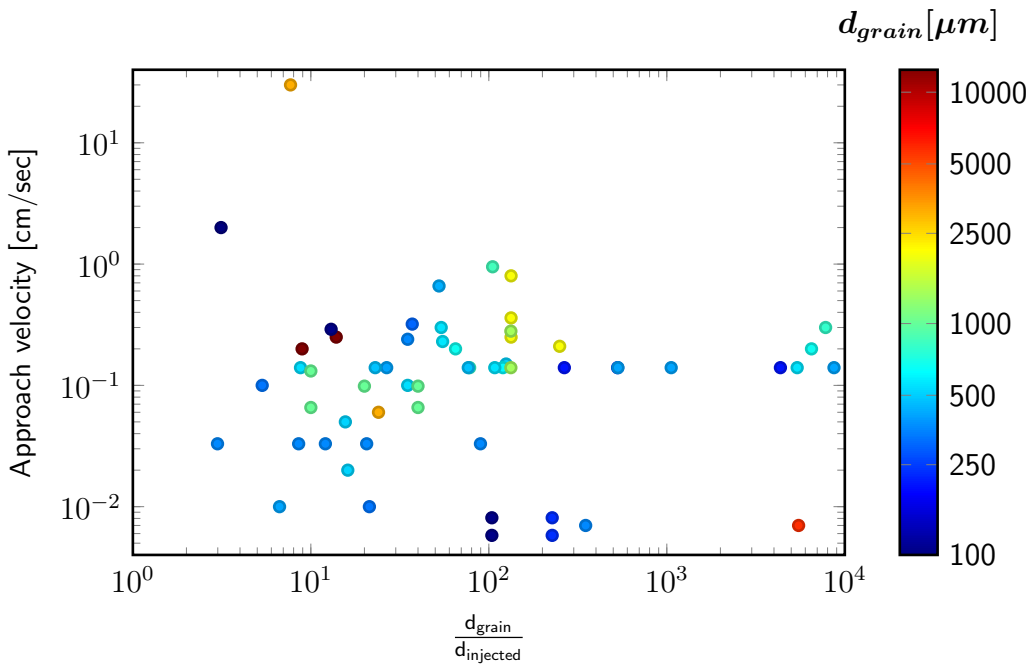

Figure 2.14: Approach velocity of the injected particles plotted against the ratio of porous medium grain diameter to injected particle diameter [21, 62, 63, 80, 86, 87, 95, 96, 107, 112, 138, 158, 178, 190]. The marker color represents the diameter of the porous medium grain.

captured by the detector. The attenuated x-rays captured at the detector, dictated by the electron structure of the sample, give a measure of the attenuation coefficient, and therefore the density, of the sample using the Beer-Lambert law:

$$I_1 = I_0 \cdot e^{(\mu t)} \tag{2.26}$$

where I_0 = x-ray intensity at the source, I_1 = x-ray intensity measured at the detector, μ = attenuation coefficient, and t = thickness of the absorbing medium.

3D tomogram of the sample is reconstructed by combining x-ray images obtained from different angles and solving a system of equations. The scanner setup can be such that either the source is fixed and the sample is rotated (in case of micro-tomographs), or the source can rotate with the sample fixed in its position (in case of medical CT scanners).

Time-lapse radiography has been used to detect the relative permeability and saturation evolution during multiphase flow [40, 126]. The same principle has been applied in formation damage studies to determine the porosity change due to the flooding experiment [107] and the spatial location of injected particle [12] at the end point. Recently continuous time-lapse imaging has been successfully used to determine the time-evolution of porosity due to particle deposition [76].

Micromodels, which are quasi-2D physical models with the pore structure etched on silicon wafers [33, 199] with a bonded glass cover, are another very common way to image and visually observe flow mechanisms. They have been extensively used to study two-phase pore-scale flow mechanisms in porous media [59, 67, 161, 200]. The glass cover allows direct visual observation (and optical imaging) of the pore-scale mechanisms [104, 118]. Additionally, the surface properties of the micromodel can be modified to incorporate the effect of wettability [77, 187] and the pore/throat sizes can be varied in depth [20, 210].

Micromodels have been used to study single-phase [20] and dual-phase [198] colloid transport in porous media. They are a good method to understand the mechanisms related to surface deposition, where the size of the injected particles is significantly smaller than the

pore/throat size, but struggle to capture the mechanisms associated with straining as the pore/throat become plugged. The main limitation is the depth of the model, which is one grain deep, and does not capture the effect of flow re-routing to the adjacent pore in the third dimension.

2.2.7 Pore-scale modeling approaches for particulate flow and retention

Pore-scale modeling of formation damage can be done using either Eulerian methods or Lagrangian methods. Eulerian methods describe the particle concentration in space and time and are not concerned with the location of each particle at a specific time. Lagrangian methods describe the trajectory of the particle and record the location of each particle at any specific time. The two methods discussed here are: computational fluid dynamics – discrete elements method (CFD-DEM) and pore network models (PNM).

Computational fluid dynamics – Discrete element method Computational fluid dynamics method solves the Navier-Stokes equation by discretizing it in space and time (Eq. 2.27). This method has the advantage of simulating fluid flow with large viscosity and density ratios and has been utilized to approximate macroscopic rock properties [142, 166]. The biggest challenge in porous media application is proper spatial discretization of the flow domain.

$$\rho\frac{Du}{Dt} = -\nabla p + \mu\nabla^2 u + \frac{1}{3}\mu\nabla(\nabla\cdot u) + \rho g \tag{2.27}$$

Discrete element method is used for computing the effect and motion of discrete particles. It has been used to model the behavior of granular media, with applications in rock physics [51, 174]. The point of contacts of the particle are modeled as a spring-dashpot system (Figure 2.15). The normal and tangential force, based on a linear spring-dashpot system,

are:

$$F_n = -k_n \Delta x_{p,n} + \gamma_n \Delta u_{p,n} \tag{2.28a}$$

$$F_t = min\{|k_t \Delta x_{p,t} + \gamma_t \Delta u_{p,t}|, fF_n\} \tag{2.28b}$$

where k = stiffness, Δx = overlap between particle, γ = damping constant, Δu = relative velocity between particles, fF_n = Coulomb frictional limit, and the subscript n and t stand for normal and tangential respectively.

Open source software such as OpenFOAM [1] and LIGGGHTS [119] have been used to simulate particle flow in porous media by a coupled CFD-DEM approach [144, 148, 155], with fairly close approximation of the porosity profiles [145].

Pore network models Pore network models simplify the porous network into an interconnected network of pores (balls) and throats (tubes) (Figure 2.16) and simulate flow by solving mass conservation equations at each pore (Eq. 2.29) [66, 207]. Traditionally each pore or throat was assumed to be spherical or tubular [29], but high resolution micro-CT scans show that they can have different shapes. Pore networks can be extracted from high resolution micro-CT images [30, 57, 207].

$$\sum_{j=1}^{N_i^{th}} \frac{g_{i,j}}{\mu}(P_j - P_i) = 0 \tag{2.29}$$

where $g_{i,j}$ = hydraulic conductivity of the throat connecting pores i and j, P = pressure in pore, and μ = fluid viscosity.

Pore network models for formation have been used in formation damage studies [173, 184, 192]. At each time iteration, the pore hydraulic conductivity is updated based on the volume

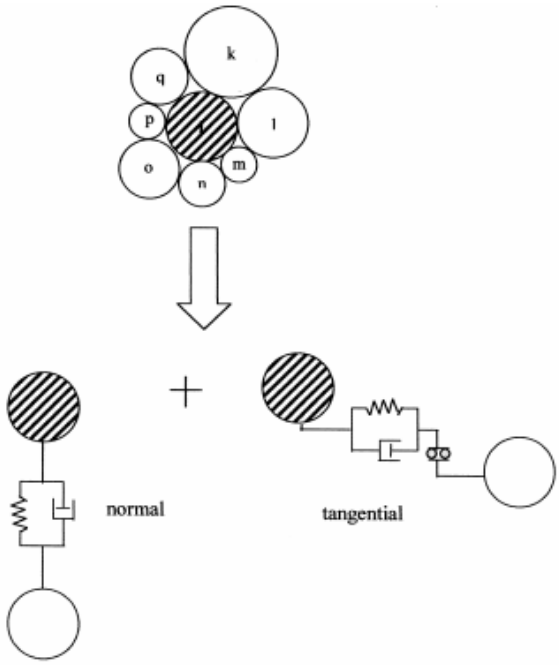

Figure 2.15: Schematic representation of spring-dashpot model in the normal and tangential directions (reproduced from Rajamani et al. [167]).

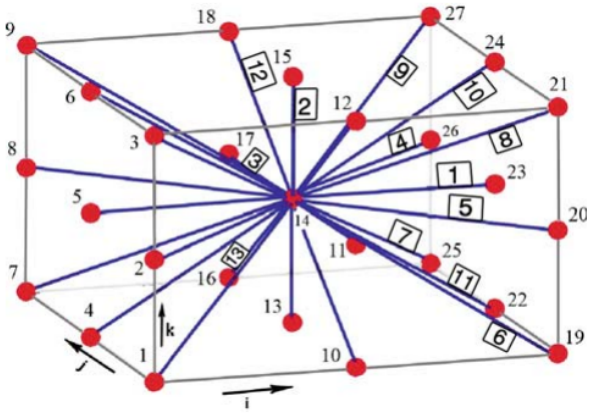

Figure 2.16: Cubic lattice with 26 pore coordination number (reproduced from Raoof and Hassanizadeh [169]).

of deposited particles [212] which results in the change in shape of the pore throat. Details about this methodology can be found in Yang [211].

2.2.8 Prior work on particulate entrapment in synthetic porous media

At this point the reader is advised to have a look at my Masters thesis [105] which details the particulate entrapment experiments in homogeneous media.

In summary, I fabricate homogeneous porous media using 1.0 mm diameter glass beads as the matrix grain and inject smaller-sized glass beads at three unique injection particle concentration (0.5%, 1.0%, and 2.0% v/v) and two unique flow rates (40 and 60 ml/min). The two flow rates result in the particle approach velocity of 0.0657 cm/sec and 0.0985 cm/sec, which are in accordance with the values found in the literature (Figure 2.14). The injected glass beads (25 μm, 50 μm, and 100 μm) are injected as bi-modal sets, and the total volume of injected glass beads for all the flow cases is kept the same. I measure and quantify the changes in porosity using computed tomography (CT) scans and the changes in permeability using continuous pressure measurements.

The study reached the following conclusion:

1. Injected particle size plays the chief role in formation damage. Larger sized particles have a higher damage as compared to the smaller sized particles. If the injected particle size is very small, the flow rate and concentration have no sizeable effect on the porosity and permeability.

2. Size exclusion (entrapment) causes a larger loss in formation permeability as compared to surface deposition.

3. External filter cake significantly influences the internal filter cake and hence the formation damage. A higher flow rate can cause fingering in the external filter cake and hence change the expected change in porosity and permeability.

4. Small core can have end effects and this can significantly alter the porosity and permeability measurements.

To better quantify and predict formation damage, the experimental results were combined with two different numerical models (each focusing on a different mechanism/length scale) to predict permeability reduction [107]. The first model took a pore-scale approach that modeled straining of larger particles through the pore structures extracted from x-ray tomographic images of rock and grain pack samples from first principles.

The detailed pore structure output from the first model was used as an input for the second model, which is a network model. This pore network model simulates permeability impairment caused by both large and small particles deposition in porous media. Forces exerted on small particles include hydraulic drag, gravity, buoyancy, electric double layer, and van der Waals. Particle trajectories in a converging- diverging pore throat were calculated dynamically, and surface roughness and particle-surface interaction are incorporated to determine particle detachment and attachment. Pore throat structure and hydraulic conductivities were updated dynamically to account for the effect of previously deposited particles. The comparison of experimental and simulation predictions showed that the combined pore- scale model was capable of predicting the porosity of the invaded core only in the deeper regions of the core.

The workflow was modified to decouple the deposition of small and large particles and introduce a new upscaling procedure to get the aggregate effect of bi-modal particle injection [112]. A dual pore-scale numerical model approach (a combination of a direct pore-scale discrete element method (DEM) and a pore-scale network model) was used to predict permeability reduction by particle filtration in porous media under different mechanisms: surface deposition and straining. Capture of large particles was assumed to be independent from the deposition of small particles. Large particle deposition was modeled using the DEM in a disordered sphere pack geometry (Figure 2.17); the result was a prediction of deposition as a function of large particle concentration. Small particle deposition was modeled using the

network model; the result being a prediction of deposition as a function of small particle concentration.

The two simulation results were then combined and up-scaled to get an aggregate effect of the two grain sizes. Comparison of the experimental results with simulation predictions shows that the dual pore-scale model is capable of predicting the permeability of the invaded core in the regions away from the injection face. Permeability prediction in the region adjacent to the injection face is improved by incorporating the influence of the external filter cake.

2.3 Differences between sandstone and carbonate rocks

Sandstones typically have a single-scale porosity and pore size distribution and limited chemical reactivity [37]. On the other hand, carbonates are complex rocks having a wide variety of pore types, pore sizes, pore distributions [71, 204], and greater chemical reactivity. Inter-granular pores comprise the primary porosity in carbonate rock [151] while dissolution, mineral replacement, and recrystallization, to name a few, can lead to secondary porosity on a localized level [5, 7] (Figure 2.18). Song et al. [188] experimentally showed that carbonates have pores on different length scales with complex spatial distributions of pore and pore connectivity.

Voids larger than the normally expected interparticle pore space are called vugs. These can be formed by the dissolution of the rock fabric or recrystallization of the carbonate mineral [151, 218]. Lucia [131] classified the vuggy pore space based on the connectivity of the pore space and rock fabric (Figure 2.19).

Vug spaces contribute significantly to the local porosity of rock, however permeability strongly depends on vug connectivity. High contrast between the size of the vug and the pore space results in a very heterogeneous flow [13, 217] and makes it difficult to characterize and predict carbonate rock properties [6]. Core samples, which are not always available, are too heterogeneous and complex to isolate the effects of several quantifiable parameters. Therefore,

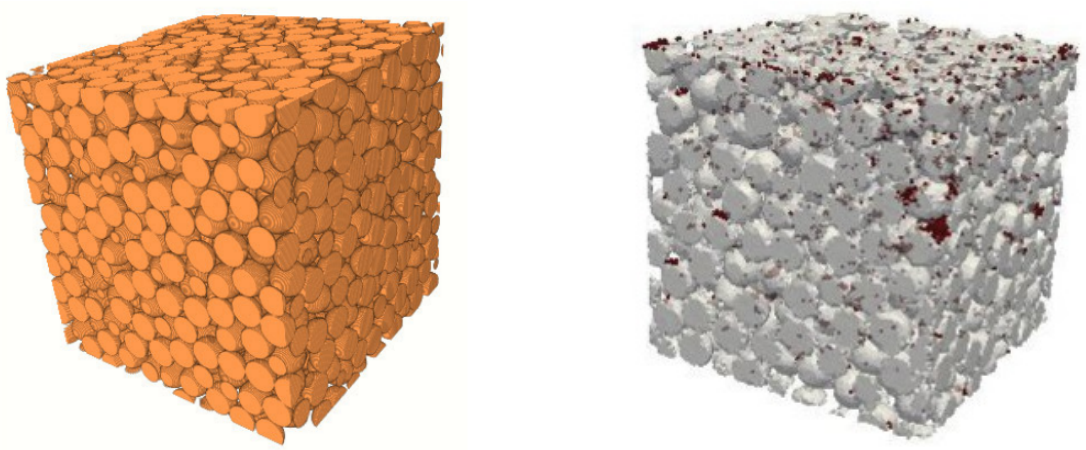

(a) 3D visualization of disordered sphere pack – 8 mm × 8 mm × 8 mm (reproduced from Mirabolghasemi [144]).

(b) 3D visualization of gray porous medium grains and red injected large particles (reproduced from Khan et al. [112]).

Figure 2.17: Disordered sphere pack before and after particle entrapment.

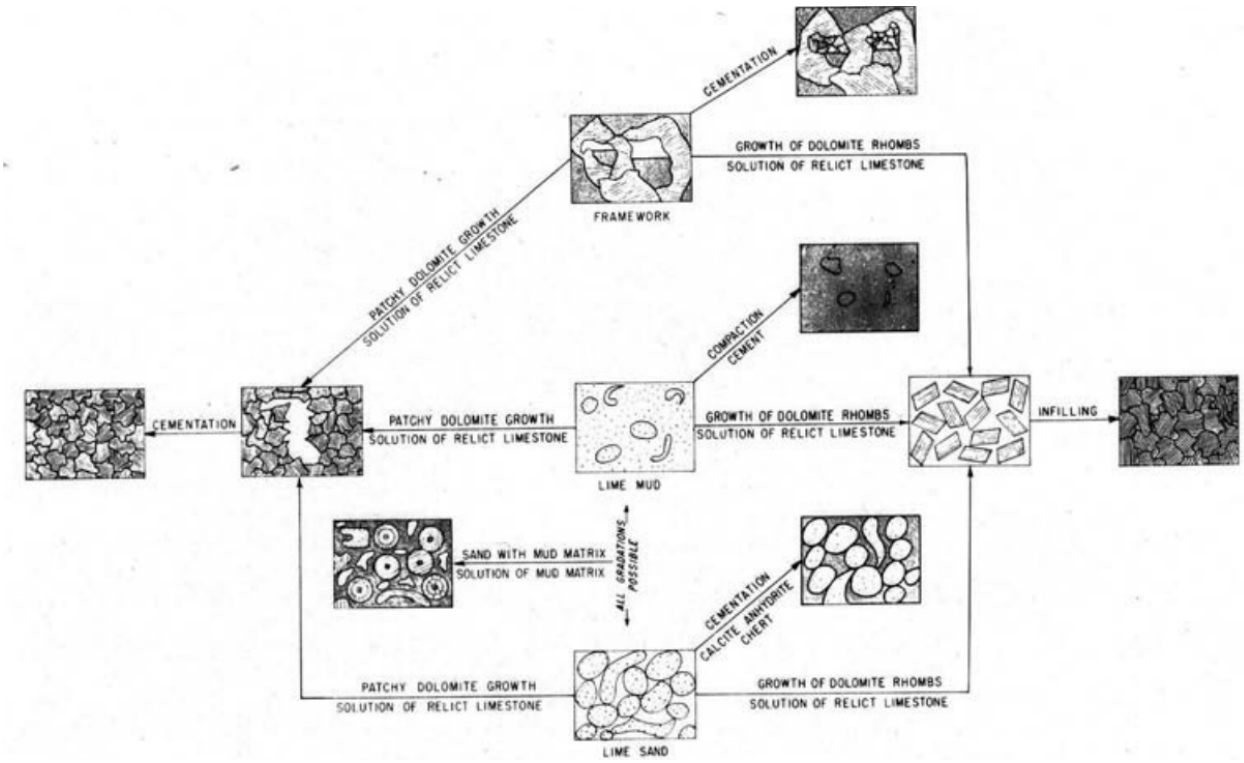

Figure 2.18: Evolution of lime mud (center) into different carbonate pore types by chemical processes (reproduced from Murray [151]).

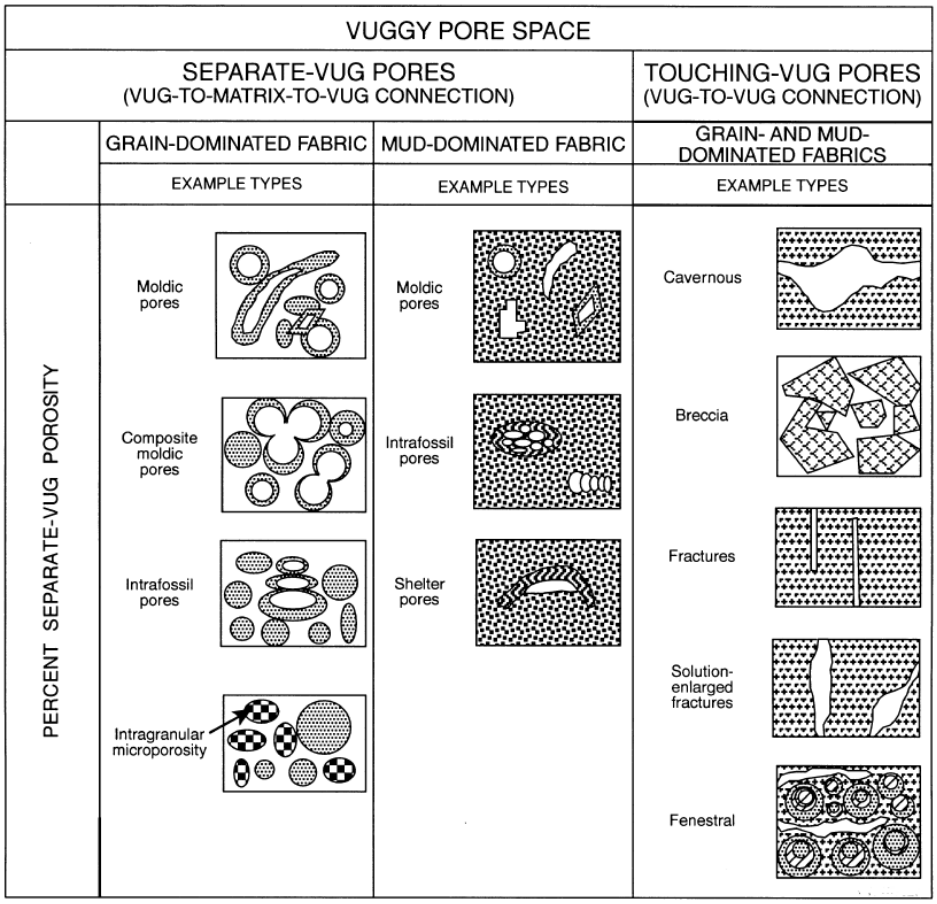

Figure 2.19: Geological and petrophysical classification of vuggy pore space (reproduced from Lucia [131]).

very little is currently known about the two-phase flow behavior in vuggy carbonates [34]. Combining the effect of particulate movement in this media, the estimation of formation damage in carbonates becomes a stumbling block.

Assessing permeability of vuggy carbonates is an outstanding problem in formation evaluation [197]. Carbonate pore space is complex to start with, and the standard formulae (e.g. Timur-Coates) do not apply. Furthermore, formation near the wellbore is damaged and that is not accounted for in the formulae.

2.4 Problem statement

From extensive literature review, it has been identified that:

1. Formation damage due to straining and surface deposition has been studied in multiple disciplines of science (from water resource management to medical engineering) and the problem is generally understood. Many contrasting theories have been suggested of how the filtration process progresses in porous media.
2. The majority of the work has been done in uniform porous media, specifically sandstone rocks in the petroleum engineering and water resource literature.
3. Little work related to solids transport in carbonate rocks is found in the literature.

The main challenge in carbonates is pore space heterogeneity as pore sizes vary from below micron length scale in micro-porous regions to millimeter scale vugs or dissolution features. In this work I focus on singling out the effect of pore-size heterogeneity by answering the following questions:

1. Can a proxy core be fabricated that is similar to a real carbonate in its pore heterogeneity but does not posses its chemical reactivity and surface forces?
2. What would be the effect of pore heterogeneity on straining and surface deposition for different proxy core configurations?
3. Can we predict how much formation damage would occur and where would it occur?

2.4.1 Experimental considerations

In the work presented here, I attempt to fill in the gaps found in the literature. The size of the grain was chosen as 1 mm, on the upper echelons of the sand sized particles (Figure 2.13), while the injecting particles were chosen as 25, 50, and 100 μm. These sizes cover the two extremes of the deposition processes as discussed in the literature, and also considers the transition zone between surface deposition and straining processes. The particle approach

velocities in the proposed study is in the range 0.06 to 0.1 cm/sec, which is in the center of the velocity spectrum present in the literature (Figure 2.14).

The other matter of importance is the material used for the porous bed and the injected phase. The literature has a wide medley of material used in experiments. which range from anthracite, sand, calcium carbonate, and glass for the filter medium and $Fe(OH)_2$, algae, pollen, and quartz powder for the injected phase. A few desired material qualities are:

1. Low surface forces as the focus will be on straining, i.e. size exclusion.
2. Capability of doing repeatable experiments.
3. Homogeneous and uniform injected phase.
4. Material that is easily penetrable by x-rays to allow 3D spatial investigation.

Review of commonly used material resulted in identifying the following properties for glass: low surface forces, high sphericity, uniform bead size, high mechanical strength, and chemically non-reactivity. Combining these with the ease of handling, low cost, and ease of availability, I selected and used glass beads for this work. A few more positives resulting from using glass beads include the ease of having repeatability and comparison with simulation models based on bead packs. I have thus aimed at 3D variants of micromodels, so to speak: simple as possible, but no simpler.

Chapter 3: Vuggy carbonate benchmark and image-based vug characterization

Rocks in nature, specifically vuggy carbonates, are complex real rocks [34] with a large variety of pore openings present in them [71, 204]. These openings are difficult to observe under the naked eye and are usually observed using a combination of multiple scanning techniques [205]. When interacting with the suspended solids these differences in pore sizes, spanning multiple orders of magnitude, result in different particle deposition mechanisms, and therefore different particle deposition patterns. Furthermore the matrix is naturally chemically reactive, and therefore evolves over time with transport of fluid in the subsurface. The combined effect of these factors makes it very difficult to discern the exact characteristics of particle deposition in these vuggy medium.

The objective of this chapter are two-fold: (i) generate a laboratory core measurements benchmark dataset for a complex carbonate formation; and (ii) produce workflows based on high resolution images to identify and characterize the vugs. In this chapter, I first measure and report routine petrophysical properties (e.g. porosity, permeability etc) for a highly heterogeneous Guelph dolomite rock core. Then I scan the core in a computed tomography (CT) scanner to get low and high resolution digital image sets of the core and apply image analysis workflows on them to identify and characterize the vugs.

Rock characterization in petroleum engineering is usually done with respect to the petrophysical properties of the rock; here I characterize the vugs inside the rock based on the

vug size, vug shape, and the vug distribution. These parameters are important in reference to the particulate entrapment in porous media, as will be discussed in the later chapters. Figure 3.1 shows the general workflow for this study.

3.1 Experimental measurements

A core measuring 1.5 inch in diameter and 3 inch in length was cut from a Guelph dolomite block (courtesy of Dr. Gary Pope). The core was dried in an oven operating at 200 °C and routine petrophysical measurements (porosity, permeabililty, NMR T_2, and elastic properties) were experimentally determined. The core was then imaged at two different resolution in the x,y-direction: 250 μm in a medical CT scanner and 23 μm in a micro-CT scanner.

The core was then saturated with 2% $CaCl_2$ solution as the equalization brine, which had been found to be non-reactive to the rock [58], and elastic properties were again determined. The core was then CT scanned at the two resolutions. This section highlights the methods used to determine the petrophysical properties.

3.1.1 Petrophysical properties

Porosity The porosity measurements are obtained through multiple experimental methods and the results are listed in Table 3.1:

1. Helium porosimeter on dry core,
2. Bulk measurements for dry and saturated core,
3. Nuclear Magnetic Resonance (NMR) T_2 measurement, and
4. CT scan on dry and saturated core.

Different techniques give diferent porosities, with the average porosity value calculated as $(14.3 \pm 0.73)\%$. The high error value can be attributed to the difference in scale of observation and limitation of the different measurement techniques. For example the CT scanning

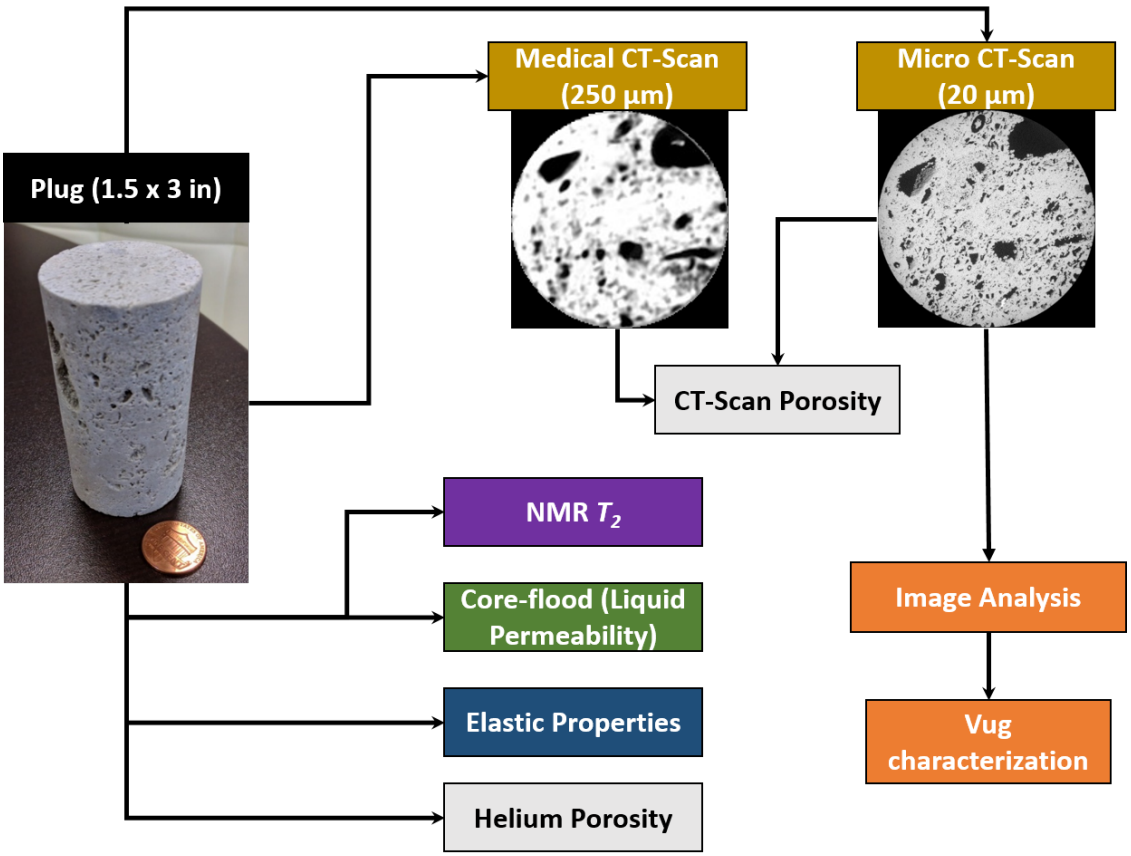

Figure 3.1: Overall project workflow.

would observe the total pore space while the fluid transport based methods, like Helium porosimetry, would only access the connected pore space. Therefore, based on the different measuremnt methods, we can estimate that the total porosity is ∼15.1% out of which the effective porosity is ∼14.6%. These values are similar to ones presented in the literature [39, 58, 83] for the same rock, though the variations can be significant based on the zone where the core is cut and how the vugs are distributed. The medical CT scanner, operating at a resolution of 250 μm, does not have enough resolution to look at the small pores and therefore significantly underestimates the porosity. Furthermore, a few vugs are present on the side surface of the core which can be partially filled during the porosity measurement (e.g. NMR) and therefore skew the measurement.

Brine permeability measurements Brine permeability is measured in the full core (1.5 in x 3 in) using the set up shown in Figure 3.2: the core is first dry vacuumed for 12 hours and then vacuum saturated for another 12 hours. It is then flooded with 10 pore volumes of the equalization brine, under 300 psi back-pressure, in order to guarantee that the sample is fully saturated. The brine is then pumped at multiple flow rates, under two different back-pressures (300 and 500 psi), and the pressure drop along the core is measured. The stabilized pressure is used to calculate the brine permeability of the core. The average permeability of the rock is calculated as 114.9 mD (Table 3.2), which lies within the range of permeability

Table 3.1: Porosity measurement using different methods.

Method	**Porosity (%)**
Helium porosimeter	14.6
Nuclear Magnetic Resonance T_2 scan	13.4
Bulk measurement	15.1
Medical CT scan	13.4
Micro-CT scan	15.2

values present in the literature [14, 39, 58].

NMR T_2 measurements NMR T_2 distribution of the saturated core sample is measured using a benchtop 2 MHz-frequency Magritek NMR spectrometer to measure T_2 distribution to estimate the pore size distribution. The Spectrometer uses Carr-Purcell-Meiboom-Gill (CPMG) pulse sequence with 50,000 echoes and with an echo time of 100 μs for measuring magnetization decay [48]. The T_2 distributions are estimated from inversion of NMR magnetization decay measurements incorporated in the NMR equipment software. A minimum signal to noise ratio (SNR) of 200 is set to guarantee reliable results. Four unique zones, colored differently based on their pore size (Figure 3.4), are identified from the resultant plot.

Elastic properties Acoustic measurements are made on dry and brine saturated core using 500 kHz and 250 kHz input signal for P-wave and S-wave respectively. The signal is passed along the length and diameter of the core and measured on a Keysight DSOX2024A Oscilloscope. The measured properties, for dry and brine saturated sample, are presented in Table 3.3.

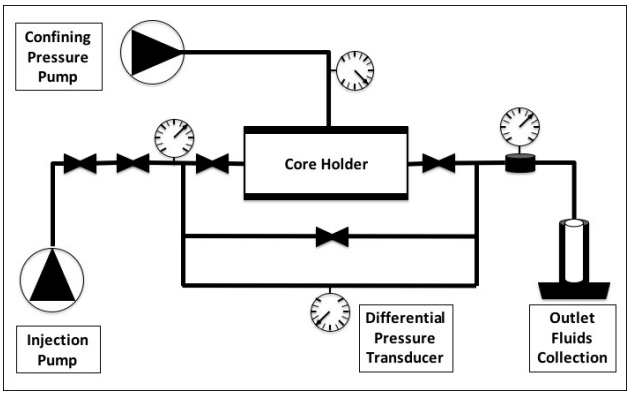

Figure 3.2: Core flooding setup schematics.

Table 3.2: Brine permeability measured for the Guelph dolomite core at different flow rates with multiple back-pressures.

Sample ID	**GD#1-1**	**GD#1-2**	**GD#1-3**	**GD#1-4**
Diameter [cm]	3.77	3.77	3.77	3.77
Length [cm]	7.57	7.57	7.57	7.57
Area [cm^2]	11.19	11.19	11.19	11.19
Flow rate [ml/hr]	180	360	200	400
Differential pressure [psi]	4.30	9.17	4.46	9.88
Back pressure [psi]	300	300	500	500
Permeability [mD]	115.6	108.5	123.9	111.8

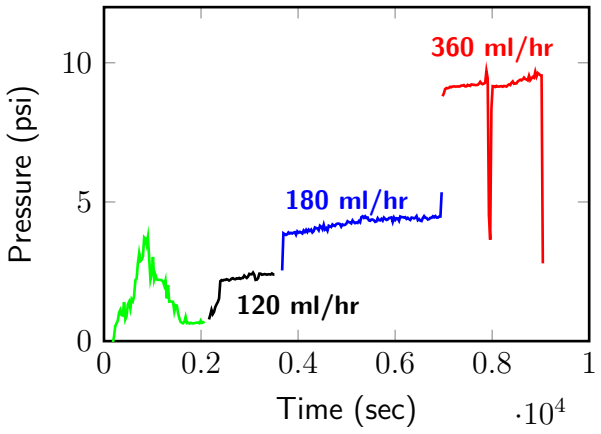

Figure 3.3: Pressure trace for brine permeability measurement at different flow rates with a back pressure of 300 psi.

Table 3.3: Elastic properties determined for the Guelph dolomite core.

Property	**Bulk modulus [10^6]**	**Shear modulus [10^6]**	**Youngs modulus [10^6]**	**Poisson's ratio**
Dry core	6.07	3.51	8.82	0.258
Wet core	6.68	3.44	8.81	0.280

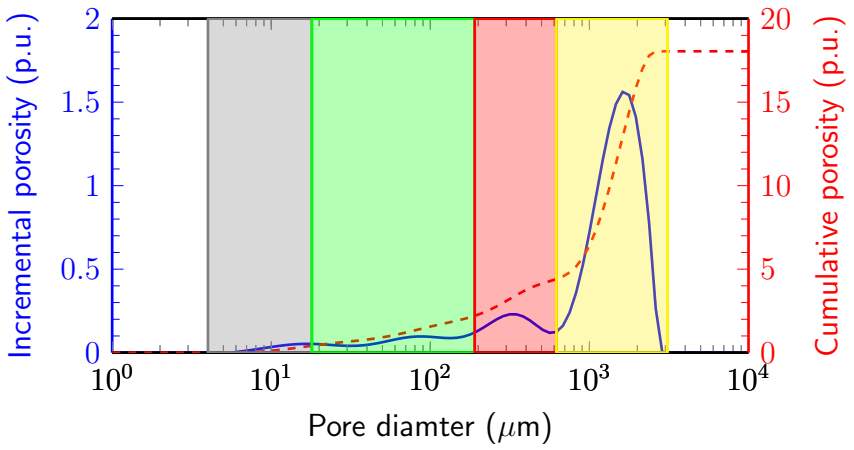

Figure 3.4: NMR T_2 distribution for the Guelph dolomite sample. Four prominent pore sizes (shading colors) are evident from the T_2 distribution.

3.1.2 Computed tomography (CT) scanning

CT scanning is performed in-house on the whole core at different resolution: low resolution scans on the medical CT scanner and the high resolution scans on the micro-CT scanner (Figure 4.3).

Medical CT scanner The medical CT scanner, which operates at a resolution of up to 250 μm in x,y-direction and 3 mm in z-direction, is used to identify the macroscopic features of the core. The scan parameters used are 3 second scan time, 1.5 mm scan thickness, 1.5 mm scan spacing, 130 kV voltage, and 200 mA current. More details about the scanner are presented in the next chapter (Section 4.1.5).

Figure 3.5 shows the porosity map generated from the low resolution CT images. Large pore openings (vugs) are observed spread throughout the core; these account for the high porosity estimates for the rock.

Micro-CT scanner The micro-CT scanner, which can operate at a resolution of up to 3 μm, is used to scan the whole core at a resolution of 23 μm. The resolution is high enough

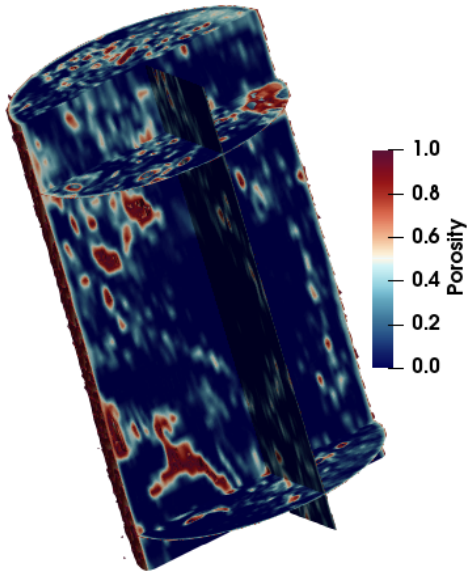

Figure 3.5: Porosity map visualization based on the low resolution (medical) CT scans.

to identify a lot of the small vugs that were sub-resolution in the medical CT scan (Figure 3.1) and results in well defined boundary for the larger vugs. More details about the scanner are presented in the next chapter (Section 4.1.5).

3.2 Image analysis workflow for vug and pore size characterization

Rock characterization groups together rocks with similar physical properties: in petroleum engineering this is done with respect to the petrophysical properties of the rock. The vugs can be classified on the basis of volume or shape: here I characterize the vuggy rock, first on the basis of the pore sizes, and subsequently on the basis of vug structure inside the rock based on the surface to volume ratio. The vug parameters (vug size, vug shape, and the vug distribution) are important in reference to the particle entrapment physics in the vuggy porous medium as evidenced in the subsequent chapters.

Rock fabric pore size characterization From the high resolution micro-CT scans, a 100-slice subsection from the middle of the core is selected as the image stack. The image

stack is opened in FIJI-ImageJ [180] and is processed to clear the zone outside the core and isolate the rock. The image is then denoised which enhances the small features present in the image (Figure 3.7).

Intensity profile along the width of the core image shows that different vug sizes tend to show different gray values (Figure 3.8) because of blurring and non-sharp boundaries. These can cause errors when thresholding and segmenting the image. A non-local means filter [54] is applied to reduce this error (Figure 3.6).

Weka-3D machine learning algorithm [18] is applied to the image stack next to identify the pore space, matrix, and the outside region (Figure 3.9). The data set is manually trained for a couple of images and the trained classifier is then applied to the rest of the image stack. Watershed algorithm [157] is applied to the pore space in conjunction with Euclidean distance transform and the result is segmented to isolate the pore bodies. ImageJ's FIND CONNECTED REGION algorithm [127] is used to label each individual pore body. The image stack, containing the pore body labels, is exported to MATLAB [2] where the pore bodies are sorted based on volume.

The NMR previously identified four unqiue pore zones present in the rock fabric (Figure 3.4). This information, combined with the limitation of the NMR that it cannot measure anything with a relaxation time larger than that of water and the large vug that transverses across the length of the core, I have used five zones as the classifier for sorting the pore volumes.

K-means clustering, based on the the Euclidean distance [19], is used as the sorting algorithm and applied to the log of the pore volume. The sorted pore bodies are labeled individually and then combined to create the final image stack (Figure 3.10). Zone 5 is the largest vug that transverses across the length of the core and was not captured by the NMR scan.

Vug structure characterization The denoised 100-slice subsection from the middle of the core is selected as the image stack; it can be segmented to isolate the vugs using either

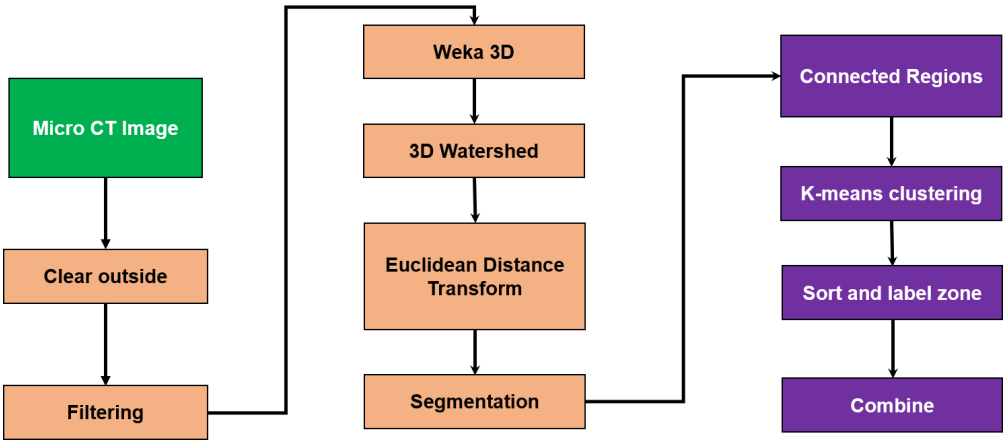

Figure 3.6: Image analysis workflow for pore size characterization.

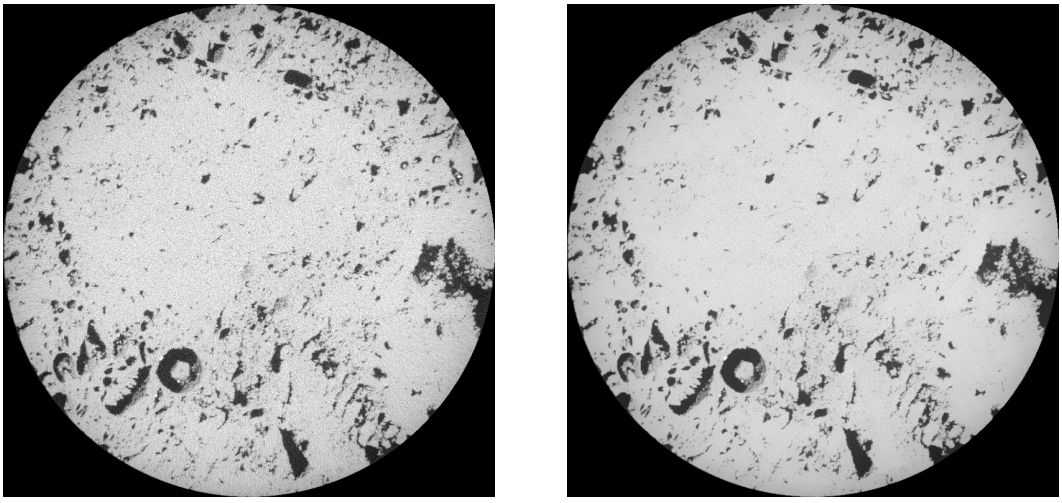

(a) Original

(b) Denoised

Figure 3.7: Image quality is improved by denoising the image.

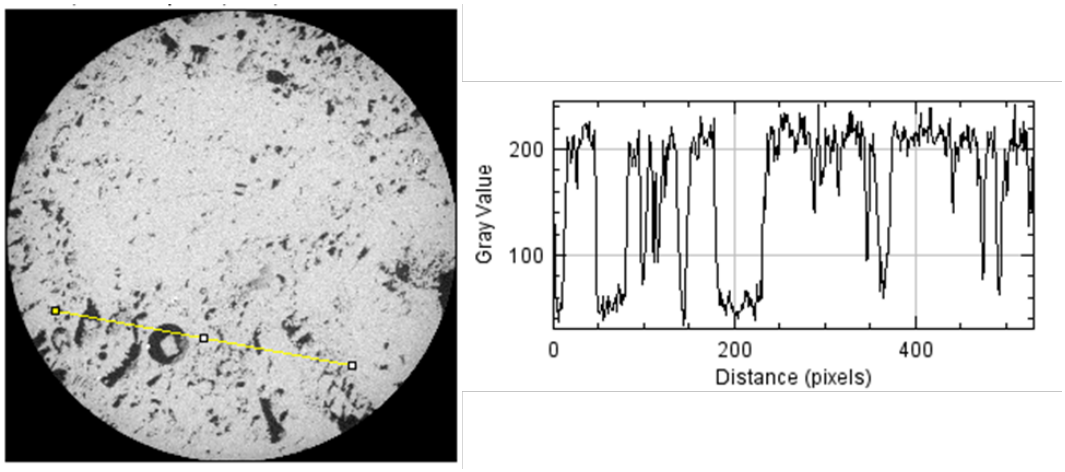

Figure 3.8: Sample image (left) and gray value profile along the yellow (right) shows different vug size tend to have different gray value. Non-local means filter is applied to reduce this difference and reduce errors in thresholding.

of the two approaches:

1. 3σ method [125] proposes that the greyscale value of the CT images follow a Gaussian distribution and the segmentation threshold can be taken as 3 times the standard deviation (σ) derived from fitting the Gaussian distribution to the CT images.
2. Deconvolution method detailed in Victor [197].

Both of these methods give similar results; for ease of application I use the 3σ method for segmentation. After segmentation, individual vugs are identified by using ImageJ's FIND CONNECTED REGION algorithm [127] and then imported into MATLAB to calculate the physical properties (volume, surface etc.) of each individual vug. Vugs here are defined as pore openings that are larger than the image resolution (23 μm).

Vugs make up most of the pore space, accounting for 12.2% porosity, compared to 15.2% porosity determined via micro-CT (Table 3.1). Figure 3.11 shows the segmented vugs colored by the size of the aperture.

The surface to volume ratio, also the inverse of the effective radius, is a measure of the shape of the body. A smaller the S/V ratio for a vug, large aspect ratio (ratio of largest dimension

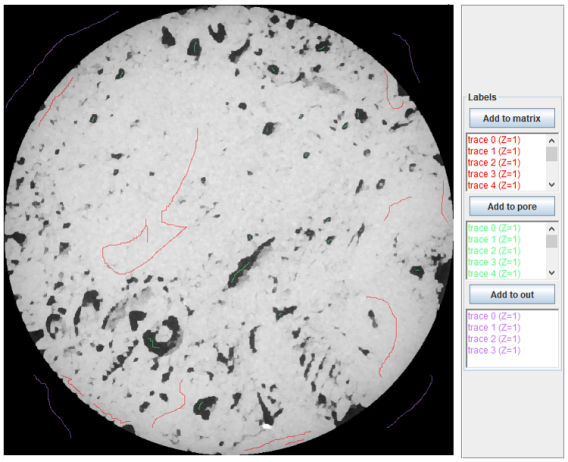

(a) Input control for the Weka-3D package [18] in Fiji-ImageJ. Different zones are identified to train the classifier.

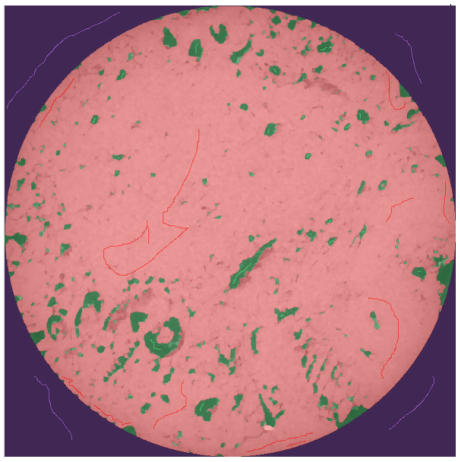

(b) Classifier image which identifies the zones similar to the chosen ones based on the image statistics (mean, median, mode etc). Image classification can be repeated until the desired output is achieved.

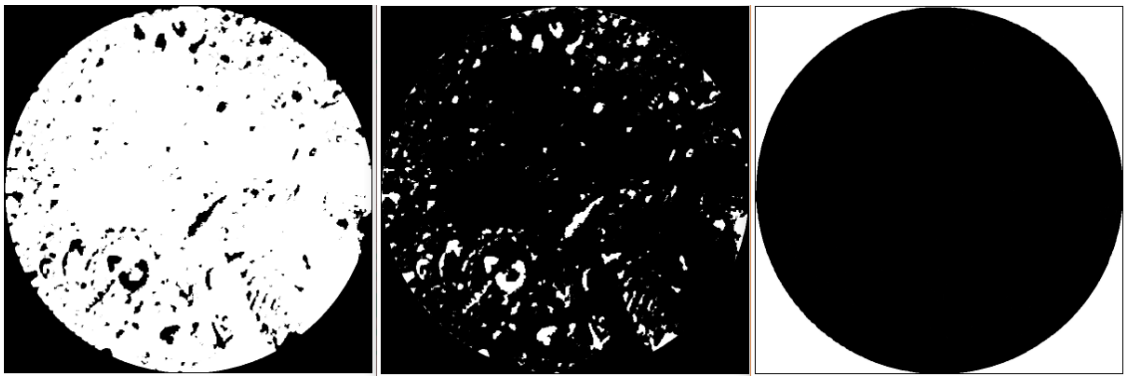

(c) Classified images from Weka-3D from left to right: matrix, vug, and outside.

Figure 3.9: Once the classifier is trained on an image, it can be applied to the rest of the image stack and segmentation can be done very quickly. For this case, the classifier has been trained to identify three zones: vug, matrix, and outside.

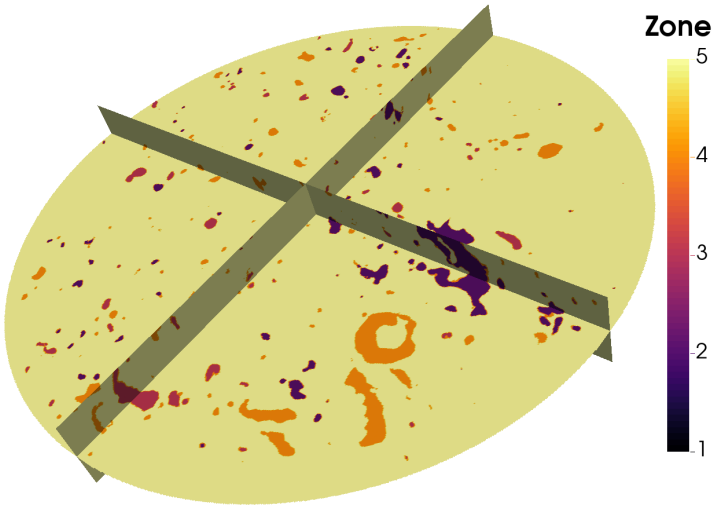

Figure 3.10: Zones characterized based on connected pore volume. Zone 1 has the smallest pore volumes and zone 5 consists of one large vug that transverses across the sub-section.

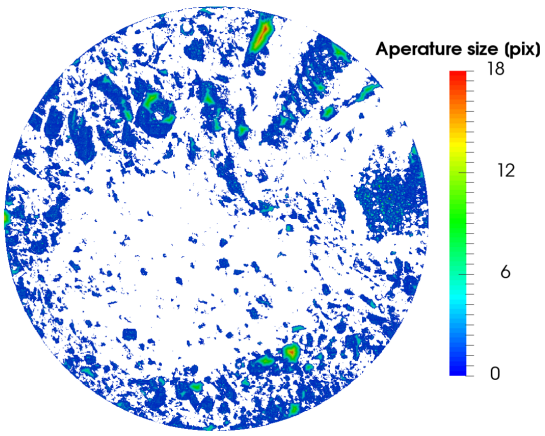

Figure 3.11: Vug spatial distribution based on its aperture size.

to the smallest dimenstion), implies an elongated vug. Therefore the shape of the vug can be estimated based on its S/V ratio derived from the image stack.

The S/V ratio for simple geometrical bodies can be calculated based on progression series: for simple face-connected cubes, S/V ratio can be calculated as:

$$\frac{S}{V} = \frac{2mn + (2m + 2n) \times i}{mni} \tag{3.1}$$

where i, n, and m = number of cells in x, y, and z-direction (Figure 3.12). Therefore a cube shaped vug, which is one voxel across, will have a S/V of 6 and a cube shaped vug, which is two voxels across, will have a S/V of 5. Similarly, the S/V ratio of edge connected bodies can be calculated as:

$$\frac{S}{V} = \frac{4i + 2n + 2}{i} \quad \forall i \geq n + 1 \tag{3.2}$$

where i, n, and m = number of cells in x, y, and z-direction. Figure 3.13 shows the possible S/V ratios for simple edge-connected and face-connected vug bodies upto15 voxels long in each dimension. The edge-connected bodies, due to reduction in the number of external faces, tend to have a higher S/V ratio while the face-connected have a smaller S/V ratio.

Figure 3.14 shows the normalized volume of each connected vug, with respect to the total vug volume, plotted against the S/V ratio. One vug, with a S/V value of 0.8327, contributes ∼75% of the total vug volume and transverses through the image stack. The S/V ratio also suggests that the vug will have a high aspect ratio, i.e. an elongated shape. This large vug is easily identifiable in the image stack (Figure 3.15).

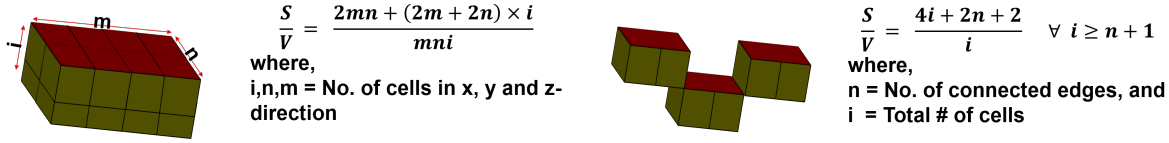

Figure 3.12: Vug shape: face-connected (left) or edge-connected (right).

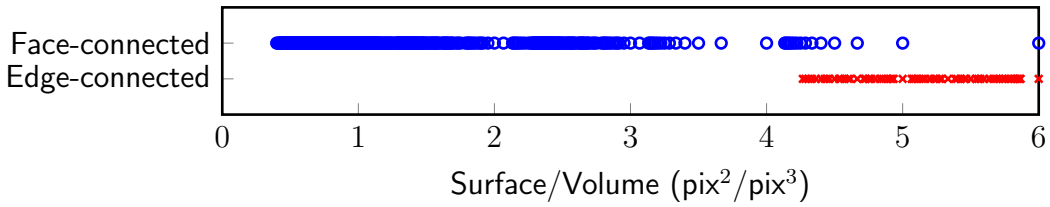

Figure 3.13: Simple vug shapes can be either face- or edge-connected. The S/V ratio uniquely possible for a combination of 15 voxel in each direction are plotted.

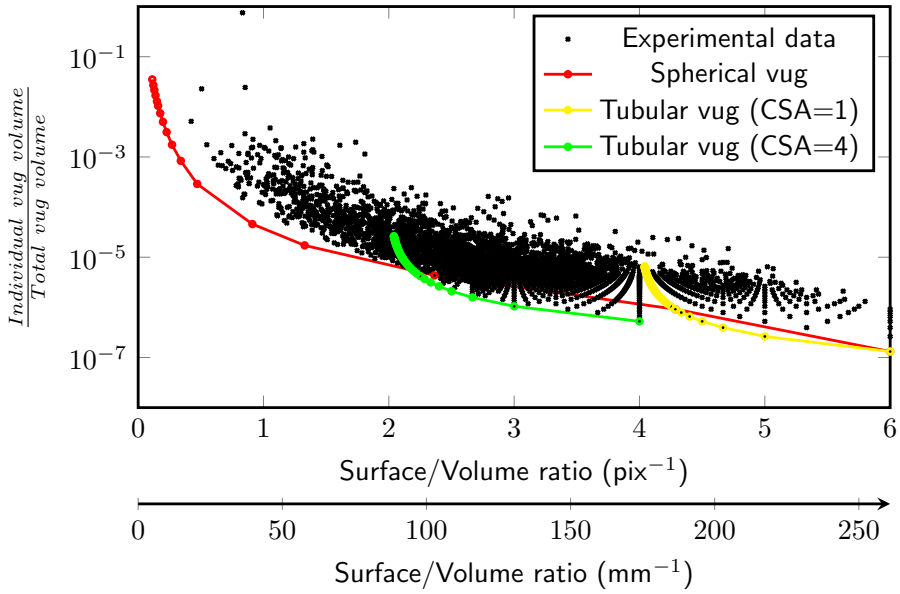

Figure 3.14: Normalized volume of each unique vug plotted against its S/V ratio along with the theoretical distribution for a spherical vug and tubular vug with one and four square voxel cross-section.

Figure 3.14 also plots the expected normalized volume against the S/V ratio for a spherical vug (red), and elongated tubular vugs with one (yellow) and four (green) square voxel cross-sectional area. The longer vug bodies have a larger normalized volume, and ultimately a smaller S/V ratio. The vug data from the image stack suggests that most of the vugs have low sphericity and are generally elongated with a high aspect ratio.

Figure 3.16 shows the probability of the S/V ratios present in the image stack. The most prominent S/V ratio, which accounts for ∼60% of the vugs has a value of 6 and the most prominent vug volume is 1 voxel. An interesting point to note is that multiple vug volumes are associated with this S/V ratio (Figure 3.14), which is only possible when there are no face connections and a one voxel cube is present. Out of all the vugs with S/V ratio 6, 91% have a volume equal to one voxel. This means that there are multiple vugs which are larger than one voxel, have no face-connections, and therefore have atleast one edge-connection.

The vug separation and distribution can be calculated by generating a Euclidean distance map of the image stack (Figure 3.17). The Euclidean distance, or nearest neighbor, is a measure of the separation between two disconnected neighboring bodies. Most of the vugs are located within 20 voxels (0.46 mm) from another vug (Figure 3.18).

3.3 Summary

Using established laboratory measurement techniques, I have measured several petrophysical properties of a Guelph dolomite core. Due to the complex nature of the rock fabric and differences in measurement principle, variations in the petrophysical properties are observed. Based on high resolution CT images, I have established a workflow for pore size and vug structure characterization.

All the pores (including the vugs) are characterized based on the pore volume and divided into zones based on the input number of regions from the NMR. As a result, a 3D map of the pore sizes present in the core can be generated. This is useful for recognizing re-

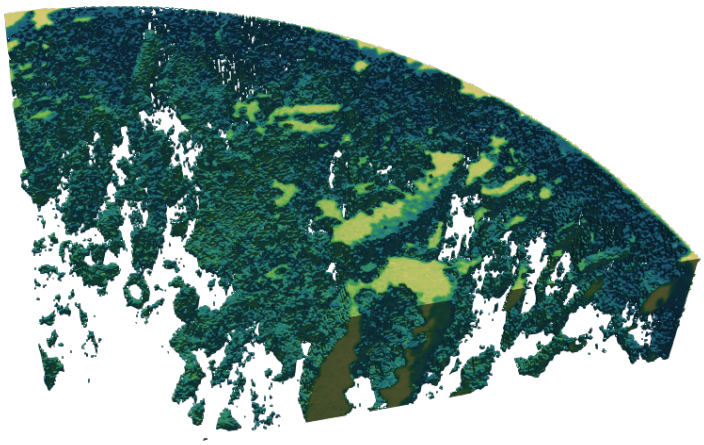

Figure 3.15: Large vug transverses across the thickness of the image stack and consists of ∼75% of the total vug volume.

gions with similar petrophysical properties, and thus identifying zones for further physical sub-sampling (coring) to get region-wise petrophysical property measurement using higher resolution equipment (e.g. SEM, TEM etc). Thus we have developed a scale-dependent workflow for core plug subsampling. The properties derived from the smaller subsamples can be combined to generate an upscaling model for the rock.

The vugs are characterized based on the vug shape, vug volume, and vug separation (distribution). In the grander scheme of things, specifically related to the particle entrapment studies that are presented in the following chapters, the size and spatial distribution of the vugs is of prime importance as it affects the particle entrapment mechanism. For real rocks, where the vugs are of variable sizes and are dispersed throughout the medium, estimating these distribution will result in a clearer approximation of where and when the particulate will be retained.

For the Guelph dolomite core, I found that most of the vugs are: small in size (< 0.23 mm in diameter), have low sphericity resulting in an elongated cuboidal shape, and are located close to each other (0.69 mm mean separation).

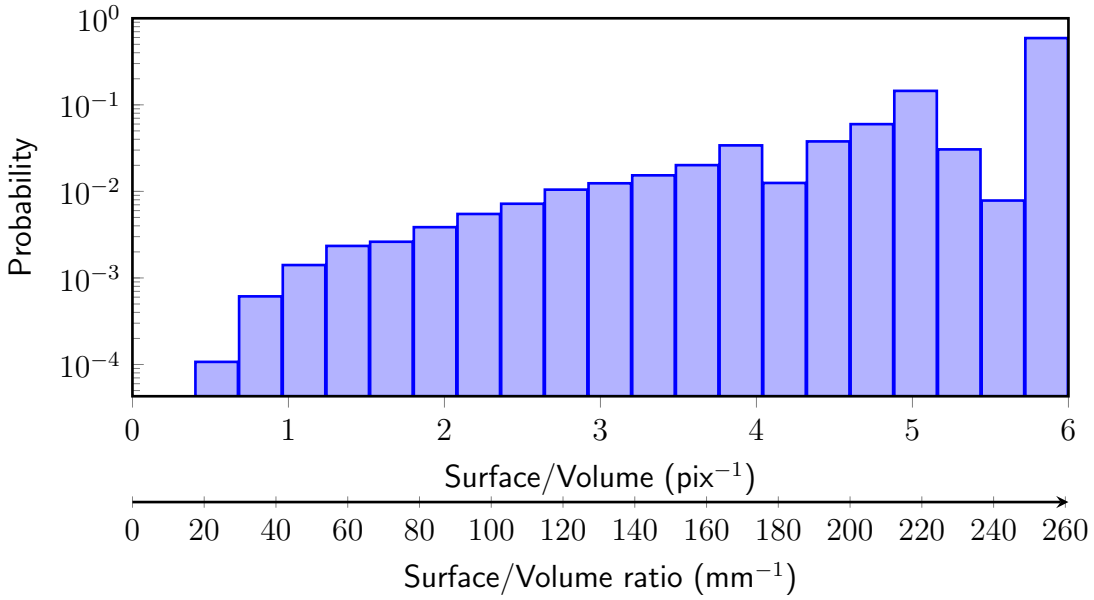

(a) Surface to volume ratio histogram for the vugs present in the image stack. The most common S/V ratio is 6 pix^{-1}.

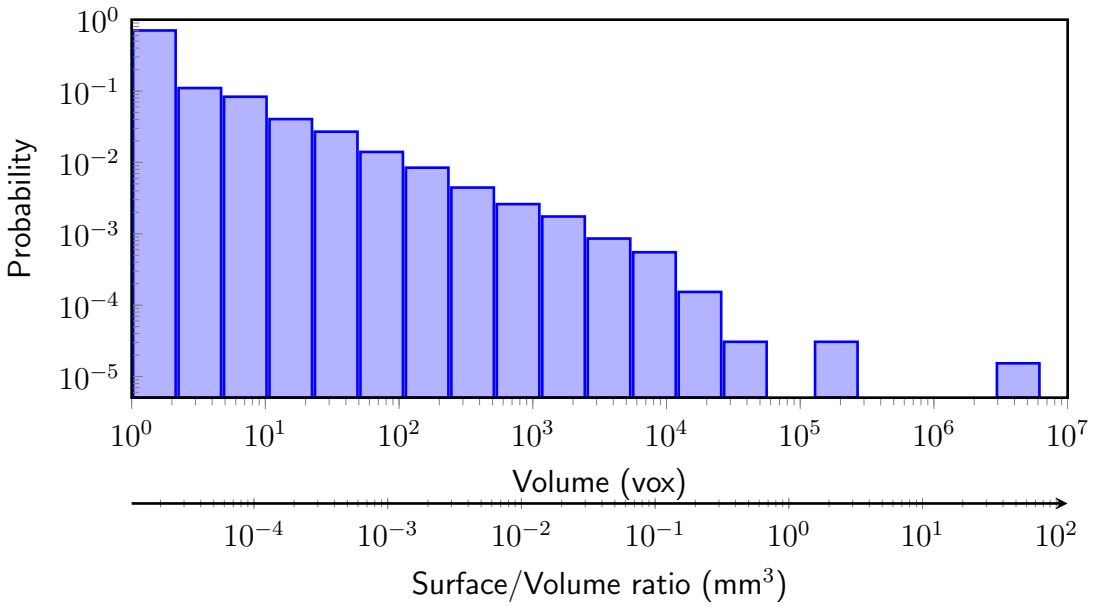

(b) Vug volume histogram. The volume of the vugs varies over multiple orders of magnitude.

Figure 3.16: The histograms suggest that most of the vugs are one-voxel cubes.

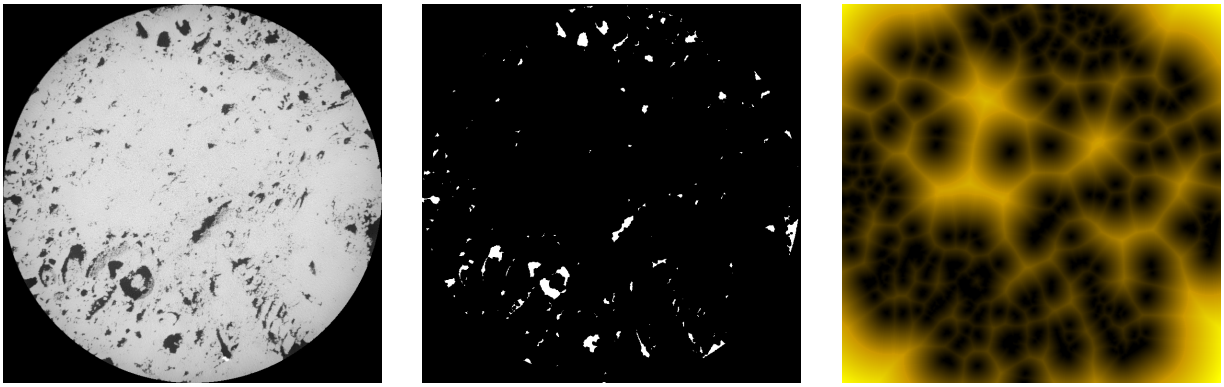

(a) Slice 4 - top of image stack

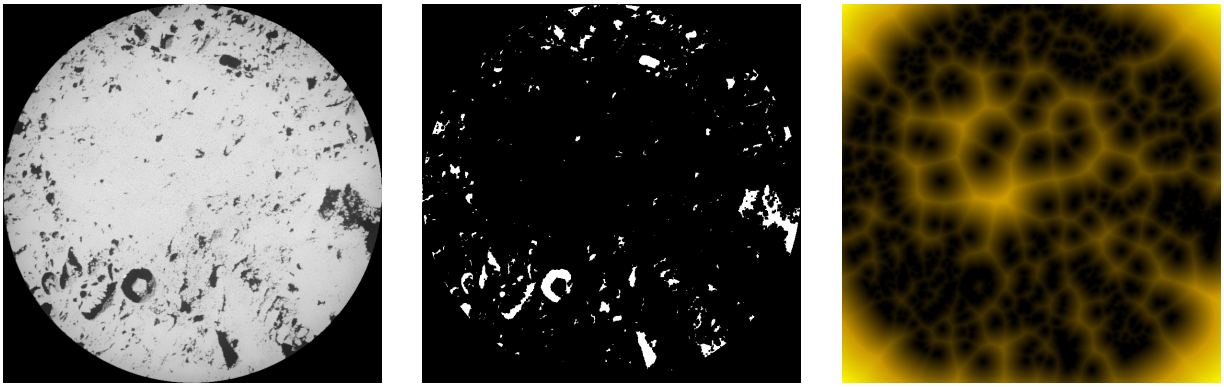

(b) Slice 43 - middle of image stack

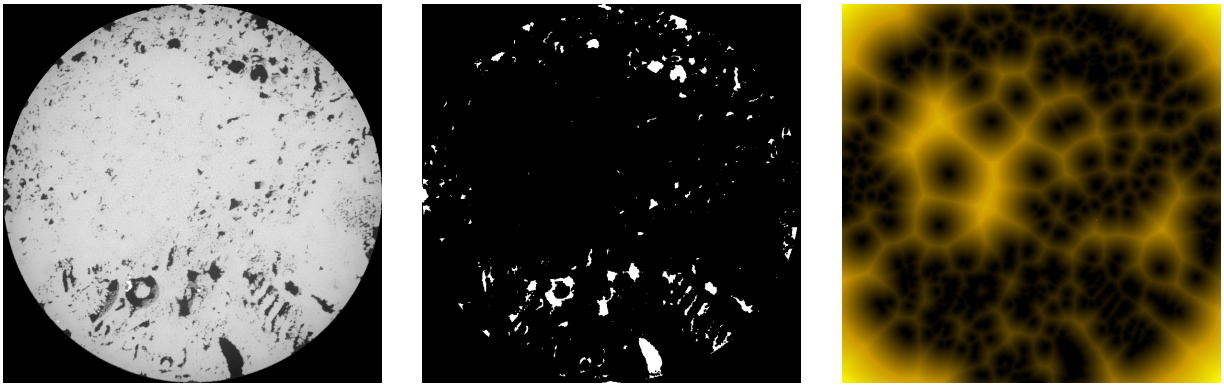

(c) Slice 93 - bottom of image stack

Figure 3.17: The input image stack is denoised (left) and individual vugs are identified (center). Euclidean distance map (left) for the vugs is calculated, which gives an estimation of the separation between individual vugs.

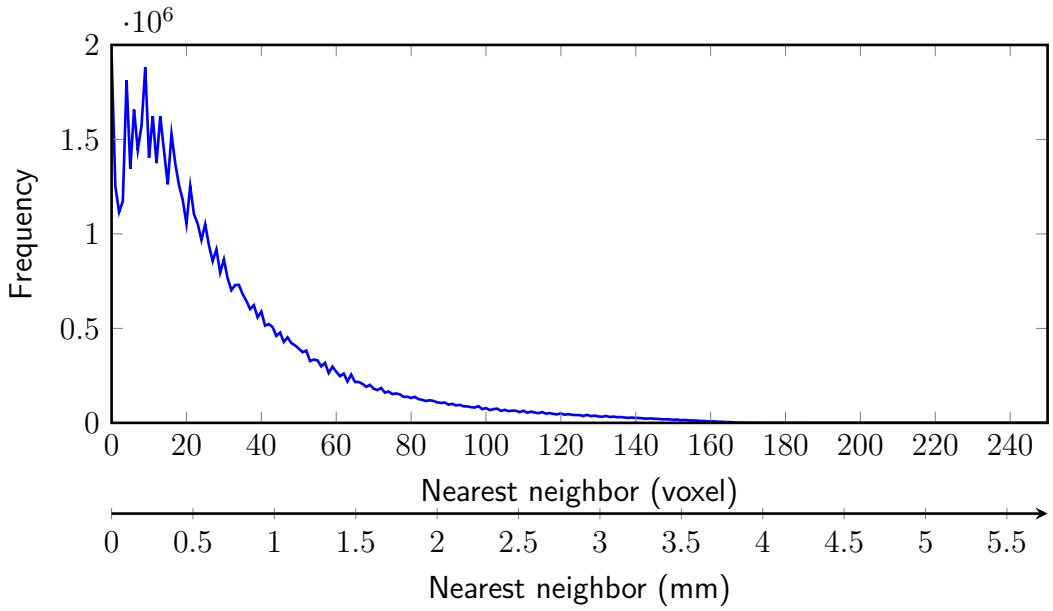

Figure 3.18: Nearest neighbor distance histogram measures the separation of the vug bodies from it nearest neighbor. The vugs are positioned closely with a mean separation of 30 voxel (0.69 mm).

3.4 Future work

This work can be carried forward by building onto the established workflow (Figure 3.1) to do a multiscale analysis on it. After doing petrophysical measurements on the core, CT images can be generated which can be used to identify zones of similar pore sizes. These subsamples can then be cored and subsequently petrophysical measurements made on them. Higher resolution imaging can then again be employed to get a detailed picture of the zone. The combination of these multiscale properties would give a more detailed map of the core petrophysical properties and ultimately an upscaling model for the rock.

Chapter 4: Core fabrication [†]

Synthetic cores have been utilized in this study due to the repeatibility and high degree of control in the fabrication process. The core fabrication procedure for a homogeneous core has been worked and reported in my Masters thesis [105]. The main motivation for sintering glass beads is to remove the change in porosity and pore structure caused by movement of glass beads when:

- Physically moving the experiment to and from the computed tomography (CT) machine,
- Fluid flowing in the bead pack, and
- Conducting horizontal and back flow experiments.

In this chapter, I first give a brief overview of the laboratory equipment used for core fabrication, then a brief overview of core fabrication process as detailed in my Masters thesis [105], and finally the modifications made to the fabrication process to create proxy vuggy carbonaceous cores.

[†]This chapter is based on the following two papers:

Khan, H., Mirabolghasemi, M., Yang, H., Prodanović, M., DiCarlo, D., Balhoff, M., & Gray, K. (2016). Comparative Study of Formation Damage due to Straining and Surface Deposition in Porous Media (178930-MS). Society of Petroleum Engineers. https://doi.org/10.2118/178930-MS

Khan, H. J., DiCarlo, D., & Prodanović, M. (2018). Replicating carbonaceous vug in synthetic porous media. MethodsX, 5, 808–811. https://doi.org/10.1016/j.mex.2018.07.018

4.1 Material and equipment

4.1.1 Matrix grains

Soda-lime glass beads, manufactured by Mo-Sci Specialty Products LLC, have been used as the matrix grains in the fabrication process. These are solid glass beads that have a minimum sphericity of 85% and consist of 65 – 75% silica. A sampling of the beads is taken and observed under a microscope, and the sphericity calculation is performed based on the number of non-spherical particles found in the material. Table 4.1 shows the basic physical properties of the glass beads.The detailed data sheet can be found in Appendix A.

Five different sizes of glass beads have been utilized in the fabricating process, ranging in size from 1000 micron to 25 micron in diameter (Table 4.2).

4.1.2 Vug placeholder

Vug placeholders are defined as the shaped material used to temporarily take up the space of the vug during the sintering process. The material used, salt and gypsum depending on the method for generating vugs, are inert to the temperature cycling during the sintering phase.

Table 4.1: Physical properties of soda-lime glass beads.

Physical property	**Value**
Specific gravity	2.5
pH in water @ 25 °C	7.8
Softening temperature	650 °C
Refraction index	1.51
Compressive strength	39.9 ksi

Table 4.2: Size distribution of glass beads used in core fabrication (Mo-Sci corporation).

Part Number	**Sieve Mesh Size**	**Size Range (μm)**	**Average Size** (μm)
GL0191SB/800–1200	16 – 20	800 – 1200	1000
GL0191B4/150–212	70 – 100	150 – 212	200
GL0191B4/75–106	140 – 200	90 – 106	100
GL0191B4/38—53	270 – 400	38 – 53	50
GL0191B4/13–45	325 – 400	13 – 45	25

Salt Coarse sea salt (NaCl) grains, packaged as HEB Coarse Mediterranean Sea Salt, are used as the vug placeholder. The salt crystals are large in size, non-sperical, and can weigh up to 0.5 g each.

Gysum cement Gypsum cement, packaged as DAP® Plaster of Paris Dry Mix, is used to replicate the exact shape of the die it is set in and has a hardening time of 20 mins.

4.1.3 Graphite mold

A Galloni 3013 machined flat-bottom graphite crucible is used in the fabrication process. The dimensions of the cylinderical crucible are: 5.804 cm outer diameter, 3.594 cm inner diameter, 7.772 cm depth, and 8.725 cm height.

Figure 4.1: Galloni 3013 graphite crucible - 2.285” (5.804 cm) OD x 1.415” (3.594 cm) ID x 3.06” (7.772 cm) DP.

4.1.4 Muffle furnace

The cores are sintered in a Thermolyne FB1415M (Cole-Parmer) benchtop muffle furnace (Figure 4.2) available in UT PGE department. It is a manually-operated digitally-controlled furnace with a peak temperature of 1200 °C and can accomodate a sample of no larger than 4.25" (10.795 cm) in height. This is not a vaccuum furnace and air is present during the heating stage, resulting in a depreciation of the graphite mold quality over time.

4.1.5 CT imaging

Two types of CT scanners are available inhouse at UT PGE:

Medical CT scanner An in-house multiple energy modified medical scanner (Figure 4.3a) from Universal Systems (Universal Systems HD-350E) is available in the UT PGE department. The scanner has the ability to scan in the horizontal as well as the vertical direction, and can scan at a maximum resolution of 250 μm.

The CT numbers for the fluids and glass measured on this instrument are presented in Table 4.3.

Figure 4.2: Thermolyne FB1415M benchtop muffle furnace.

Table 4.3: CT numbers for fluid and soda-lime glass beads.

Material	CT number
Air	-1000
De-ionized water	25
Soda-lime glass beads	2500

X-ray microtomograph A Nikon XT-H 225 x-ray microtomograph (Figure 4.3b) is available in the Chevron Digital Petrophysics Laboratory at the University of Texas at Austin (UT) Petroleum & Geosystems Engineering (PGE) department, managed by Dr. Nicolas Espinoza (https://faculty.engr.utexas.edu/espinoza/microct). The microtomograph has a 225 kV microfocus x-ray source with 3 μm focal spot size and an X-ray detector Varian Paxscan 1500 by 1900 pixels.

4.1.6 Nuclear Magnetic Resonance (NMR) system

An Oxford Instruments GeoSpec2 2 MHz NMR system is available at UT PGE under the management of Dr. Hugh Daigle (http://faculty.engr.utexas.edu/daigle/daigle/laboratory). The scanner has improved signal-to-noise and ultra-short echo times – both essential features for accurate measurements on tight rocks and shales. Other features are: 40 mm and 53 mm probe, 0.05 T static field, and dual gradient coils with gradient up to 0.5 T/m.

NMR is a physical phenomenon in which the sample is first magnetically excited, and then relaxation parallel and perpendicular to external magnetic field is measured. In a 100% water saturated porous media, the characteristic relaxation time T_2 gives an estimate of the pore size distribution based on the presence of hydrogen nuclei. The water close to the pore wall surface relaxes faster compared to the bulk water, which shows a single exponential decay.

Sørland et al. [189] gives an overview of the process of getting pore size distributions from

(a) Modified medical CT scanner.

(b) Nikon XT H 225 microtomograph.

Figure 4.3: Computed tomography imaging options available at UT PGE.

NMR T_2 measurements. The T_2 relaxation time for water is estimated between 2000 and 3000 ms. Therefore the maxmimum vug size that can be observed for the soda-lime glass bead-water system would be ~350 μm, after which the bulk relaxivity of the water would dominate.

4.1.7 3D printer

A MakerBot® Replicator™ 2 is available in UT PGE Machine shop managed by Mr. Daryl Nygaard. The printer has a resolution capability of 100 μm, a 410 cubic-inch build volume, and can accomodate a maximum design of 11.2" (28.448 cm) L x 6.0" (15.240 cm) W x 6.1" (15.494 cm) H.

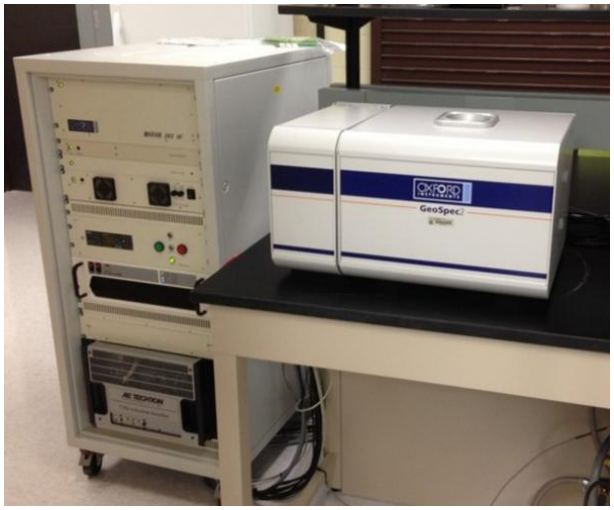

Figure 4.4: Oxford Instruments GeoSpec2 2 MHz NMR system available at UT PGE.

4.1.8 Miscellaneous

The following material were also used in the core fabrication process:

1. 2M Hydrochloric acid
2. Play-Doh®
3. De-ionized water
4. Cheesecloth

4.2 Homogeneous core fabrication

Glass beads are put in a cylinderical graphite crucible (Figure 4.1) and shaken for a few minutes. The movement settles the beads and generates a loose random pack. The graphite crucible is placed in a muffle furnace (Figure 4.2) and exposed to the temperature profile (Figure 4.5a) selected by trial-and-error. The key parameter in glass bead sintering is the exposure time above the softening point and the peak temperature. Longer the exposure time and higher peak temperature result in more deformed glass beads, and therefore a lower porosity and permeability. The process is considered repeatable as the same temperature

profile results in the same porosity, permeability, and pore structure in the bead pack.

The bead pack is taken out of the furnace after it cools down and porosity is determined using CT scans and helium porosimetry and permeability using a core flood. The resultant core (Figure 4.5b) is a consolidated bead pack with a high porosity of ∼42% and 100 Darcy permeability.

A micro-CT scan (Figure 4.6) of the core was taken to take a closer look at the features of the sintered core. The short exposure time at peak temperature during the sintering process did not affect the shape of the beads, which retain a high degree of sphericity.

The NMR T_2 relaxation time, and therefore the pore size distribution estimation, for the fabricated core can be determined using the GeoSpec2 NMR system (Figure 4.4). Figure 4.7 shows the pore size distribution for fabricated cores with 1.0 mm and 0.2 mm glass beads, with corresponding R35 pore size value of 27 μm and 165 μm respectively. This correlates well with the modified Winland R35 [121] value of 163.3 μm for the 1.0 mm diameter glass bead core:

$$log\ (r_{35}) = 0.9058 + 0.5547\ log(k) - 0.9033\ log(\phi) \tag{4.1}$$

4.3 Vuggy core fabrication method 1 - creating spherical and elongated vugs using dissolvable inserts

Rezaei et al. [175] showed a possible vuggy core creation mechanism by placing a combustible material (wood) inside the glass bead pack before sintering in a vaccuum furnace. The material is later combusted in the presence of oxygen, leaving a vug space in the sintered pack. This process was repeated in the in-house muffle furnace (Figure 4.2), which does not hold vaccuum, and was found to leave a residue inside the pore space which could not be cleared completely by repeated core floods.

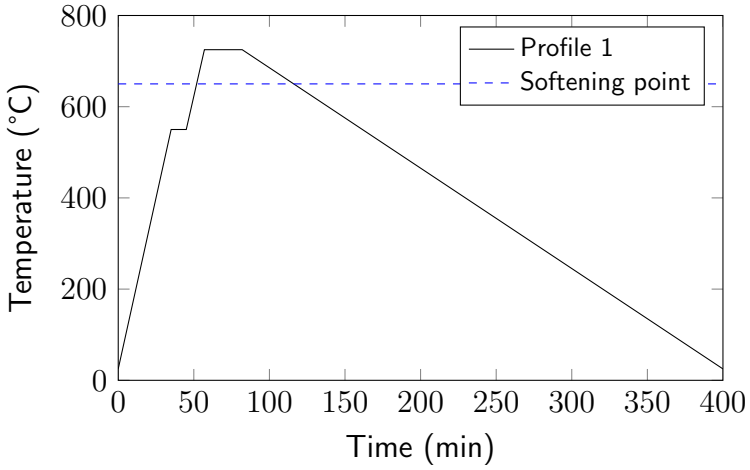

(a) Temperature profiles used for core fabrication

(b) Fabricated core

Figure 4.5: Temperature profile for a stable and highly porous core [105].

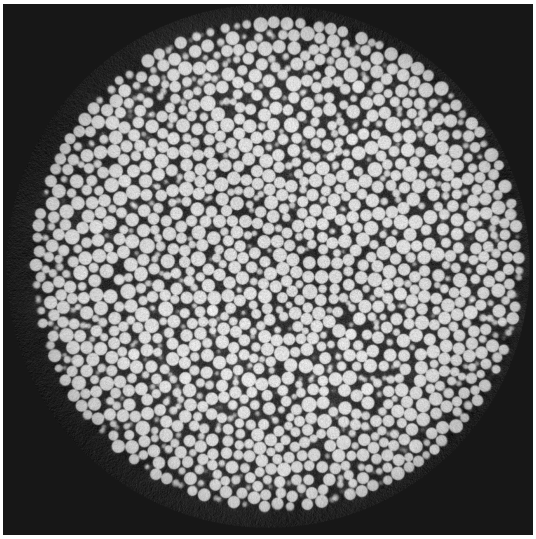

Figure 4.6: Micro-CT of sample homogeneous core with 23 μm resolution (sample diameter = 35.9 mm).

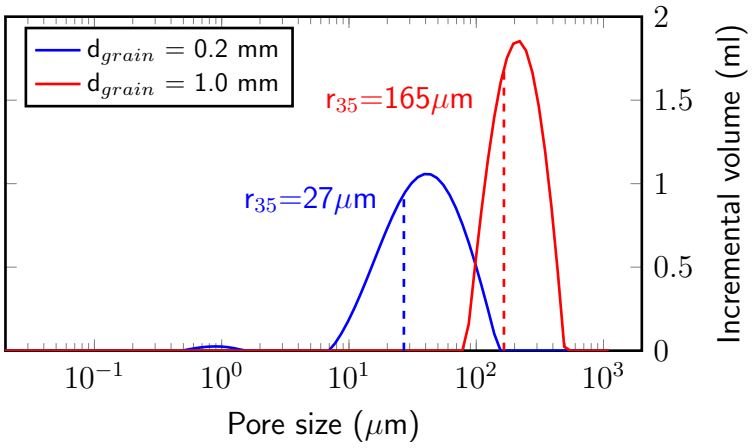

Figure 4.7: T_2 Pore size distribution of homogeneous cores with single grain size, 0.2 and 1.0 mm, and corresponding R35 pore size of 27 μm and 165 μm respectively.

This process is modified by replacing the combustible vug placeholder, wood, with an incombustible material, salt. Salt is selected as a placeholder due to its high melting point, high solubility in water, and ease of machining. Small pieces of coarse sea salt are wrapped in a thin strip of cheesecloth, firmly secured by twisting the ends, and held in a graphite mold in the desired shape. Glass beads (1.0 mm diameter) are poured to fill in the mold simultaneously. The bead pack is then sintered using the same temperature profile (Figure 8.1b) as the homogeneous cores (Section 4.2).

The core is cooled down to room temperature and flooded with de-ionized (DI) water for 1 hour. The in-situ salt dissolves in the DI water, creating a void space with the geometry of the salt packet. The cheesecloth is burned in the furnace during the sintering process and any residue is pumped out during the core flooding process. Figure 4.8 shows a micro-CT scan of the vug present inside the core after the salt has been completely dissolved along with a 3D reconstruction of the vug. No residue of the cheese cloth is observed in the high resolution (25 micron) scans.

Different vug configurations, including but not limited to vugs in series, vugs in parallel, and dispersed vugs have been created using this method and are used for different experiments in the later chapters. The vug shape and distribution used in each section is detailed therein.

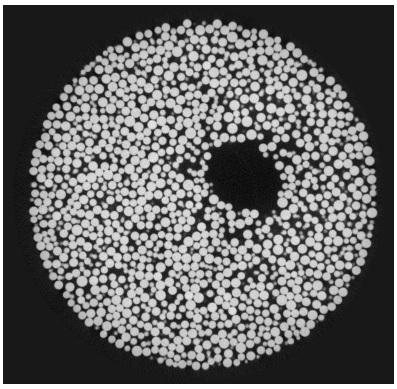

(a) μCT image with a 25 micron resolution (sample diameter = 35.9 mm).

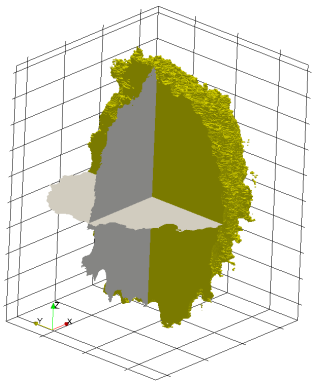

(b) 3D vug visualization based on μCT scans.

Figure 4.8: Vug space created by using water soluble salt as vug placeholder.

Single vugs have been utilized in Chapter 5: and multiple vug combinations are used in Chapter 6: and Chapter 8:.

4.4 Vuggy core fabrication method 2 - replicating exact carbonaceous vug in synthetic porous media

Khan et al. [113] outlines the process of replicating the shape of vugs in naturally occuring carbonaceous cores. The process workflow is shown in Figure 4.9.

4.4.1 Image acquisition and processing

A vuggy carbonate [106] (Section 3.1.2) is imaged using a medical CT scanner at a resolution of 250 μm with the scanning parameters as: scanning time 3 sec, scan thickness 1 mm, voltage 140 kV, and current 200 mA. The output CT data is used to generate image files (e.g. JPEG etc.). Alternatively, a CT image stack can be obtained from an online rock repository [164].

The image files are imported in Fiji-ImageJ [180], where they are scaled to incorporate

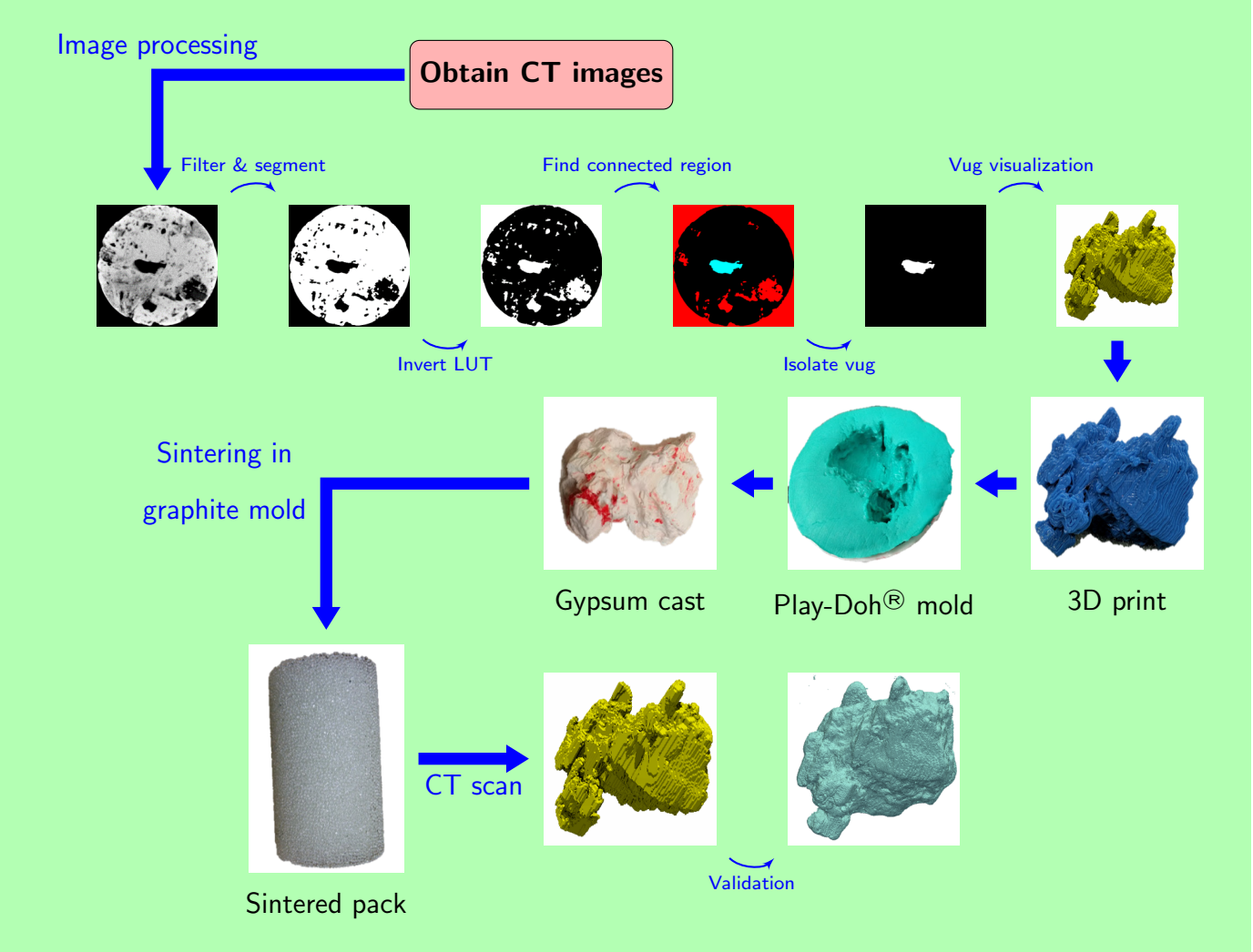

Figure 4.9: Workflow for replicating exact carbonaceous vug in synthetic porous media.

the difference in resolution in the x, y and z-axis. The image stack is filtered using the KUWAHARA FILTER [123] to reduce noise and amplify the vug space. The stack is segmented (SIMPLE THRESHOLD command in ImageJ) using the Otsu method [160] and the look-up table (LUT) for the resultant binary stack is set such that the vug space has maximum value (255 for an 8-bit image).

4.4.2 Vug surface extraction

ImageJ's built-in FIND CONNECTED REGIONS algorithm [127] is then used to find the connected spaces in 3D. The algorithm color codes and isolates the individual connected spaces (Figure 4.10). The desired vug space is selected and visualized in the built-in 3D viewer, and the surface (STL) is exported for 3D printing. The in-house 3D printer is used for printing the surface at a resolution of 100 μm.

The macro for the process above is added in Appendix B.

4.4.3 Mold creation and casting

The 3D printed sample is coated in grease and pressed between two sheets of Play-Doh®. The Play-Doh® surface is coated with grease before pressing and are pulled apart afterwards. The sample is pulled from the Play-Doh® leaving a mold behind. The Play-Doh® releases easily because of the applied grease. Two holes are drilled in the mold which connect the inner body to the outer surface. These can be simply made poking a pencil through the Play-Doh®. They are created to give a pathway to the air which escapes when fluid is poured inside the mold. Grease is applied to the template on the two sheets and they are joined together.

The mold can also be 3D printed by creating a negative of the vug surface but it is difficult to make the mold leak-proof with the low resolution printing capability available to us.

Plaster of Paris (gypsum cement) is mixed with water and cast inside the mold. The cement

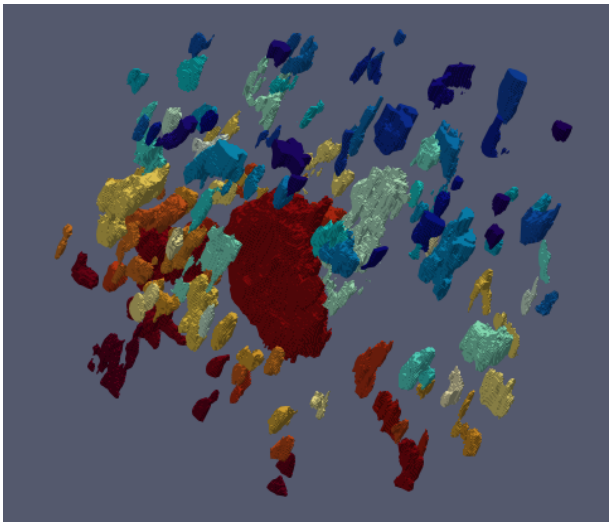

Figure 4.10: Multiple disconnected void spaces (vugs at this resolution) are present in this sample [106].

solidifies in 30 minutes, after which the Play-Doh® is removed. Excess Play-Doh® is removed by blowing with pressurized air.

4.4.4 Core fabrication and acid cleanup

A glass bead core is fabricated using the method outlined in Khan [105]. One millimeter diameter glass beads are poured in a graphite mold and the vug cast is placed at the desired depth. The mold is exposed to a peak temperature of 725 °C in a muffle furnace. The peak temperature is chosen to be higher than the softening point of soda-lime glass, at which the glass beads begin to soften up and join together. The system is allowed to cool before the sintered pack is removed from the mold.

The core is flooded for 10 hours with 2M HCl, which dissolves the gypsum cement. 10 pore volumes of de-ionized water is then cycled to clean up any solid remnants. The core is placed in a drying furnace (∼150 °C) for 2 hours to remove all fluid.

4.4.5 Fabricatrion method validation

A Guelph dolomite sample (38 mm × 72 mm) is scanned at a resolution of 250 μm [106] and thickness of 3 mm in a medical CT scanner (Universal Systems HD-350E located at UT PGE). The images are processed to isolate a vug and surface extracted. MakerBot® Replicator 2 (located at UT PGE) is used to 3D print the surface. Mold is created and cast in gypsum cement (Figure 4.11). Core is sintered with the casted vug in place and treated with acid to remove the gypsum cement.

The resultant core is dried and susequently scanned in the medical CT scanner. The vug space is reconstructed using Fiji-ImageJ (Figure 4.12) and the visualizations are compared. The extremities are not captured well in the reconstruction, but this can be attributed to the limited resolution of the 3D printed vug space.

4.5 Fabricated core

4.5.1 Petrophysical properties

Porosity and permeability The homogeneous cores created using 1.0 mm diameter glass beads and the aforementioned temperature profile (Figure 4.5) results in a highly porous, ∼42%, and permeable core (single-phase water permeability of 100 Darcy). This compares fairly well with the Karmen-Cozeny prediction of 125 Darcy for such glass bead sizes.

Figure 4.11: Surface visualization (left), resultant 3D–print (middle) and vug cast (right).

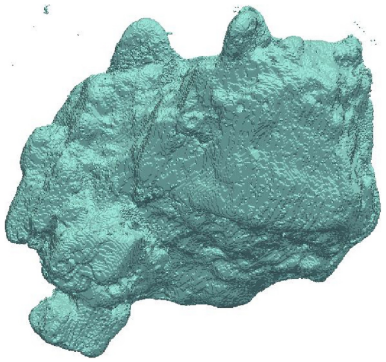

Figure 4.12: Vug space after acid flood.

Quantity and size of vug(s) significantly affects the porosity and permeability of the core. These larger pathways provide less resistance for fluid flow, however the overall permeability effect is related to their connectivity across the sample. The glass bead distribution in the region surrounding the vug is different compared to regions away from the vug. Figure 4.13 shows the porosity in a core cross-section obtained using 3D Gaussian blur, with brighter shades showing a larger value. The porosity difference can be attributed to the difference in boundary conditions for the two cases: the vugs, which are formed by solids of a size larger than the bead size, result in a looser pack, and therefore a larger porosity value.

Pore size distribution Pore size distribution of the fabricated vuggy core is measured using the GeoSpec2 NMR system (Figure 4.4) and plotted with the homogeneous core (Figure

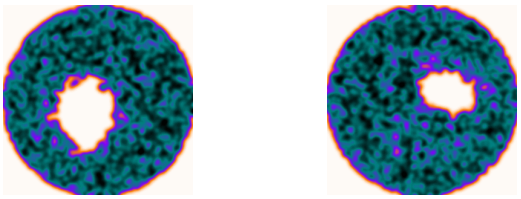

(a) Upper vug (b) Lower vug

Figure 4.13: Pore size distribution, and therefore porosity distribution, varies across the cross-section of the core. Regions surrounding the vug (bright colors) have a higher porosity value compared to the regions further away from the vug.

4.14) . One unique pore sizes is observed for both the cases, with a mean T_2 value 1500 ms, and equates to a pore size of 165 microns.

The absence of the centimeter-sized vug in the NMR is explained based on the bulk relaxation time for pure water ($\sim$ 2500 ms). Vug significantly larger than the pore size, 100x in this case, would have a T_2 relaxation time of greater than the bulk relaxation of pure water and therefore would not be measured in the NMR.

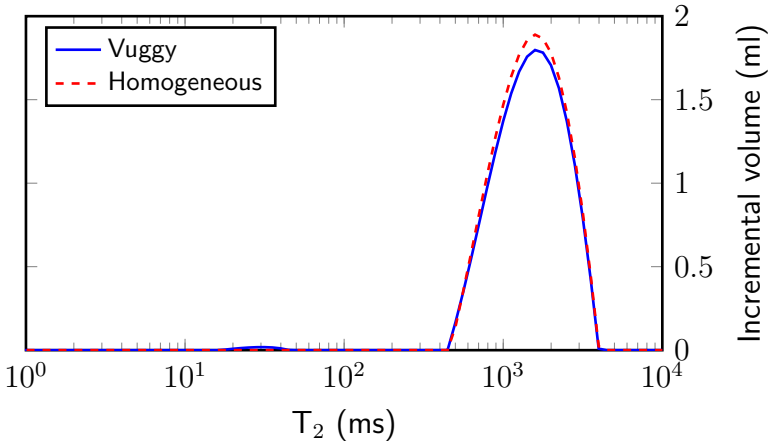

Figure 4.14: T_2 NMR of a homogeneous core fabricated with 1.0 mm glass bead and a vuggy core with the same sized glass bead and a centimeter-scale vug.

4.5.2 3D reconstruction

Vuggy cores have been scanned in the in-house micro-CT scanner at a resolution of 25 microns. Successive filters are applied, including but not limited to, GAUSSIAN BLUR and FIND CONNECTED REGIONS in Fiji-ImageJ [180] to segment the vug space, pore space, and glass beads. 3D reconstruction of the bead pack with vugs in shown in Figure 4.15; the beads are loosely packed and retain their sphericity as was observed for the homogeneous cores.

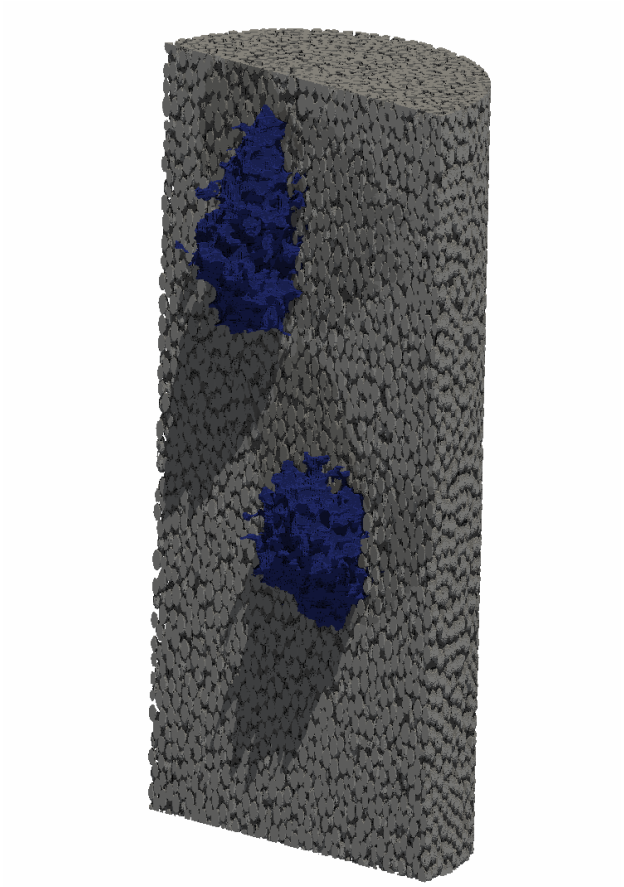

Figure 4.15: Vertical cross-section of the 3D reconstruction of vuggy porous media with the glass beads colored gray and vugs colored blue. Imaging resolution is 25 μm.

4.6 Conclusions

In this chapter I show the capability of forming vuggy glass bead cores with the desired matrix porosity, vug porosity, vug placement, and vug shape. This procedure can be extrapolated to include multiple vugs of different shapes and sizes. The core size can be changed with availability of a graphite mold of the desired size, and a furnace big enough to fit it. The pore size can be also changed by using smaller or larger glass beads as the matrix grains, and a good estimation of the pore size can determined using NMR or modified Winland R35 equation (Eq. 4.1). A combination of beads can also be used to get heterogeneity on a different scale than a vug, and can be used to create low permeability and high permeability

layers. Furthermore, the glass beads can be chemically modified [77, 187, 216] or beads made from different material used to alter the wettability of the system.

Chapter 5: The effect of vuggy porosity on straining in porous media [†]

This chapter shows a formation damage experimental study conducted on synthetic homogeneous and vuggy cores. Glass beads, used to reduce surface forces, of 1.0 mm are sintered to form a homogeneous core with a 42% porosity. Vuggy cores are made by adding dissolvable inclusion (salt) during the sintering process, and dissolving them with core floods afterwards. The vug diameter is chosen to be ∼100 times the pore diameter.

Finer sized glass beads (25 and 100 microns) are used as the infiltrate. The injected particle sizes are chosen such that straining is the dominant trapping mechanism during the flow experiment. Infiltrate particles are injected at different flow configurations in a gravity-dominated flow, and the resultant porosity, permeability, and effluent volume are measured.

The results can be summarized as: vugs get up to 32% smaller due to flow for infiltrate while the maximum change in porosity is observed at the bottom end of the core, vug shape changes to a more smooth and rounded surface, and particles go deeper (8 mm more) into the formation when vugs are present causing damage deeper inside the formation.

[†]This chapter is based on the following paper:

Khan, H. J., Prodanović, M., & DiCarlo, D. A. (2019). The Effect of Vuggy Porosity on Straining in Porous Media. SPE Journal, SPE-194201-PA. https://doi.org/10.2118/194201-PA

5.1 Introduction

In this study I use homogeneous medium and heterogeneous porous medium with pore openings on two length scales to study particle straining. Homogeneous glass bead cores and proxy vuggy carbonate glass bead cores with millimeter-size vugs and matrix grain size of 1.0 mm (thus matrix pores are approximately 1/5 mm as experimentally determined in [112]) are fabricated. The ratio of vug size to pore size is 100/1.

Bi-modal glass bead suspension, with matrix grain to injected particle size ratios as 10/1 and 40/1, are injected at six unique combinations of flowrate and injected particle concentration in the top-down direction. Changes in porosity, permeability, vug size, and deposited particle fraction caused by the flow experiment are measured. I have used flow rates as high as 60 ml/min and total injection concentrations up to 3% based on work in the literature. Responses of proxy vuggy carbonate are compared with homogeneous porous media results presented in Khan [105].

For injected fluid flowing in the top-down direction in the vuggy core, we hypothesize that the presence of vug would reduce the deposition of solids in the surrounding matrix as the fluid phase would preferably flow through the vug. Most damage/deposition would be observed at the bottom of the vug as particles will get trapped when entering the matrix after crossing the vug.

5.2 Methods

The workflow used for the experiments in shown in Figure 5.1. A core, homogeneous or vuggy, is fabricated using the procedure outlined in Section 4.3. An initial CT scan of the core is taken to act as the baseline. Core flooding experiments are conducted during which permeability and total effluent volume are measured. A final round of CT scans is then performed. The generated images are processed using image analysis techniques to give changes in porosity and the vug volume due to infiltrate flow.

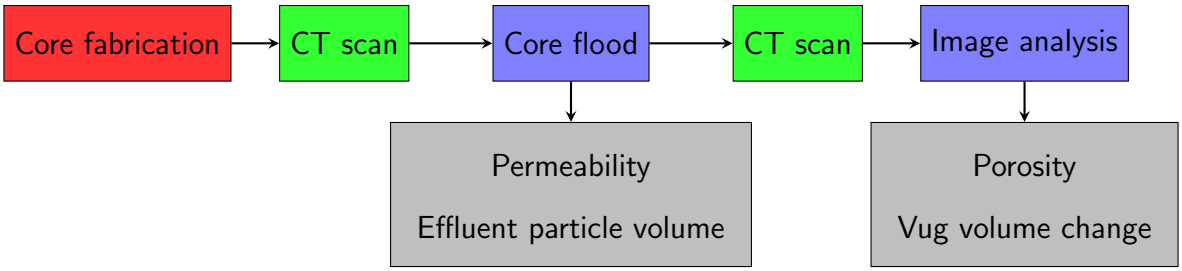

Figure 5.1: Process workflow: Core is fabricated and CT scanned. Core floods are conducted with real-time measurement of pressure and total effluent volume bfore the core is scanned again. Image analysis is performed to deduce porosity change and vug volume change due to injection.

5.2.1 Fabricating the cores

Two core configurations are chosen for these experiments: a homogeneous core with no vug and a vuggy core with a single vug. The vuggy cores are fabricated using the procedure outlined in Section 4.3, where salt was wrapped in cheesecloth in a spherical shape to make a uniform ball prior to sintering. The vug volume is kept constant for all the cores. Figure 5.2 shows a schematic of the core configurations used for this study. Figure 5.3 shows the initial porosity for vuggy and non-vuggy core determined from CT scans.

Based on previous studies [105, 108, 112], a prominent change in porosity is observed in the top 25 mm of the core. Small changes in porosity, and in effect particle trapping, is observed deeper inside the formation. The center of the vug was placed at a depth that allows passage of suspended particles inside the vug.

5.2.2 Flooding experiments

The experimental setup is shown in Figure 5.4. Equal volumes of 25 μm and 100 μm glass bead (fine) suspensions are injected, in the top-down direction, in the core at three total injection concentrations (0.5%, 1% and 2% v/v) and two flow rates (40 and 60 ml/min), resulting in six unique flow conditions (Table 6.1) for each core type.

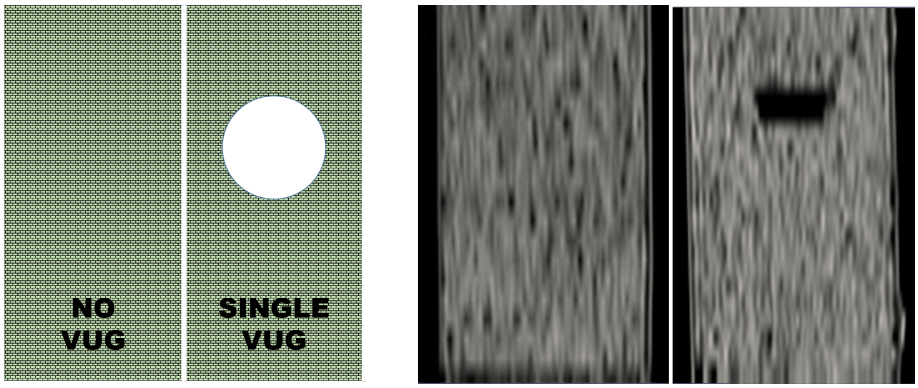

(a) Schematic

(b) Reconstructed from medical CT scan (Sample diameter = 35.9 mm). The image has been scaled in the z-direction, where the resolution is 3 mm compared to 0.25 mm in the xy-plane.

Figure 5.2: Core configurations fabricated: homogeneous core and vuggy core.

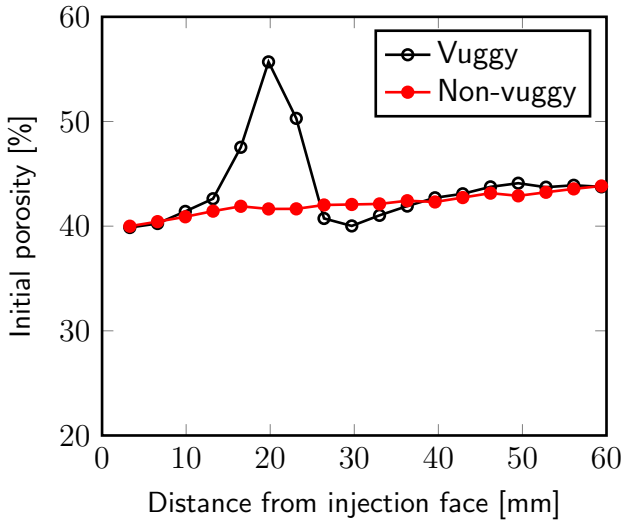

Figure 5.3: Porosity distribution for vuggy and non-vuggy core.

For each flow case, the total volume of solids injected is kept constant and equal to the total pore volume in the core ($V_p = \phi \cdot V_b \approx 27ml$). $PV_{SI}\ (t)$ can be defined as the ratio of total volume of the solid infiltrate injected at time t to the total pore volume. For constant solid volume injected, the total injection time for a specific injection concentration and flow rate can be calculated by keeping $\int_0^{t_{inj}} PV_{SI}\ dt = 1$ in Eq. 5.1.

$$PV_{SI}\ (t) = \left(\frac{q \cdot c_{total}}{\phi \cdot V_b}\right) \cdot t \tag{5.1}$$

where,

PV_{SI} = pore volume occupied by the solid infiltrate [ ]

V_b = core bulk volume [ml]

ϕ = core total porosity [ ]

q = flow rate [ml/min]

c_{total} = total injected particle concentration [% v/v]

t = time [min]

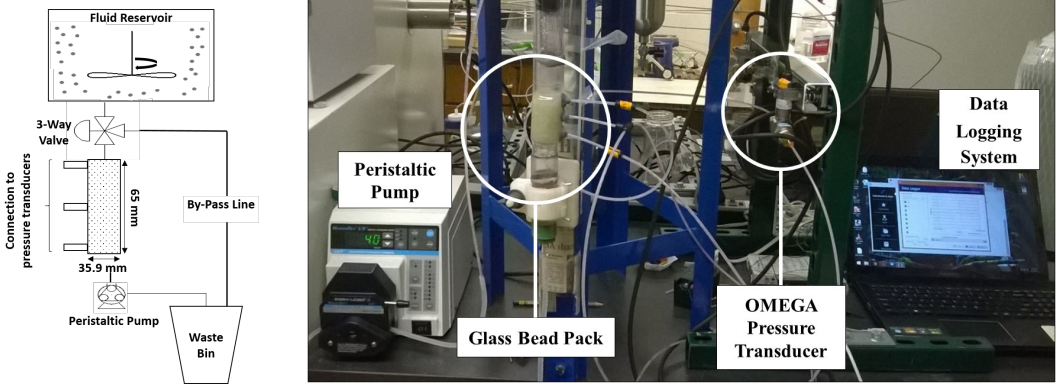

(a) Setup schematic (b) Lab setup

Figure 5.4: Experimental setup for conducting flooding experiments. Pressure is measured in real-time and cumulative effluent volume is collected.

Table 5.1: Experimental flow conditions for each vug configuration.

Core ID	**Flow rate [ml/min]**	**Total injection concentration [vol %]**	**Injection time [min]**
α6020	60	2.0	22.50
α4020	40	2.0	33.75
α6010	60	1.0	45.00
α4010	40	1.0	67.50
α6005	60	0.5	90.00
α4005	40	0.5	135.0

The fines suspension, at desired total injected particle concentration, is held in a reservoir above the core and maintained by operating a stirrer (Figure 5.4a) at 8000 RPM. The 3-way valve is opened to allow suspension passage to the core. The injection flow rate is controlled by a peristaltic pump at the outlet of the core. The fluid passes through the core which has three pressure ports attached to it. These connect to Omega pressure transducers (range 0-7 kPa) that log real-time pressure data (Figure 8.8). Differential pressure measurements are made across the first/second and second/third pressure taps resulting in the top and bottom zone permeabilities respectively (Figure 5.4a). The pressure data is a direct measure of the permeability, and is calculated in the top and bottom zone of the core continuously over time. The measured pressure data is very noisy and needs to be cleaned prior to calculate permeability. Appendix C highlights the general workflow used to filter and clean the pressure data.

The total effluent volume is collected and passed twice through a 10 μm filter paper to collect the fines. The residue is dried in a mid-temperature ($\sim$200 °C) drying oven and weighed. Material balance calculation is performed on the effluent solid volume and total injected particle volume to ratify the porosity change determined via CT scans.

An in-house multiple energy modified medical scanner (Universal Systems HD-350E) is used to conduct Computed Tomography (CT) scans of the core (Figure 4.3a). The scan parameters used to get a resolution of 200 μm are: 3 second scan time, 3 mm scan thickness, 3 mm scan index, 200mA current and 100 kV voltage. The scanner is calibrated to give -1000 HU for air, 25 HU for de-ionized water and 2500 HU for soda-lime glass (Table 4.3).

A simple mixing formula (Eq. 5.2) can be used to determine the change in porosity of the scan using a baseline measurement. A CT scan is conducted of the water flooded core before starting the flow experiments (Figure 5.5a) while another scan is conducted after completing the flow experiment (Figure 5.5b). Flow experiments are conducted outside the CT scanner, after which the core is lowered in the CT scanner. A baseline is determined from the initial scan and the deviation from the baseline results in the change in porosity. Since the core is sintered and fluid used is same for both the cases, any change in CT value can be attributed to the deposition of the glass infiltrate.

$$\Delta\phi = \frac{CT_{after} - CT_{before}}{CT_{glass} - CT_{water}} \tag{5.2}$$

5.2.3 Image analysis

Image analysis is performed on the CT images to determine the change in shape and volume of the vug. Fiji-ImageJ [180] is used as the image analysis tool. The output data is scaled and stored as an 8-bit image, and then segmented (Figure 5.6) using the Otsu method [160] with a gray value of 76.

ImageJ-Fiji's built-in"Find connected region" algorithm is used to identify and isolate the vug-space. The 3D vug-space is visualized (Figure 5.7a) using ImageJ's built-in 3D viewer [181] and the vug volume is computed using a MATLAB routine. The initial and final CT images show the change in vug-space shape and volume. The process flow chart is shown in Figure 5.8.

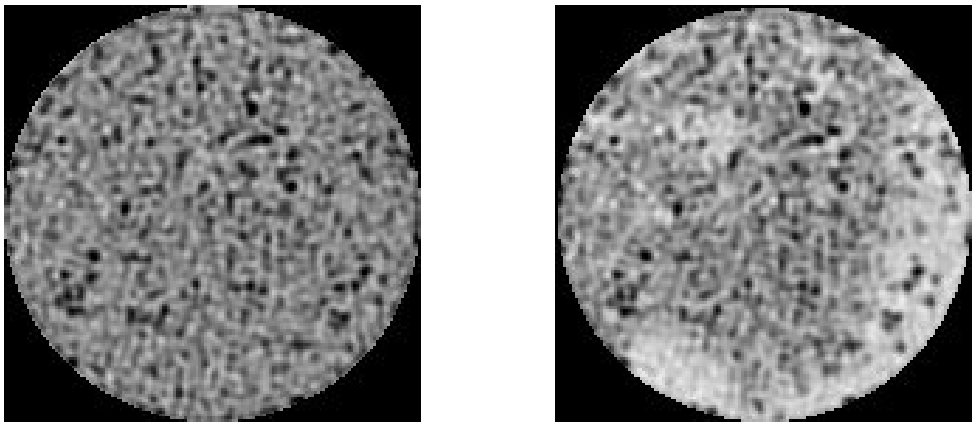

(a) Before flooding (b) After flooding

Figure 5.5: Vertical cross-section at the same depth (45 mm) before and after flooding experiment (experiment H6020). The change in gray value is attributed to infiltrate deposition. (Sample diameter = 35.9 mm)

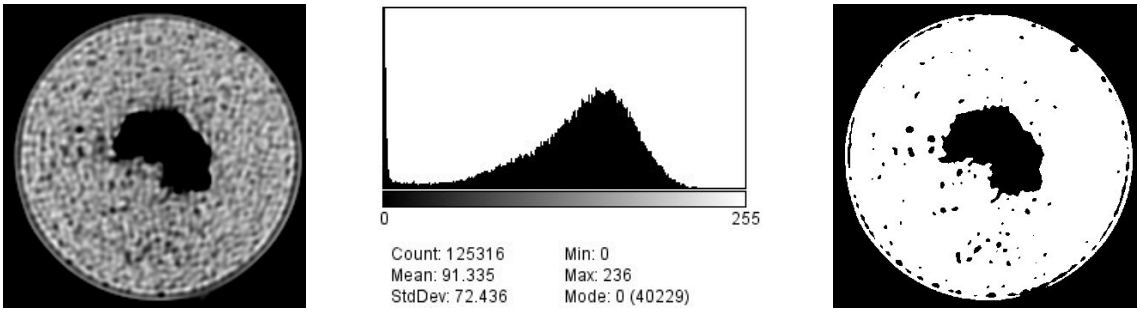

(a) Input image (b) Histogram (c) Segmented image

Figure 5.6: Segmentation process for experiment G4020. (Sample diameter = 35.9 mm)

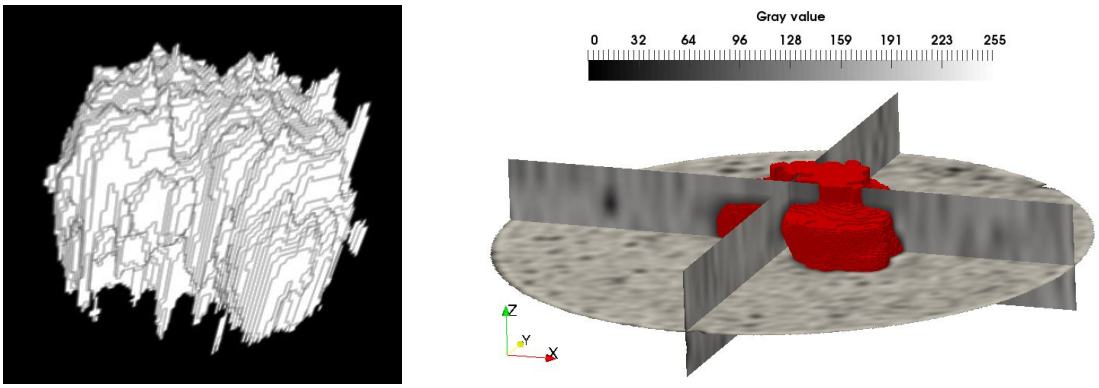

(a) 3D vug visualiztion before injection.

(b) Orthogonal projections after injection. Vug is colored red. (Sample diameter = 35.9 mm)

Figure 5.7: 3D vug views before and after injection.

5.2.4 CMG simulation

A 2D CMG-IMEX [46] simulation was setup to understand the change in streamlines due to presence of a vug. This simulation is neither modeling the particle deposition process nor measuring the change in vug volume but is setup to gain basic insight into initial path of particulates. The problem is simplified to a quasi-2D system and a Cartesian grid ($74 \times 131 \times 1$), with a cuboidal vug, based on the cross-section from CT scans is created (Figure 5.9). No grid refining is used. The reservoir is saturated with single-phase water with pressure greater than the bubble point pressure. Ratio of vug volume to total bulk volume and position of vug inside the core is kept consistent the CT scan. Single phase fluid (water) is injected from the top end and produced from the bottom end at a constant flow rate of 3280 bbl/day (upscaled from 60 ml/min). The flow rate is calculated by keeping the spatial and temporal upscaling ratio the same. The vug has a porosity of 99% compared to 41.6% for the matrix while the permeability of the vug is two orders of magnitude greater than the surrounding matrix (200 mD). CMG input parameters are presented in Table 5.2.

The effect of particle entrapment can be modeled by reducing the permeability of the vuggy zone and the effect of particle deposition inside the vug can be captured by reducing the

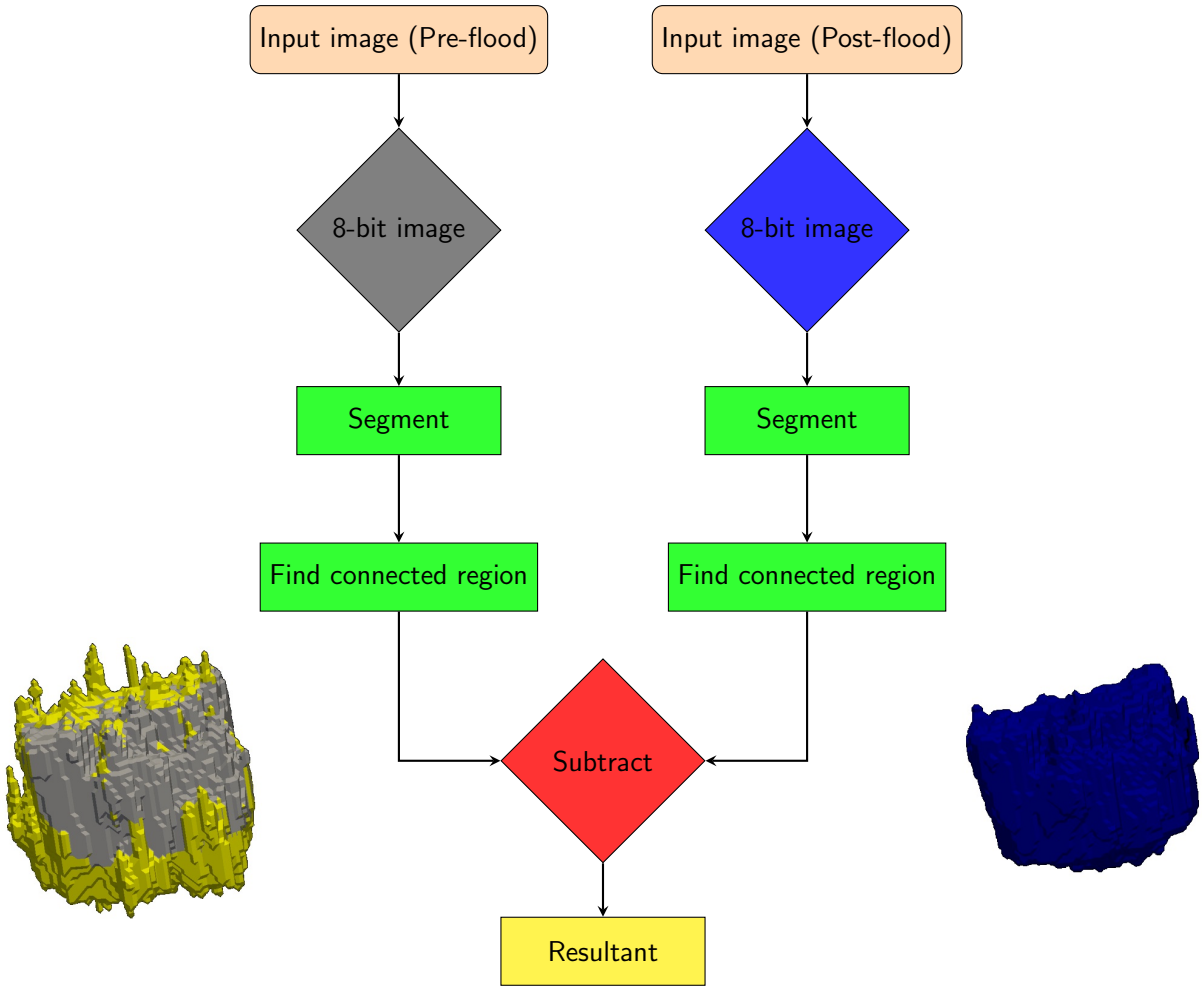

Figure 5.8: Image analysis workflow to determine the vug volume change, aided by vug surface visualizations. Both, image analysis flowchart and the vug surface visualizations, are color coded such that gray is the pre-flood vug, blue is the post-flood vug, and yellow is the change in vug geometry due to flooding experiment.

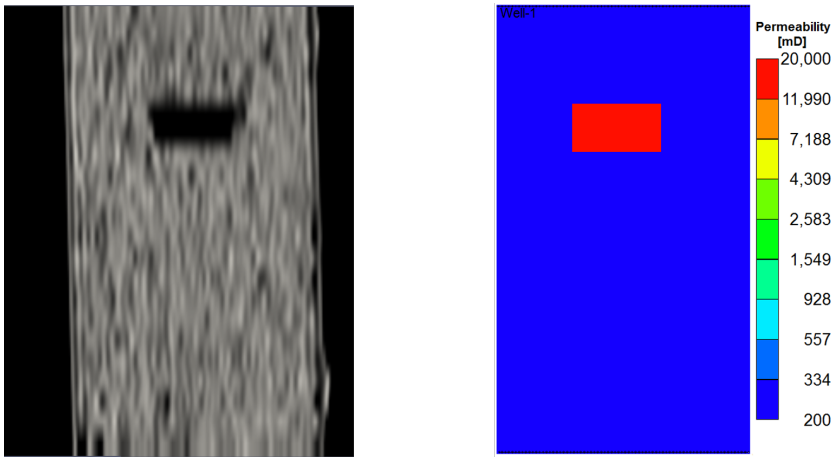

Figure 5.9: CT scan of core (XZ plane) and resultant Cartesian grid used for simulation. (Sample diameter = 35.9 mm)

Table 5.2: CMG input parameters.

Input parameter	**Value**
Simulator	IMEX
Coordinate system	Cartesian
Grid size	$74 \times 131 \times 1$
Voxel size	$1 \times 1 \times 1$ (ft^3)
Matrix porosity	0.416
Matrix permeability	200 mD
Vug porosity	0.99
Vug permeability	20000 mD
Fluid	Single phase water
Inlet & outlet boundary	Constant flow rate
Flow rate	3280 bbl/day

vug size. We study two scenarios: vug permeability reduces by a factor of 10 and vug size reduced by three units at the bottom and one unit on all other boundaries. The latter is based on the relative deposition of particles observed from CT scans. These system are run after steady-state flow is achieved.

5.3 Results

Two core configurations are tested with six unique flow conditions. The porosity and permeability results are arranged for each core configuration.

5.3.1 Effluent particulate volume

The ratio of effluent particle volume to total injected particle volume is plotted in Figure 5.10. Two trends can be generalized for the homogeneous cores: at the higher flow rate, 60 ml/min, the effluent particle volume ratio increases, albiet slightly, with a decrease in particle concentration while the opposite behavior is observed at the lower flow rate. The same trend, with more pronounced changes, is observed for the vuggy core.

5.3.2 Porosity

Porosity results are shown in Figure 5.11; results from the first and last scan are ignored as they are prone to boundary effects. The porosity changes for all experiments are calculated across complete cross-section of the core, and not just the matrix cross-section. The homogeneous cores show an exponential decay in the porosity change with depth in the top part of the core for all the experimental cases. Maximum change in porosity is observed in the top part of the core with the porosity loss being reduced deeper inside the core. The average porosity change is measured at 10%. This behavior is expected according to deep bed filtration theory, where the injected particles are trapped in the shallow depth. The

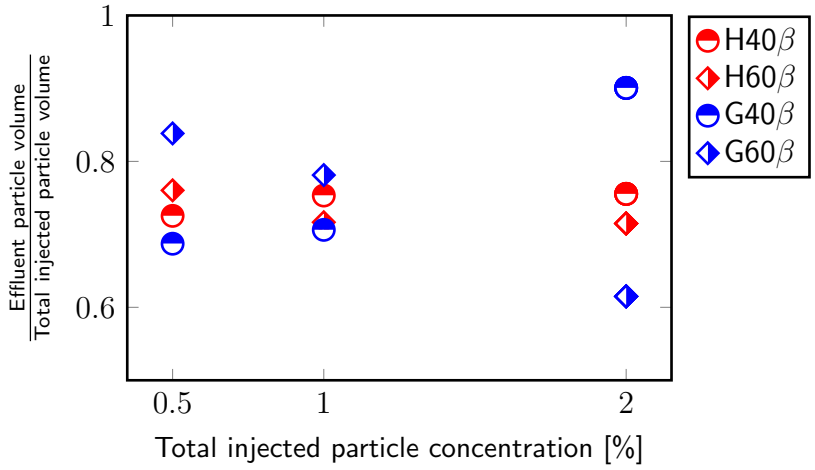

Figure 5.10: Effluent volume is collected and filtered to isolate the suspended infiltrate. (β is ten times the total injected particle concentration)

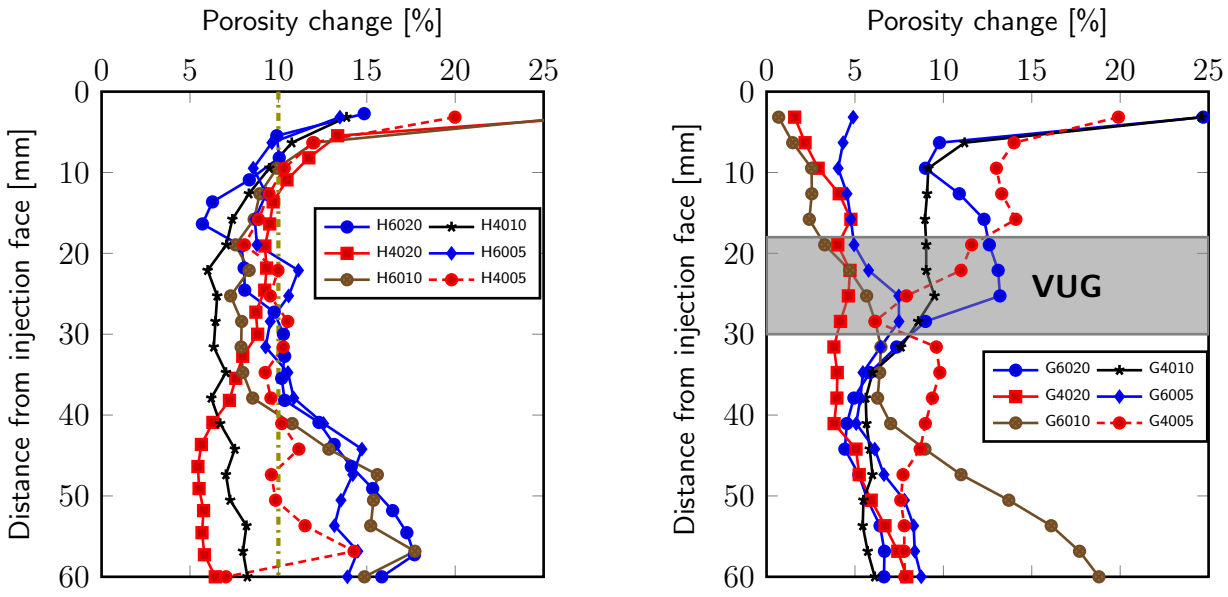

(a) Hx - homogeneous core

(b) G0x - vuggy core

Figure 5.11: Porosity change with depth at the end of flow. Same volume of solid infiltrate is injected in all cases. (Experiments are labeled: the letter is the core type, the first two-digit number is the flow rate and last two-digit number is ten times the total injected particle concentration.)

fluid reaching the deeper depths has a lower concentration of suspended particles and resultantly less particles are deposited in those zones. In the lower part of the core the porosity change increases as the flow rate increases; with the high flow rate showing less spread in the porosity change. The porosity change increases sequentially at low flow rate in decreasing concentration values and at high flow rate in increasing concentrations.

All the cases with the high flow rate have an increasing trend in the lower part of the core, with respect to the average, as shown in Figure 5.11a (olive line). Experiment H4005 is keeping about the average value, with a small spread and no consistent trend. One value shows a large jump in porosity change but we do not think that is evidence enough to conclude that it has a similar porosity loss to the high flow rate cases.

In contrast, the vuggy cores generally show a steady increase in porosity loss with depth. Two opposing behaviors in the top zone are observed: high porosity loss (Group A - experiments G6020, G4010 and G4005), which is quite similar to the homogeneous case but with an average porosity change at 12%, and low, less than 5%, porosity loss (Group B - experiments G4020, G6010 and G6005). The flow cases are grouped based on the observed porosity results and are not known a-priori. Similar cores are used for all the flow cases, and this is discussed in Section 5.4. In the lower half of the core a similar porosity profile is observed for all the flow cases except G6010, which shows a very large porosity change (3x larger than the other flow cases). Group A shows an exponential growth in porosity loss with depth while Group B show a similar change before the end of vug, reducing after that.

For homogeneous cores, porosity change above the average is observed in the top 8 mm of the core (Figure 5.11a). On the other hand, vuggy cores show porosity change above the average at 24 mm for both the observed groups. Considering the unhindered flow of particles inside the vug, the maximum porosity change in a 12 mm long vug is expected at a depth of 20 mm. This is 4 mm smaller than the observed value for vuggy cores.

An important point to note: the vug occupies $\sim$11% of the cross-section area of the slice across the maximum vug width (Figure 5.6a). Group B shows higher loss in porosity across

this region, on average double the porosity change for Group A, and on par with the porosity change in homogeneous cores.

5.3.3 Vug volume change

Two important observations can be made from the vug visualizations before and after injection (Figure 5.8). The rough features, which are present throughout the surface of the vug, are first filled by the injected particles and smoothened out. This implies that fluid flows laterally from the vug to the matrix. Filling of these extrusions is an expected behavior as these are present at the entrance to the high permeability zone, and flow is expected through them.

Secondly, we observe significant reduction in porosity in the bottom part of the vug. The fluid tries to exit the vug at the bottom part and comes in contact with the matrix. The interaction of injected particles with the matrix at this point is quite similar to what is observed at the injection face of a homogeneous core, where an external filter cake is developed.

Table 5.3 shows the change in vug volume observed for all the flow conditions when same amount of infiltrate was injected. Up to 32% decrease in the vug volume is observed during the flow experiments. CT scan shows maximum volume change in the lower end of the vug (Figure 5.12b).

When the flowrate is kept constant and concentration changes, contrasting behavior in vug volume change is observed. The higher flowrate shows a decreasing trend in volume change with concentration reduction, while a lower flowrate shows an increasing trend with a reduction in concentration.

At a constant concentration, difference in vug volume change is observed for different flow rates. At the lowest concentration, low flow rate shows the largest volume change which is almost double the change at high flow rate. At the middle concentration (1%), the vug volume change is similar for both the flow rate with the high flow rate showing a slightly

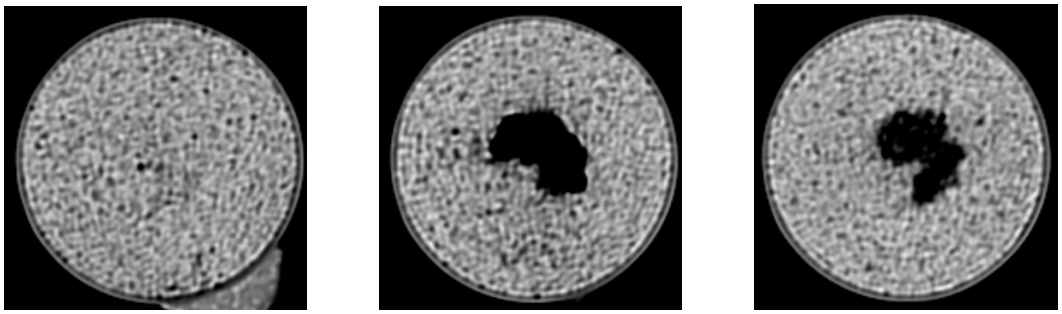

(a) Before particle injection

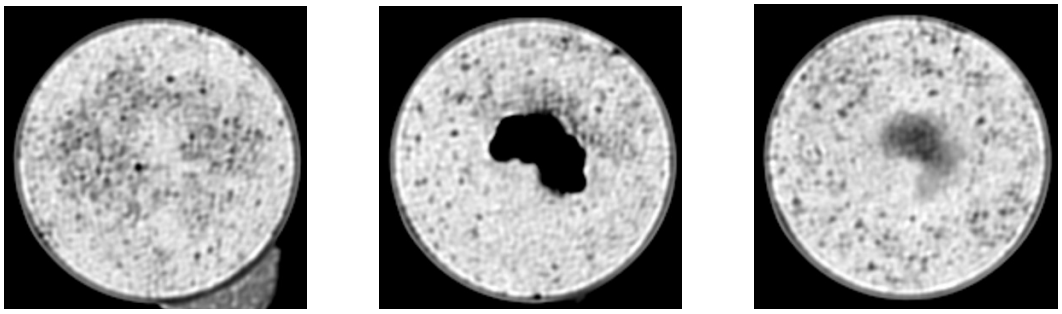

(b) After particle injection

Figure 5.12: Infiltrate deposition at different depths in the core for experiment G6020 (column-wise): prior to top of vug, middle of vug, and bottom end of vug. (Core diameter = 35.9 mm)

larger change. At the highest concentration this difference is more pronounced, with the vug volume change at the highest flow rate almost 3.5 times the change at low flow rate.

5.3.4 Permeability

Permeability change in time is measured in the top and bottom zones (Section 5.2.2) for the homogeneous and vuggy cores. Normalized permeability (with reference to initial core permeability) is plotted against solid infiltrate pore volume (Eq. 5.1) in Figure 5.13. For each flow case, the total solid volume injected is equal to the pore volume, resulting in $\int_0^{t_{inj}} PV_{SI}\ dt = 1$. The variations observed above 1 are small and caused by vibration in the system. They do not add any value to the figure and are thus cropped.

All cases show a decrease in permeability after injection of particles with different rate of permeability change at different depths. Homogeneous cores show a exponential decay in the top zone (Figure 5.13a) with a drastic decrease in permeability, up to 40%, at early times. Total permeability drop in the top zone is greater than 70% for all cases. In contrast, a smaller drop (up to ∼40%) in permeability is observed in the bottom zone for the same core (Figure 5.13b) over the complete injection duration. The injected particles are removed from flow by size exclusion, increasing the resistance to flow. Henceforth smaller concentration of particles are making it to the bottom and therefore result in a smaller reduction in permeability.

Contrasting results are observed when a vug is introduced in the system. Lower permeability

Table 5.3: Vug volume change for different flow conditions.

Flow rate [ml/min]	**Concentration [% v/v]**			
		0.5	1.0	2.0
	40	21%	13%	9%
	60	11%	17%	32%

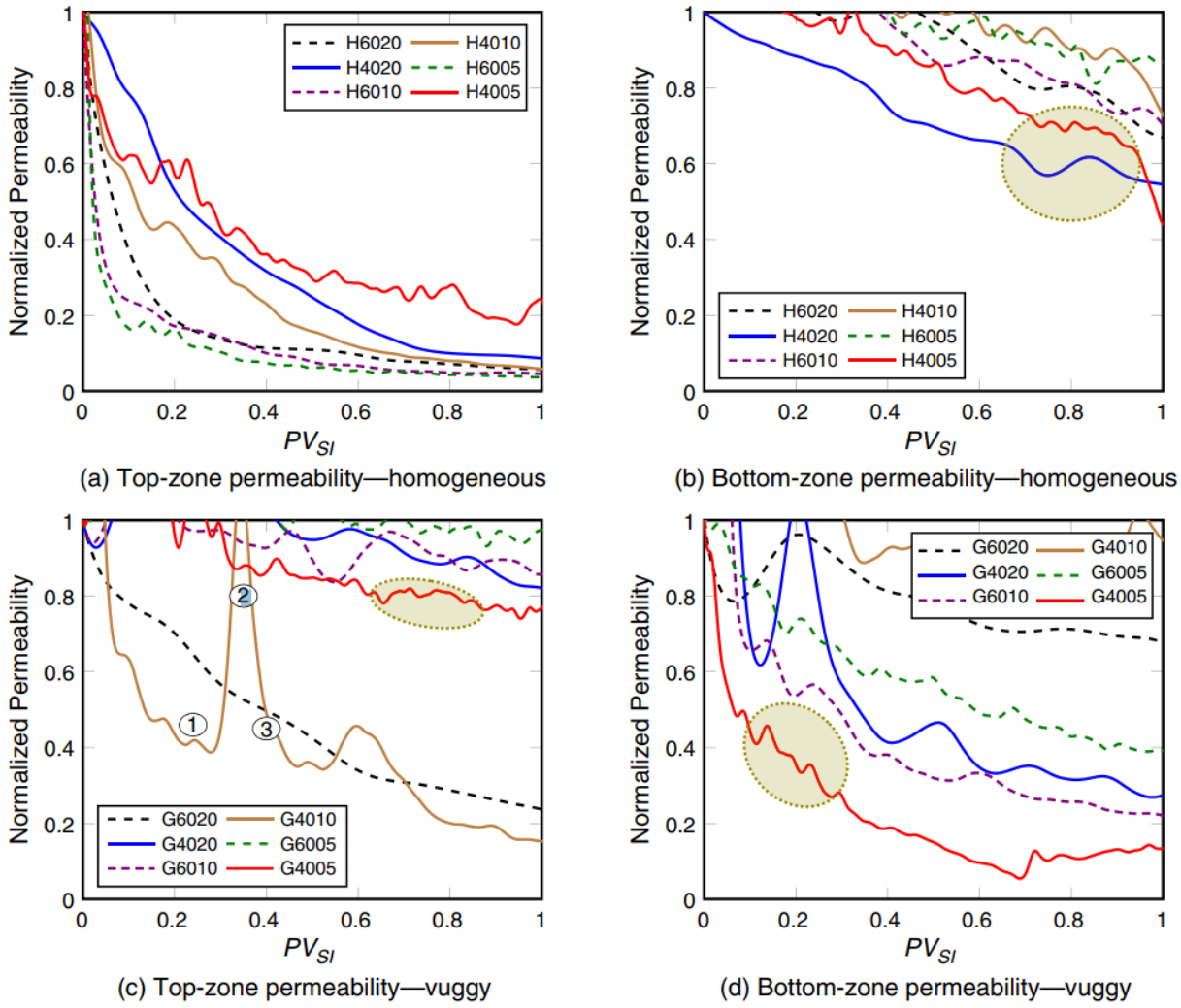

Figure 5.13: Permeability change in time: first row shows the permeability profile in top and bottom zone for homogeneous core while second row shows the same for vuggy core; first column shows permeability profile in top zones for homogeneous and vuggy cores while second column shows the same in the bottom zone. (Experiments are labeled: the letter is the core type, the first two-digit number is the flow rate and last two-digit number is ten times the total injected particle concentration.)

losses are generally observed in the top zone (Figure 5.13c), down to 20% (from 70% for homogeneous core) while more pronounced damage is seen in the lower regions (Figure 5.13d). The normalized permeability reaches values as low as 0.15 with an average end-time normalized permeability of 0.25. Less particles are trapped in the upper region and more particles go deeper in the vuggy core. This behavior is consistent with the behavior observed in the porosity profiles for Group A and Group B.

Two flow conditions that behave anomalously are part of Group A. G6020 (q = 60 cc/min and total injected particle concentration = 2%) has a larger permeability loss in the top region and lower in the bottom region. The permeability profile is very similar to one generated for a homogeneous core with the same flow conditions. G4010 (q = 40 cc/min and total injected particle concentration = 1%) has a higher permeability loss in the top region as well, but a spike in permeability value is observed in the middle of the experiment (Figure 5.13c②). The spike recovers the permeability to the virgin permeability temporarily, and it quickly falls back to the previous level (Figure 5.13c③). A similar spike is also observed in G4020 in the bottom zone, but the permeability is not anomalous. This phenomenon, and a reason for its occurrence, is discussed later in the discussion section.

All cores (different flow condition, core configuration and zonal locations) show fluctuations in permeability (olive highlights in Figure 5.13) around their main trend line. These fluctuations have been seen before as intermittent blockages [27, 98, 105], which cause pressure buildups that are then aperiodically released. The process is repeated in the deeper region of the core as evidenced by the pressure profile (Figure 5.13d).

5.3.5 Streamline simulation

This simulation is setup to gain insight into the change in fluid pathways caused by particle deposition in and around the vug. Particle flow is not modeled, rather vug properties are changed to simulate particle deposition. Steady-state flow is developed in the simulation grid with the reservoir properties shown in Table 5.2. Streamlines are generated and plotted

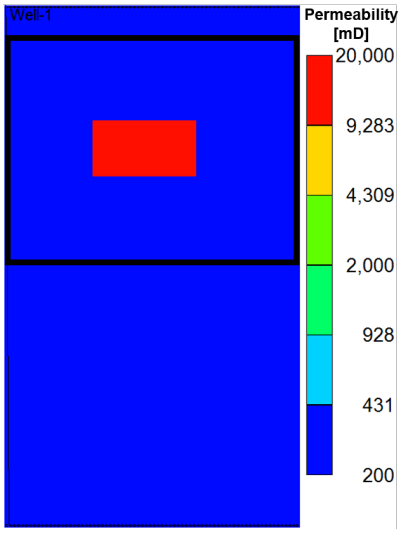

(a) Initial

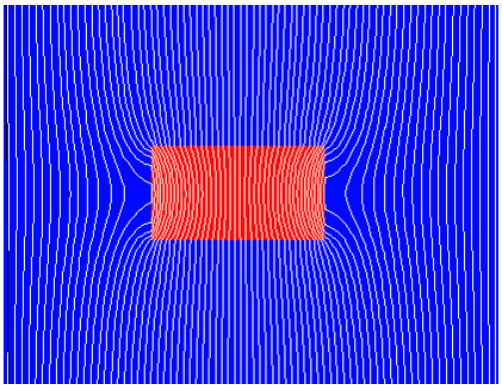

(b) Steady state

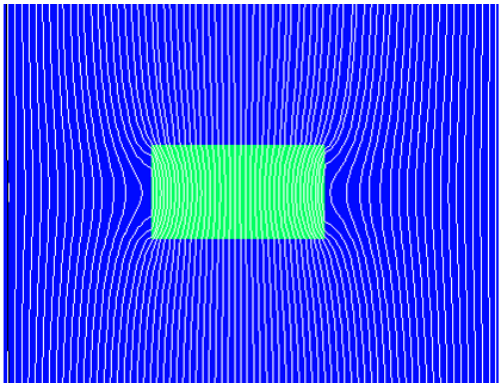

(c) k_{vug} reduced by factor of 10.

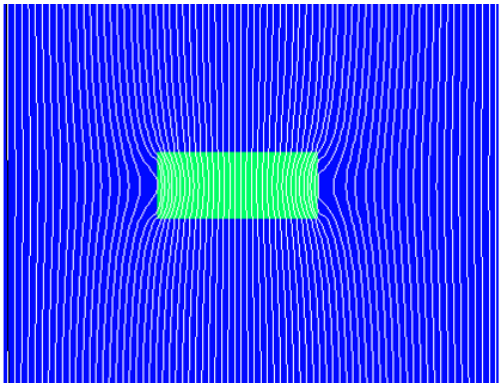

(d) Vug reduced by three units at the bottom and one unit at the other boundaries

Figure 5.14: Streamline simulation with CMG: (a) Simulation grid (blue) has a permeability of 200 mD while the vug's (red) permeability is hundred-fold greater.; (b) Convergent flow in vug at steady state. Channelization reduces with time and flow across vug is observed; (c) Reduction of permeability heterogeneity improves flow around vug; (d) Bending of the streamline is reduced as vug fills up along the top, sides and bottom.

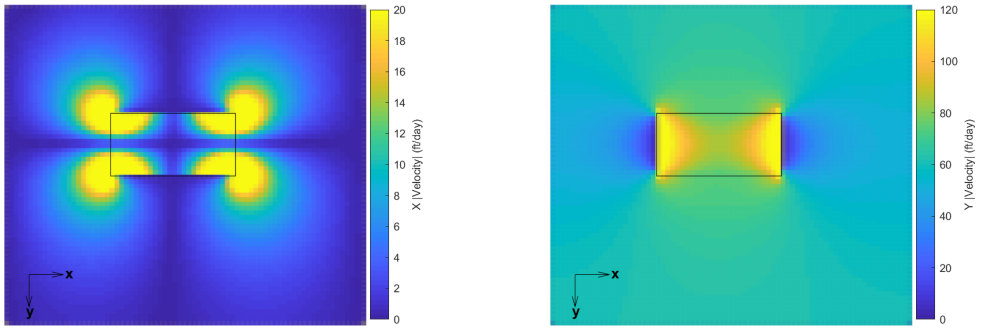

(a) Steady state

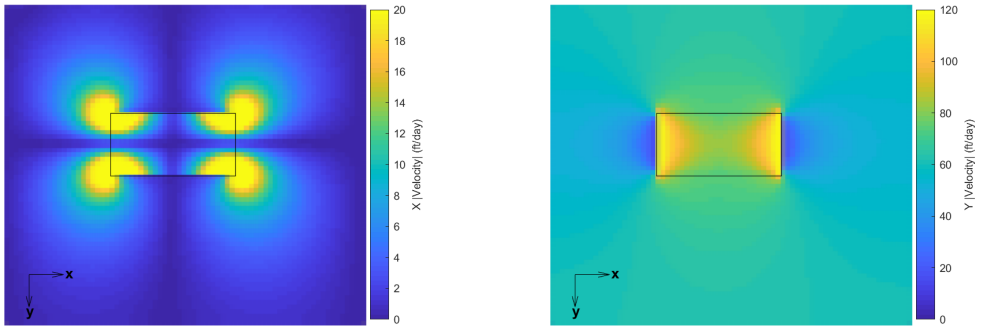

(b) k_{vug} reduced by factor of 10.

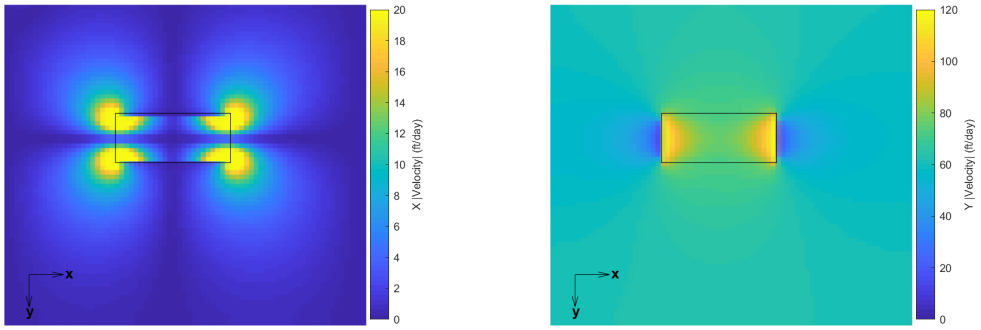

(c) Vug reduced by three units at the bottom and one unit at the other boundaries

Figure 5.15: Velocity map in x-direction (left) and y-direction (right). The black box is the location of the vug, which is constant for the first two cases and reduces for the last case.

over the core in Figure 5.14a. The vug, which has a hundred fold greater permeability (20 D), is denoted in red while the matrix (200 mD) is colored as blue. The streamlines are shown in white.

At steady-state with native reservoir properties (i.e. before any permeability changes caused by particle injection), the vug causes the streamlines to converge; specifically the vug takes up only 35% of cross-sectional area but 58% of the streamlines pass through it. The convergence factor, defined as the number of streamlines entering the vug per unit length, here initially is $0.58/0.35 = 1.69$. Of the streamlines that enter the vug, 86% come through the top face (Figure 5.14b).

Figure 5.15 shows the x- (left) and y-velocity maps (right). For the steady-state condition, the x-velocity map has two distinct features: a change in velocity at the edges of the vug and no disturbance in field in the center of the top face of the vug. Similarly, two distinct features that can be observed for the y-velocity map are: an increase in velocity on the inside of the side-wall of the vug and a reduction in velocity on the outside of the side-wall the vug.

If vug permeability is reduced to simulate particle deposition, we observe a reduction in the streamlines entering the vug (Figure 5.14c). 53% of the streamlines now enter the vug, with a convergence factor of 1.52. The disturbance in x-velocity field near the edges of the vug is reduced and the y-velocity slowdown on the outside of the side-wall of the vug is also reduced (Figure 5.15b). Similarly, reducing the size of the vug (volume reduced by 34%), further diminishes the disturbance in x- and y-velocity field (Figure 5.15c). The convergence factor reduces to 1.48 with 48% of streamlines passing through the vug (Figure 5.14d).

5.4 Discussion

Integrating the porosity, permeability, vug changes, and simulation, we observe the following differences between vuggy and non-vuggy media:

1. Deeper penetration of particles in presence of vugs;

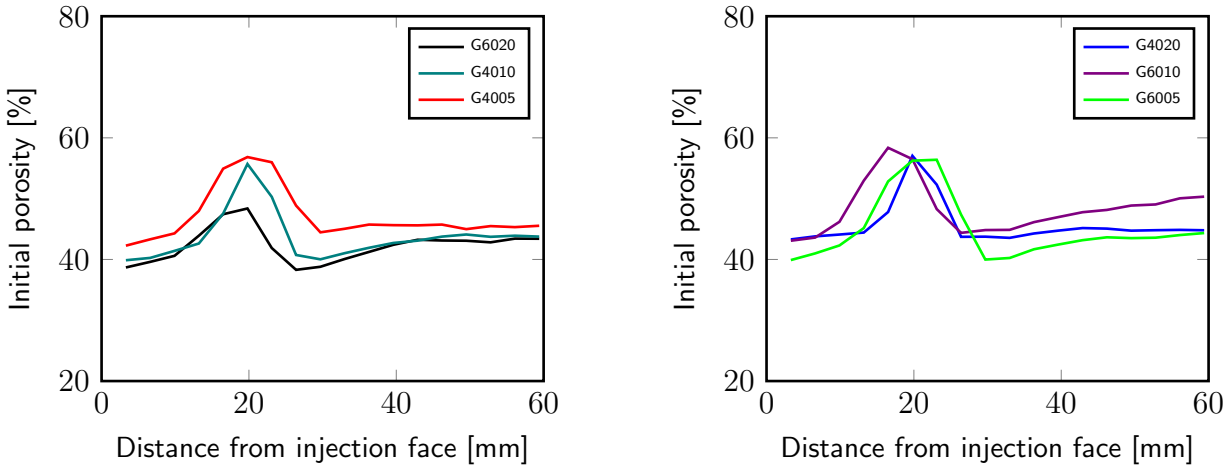

(a) Vuggy core - Group A

(b) Vuggy core - Group B

Figure 5.16: Connected porosity before injection.

2. More damage in matrix around vug;

3. Contrasting flow behavior (Group A and Group B) in the presence of a vug.

It is very likely that these results are coupled. We start the discussion on the deeper penetration of particles in the vuggy media.

In terms of penetration, a single vug of size d located in the radial center of the core should allow particles to penetrate a distance of d deeper into the media. In this test we observe maximum particle deposition at 24 mm in the presence of a 12 mm vug, 4 mm greater than the maximum deposition at 8 mm observed in the no vug case. Thus for a single vug located at the radial center of the core, the effect of the vug is greater than expected. Less particle deposition in the top zone results in deeper penetration of particles, which results in less permeability change compared to the homogeneous cores. The deeper deposited particle reduces the porosity (and permeability) of the lower zone.

In addition to the greater depth of deposition, we observe more deposition in the matrix around the vug (12% porosity change for vuggy core compared to 10% in homogeneous cores). We look for a reason for these two effects from our understanding of flow patterns

with and without a vug. With a vug, in the top part of the core, flow is uniform across the cross-section and particles are deposited evenly, like in the homogeneous core. As the vug is approached, the permeability contrast between matrix and vug bends the streamlines and directs flow towards the vug. This behavior is observed in the simulation results (Figures 5.14 and 5.15). The bending of the streamline increases the length and complexity of the flow path. Since particles have a different momentum than the fluid, the bending streamlines may cause more interaction between grains and particles resulting in more deposition. We believe there is a positive feedback from the already deposited particles as they reduce the permeability of the matrix and further enhance the permeability contrast.

For item 3, we observe contrasting behavior in porosity and permeability change in the presence of a vug. Group A shows porosity and permeability profiles similar to those observed for homogeneous core while Group B shows a difference. All the cores have been prepared using the same procedure and have the same initial average porosity. The initial porosity profiles for all the vuggy cores are plotted in Figure 5.16. All the experiments for the homogeneous cores, and some for the vuggy cores have been repeated, with similar results. Based on the current work we do not have enough data to deduce the cause of this large variation in deposition, but we observe that it only happens in the vuggy media. We speculate that a difference in bead packing, the range of sizes of injected glass beads, and/or the boundary effects play an important role in this disparity. The experiments should be repeated in wider/longer cores as well as bead sizes that are scaled by a factor close to 1 (say, 0.8 to 1.2) compared to the current size.

For both vuggy and non-vuggy media, temporal fluctuations in permeability are observed. For two flow cases in vuggy cores (G4020 in the top zone and G4010 in the bottom zone), we observe a drastic increase in permeability such that the permeability is recovered to its initial value. We believe that these are different than those discussed in Section 5.3.4 due the significant difference in magnitude and are not caused by experimental error as they occur over a long time duration. A theory is proposed that explains this behavior: as described

above, the high permeability contrast between the matrix and vug redirects the fluid to the vug. There is a preferential flow pathway that has a significantly high permeability and most of the fluid is carried via this pathway. As particles interact with the matrix, some of them are deposited. The initial preferential pathway is the first to be plugged, which results in the drastic decrease in permeability at early times. This increases the streamline length and complexity as fluid finds the next best path. For most flow conditions and/or pore distribution, this pathway is plugged such that the localized surge in pressure cannot clear it as there are less resistant pathways available in the matrix (Figure 5.13c①). For some cases (G4010 and G4005), this pathway is cleared by the localized surge in pressure as no alternate route is available. Resultantly the permeability recovers to the initial value (Figure 5.13c②) until is blocked again and we see a drastic fall in permeability (Figure 5.13c③). This fall is quicker than the initial decline as the alternate pathways have high resistance to flow compared to the alternate pathways available at initial time.

The flow rate does not seem to have an effect on the change in porosity in the top zone of the homogeneous core, though a change is observed in the permeability in this zone. A higher flow rate (and lower injected particle concentration) result in more damage. In contrast, the bottom zone has more spread in the porosity change. On average, the high flow rate results in twice the porosity change observed for low flow rate. Permeability shows a change with flow rate (except H4010), with a faster flow rate resulting in less change in permeability. This change is not as pronounced as with porosity; the low flow results in 1.5 times the permeability at high flow rate. The vuggy core does not show this behavior. The upper zone has two distinct behaviors' (resulting in the group classification), but they are not influenced by flow rate only. The bottom zone in the vuggy core shows less spread (except G6010) compared to homogeneous cores.

5.5 Conclusions

Three hypotheses were proposed at the start of the study: (1) the presence of vug would reduce the deposition of solids in the surrounding matrix, (2) the fluid phase would preferably flow through the vug, and (3) most damage/deposition would be observed at the bottom of the vug.

Our findings contradict the first hypothesis. At the depths across the vug, the average porosity change for all the vuggy cores is greater than the average porosity change for the non-vuggy cores. This is further enhanced if only the matrix area ($\sim$ 89% of total cross-section) is considered. Further, the simulation study run to explain analyze this shows streamlines converging towards the vug. The permeability ratio plays an important part in this convergence as it controls the deviation of the streamlines. Reducing the permeability ratio (which can be achieved by reducing the vug size) reduces the deviation of the streamlines, and thus the range/distance of influence of the vug. For three vug/matrix permeability ratios considered, the flow preferably flows through the vug. Thus the second hypothesis is valid (actually is somewhat obvious) and is consistent with our first finding.

CT scan results show particulate accumulation in the lower end of the vug. Though maximum porosity in the vug region for all the flow cases is not always the deepest one due to averaging across the core depth and irregular shape of the vug, only one case shows a decreasing trend in porosity change in the vug region. The third hypothesis is thus true. In addition, we find that the presence of the vug enhances the depth of penetration and that the vug roughness is smoothed out by particle deposition. Note that the vug roughness is on the order of matrix grain size, and any particles of size small enough to penetrate the matrix are expected to fill in vug roughness, thus smoothing it out.

Finally, in terms of broader implications for particle transport into vuggy carbonates, the presence of pore bodies on multiple length scales changes the particle entrapment mechanics. Real-world injection fluid has suspended particles (from colloidal size to few millimeters in

diameter) that can plug up the formation and/or the vug system while the pore size to vug size ratio in carbonates can vary over multiple orders of magnitude, and it matters whether we have a connected vug system or not. This study is a starting point, based on a single spherical vug located in the top half of the core. We cannot claim that the conclusions drawn from the results here hold for another system, with variation(s) in vug geometry, vug number, location, surface roughness, and/or vug size. But this study suggests and it is highly likely that all these parameters will affect the porosity and permeability, with deeper penetration of particles.

Note: All data generated in this work can be found at Khan et al. [109].

Nomenclature

c_{total} = total injected particle concentration, v/v %

CT = computed tomography

G = vuggy core

H = homogeneous non-vuggy core

HU = Hounsfield units

PV_{SI} = pore volume occupied by the solid infiltrate, dimensionless time

q = flow rate. ml/min

t = time, min

t_{inj} = injection time, min

V_b = core bulk volume, ml

α = core type

ϕ = core total porosity, dimensionless

Chapter 6: The effect of vug porosity and vug distribution on particle straining in permeable media [†]

This chapter shows an experimental formation damage study conducted on multiple spatial distribution of two vugs in a proxy core. Glass beads, used to reduce surface forces, of 1.0 mm are sintered to form a homogeneous core with a 42% porosity. Vuggy cores are made by adding dissolvable inclusion (salt) in series and parallel configuration with flow during the sintering process, and dissolving them with core floods afterwards. The total vug volume (sum of the two vugs) is chosen to be similar to the vug volume in Chapter 5:.

Finer sized glass beads (25 and 100 microns) are used as the infiltrate. The injected particle sizes are chosen such that straining is the dominant trapping mechanism during the flow experiment. Infiltrate particles are injected at different flow configurations in a gravity-dominated flow, and the resultant porosity, permeability, and effluent volume are measured.

The results can be summarized as: vugs that are parallel to the flow direction behave independently with retention profiles similar to single vugs of the same volume [114], vugs in series have different retention profiles in each vug and injected particles penetrate deeper in the series vug configuration. We perform flow simulations for both configurations and

[†]This chapter is based on the following paper:

Khan, H.J., DiCarlo, D.A., & Prodanović, M. (2019). The Effect of Vug Distribution on Particle Straining in Permeable Media. Journal of Hydrology. https://doi.org/10.1016/j.jhydrol.2019.124306

find the experimentally observed particle deposition is consistent with changes in the flow streamlines. In particular, retention is enhanced where streamlines converge, which in turns alters the vug size and straining potential of the porous medium over time.

6.1 Introduction

Straining of particulates in porous and permeable media is of fundamental importance to many branches of science: it changes the storativity of water aquifers over time [122], it changes the surface pressures required to pump fluids insubsurface disposal wells [103, 201], and it evolves the filtration efficiency in a car air filter [61].

Many fresh water aquifers around the world are in karst rocks [70, 136, 215]. For instance the Edwards aquifer in south-central Texas, composed of a heterogeneous limestone group inter-bedded with sand/gravel sediments [133], supplies water for about two million people in the cities of Austin and San Antonio. It is a karstic limestone with multiple layers of highly heterogeneous porous rocks formed by leaching of evaporitic and reefal deposits creating pre-dominantly small inter-particle, intra-particle, and inter-crystalline pores [68, 133, 134]. The limestone rock matrix is reactive to the groundwater and releases sediments which are transported within the aquifer [135]. Furthermore rapid transportation of groundwater, with little time for subsurface filtration of particulates, occurs through the karstic features [159, 185] and introduces surface solids into the aquifer. These solid sediments can get trapped and jam the flow pathways present in the rock [97], thereby reducing the inherent permeability of the rock. This reduction of the rock permeability is also called formation damage [42] and can reduce the flow capabilities of the aquifer over time.

Formation damage caused by fines movement has been studied extensively [80, 85, 87, 112, 138, 145], with focus on particle straining (by the process of size exclusion) and surface deposition. Herzig et al. [87] suggests straining is the dominant mechanism when infiltrate particle diameter is greater than 30 μm. Surface deposition is more prominent for smaller-sized infiltrate (smaller injected particle to medium grain ratio) as surface forces such as

electrostatic and van der Waals forces become significant (Figure 6.1).

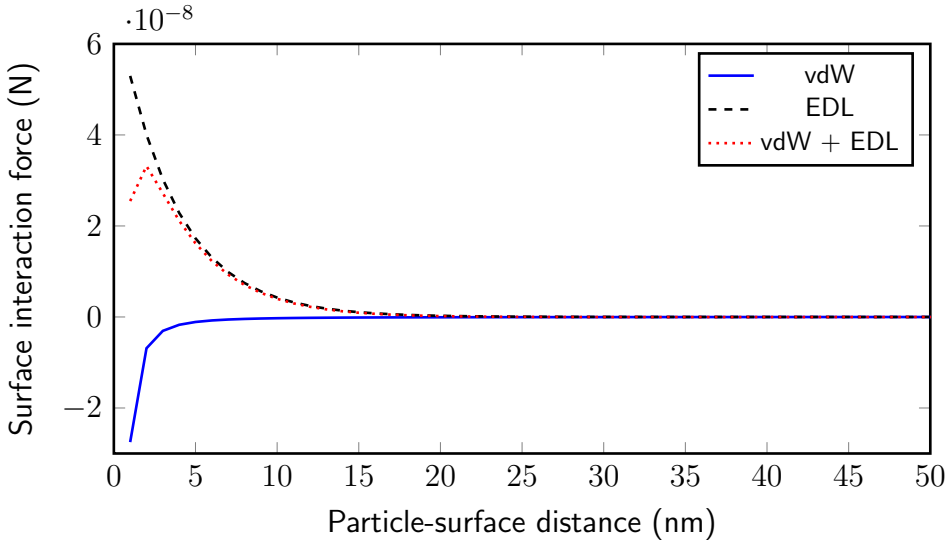

(a) van der Waals force (vdW), electric double layer (EDL) force, and the sum of the two forces plotted against the distance between infiltrate particle and grain surface for $d_p = 25$ μm.

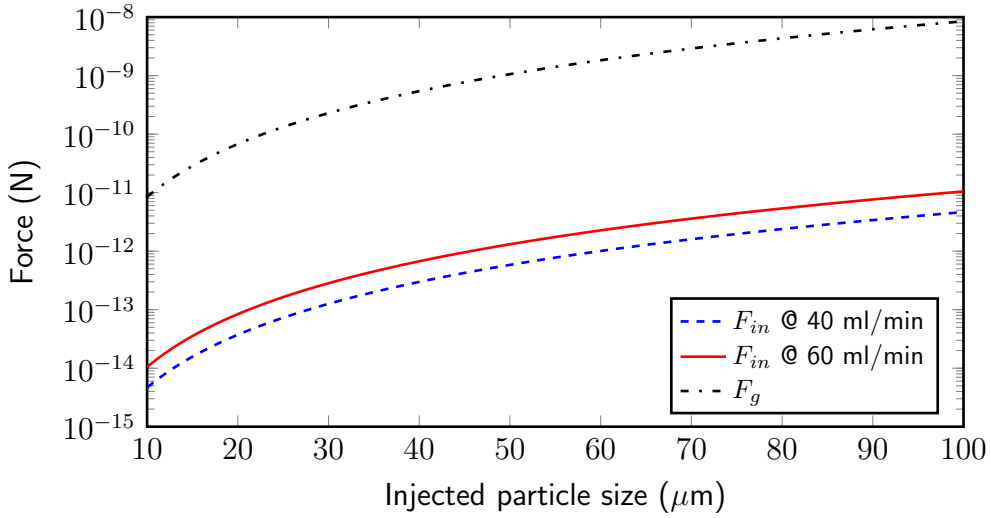

(b) Comparison of inertial F_{in} and gravity forces F_g.

Figure 6.1: For the particle sizes and flow rates used in this paper, the inertial and gravitational forces are significantly larger than the surface forces. Thus gravitational-driven particle straining should dominate over surface deposition.

Numerous studies [10, 21, 23, 80, 87, 147] have measured the filtration processes in ho-

mogeneous sandstone media, while not much attention has been afforded to carbonates. Carbonates are complex rocks with a wide range of porosity, and pore size distribution [6, 72, 149, 172]. Vugs (pore openings on a larger length scale) are a prominent feature in carbonates and contribute significantly to the local porosity of the rock, however permeability strongly depends on vug connectivity. A high contrast exists between the two length scales, i.e. the size of the vug and the pore size, which results in a heterogeneous flow [13, 217] making it difficult to discern the particle retention patterns in a vuggy porous medium.

A previous study [114] looked at vug changes and changes in matrix deposition for a single vug. It showed that the injected particles partially fill up the vug and are deposited in the matrix surrounding the vug. The particles penetrate deeper inside the porous medium and a higher particle deposition (higher porosity loss) is observed in the vug surroundings. The question that arises next is how would the particle deposition patterns vary, in the vug and in the matrix, when we have more than one vug?

Here, we study the effects of multiple vugs on particle deposition. The simplest spatial distributions possible for two vugs in a porous medium are: two vugs in parallel or two vugs in series relative to the direction of fluid flow. We synthesize glass bead (1.0 mm) cores with the desired porosity and vug structures, and inject smaller-sized glass beads (25 and 100 μm) at different flow rates (40 and 60 ml/min) and total injected particle concentrations (0.5%, 1%, and 2%). We measure the continuous pressure drop, and therefore the permeability change, along the core and collect the effluent fluid. We scan the pre-flood and post-flood core in a computed tomography scanner ($\sim$250 μm) to get an estimate of the porosity change and the particle deposition patterns in the matrix and vugs. The aim of this study is to identify the influence of vug-vug interaction and the vug spatial distribution on the particle deposition patterns in the vug and the surrounding matrix.

We measure the continuous pressure drop, and therefore the permeability change, along the core and collect the effluent fluid. We scan the pre-flood and post-flood core in a computed

tomography scanner (∼250 μm resolution) to get an estimate of the porosity change and the particle deposition patterns in the matrix and vugs. The aim of this study is to identify the influence of vug-vug interaction and the vug spatial distribution on the particle deposition patterns in the vug and the surrounding matrix.

This work has not focused on creating a mathematical model. lOver the three years that we have studied this problem, a simple mathematical model has not proven to be feasible [107, 112, 211, 212]. Multiscale modeling approaches have been tried [112] with limited success. Based on the previous work done on modeling particulate flow in homogeneous porous media [144, 145], we know that a more detailed numerical model in vuggy media is computationally demanding and the extent of the work is thus beyond the scope of this paper.

We find that a vugs in series affect the particle deposition patterns in the other vug, with variations in porosity profile observed. The vugs in parallel, i.e. vugs at the same depth inside the porous medium, have no discernible impact on the particle retention behavior of each other. Similar deposition pattern, and therefore porosity profile, is observed in either vug implying that the separation between the vugs is larger than their area of influence.

6.2 Methods

6.2.1 Experimental methods

Vugs are created in sintered glass bead packs (1.0 mm diameter) by adding dissolvable salt inclusions wrapped in cheesecloth to a 1.0 mm glass bead mixture placed in a graphite mould (35.9 mm ID × 77.7 mm depth) and sintering in a muffle furnace at 725 °C in the presence of air. Flooding the core after cooling clears any cheesecloth residue left behind from the combustion process and dissolves the salt creating 12 mm diameter spherical vugs. Alternatively, the vugs can be created by the method prescribed in Khan et al. [113].

Two new vuggy core configurations are created (Figure 6.2) with the same total vug volume:

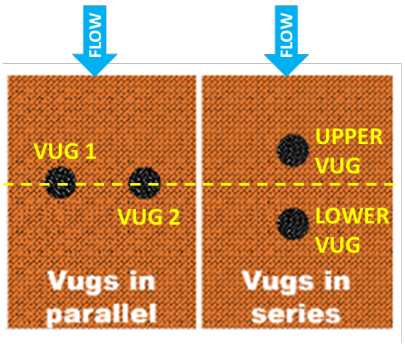

Figure 6.2: Fabricated core configuration schematic: two vugs in parallel (VP) and two vugs in series (VS). The total vug volume is constant for all the cases.

two equal-sized vugs in series and two equal-sized vugs in parallel relative to the direction of flow (Figure 6.3). The two vugs in the parallel configuration are arbitrarily named vug 1 and vug 2 while the two vugs in series are named upper and lower vug, based on their spatial location. The depth of the vugs is chosen such that the geometric center of the two vug system is the same. To simplify the reference to these vuggy core configuration, from here on we will be referring to these as the series and parallel configuration respectively.

The cores act as proxy rock for core flood experiments: equal volumes of 25 μm and 100 μm glass bead (fine) suspensions are injected, in the top-down direction, in the core at three total injection concentrations (0.5%, 1%, and 2% v/v) and two flow rates (40 and 60 ml/min), resulting in six unique flow conditions (Table 6.1) for each core type.

The total volume of injected particles is kept constant for all experiments and is equal to the pore volume of a homogeneous core ($\simeq 27cm^3$). PV_{SI} (t) can be defined as the ratio of total volume of the solid infiltrates injected at time t to the total pore volume. The total injection time for a specific injection concentration and flow rate, for constant solid volume injected, can be calculated by keeping $\int_0^{t_{inj}} PV_{SI}\, dt = 1$ in Eq. 6.1.

$$PV_{SI}(t) = \left\{ \frac{q \cdot c_{total}}{\phi \cdot V_b} \right\} \cdot t \tag{6.1}$$

where PV_{SI} = pore volume occupied by the solid infiltrate [frac]; V_b = core bulk volume

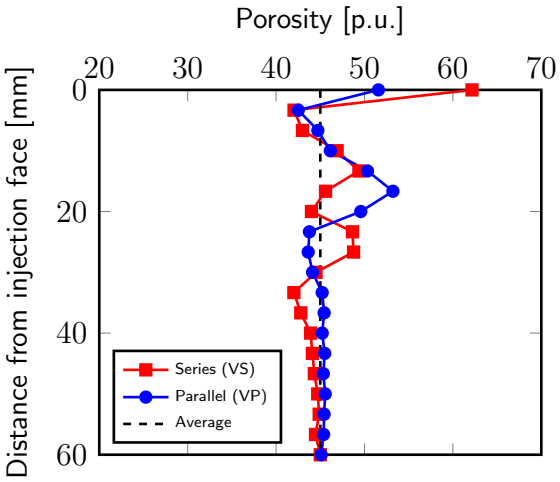

Figure 6.3: Initial porosity for the generated cores: VP and VS. Vugs in series show two protrusions above than the average porosity while vugs in parallel results in one protrusion above the average porosity.

[cm^3]; ϕ = total core porosity [frac]; q = fluid flow rate [cm^3/min]; t = time [minutes]; c_{total} = total injected particle concentration [vol %].

Four parameters are measured for each experiment:

1. Vug volume reduction – The vugs are extraced from the CT images (8-bit) by the sequential application of filters, segmentation, and Fiji-ImageJ's [127] built-in FIND CONNECTED REGIONS algorithm with 26-connectivity. The images is segmented using the Otsu method, with the threshold gray value set at 76. The difference between the pre-flood and post-flood CT stack results in the vug volume change caused by particle deposition and the 3D reconstruction of the difference gives a qualitative description of the spatial deposition of particle with respect to the vug.

2. Porosity change – Pre- and post-flood porosity of each core is measured using an in-house multiple energy modified medical computed tomography (CT) scanner (Universal Systems HD-350E) at a resolution of 250 microns. The difference in the gray values between the two sets of images gives the change in porosity (Eq. 6.2) caused by particle deposition during the experiment.

Table 6.1: Experimental flow conditions for each vug configuration.

Experiment name[ii]	**Flow rate [ml/min]**	**Total injection concentration [vol %]**	**Injection time [min]**
Γ6020	60	2.0	22.50
Γ4020	40	2.0	33.75
Γ6010	60	1.0	45.00
Γ4010	40	1.0	67.50
Γ6005	60	0.5	90.00
Γ4005	40	0.5	135.0

[ii] Γ identifies the core type: VP = parallel configuration; & VS = series configuration

$$\Delta\phi = \frac{CT_{after} - CT_{before}}{CT_{glass} - CT_{water}} \tag{6.2}$$

3. Permeability change over time – Three pressure taps (inlet, middle, and outlet) are connected to the core and continuously log differential pressure measurements in the top (inlet and middle) and bottom (middle and outlet) part of the core. The continuous pressure trace is converted to a continuous permeability trace using Darcy's law.

4. Total particle effluent – The total effluent volume is collected, filtered twice using a 10-μm filter paper, dried, and weighed. The solid mass in the total effluent gives a measure of the ratio of injected particles deposited in the porous medium. A material balance calculation is performed on the total injected particles and porosity change to ratify the total effluent particle collected.

The experimental workflow, setup schematics, and detailed procedure is outlined in Khan et al. [114]. In brief, the core is first fabricated with the desired vug configuration and installed in the core hanger (Figure 6.6). A pre-flood CT scan of the core is acquired in the

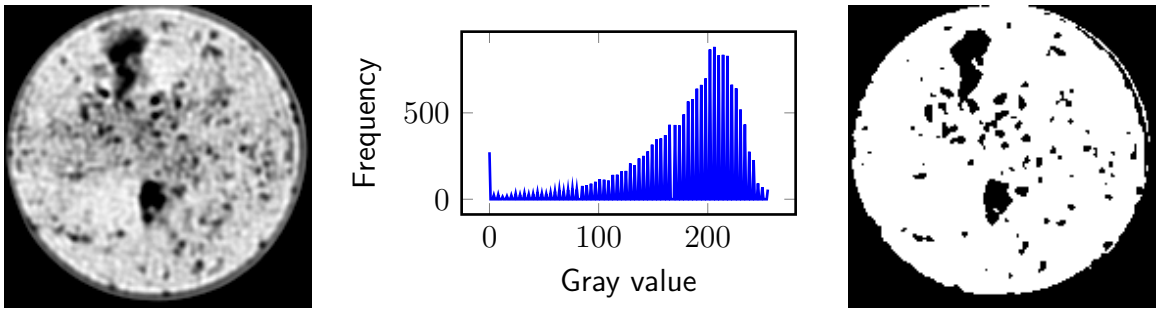

(a) CT output (b) Histogram (c) Segmented image

Figure 6.4: Cross-section across the vug for VP4010 after injection, the calculated histogram, and the segmented image. The difference in matrix and vug space is quite large, making it easy to segment.

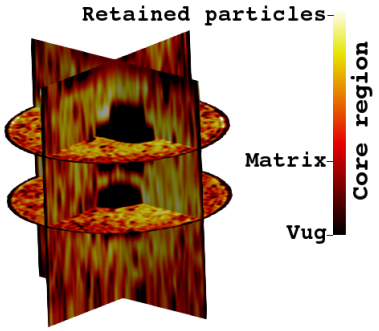

(a) Multiple cross-sectional slices through the core (VS6005); black represents the void space with lighter shades representing the degree of retention

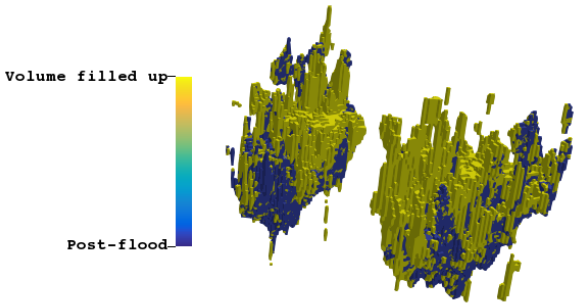

(b) Vug visualization for VP4010 with the filled up region marked in yellow

Figure 6.5: 3D visualization of the core and the vug.

medical CT scanner at a resolution of 250 μm. Different concentrations of 25 and 100 μm glass bead suspension are injected in the fabricated core at different fluid flow rates in the top-down direction. The effluent is collected and the filtered twice to remove and isolate the suspended particles. Continuous pressure recordings are acquired during the injection phase in the three equidistant pressure transducers to give a continuous permeability trace. A post-flood CT scan of the fabricated core is acquired; combination of this with the pre-flood scan results in the porosity reduction and the vug volume change. The complete experimental process is outlined in Figure 6.7.

6.2.2 CMG simulation

A 2D CMG-IMEX [46] simulation is set up to understand the change in streamlines caused by the spatial distribution of vugs. This simulation is neither modeling the particle-deposition process nor measuring the change in the vug volume, but it is set up to gain an insight into streamlines taken by the injected particles, by solving the Darcy's law equation for the vug-matrix system. The difference between flow in matrix and in vug is not only the domain size, but also the dimension. Flow in matrix can be assumed as 1D, but flow in vug is 3D in nature (in particular cases, it can be simplified to 2D). Sophisticated models, such as the Brinkman equation (Darcy's law in the matrix and Stokes equation in the vug), are required to model the flow in vug-matrix system and would be an appropriate approximation to resolve the flow inside the vug in more detail, however it is more computationally involved, and we are assessing the first order approximation of the problem [99, 152] and more interested in the interactions happening at the vug/matrix interface rather than inside the vug. Both approaches hold the same assumptions on the flow (small Reynolds number) but have different level of detail in the vugs vs. matrix. The problem is simplified to a quasi-2D system using a Cartesian grid ($74 \times 131 \times 1$) with two cuboidal vugs (combined vug volume equal to the single vug volume in Khan et al. [114]). No grid refining is used.

The reservoir is saturated with single-phase water with pressure greater than the bubble

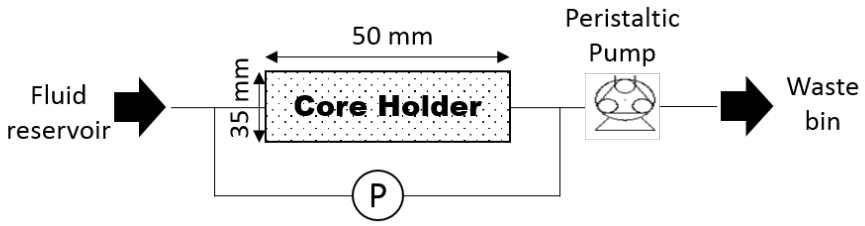

Figure 6.6: Experimental setup: The fabricated core is wrapped in a heat shrink tubing with three equi-distant pressure ports and connected to the fluid reservoir at the top and the peristaltic pump below. 25 and 100 μ glass beads are kept in suspension by a stirrer operating at 7000 rpm in the fluid reservoir. The 3-way valve between the fluid reservoir and the core is opened; the glass bead suspension flows in the vuggy core in the top-down direction with the flow rate controlled by the peristaltic pump at the bottom. Continuous pressure measurements are recorded by the pressure transducers connected to the three pressure ports along the core length.

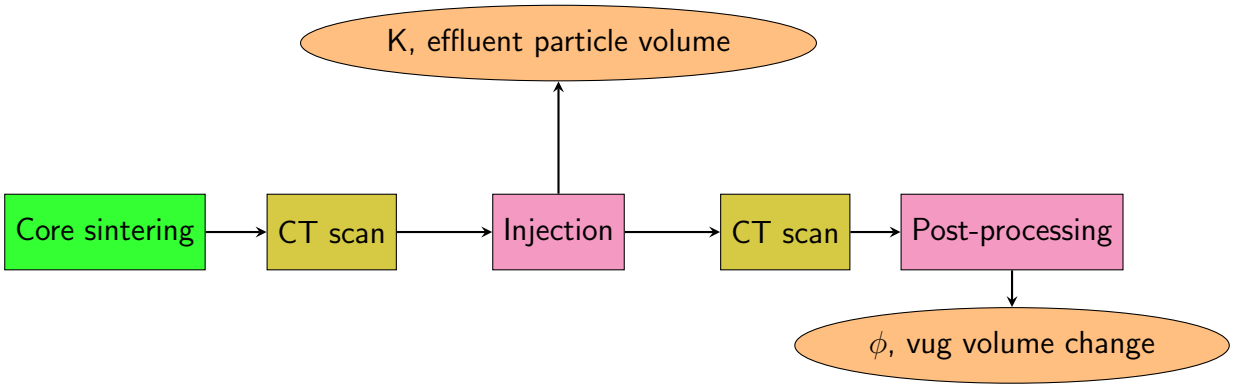

Figure 6.7: Process workflow: Glass bead core is sintered and CT scanned. Core floods are conducted with real-time measurement of pressure and total effluent volume before the core is scanned again. Porosity change and vug volume change due to injection are determined during the post-processing.

point pressure. Single phase fluid (water) is injected from the top end and produced from the bottom end at a constant flow rate of 3280 bbl/day (upscaled from 60 ml/min). The flow rate is calculated by keeping the spatial and temporal upscaling ratio the same. The vug has a porosity of 99% compared to 41.6% for the matrix while the permeability of the vug is two orders of magnitude greater than the surrounding matrix (200 mD). Since the vug size is one order of magnitude larger than the pore size and the permeability scales as a square with the pore size, the vug permeability is chosen to be two order of magnitude larger (20000 mD) than the matrix permeability. CMG input parameters are presented in Table 6.2.

6.3 Results

6.3.1 Vug volume change

Previous measurements of a single vug [114] in porous medium showed that the outer surface of the vug was first filled with particles smoothing the vug surface, therefore a large damage was observed in the middle cross-section of the vug. The maximum damage was observed at the bottom end of the vug. For multiple vug configurations, the vug volume change due to particle entrapment for each vug at different flow conditions is presented in Table 6.3. Vug 1 and vug 2 in the parallel configuration are named arbitrarily as both the vugs are of a similar shape and size, and are placed at the same depth inside the core. For a steady state system with a uniform influx of particles, the two parallel vugs expectedly show a similar loss in vug volume and a similar deposition profile (Figure 6.8) for each flow condition. Upper and lower vug in the series are named according to their spatial locations inside the core.

A complete or partial (>50%) fill-up of vugs is observed in two instances (Figure 6.9), both of them in the series configuration. The lower vug in VS4020 is completely filled up while the upper vug in VS6010 is partially filled. For the partially filled vug, we observe that the sides of the vug in a cross-section are filled up and a fluid pathway is present through the

Table 6.2: CMG input parameters.

Input parameter	**Value**
Simulator	IMEX
Coordinate system	Cartesian
Grid size	$74 \times 131 \times 1$
Voxel size	$1 \times 1 \times 1$ (ft^3)
Vug size	$[18 \times 10 \times 1] \times 2$
Matrix porosity	0.416
Matrix permeability	200 mD
Vug porosity	0.99
Vug permeability	20,000 mD
Fluid	Single phase water
Inlet & outlet boundary	Constant flow rate
Flow rate	3280 bbl/day

Experiment	**SERIES**		**PARALLEL**	
	Upper	**Lower**	**Vug 1**	**Vug 2**
Γ4005	17.25	14.08	13.67	14.84
Γ4010	22.08	18.40	5.42	14.62
Γ4020	29.67	99.96	35.39	37.20
Γ6005	18.54	19.67	14.68	7.80
Γ6010	79.76	13.18	10.93	13.94
Γ6020	17.24	21.13	19.93	12.61

Table 6.3: Percentage change in vug volume for different vug configuration and flow conditions.

center of the vug.

For the series configuration, the spatial location of maximum damage is not the same in the upper and lower vug. The upper vug generally has a maximum volume loss in the middle of the vug while the lower vug generally has a maximum loss at the top of the vug. This is an interesting observation which tells us about the difference in streamlines, and therefore the particle movement, observed by each vug. The flow carrying the injected particles enters the upper vug from all sides and losses the particles at the vug-matrix interface. The flow then channels from the upper vug to the lower vug, and the particles are deposited at the top part (matrix between the two vugs) of the lower vug.

For the parallel configuration, the maximum vug volume change is observed in the middle cross-section of the vug (Figure 6.8), which is inline with the results observed for a single vug. This implies that the injected particles, and therefore the streamlines, are entering the vug from all the sides and not only from the top. The middle slice through the spherical vug has the largest perimeter and would therefore have a higher deposition of particles, resulting in maximum damage.

For either vug configuration at 0.5% and 1% total injected particle concentration, the higher flowrate has a larger vug volume loss than IN the corresponding vug at the lower flowrate, and the opposite is observed for the 2% total injected particle concentration, where the lower flowrate has a higher vug volume loss.

6.3.2 Porosity

Porosity results, calculated across the cross-section, are presented in Figure 6.10; the first and last scans are ignored as they are prone to boundary errors. The porosity change can be defined into three zones: (i) above the top of the upper vug; (ii)top of the upper vug to the bottom of the lower vug; and (iii) below the bottom of the lower vug. Generally, a higher loss in porosity is observed in series configuration than in parallel configuration, i.e. more

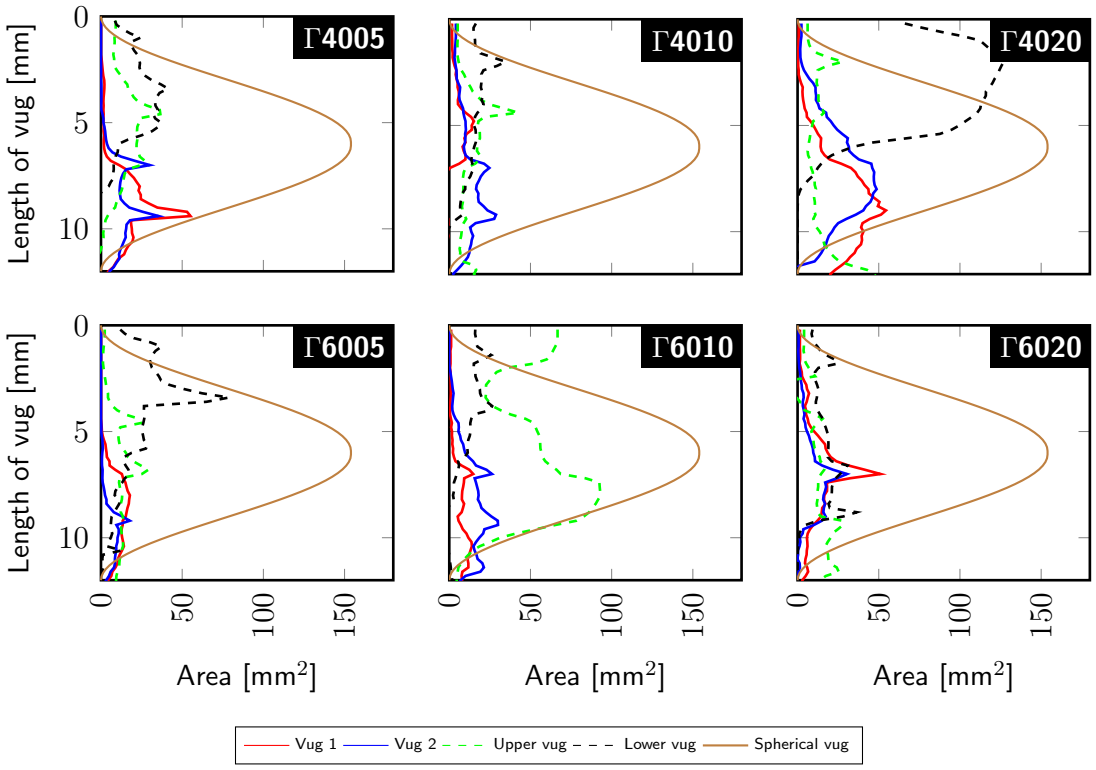

Figure 6.8: Vug area change profile along the depth of the vugs in the two configurations (Γ): parallel (vug 1 and vug 2) and series (upper and lower vug), and the theoretical area of a similar sized spherical vug. The vug area change is calculated by taking the slice-by-slice difference between the post-flood and pre-flood vug derived from CT images.

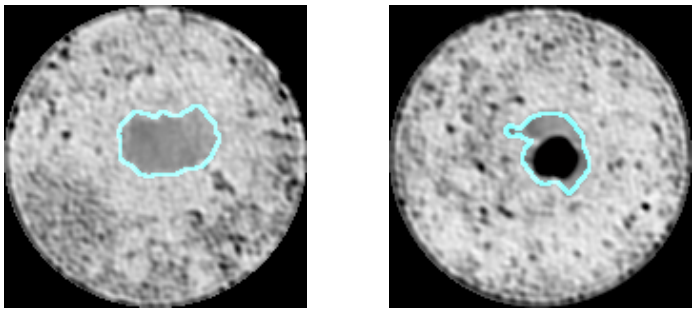

(a) Complete vug fill-up in the lower vug at a depth of 3 mm inside the vug – VS4020

(b) Partial vug fill-up in the upper vug at a depth of 8 mm inside the vug– VS6010

Figure 6.9: Partial and complete fill-up of the vug in series configuration with the initial pre-flood edge of the vug highlighted in blue.

particles have deposited in the porous media for the series configuration.

For series configuration (Figure 6.10a), the first zone has an average porosity change of 10%, and is a function of the total injected particle concentration. The lowest concentration has the lowest change, while the highest concentration has the middle change. A similar behavior is observed in the second zone, with the highest porosity reduction observed in the middle of the vugs, as evident from the vug volume change as well (Figure 6.8). At each concentration, the higher flowrate results in more porosity loss. The third zone does not depend on the flow rate, with the lowest average porosity change of ∼8%. An anomaly is observed for the experiment VS4010, which shows a consistently high porosity drop (∼16%) at all depths.

For parallel configuration (Figure 6.10b), the first zone is thicker than the series configuration as the vugs are placed deeper inside the formation. It shows a lower porosity loss compared to the series configuration, with little variation, and shows no dependency on flow conditions. This can be explained a larger cross-sectional area of the vug in the case of parallel configuration, resulting in a higher flow deviation caused by the vugs. Experiment VP4020 acts as the anomaly, with a large porosity loss (∼10%) that increases with depth. The second

zone shows a higher porosity loss at the top, with the porosity loss reducing as we go deeper. Again, no flow dependency is evident in the porosity loss, even though the spread is higher compared to the same zone in the series configuration (Figure 6.10a). Porosity loss in the third zone shows a dependency on the flow conditions and depth. The highest total injection concentration results in the lowest change in porosity ($\sim$0%) which reduces with depth, the middle concentration results in the highest porosity loss ($\sim$7%) which remains uniform with depth, while the lowest concentration results in the middle porosity drop ($\sim$4%) which increases with depth. An anomaly is observed for the experiment VP4020, where the porosity drop at the near injection face is the highest at $\sim$10%, and remains higher than any of the others until it crosses the middle of the vugs.

6.3.3 Permeability

Temporal changes in pressure are measured in the top- and bottom-zones for the series and parallel configuration, converted to permeability, and normalized with reference to the initial core permeability. For each flow case, the total solid volume injected is equal to the pore volume of a clean homogeneous core (Eq. 6.1), resulting in $\int_0^{t_{inj}} PV_{SI}\ dt = 1$. Normalized permeability for each experiment is plotted against the solid-infiltrate pore volume (PV_{SI}) for the top- and bottom-zones in Figures 6.11 and 6.12 respectively. The top-zone permeability is plotted on a logarithmic scale due to the large variations in permeability. Generally, a decrease in permeability over time is observed for all the experiments. An initial large drop in permeability is observed in the top-zone, whereas a delayed permeability drop response is observed in the bottom-zone. For each individual experiment, the top-zone permeability drop is larger than the bottom-zone permeability drop.

The top-zone permeability versus time in the series configuration is plotted in Figure 6.11a. The permeability profile can be divided into two sections: (i) a high gradient (with time) permeability drop at initial time; and (ii) a gentler constant gradient (in the logarithmic scale) at later times. The point of inflection in the permeability profile is observed at two

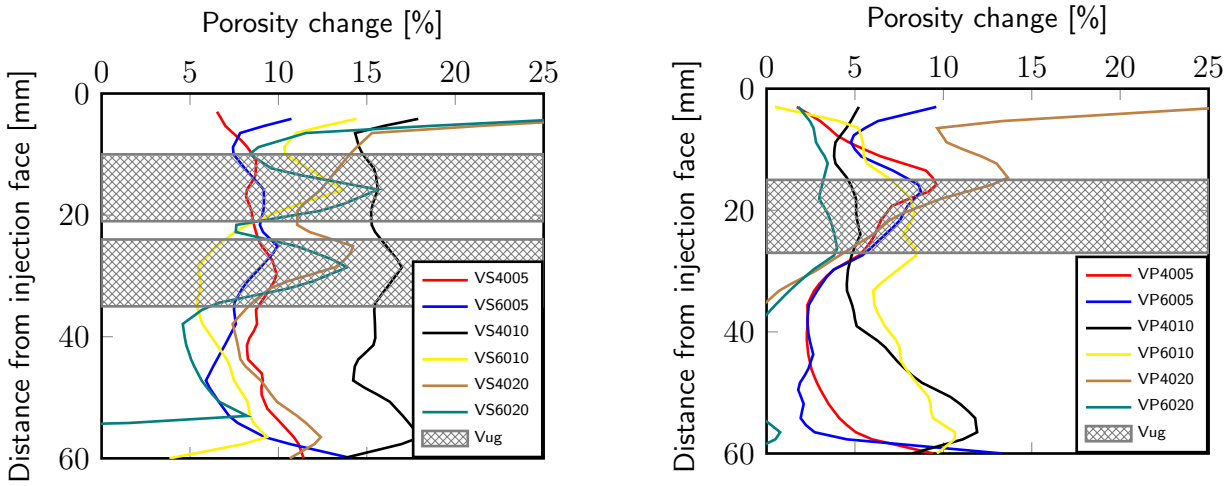

(a) VSx - Vugs in series

(b) VPx - Vugs in parallel

Figure 6.10: Porosity change with depth at the end of flow. Same volume of solid infiltrate is injected in all cases.

(Experiments are labeled as: the letters denote the vug configuration, the first two-digit number is the flow rate, and last two-digit number is ten times the total injected particle concentration.)

different time values: short-duration (0.04 PVSI) with 50% permeability loss and long-duration (0.1 PVSI) with 85% permeability loss. The short-duration inflection point is present for the 0.5% and 1% injected particle concentration while the long-duration inflection point is observed for highest injected particle concentrations (2.0%). The same rate of permeability decline is observed for all the short-duration cases and experiment VS6020. Experiment VS4020 is the anomaly in this case, and shows a lower rate of permeability decline. The maximum damage by the end of injection, i.e. permeability loss, is observed at the highest concentration and highest flow rate.

The same zones in the parallel configuration yields different permeability profiles (Figure 6.11b). Two general trends are observed: (i) constant gradient decline for the low flow rates (40 ml/min); and (ii) an initial high gradient decline followed by a gentler gradient decline for the high flow rate (60 ml/min). The first trend shows a lower damage by the end of injection, upto a maximum of 75% permeability loss for experiment VP4020, with damage increasing with the total injected particle concentration. The second trend shows the opposite behavior, with generally a higher permeability loss which is inversely related to the total injected particle concentrations. The maximum damage, 95% permeability loss, is observed for the experiment VP6005.

A delayed response in the permeability loss in the bottom-zone is observed in both the core configurations (Figure 6.12). Two possibilities for this happening are:

1. The larger-sized injected particles are deposited in the top-zone, and possibly on the outer surface forming an external filter cake, and block all the subsequent particles from getting to the bottom-zone. After a certain thickness of the external filter cake is generated, the fluid finds it difficult to get to the porous media and thereby creates wormholes in the external filter cake, which allow the passage of the fluid and suspended particles into the bottom-zone.

2. The initial suspension mixture contains the large particles only which cannot get to the bottom-zone. The subsequent suspension mixture contains a combination of the

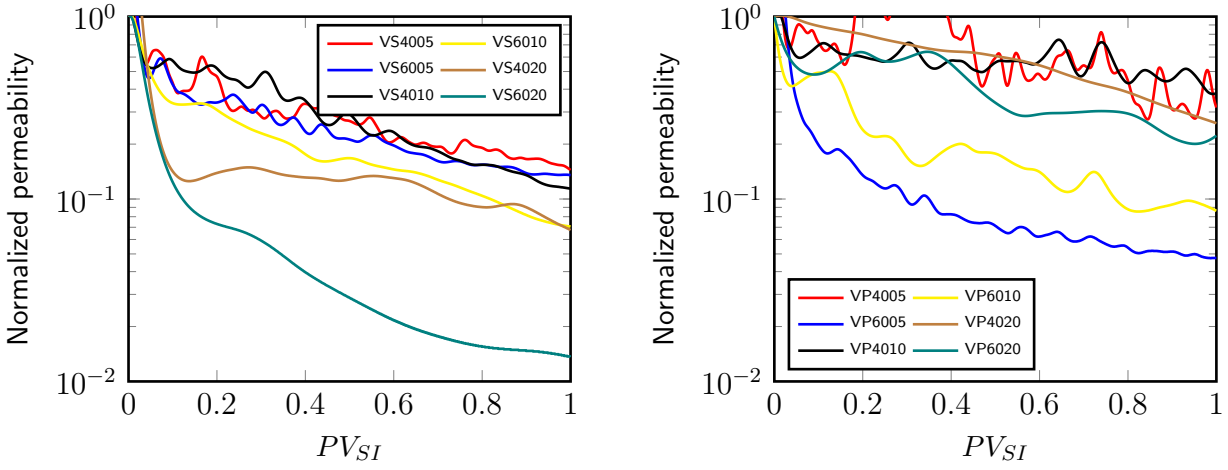

(a) Series configuration

(b) Parallel configuration

Figure 6.11: Normalized permeability change against the solid-infiltrate pore volume in the top-zone of the cores. (Experiments are labeled as: the letters denote the vug configuration, the first two-digit number is the flow rate, and last two-digit number is ten times the total injected particle concentration.)

two particle sizes, from which the smaller-sized particles get to the bottom-zone.

We believe the first possibility is more likely based on our observation of the suspension mixture having both the particle sizes from the very start and presence of small external filter cake for some experiments.

The bottom-zone permeability versus time in the series configuration is plotted in Figure 6.12a. A parabolic decline is observed for all the experiments; little variations are observed in the starting point for the 0.5% and 1% total injection concentration, which is less than the starting point for the 2% total injection concentration. All the experiments result in ∼40-50% loss in permeability by end of injection.

The bottom-zone versus time for the parallel configuration yields almost no change in permeability for most cases, with the highest change being 20% for experiment VP6010 (Figure 6.12b). This is expected from the low changes in porosity (Figure 6.10b) observed in the bottom-zone. A point to note here is that this zone is devoid of the vug, unlike the three

zones mentioned before (top- and bottom-zone in the series configuration and the top-zone in the parallel configuration), as evidenced from the initial core porosity profile (Figure 6.3).

6.3.4 Effluent particulate volume

The collected effluent is filtered twice, dried, and weighed. The deposition parameter (Eq. 6.3) is calculated for each experiment, where the total injected particle volume (mass) for each experiment is the controlling factor, and is kept the same. The data is plotted in Figure 6.13 for all the experiment cases.

$$\%\ Deposition = \left(\frac{m_{inj} \ - \ m_{eff} \ - \ m_{FC}}{m_{inj}} \right) \times 100\% \tag{6.3}$$

The data is plotted in Figure 6.13 for all the experiment cases. A general observation can be made about the relative particle deposition in the series and parallel configurations: the highest total injected particle concentration (2%) results in a higher deposition for the parallel configuration while the other total injected particle concentrations (0.5% and 1%) have a higher deposition in the series configuration.

For the parallel configuration, a direct relation between deposition and total injected particle concentration in observed at constant flowrate. An increase in total injected particle concentration results in an increase in particle deposition. Changing the flowrate only has an impact on deposition at the lowest total injected particle concentration; the other concentrations show very little variation.

The same is not true for the series configuration. For a constant flowrate, the deposition at the highest and lowest total injected particle concentrations (0.5% and 2%) show similar results while the 1% experiments show different values. At the lower flowrate, more deposition is observed for the experiments with 1% total injected particle concentration compared to the other two concentrations (0.5% and 2%). The opposite is observed for the higher flowrate, where the 1% total injection concentration has the lowest deposition compared to

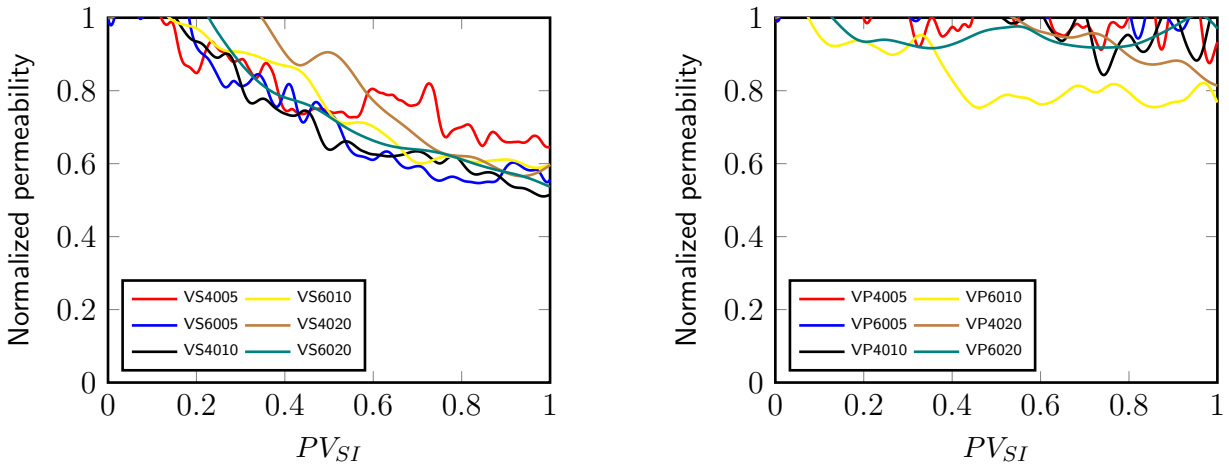

(a) Series configuration

(b) Parallel configuration

Figure 6.12: Normalized permeability change against the solid-infiltrate pore volume in the bottom-zone of the cores. (Experiments are labeled as: the letters denote the vug configuration, the first two-digit number is the flow rate, and last two-digit number is ten times the total injected particle concentration.)

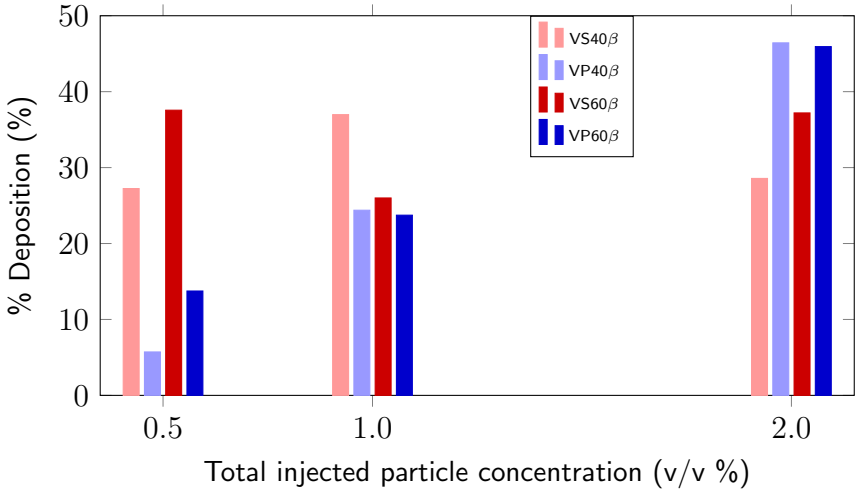

Figure 6.13: Suspended solids present in the effluent, presented as particle volume to total injected particle volume ratio, for both vug configuration at each flow condition. β is the total injected particle concentration.

the other concentrations.

6.3.5 Streamline simulation

This quasi-2D simulation has been setup to gain an insight into the streamline changes caused by the presence of series/parallel vugs, reduction in vug permeability, and decrease in the vug size. This simulation does not model any particulate flow, but gives us an indication of how the streamlines change with a change in permeability which are helpful in better understanding the spatial distribution of the particulate deposition. Streamlines (white) are generated and plotted over the core (blue) in series (Figure 6.14) and parallel configuration (Figure 6.15). The vug, with 100 times the core permeability, is colored red. We find that increasing the permeability greater than a factor of 100 has no significant effect on the streamline deviation, as a critical threshold has been achieved and the maximum flow that can be diverted to the vugs has been achieved. The initial spatial location of the vug, in the series and parallel configuration, is shown in Figures 6.14a and 6.15a respectively.

At steady-state with native reservoir properties, each vug occupies 24% of the cross-section. Streamlines at the top of the vug tend to converge, and we observe that 43% of the streamlines are redirected towards the upper vug in the series configuration (Figure 6.14). This results in a *streamline convergence (SC) factor*, defined as the number of streamlines entering the vug per unit length, of $0.43/0.24 = 1.78$. The SC factors have been calculated for all the scenarios studied in Figures 6.14 and 6.15, and are shown in Table 6.4.

For the series configuration, the upper vug always has a higher SC factor compared to the lower vug, i.e. more flow is redirected towards the upper vug in comparison with the lower vug. Simulating particle entrapment by reducing the vug permeability, i.e. enhancing the permeability contrast between the porous bed and vug, reduces the SC factor to 1.67 and 1.56 in the upper and lower vug respectively. If the vug size is reduced by one pixel on the sides and three pixels at the bottom (34% volume reduction), a SC factor of 1.63 is achieved in both the vugs.

Since the parallel configuration is mirrored along the space in the center of the two vugs, equal SC factors should be observed. We always observe a higher SC factor in the left vug (Table 6.4), which is an error possibly caused by the low density of streamlines plotted. Therefore for the parallel configuration, we will only consider the combined effect of the vugs.

For the parallel configuration, the neighboring vugs compete for flow. Therefore each simulation scenario results in a lower SC factor compared to the series configuration. Steady-state conditions with native reservoir properties results in a SC factor of 1.61 which reduces to 1.33 and 1.47 for the vug permeability reduction and vug size reduction respectively.

In summary, the vug permeability reduction (i.e. permeability contrast reduction) has a more pronounced effect on the parallel configuration (20% change in SC factor compared to 6% and 9% in the upper and lower vug in series configuration) while the vug size reduction has the least effect on the lower vug in series configuration ($\sim$5% change in SC factor).

6.4 Discussion

We integrate the results for the vug volume change, porosity, permeability, and effluent particulate volume, and compare the formation damage between the single vug and dual-vugs in series configuration and parallel configuration. Again, the total vug volume for a

Table 6.4: Streamline convergence factor, i.e. the number of streamlines entering the vug per unit length, for the series and parallel vug configurations.

Simulation scenario	**Series (Figure 6.14)**		**Parallel (Figure 6.15)**		
	Upper	Lower	Left	Right	Combined
Steady-state conditions	1.78	1.72	1.67	1.56	1.61
Vug permeability reduction	1.67	1.56	1.33	1.33	1.33
Vug size reduction	1.63	1.63	1.50	1.44	1.47

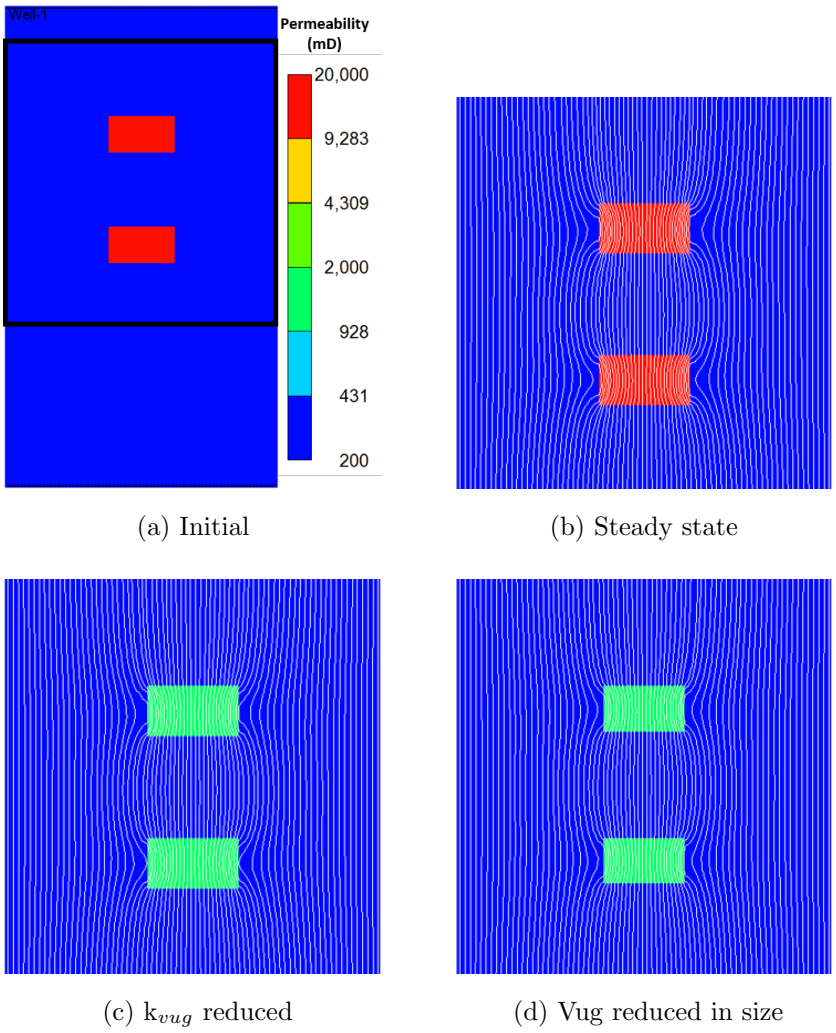

(a) Initial

(b) Steady state

(c) k_{vug} reduced

(d) Vug reduced in size

Figure 6.14: Streamline simulation - Series

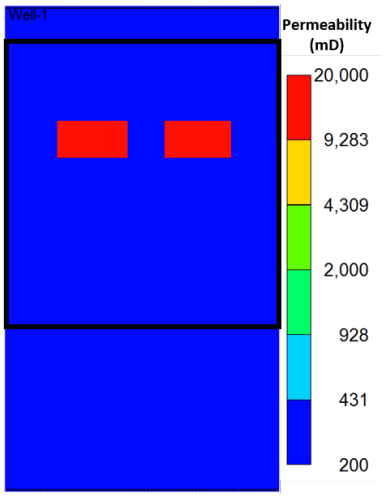

(a) Initial

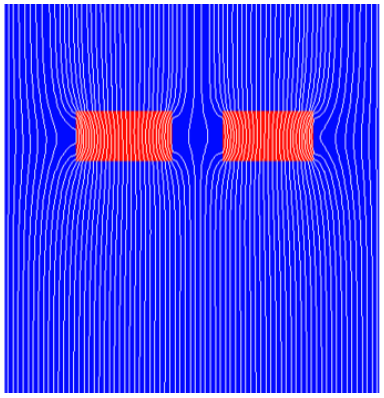

(b) Steady state

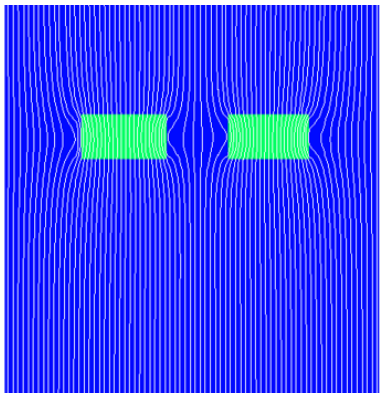

(c) k_{vug} reduced by permeability

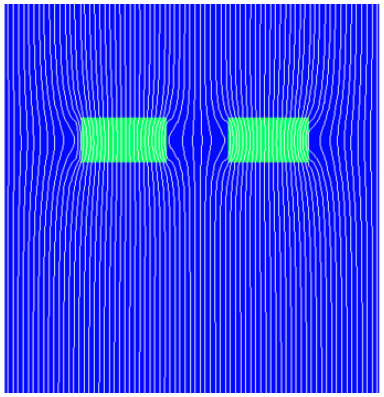

(d) Vug reduced in size

Figure 6.15: Streamline simulation - Parallel

single vug is the same as the sum of the total vug volume of the two vugs in series and parallel configuration, and the geometric center of the single vug and the two dual-vug configurations is the same. As mentioned above, surface deposition is more prominent for smaller-sized infiltrate particle size where surface forces such as electrostatic and van der Waals forces become significant. In this study we have utilized larger-sized particles and straining is the prominent mechanism of deposition.

We start the discussion by highlighting the results obtained for a single vug [114]: the vug causes injected particles to deposit deeper inside the core; maximum particle deposition happens at the extremes of the vug; and more particle deposition occurs in the matrix around a vug.

For the series vug configuration we observe a deeper penetration of injected particles compared to the single vug (Figure 6.10a), a higher vug volume loss (Table 6.3), a maximum vug volume loss at the upstream end of the vug, and a larger volume of injected particle retention in the core (combined effect in matrix and vug). The simulation results show a convergence of streamlines at the inlet of the vug (Figure 6.14b), with 45% of the streamlines entering 24% of the cross-section. Combining the experimental and simulation results, we believe that the main phenomenon by which the greater number of injected particles deposit at the upstream end of the vug in a series configuration is *fluid flow focusing* in the radial center of the vug prior to entry inside the vug. This is primarily due to the permeability contrast between the vug and the matrix. This convergence of flow increases the particle-particle and particle-grain collisions, which ultimately results in particles falling out of the fluid flow pathways and depositing in the porous medium. The fluid passes through the vug and diverges at the downstream end when it exits the vug. At this point, the lower vug causes the fluid to again converge towards the radial center of the vug, prior to entering the lower vug, and is potentially why we observe complete or partial fill-ups near the downstream end of the upper vug and the upstream end of the lower vug (Figure 6.9). We again observe a jump in the vug volume loss at the upstream end of the lower vug. The meandering of the

streamlines along the depth is also why we observe a deeper deposition of injected particles in the series configuration, and a higher volume of particles retained in the core.

Results for the parallel vug configuration are different in comparison with the series configuration; we observe a shallower penetration of particles (Figure 6.10b), a lower vug volume loss, and the maximum vug volume is lost at the center cross-section of the vug. The simulation results again show a convergence of flow at the upstream end of the parallel vugs (Figure 6.15b), but here the two parallel vugs compete among each other and dilute the effect an individual vug (Table 6.4). The fluid flow focusing behavior, as observed in the series configuration, is reduced here and the flow is not centered towards the radial center of the core. Most injected particles are not deposited at the upstream end of the vug(s) and penetrate below the top of the vug. With increasing depths up to the center cross-section, the perimeter of the vug increases and the effect of the other vug is minimized; the streamlines converge towards the vug resulting in a larger particle retention in the middle cross-section across the vug. A similar vug volume loss across all depths is observed in both the vugs in the parallel configuration (Figure 6.8), therefore we believe that each vug acts independently as a single vug.

Combining the above results, we can deduce that fluid flow focusing is more prominent in the series configuration and results in a higher particle deposition at the upstream end of the vug. Each vug in parallel acts independently as a separate vug, with the separation between the vugs greater than their sphere of influence, and therefore does not dictate the deposition of injected particles in the other vug. Continuing along the same lines, if there is no overlap in the spheres of influence of the two parallel vugs, each vug will only affect the particles that are within its sphere of influence. If the sphere of influence of the two vugs overlap, the particle will be affected by both the vugs, with the dominance depending on the distance between the particle and the vug.

At this point we would like to point out that having solid retention profiles at different times would be highly desirable, but unfortunately in this setup we only have the pre-flood

and post-flood CT scans, and therefore the temporal distribution of the particle concentration, breakthrough concentrations, vug volume change, and porosity change cannot be reconstructed.

Vuggy carbonates have a plethora of vugs which are not arranged in either a series or parallel manner with respect to the flow, but are a combination of the two. The formation damage effect in carbonates would therefore be a combination of the two as well, with the shallower vugs retaining particles and focusing flow for the deeper vugs, which in turn would do the same for more deeper vugs. Parallel vugs at the same depth inside the formation would act as separate vugs and not influence the retention pattern in the other vugs.

The question that remains is, would any connected vug act as a flow focuser regardless of the vug configuration?

6.5 Conclusions

The evolution of flow patterns due to particle entrapment and its effect of particle deposition in vuggy permeable media have been studied. Combining the results mentioned above we can conclude that, for two vugs of similar shape and volume present in a uniform porous medium: (i) the vugs in series focus the flow and increase the depth of particle deposition and the total volume of particles deposited in the core; and (ii) the vugs in parallel acts independently as separate vugs, with their separation greater than their individual sphere of influence, and do not dictate the deposition of injected particles.

Fluid flow focusing is an important factor in particle transport and deposition in a vuggy permeable medium, and therefore needs to be incorporated in the modeling of particle transport in vuggy porous media to get a realistic picture of particle retention in the permeable medium.

Note: All the data generated here can be found at Khan et al. [111].

Nomenclature

c_{total} = Total injected particle concentration, v/v %

CT = Computed tomography

m_{inj} = Injected particle mass, g

m_{eff} = Effluent particles mass, g

m_{FC} = Filter cake mass, g

PV_{SI} = Pore volume occupied by the solid infiltrate, dimensionless time

q = Flow rate, ml/min

t = Time, min

V_b = Core bulk volume, ml

VP = Parallel vug configuration

VS = Series vug configuration

Γ = core type

ϕ = core total porosity, dimensionless

Chapter 7: Particle deposition patterns over time [†]

This chapter shows a time-lapse experimental study on formation damage in a single vug proxy core. The proxy core is fabricated with 1 mm diameter glass beads and injected with a 1 vol/vol % uni-modal 50 μm glass bead suspension whilst hung inside a medical CT scanner. The injected particle size is chosen such that straining is the dominant trapping mechanism.

The results show that the initial particle deposition is observed in the matrix adjacent to the top of the vug with little or no deposition in the rest of the matrix. With time, the deposition is observed at the bottom end of the vug and in the matrix right outside the vug. At later times, particle deposition increases in the matrix around the vug.

The simplest explanation for these observations is that the permeability contrast between the vug and matrix causes the streamlines to converge at the top end of the vug. With time, particles deposit in the matrix outside the vug which reduces the permeability of the matrix resulting in the streamlines entering the vug at a deeper depth. This causes particle deposition in the surrounding matrix which fills up the extrusions on the interface making it smoother.

[†]This section is part of the future paper:

Khan, H.J., Prodanović, M., & DiCarlo, D. Spatial And Temporal Patterns In Particle Retention In Vuggy Porous Media (199246-MS). Society of Petroleum Engineers. To be presented at SPE International Conference and Exhibition on Formation Damage Control in Lafayette, LA in February 2020.

7.1 Introduction

Carbonates are complex rocks mostly generated by biological activity, with a wide variety of pore size, pore shape, and pore spatial distribution [34, 72, 188, 204]. Intergranular pores comprise the primary porosity in carbonate rock [151] while dissolution, mineral replacement, and recrystallization, to name a few, can lead to secondary porosity on a localized level [5, 7]. They often contain large visible openings, called vugs [52], which result in a very heterogeneous flow and affect the flow and transport properties of the porous medium [13, 217]. Core samples, which are not always available, are too heterogeneous and complex to isolate the effects of several quantifiable parameters, therefore very little is currently known about the two-phase flow behavior in vuggy carbonates [34].

Assessing permeability of vuggy carbonates is an outstanding problem in formation evaluation [197]: no dominant pore throat size due to pore size heterogeneity and unavailability of representative rock samples for lab calculations [209]. Carbonate pore space is complex to start with, and the standard formulae (e.g. Kozeny-Carmen and Timur-Coates) do not apply. Furthermore, formation near the wellbore is damaged by particle deposition and that is not accounted for in the developed formulae. Recent publication [146] have used numerical simulation to model the mud-filtrate invasion in carbonates for assessment of permeability using the same methodology as in homogeneous pore structures, but the estimation of formation damage in vuggy carbonates is not a straightforward problem with the complexity of the vug size and vug shape heterogeneity.

Previous studies were conducted to experimentally measure particle straining in synthetic vuggy porous medium [110, 114] by isolating one parameter (vug spatial distribution) of the vuggy carbonates and keeping other parameters (matrix porosity and total vug volume) constant. The particle deposition results, generated by contrasting the core scans at pre-flood and post-flood conditions, showed that the injected particles build-up in the near vug region, deposit on the vug-matrix interface, and penetrate deeper inside the matrix with the presence of a vug. Temporal changes in the particle retention and the particle retention rate

in different spatial locations was not measured and thus the deposition patterns of particles could not be accurately measured.

Here, we do a similar particle retention experiments in fabricated vuggy porous medium inside a medical CT scanner and track particle deposition patterns over time. Glass bead core with a single vug (similar to Chapter 5:) are generated and flooded with a 50 micron glass bead suspension. The chosen particle size, or rather the chosen injected particle to grain size ratio (1/20), ensures particle straining is the primary retention mechanism [115]. Multiple CT scans are conducted over the course of the flooding experiment to allow for calculating time-lapse particle retention maps.

7.2 Experimental setup

A single vug glass bead core is fabricated, enclosed in a heat-shrink tubing, and then hung in a medical computed tomographic (CT) scanner (Figure 7.1). Fluid reservoir, with a 1% vol/vol glass bead (50 micron diameter) suspension in deionized (DI) water, is connected at the top of the core and a peristaltic pump to control the flow rate is connected at the bottom of the core. A stirrer operating at 7000 rpm keeps the glass beads in suspension, which eventually flow under gravity at a flowrate of 40 ml/min controlled by the peristaltic pump. The effluent is collected in a beaker with its mass continuously logged.

The core is initially flooded with DI water and a baseline CT scan is conducted at a resolution of 250 micron in the x,y-direction and 1.5 mm in the z-direction. The operating parameters for CT scans are: scan thickness 1.5 mm, scan step 1.5 mm, scan time 1 sec, current 100 mA, and voltage 130 kV. The peristaltic pump is turned on and the glass bead suspension flow in the top-down direction through the core. Some of the glass beads are trapped in the core and few pass through the core and are present in the effluent.

Time-lapse CT scans of the core are conducted for the duration of the flow experiment and the collected effluent is continuously logged to determine the mass of particles in the

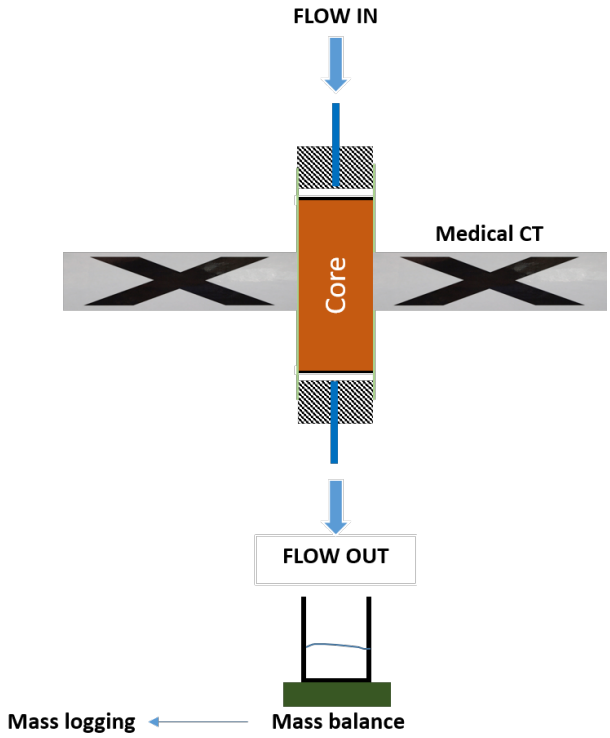

Figure 7.1: Experimental set up for time-lapse CT measurements.

effluent. CT measurements are conducted at different time steps during the injection phase at a resolution of 250 μm in the x,y-direction and 1.5 mm in the z-direction. The timesteps are dictated by the limitation of the CT machine heating and cooling cycles and the total time for the scan; 19 scans (top 28.5 mm) of the core are taken at each time step (Table 7.1).

7.3 CT observations

The CT outputs an 8-bit image for each slice at each time step. Spatial and temporal particle retention maps are calculated by subtracting the CT output for each time step from the baseline scan. Figures 7.2, 7.3, and 7.4 show the temporal particle deposition maps at different depths along the core.

The top end of the core (Figure 7.2) shows a large increase in particle retention at the inlet

Table 7.1: Time steps for temporal CT scans.

Time step name	**Time (min:sec)**	**Time step name**	**Time (min:sec)**
T00	00:00	T08	29:30
T01	01:45	T09	35:00
T02	04:30	T10	39:20
T03	07:15	T11	44:00
T04	11:00	T12	49:00
T05	15:00	T13	54:00
T06	20:00	T14	59:00
T07	24:30	T15	64:30

of the vug over the duration of the experiment. Particle deposition in the vug surrounding region is also observed at later times. The deposition density reduces in the middle cross-section (Figure 7.3) where it mostly deposits at the vug-matrix interface. At later times, particle deposition is also visible in the periphery of the vug. The lower end of the vug (Figure 7.4) shows a more pronounced deposition from the offset, which spreads radially over time.

The same data can represented as a 3D deposition map in the vug and in its periphery. These are generated by taking the product of the particle deposition map with the binarized vug image, which is calculated using CONNECTED REGIONS ALGORITHM in MATLAB [2].

Figure 7.5 shows the particle deposition over time in the vug, with the color intensity representing the deposited particle density. The maximum deposition of particles is observed at the inlet and outlet end of the vug. Particle deposition in the vug periphery (1 mm thickness from the vug) is shown in Figure 7.6, where the maximum deposition is observed in the lower part of the vug, with little damage in the top and surrounding regions.

Figure 7.7 shows the particle deposition over time in the matrix for half of the core. A drastic increase in particle deposition at the inlet and outlet of the vug is observed, with

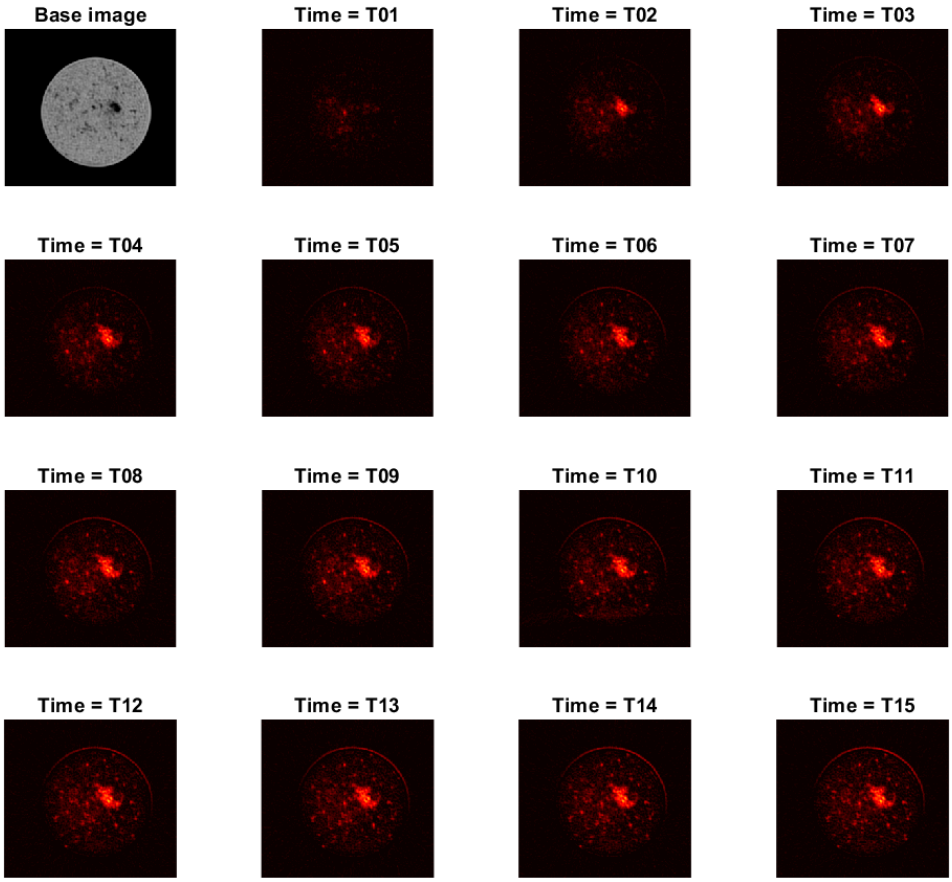

Figure 7.2: Time-lapse particle deposition maps at the top slice of the vug. The color intensity represents the particle density and is calculated by taking the difference between the CT value at time T and the baseline scan.

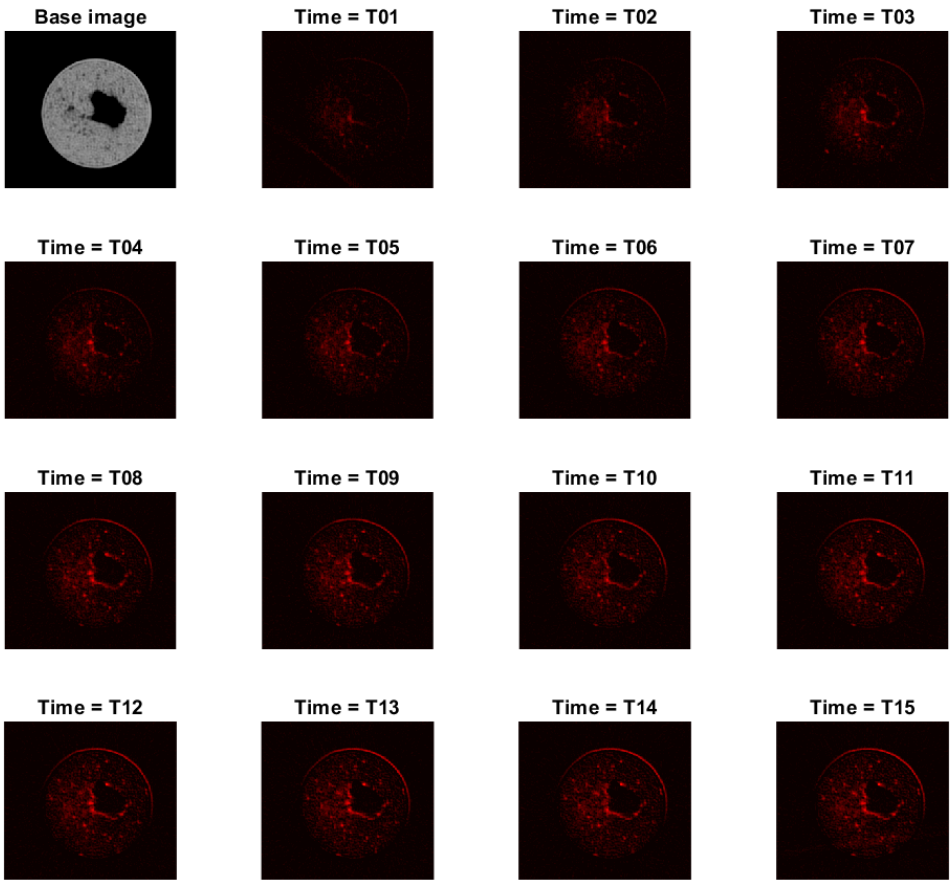

Figure 7.3: Time-lapse particle deposition maps at the middle cross-section of the vug. The color intensity represents the particle density and is calculated by taking the difference between the CT value at time T and the baseline scan.

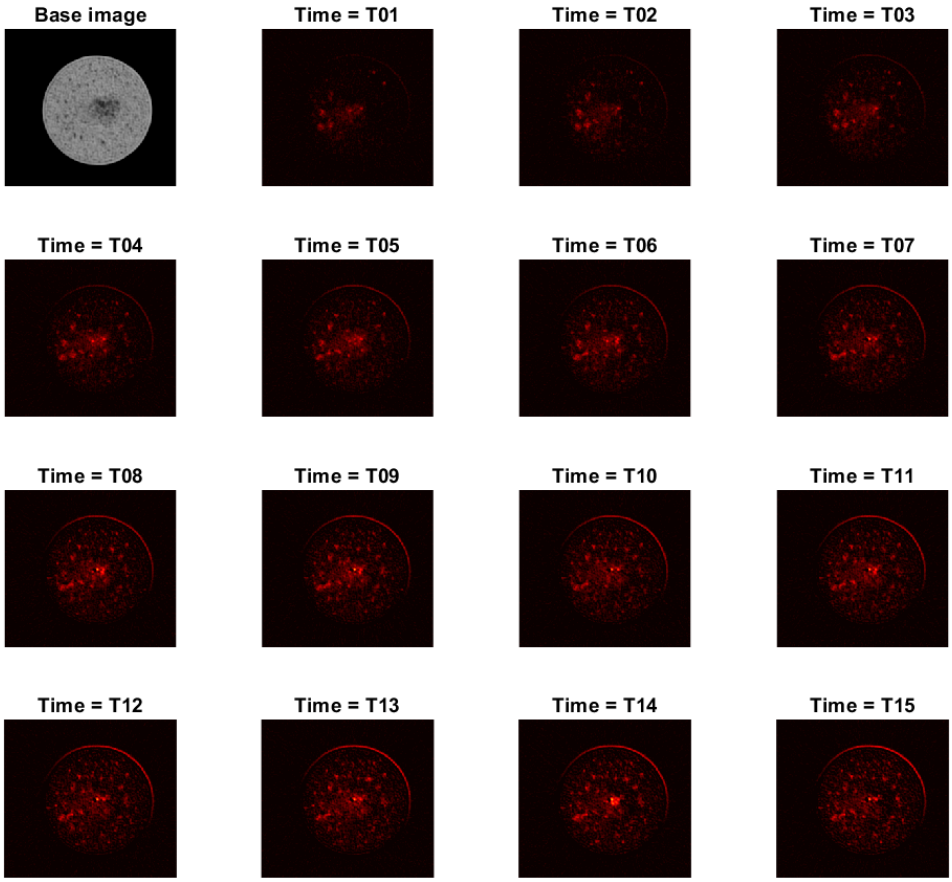

Figure 7.4: Time-lapse particle deposition maps at the end slice of the vug. The color intensity represents the particle density and is calculated by taking the difference between the CT value at time T and the baseline scan.

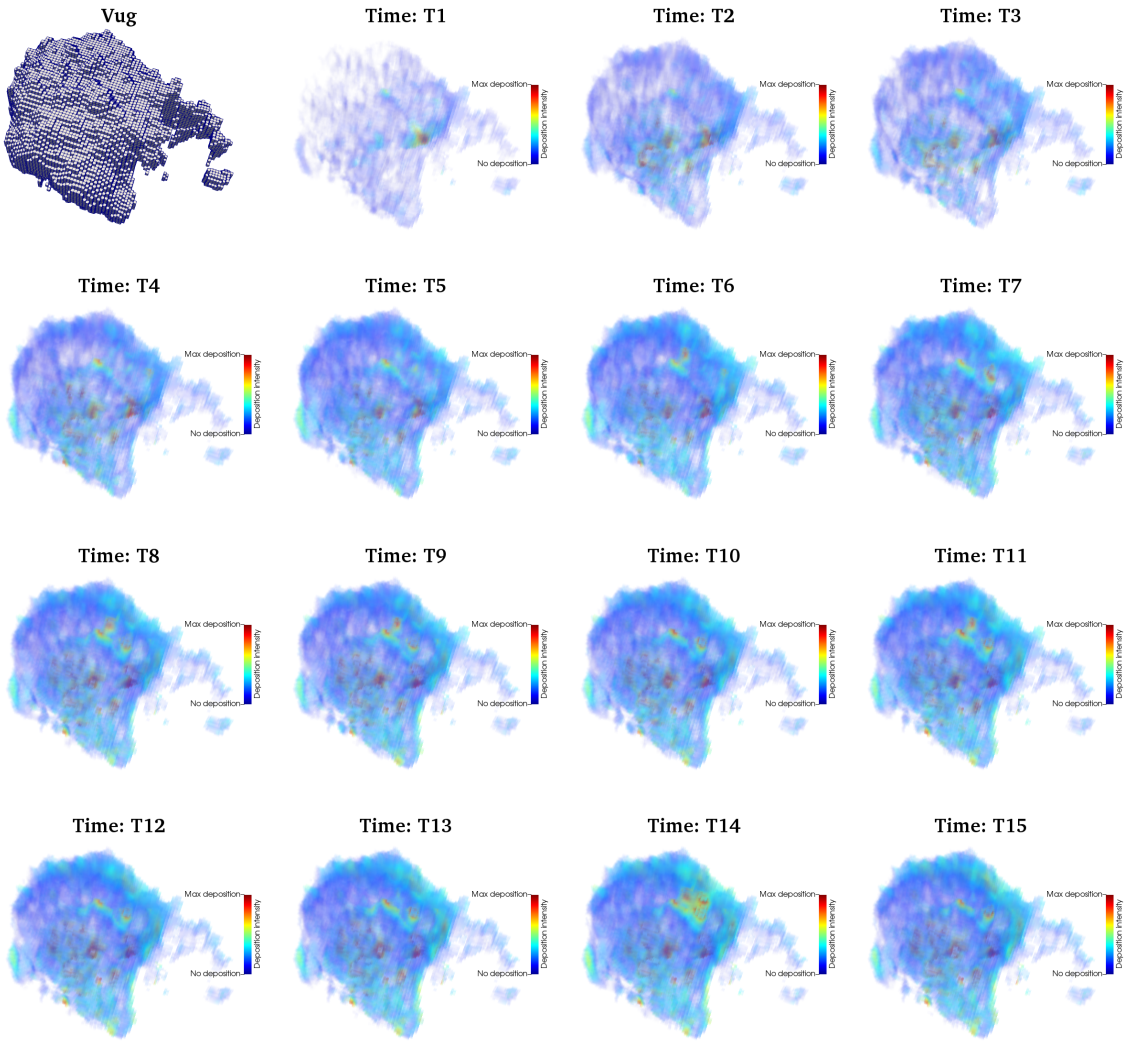

Figure 7.5: Particle retention map in the vug for a single vug core configuration and an injected particle size of 50 μm. The color map represents the density of particles retained in the vug over time, with red showing maximum retention and blue showing minimum retention. Maximum particle deposition is observed at the bottom of the core and a large deposition is observed at the top of the core.

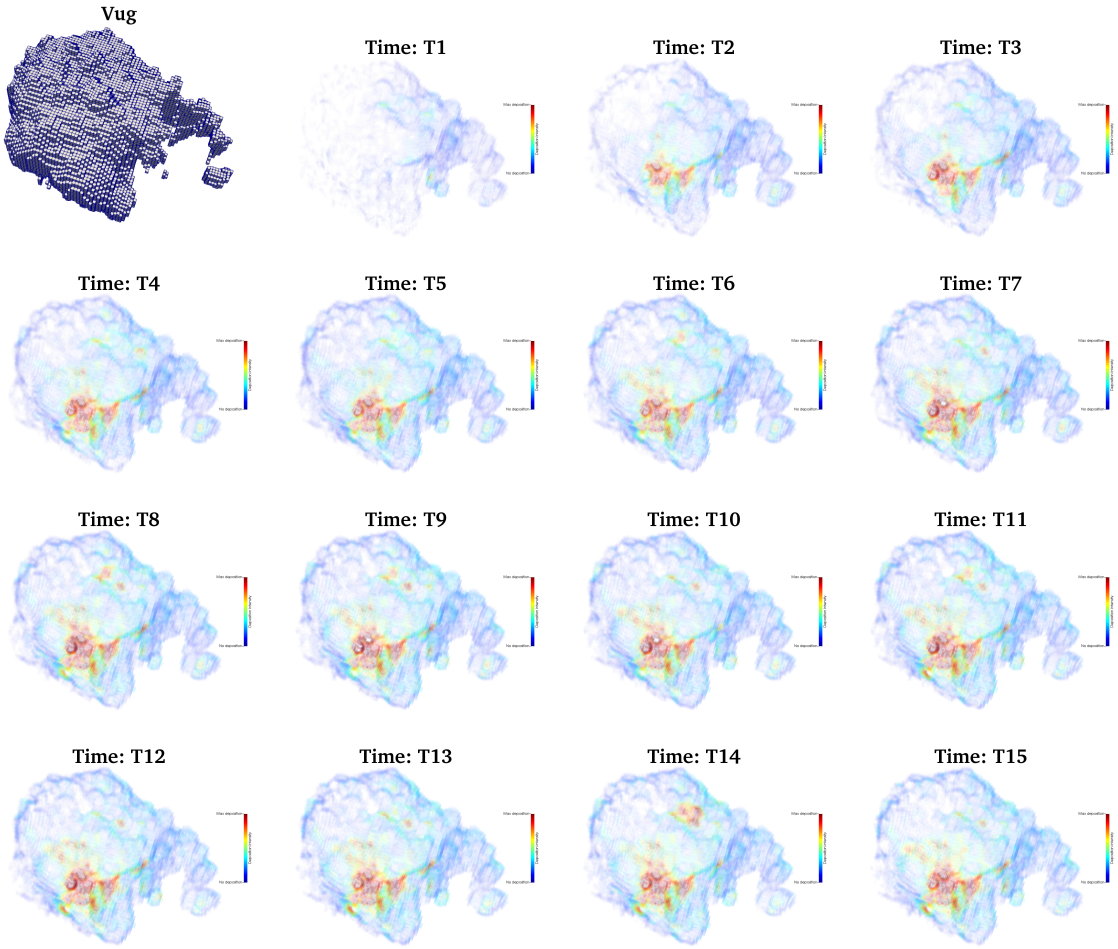

Figure 7.6: Particle retention map in the vug periphery (1 mm thickness from vug) for a single vug core configuration and an injected particle size of 50 μm. The color map represent the particle retention density around the vug over time, with red showing maximum retention and blue showing minimum retention.

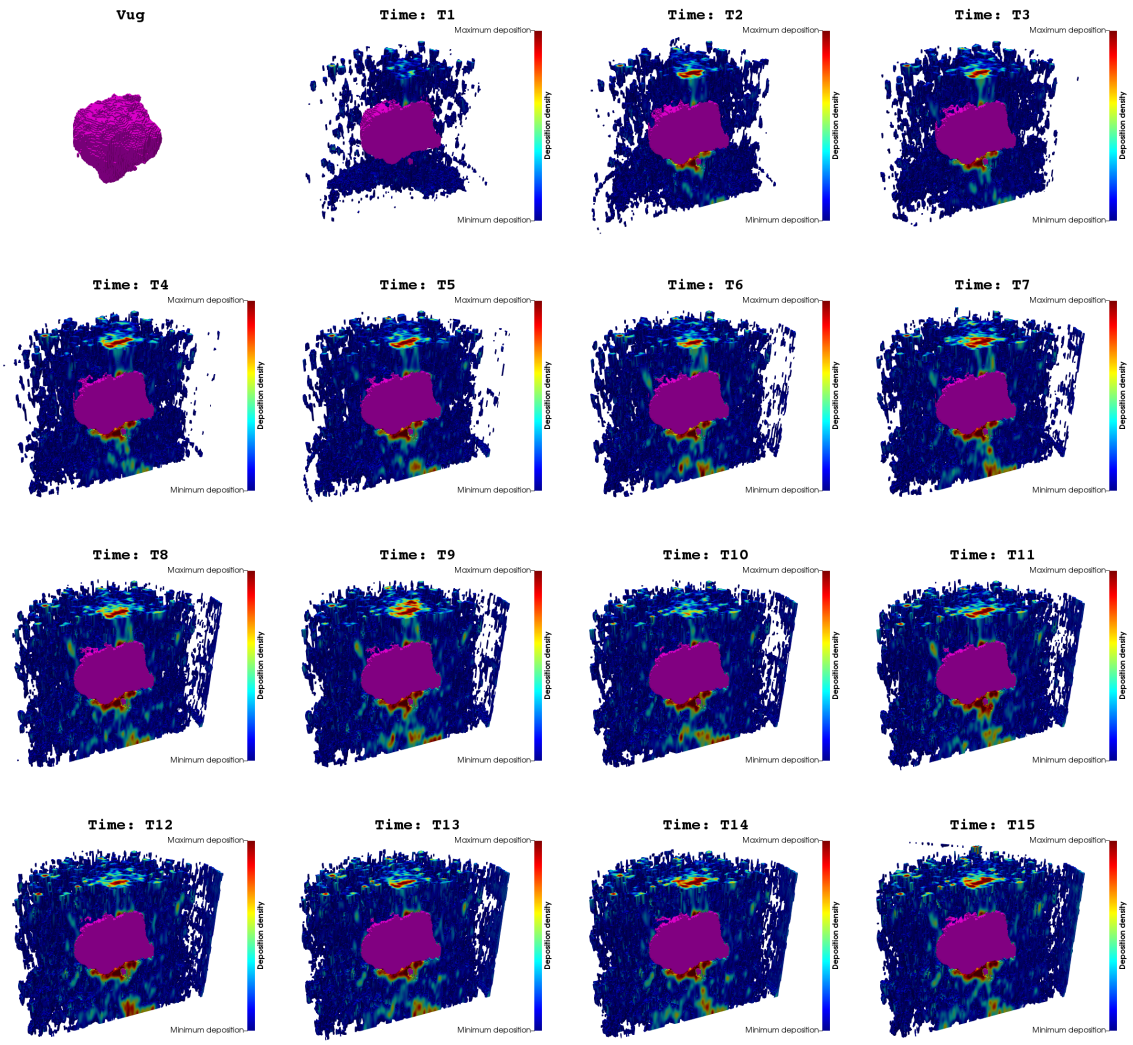

Figure 7.7: Particle retention map in the matrix (excluding the vug and periphery) for a single vug core configuration and an injected particle size of 50 μm. The image is clipped in the middle, across the radial center of the vug. The color map represent the particle retention density in the matrix over time, with red showing maximum retention and blue showing minimum retention. The top-left figure shows the complete vug, which is represented in magenta color.

limited deposition in the matrix away from the vug (Figure 7.8).

7.4 Temporal deposition patterns

Based on the observations of particle deposition patterns in the vug, the vug periphery, and the matrix (Figure 7.5 through Figure 7.8) during the experiment, the following sequence of particle deposition steps is proposed (Figure 7.9):

Step 1 – Fluid is injected in the top-down direction inside a fully water saturated glass bead core with a single vug.

Step 2 – Due to the high permeability contrast between the vug and the matrix, the streamlines converge and the fluid preferentially flows through the vug.

Step 3 – Particle suspension is now introduced in the core.

Step 4 – The injected particles permeate inside the core with the flow and start depositing in the near injection face.

Step 5 – As time progresses, more particles are introduced in the system and they permeate deeper inside the core. Due to convergence of the streamlines at the vug inlet the particle-particle and particle-grain interactions increases and particles drop out of the flow streams. The converging streamlines also increases the fluid velocity which can effectively reduce particle deposition by dislodging the retained particles. The results suggest that particle drop-out dominate the cleanup in this zone.

Step 6 – Particles are also carried inside the vug, driven by the combined effect of gravity and flow field (solid green arrows), and move to the bottom of the vug. As the fluid exits the vug into the matrix, the particles are trapped inside the vug and downstream of the vug. This is similar to what is observed at the core near injection face, where maximum particle deposition is usually observed.

Step 7 – Over time the permeability at the vug inlet is reduced due to the increased particle

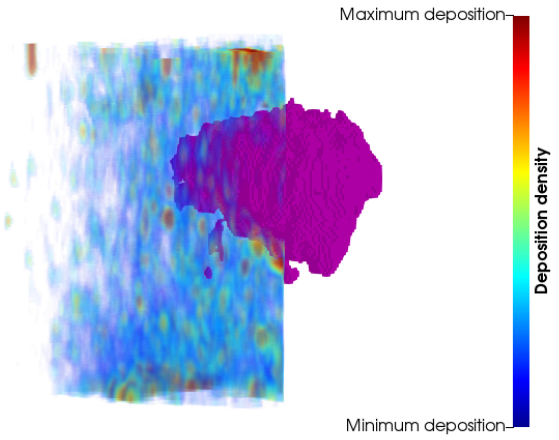

Figure 7.8: Distribution of deposited particle density in the matrix at the last time step (T14). Higher deposition is observed at the upstream and downstream end of the vug. The vug is represented in magenta color.

deposition. The streamlines therefore deviate and enter the vug at a deeper depth (dashed green arrows) carrying injected particles with them. Subsequently, the injected particles start depositing in the radial extent outside the vug.

Step 8 – Over time particles start depositing all around the periphery of the vug, ultimately shielding the vug from further particle deposition.

It is proposed that the particles would sequentially deposit all around the vug and reduce the permeability of the vug-matrix boundary. This would block the flow from entering the vug, and therefore no particle would enter the vug. Eventually the vug would be shielded from the outside (matrix) and remain partially empty while particle deposition would continue in the vug periphery.

7.5 Summary

The results suggest particle deposition in a vuggy porous media is significantly affected by the presence of a vug. The drastic changes in permeability between the vug and matrix

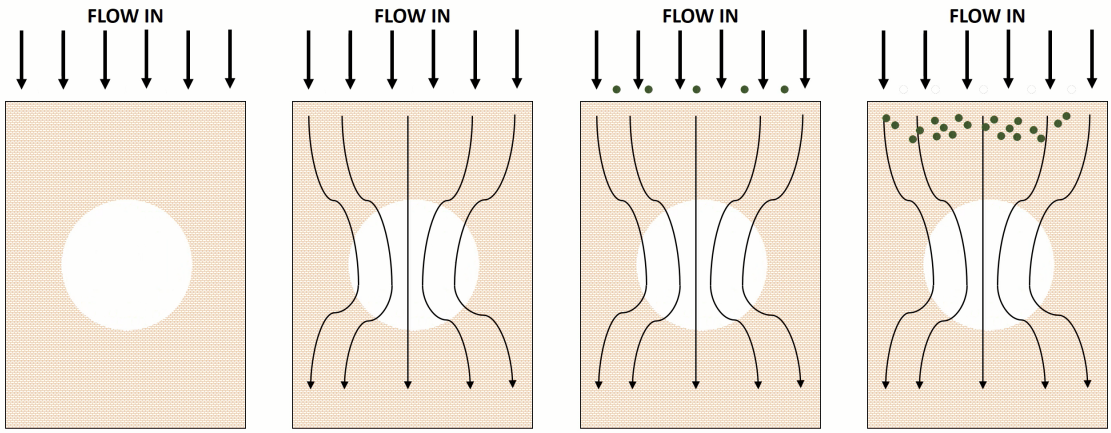

(a) Step 1 (b) Step 2 (c) Step 3 (d) Step 4

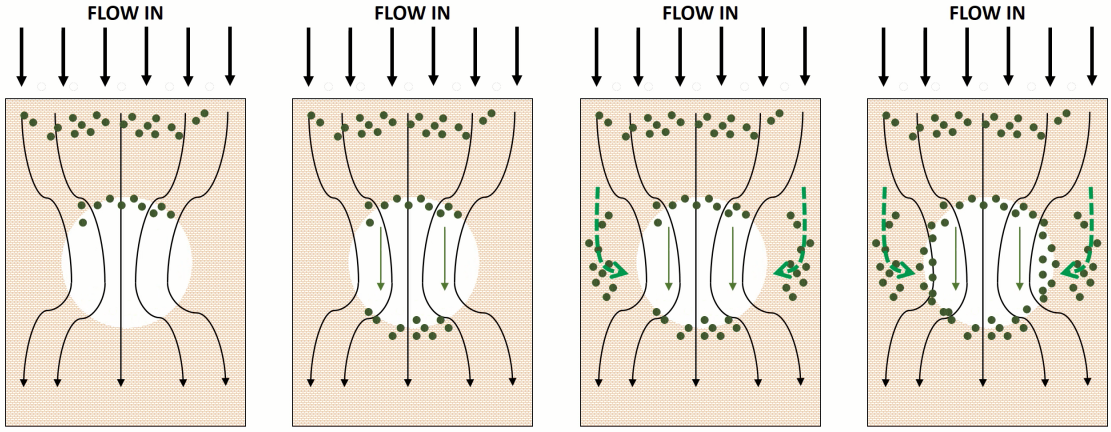

(e) Step 5 (f) Step 6 (g) Step 7 (h) Step 8

Figure 7.9: Temporal particle deposition mechanism in the vug-matrix system.

result in converging streamlines, which carry particles with them to the vug-matrix interface. Large deposition is observed at the inlet and the downstream end of the vug, which particle buildup in the matrix developing over time.

To be conclusive, more experiments need to be done with the same vug configuration (to determine repeatability) and with different vug configurations. Long duration experiment should also be conducted to test the validity of the hypothesis that the vug periphery would eventually fill up and create an impermeable surface, which would stop particle deposition inside the vug.

Chapter 8: Capillary rise in vuggy media [†]

Carbonates are highly heterogenous formations with large variations in pore size distribution and pore space topology, which results in complex multiphase flow behavior. This chapter investigates the spontaneous imbibition behavior of fluid in vuggy carbonates. Glass beads of 1.0 mm diameter, with dissolvable inclusions, are sintered to form multiple configurations of heterogeneous vuggy core with variations in matrix porosity, vug size, vug spatial location, and number of vugs. The synthetic core fabrication process (Chapter 4:) and capillary rise experiments are repeatable and allow the impacts of vug textural properties to be investigated in a controlled manner.

Capillary rise experiments are conducted in these vuggy carbonate core proxies and compared with the homogeneous non-vuggy core as reference. Continuous optical imaging is performed to track the position of the air-water interface in the cores. To understand the change in capillary height in the presence of a vug, a volume-of-fluid two-phase numerical simulation is performed in parallel set of connected and disconnected tubes. Finally x-ray tomography scans are performed to identify the shape of the air-water interface in a select few cores.

The results can be summarized as follows: vugs act as capillary barriers and their presence results in a higher capillary rise in the porous medium. The rising liquid column's momentum diverts fluid to smaller pores when obstructed by vugs. For water displacing air in the water-wet media, the advancing contact angle is larger than the receding contact angle and therefore

[†]This chapter is based on the following paper:

Khan, H.J., Mehmani, A., Prodanović, M., DiCarlo, D., & Dayeed, J.K., In preparation

a higher capillary pressure is required by the fluid to enter the vug, the fluid is stuck in that position and does not fall back. The results of this work highlight that radius of spontaneous invasion of aqueous phases, such as fracture fluid and hazardous wastes, are affected by vug porosity but not their distribution.

8.1 Introduction

Carbonate rocks are highly heterogeneous, complex rocks with a variety of pore types, pore shapes, and a wide pore size distribution [6, 37, 69, 130, 151, 156, 182]. The pore size can vary over multiple length scales [188]: the intergranular pores comprise the primary porosity in carbonate rock while dissolution, mineral replacement, and recrystallization [50, 131, 218], to name a few, can lead to secondary porosity on a localized level [7]. The two main types of rock classification suggested for carbonates are: textural classification [60], preferred by petrophysicts and reservoir engineers, and fabric/non-fabric selective pore classification [37], preferred by petroleum geologists and petrographers. Lucia [129], following Dunham [60], proposed rock typing based on carbonate pore space, with the first-order division made between vuggy and interparticle porosity.

Large disconnected pore space, such as a vug, is formed by dissolution and recrystallization of the carbonate rock fabric. Lucia [129] showed that though isolated vugs significantly increase the porosity, they have negligible effect on the overall rock permeability. Fluid flow is controlled by the matrix pore size, and the presence of disconnected vugs fails to improve the capillary entry pressures [47]. Furthermore, these display a higher Archie cementation exponent, and can act as capillary barriers to flow. Mehmani et al. [143] saw a similar behavior in fractures, where the fluid by-passes the fractures and preferentially flows through the matrix. Spontaneous imbibition study for these can improve the understanding of how far the fracturing fluid permeates during the soaking time, and can give an indication about the spatial location of the non-recovered frac fluid [124].

The handling of radioactive elements has been increasing with the global increase in nuclear

power generation [89], increasing the probability of a spillage incident occurring. Furthermore, radioactive elements are found in many commercial products that end up in the junkyard at the end of their life cycle, and can potentially leach into the soil. In either case radionuclides can enter the plants through the soil, and spread further within the food chain [219]. From a containment perspective it is pivotal to know the radius of contamination. For a carbonate rock in the presence of a vug, would the vug be filled and limit the radius of damage? Or would the fluid by-pass the vug and penetrate deeper inside the formation?

Micromodels, which are quasi-2D physical models with the pore structure etched on silicon wafers [199], have been extensively used to study 2-phase pore-scale flow mechanisms in porous media [59, 67, 161, 200]. We believe that the quasi-2D micromodels will not be able to capture the capillary flow in presence of a vug, and therefore we have used synthetic glass bead cores with inclusions for our experiments. These are the same cores as produced in Chapter 4:.

In this paper we investigate the effect of vug(s) on core rock physics: we generate a set of synthetic glass bead cores with vug(s), experimentally determine petrophysical parameters for these core, observe the behavior of vug(s) on spontaneous imbibition and contrast with Washburn [202]. We also do a computational fluid dynamics (CFD) simulation of spontaneous imbibition to compare with the experimental results. Finally, we combine the results with observations from micro-CT scans to come up with our conclusions.

8.2 Core preparation

Proxy carbonate cores are fabricated by sintering 1.0 mm diameter glass beads with dissolvable inclusions [114], salt wrapped in cheesecloth, placed in a graphite mold in a muffle furnace in the presence of air (Figure 8.1). The cheesecloth is burned during the sintering process and the salt is dissolved by flushing the core with de-ionized (DI) water after it cools down. Alternatively, gypsum cement can be used as the dissolvable inclusion [113], which is cleared by flushing with HCl acid (Chapter 4:).

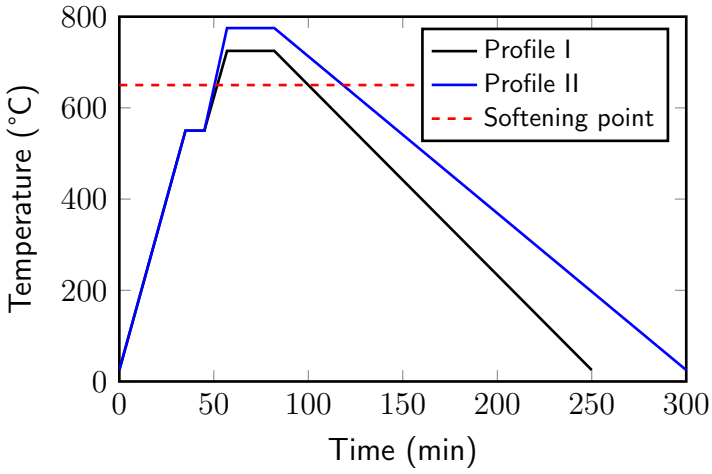

(a) Temperature profiles used for core fabrication

(b) Fabricated core

Figure 8.1: Temperature profile for a stable and highly porous core.

Here we fabricate multiple glass bead cores with different vug heterogeneities (Figure 8.2) using two different temperature profiles (Figure 8.1a): (i) Profile I with a peak temperature of 725 °C and exposure time of 25 minutes; and (ii) Profile II with a peak temperature of 775 °C and exposure time of 25 minutes. The matrix porosity values for the two profiles are 41.6% and 19.5% respectively. Micro-CT scan across the middle of the vug for two different cores is shown in Figure 8.3.

The difference between ADM01, ADM06 and ADM11 is the spatial location of a same-sized vug, while the difference in ADM11 and ADM51 is the size of vug. Vug volume in ADM51 is 35% of the vug volume in ADM11. ADM03 and ADM13 are connected vugs, with ADM03 having a larger cross-section and a vug volume fraction of ∼11%

8.2.1 Core-fluid petrophysical properties

The petrophysical properties for all the fabricated cores are determined experimentally. The methods are outlined below and the petrophysical values for all the cores are presented in Table 8.1.

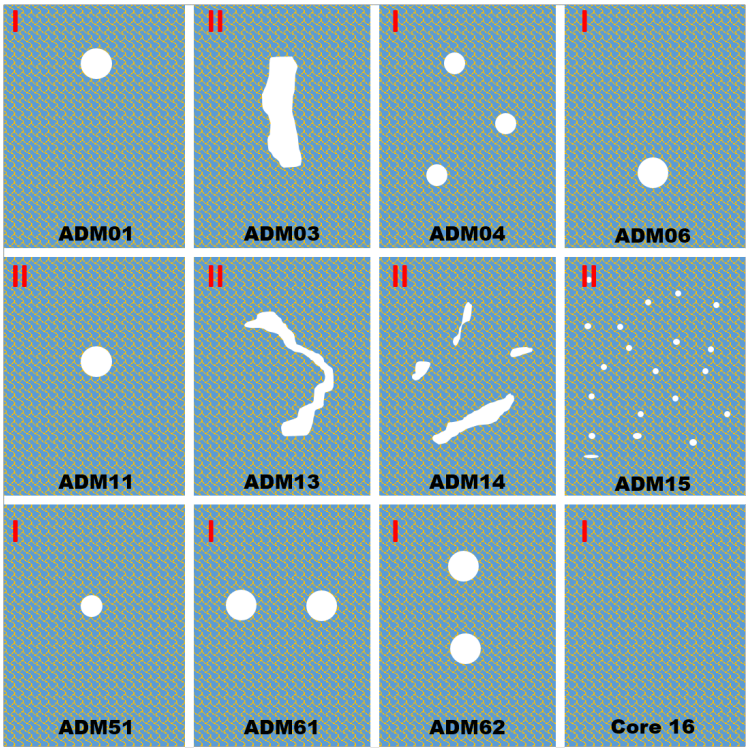

Figure 8.2: Vug distribution (white) in the fabricated cores under study with the core name at the lower end of the core. The number on the top left of the core represents the temperature profile used for core fabrication. Note that the homogeneous core is the control case and does not include any vug.

Table 8.1: Experimentally determined physical and petrophysical properties for each core along with the temperature profile that was used to create that core.

Core No	Temp Profile	$\bar{\phi}_{CT}$ (%)	k_{liquid} (Darcy)	Vug vol. (frac.)	$\bar{r}_{pore}$ (μm)
ADM01	I	41.0	978	0.024	384
ADM03	II	50.2	12417	0.109	1477
ADM04	I	44.9	420	0.039	203
ADM06	I	43.2	692	0.021	291
ADM11	II	31.0	90	0.047	127
ADM13	II	24.1	63	0.044	132
ADM14	II	19.2	43	0.011	129
ADM15	II	23.5	107	0.016	188
ADM51	I	43.9	404	0.014	203
ADM61	I	52.9	430	0.049	169
ADM62	I	53.8	456	0.032	171
Core 16	I	41.6	100	NO VUG	97.8 ‡

‡ *Figure 8.9*

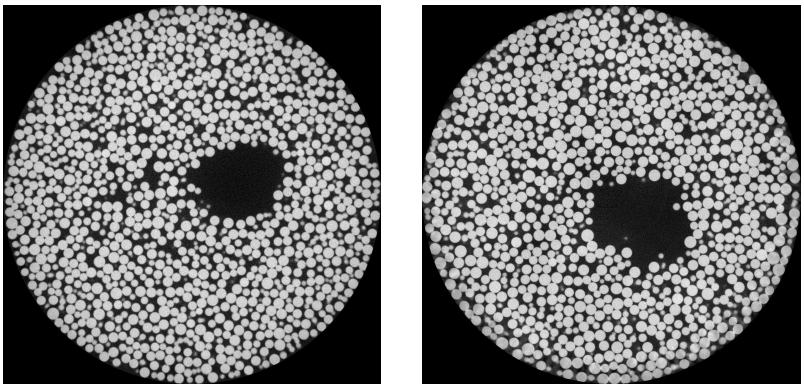

(a) μCT of vug space in core ADM04 (Resolution = 29 μm).

(b) μCT of vug space in core ADM06 (Resolution = 25 μm).

Figure 8.3: The core fabrication process results in clear and well defined vug(s), with no salt or cheese cloth residue.

Porosity using computerized tomography (CT) imaging Core porosity is determined using an in-house modified medical computed tomography scanner from Universal Systems (HD-350E) (Figure 4.2). The core is 100% saturated with DI water, placed in the CT scanner, and scanned at a resolution of 250 μm. The scan parameters used are: 3 seconds scan time, 3 mm scan thickness, 3 mm scan point distance, 100 keV voltage, and 100 mA current. Since the core volume consists of only glass beads and DI water, the porosity can be determined by taking a weighted average (Eq. 8.1) of the individual CT values for these two substances. The CT number for DI water and glass beads for this machine have been measured to be 25 HU and 2500 HU respectively.

$$\phi = \frac{CT_{glass} - CT_{total}}{CT_{glass} - CT_{water}} \tag{8.1}$$

Figure 8.4 shows CT scans along different cross-sections of a core and Figure 8.5 shows the change in porosity along the depth inside the core. The peak porosity value at the lower end of the core corresponds to the vug present in the core.

The CT output is segmented (Figure 8.6) using the Otsu method [160] and the vug is isolated

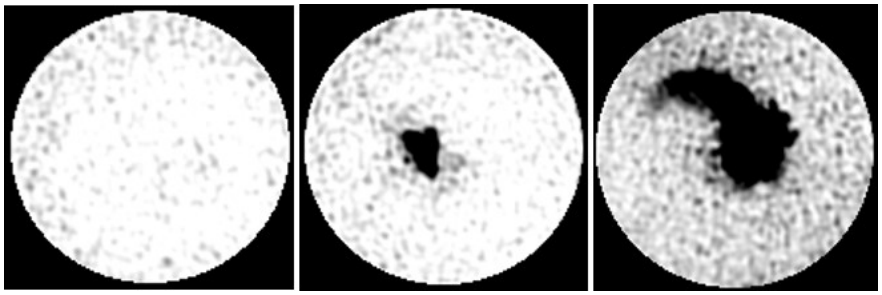

Figure 8.4: CT scan images 6 mm, 21 mm, and 42 mm (L-R) inside core ADM13 using a modified medical scanner (x,y-resolution = 0.25 mm; z-resolution = 3 mm).

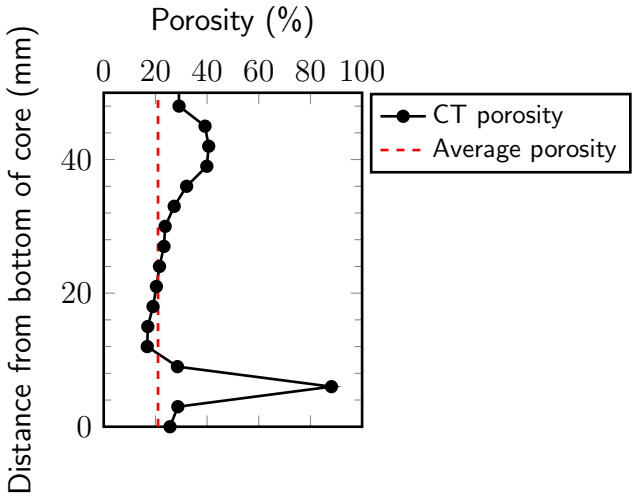

Figure 8.5: Porosity profile along length of core for ADM11 (using temperature profile II).

by using a connected region algorithm in ImageJ-Fiji [180, 183]. Figure 8.7 shows the 3D visualization of the isolated vug surface.

Single phase permeability using constant flow injection Figure 8.8 shows the experimental setup used to measure the single-phase liquid permeability of the cores. DI water is pumped through the proxy core at variable flow rate (40, 50, and 60 ml/min) and pressure drop along the core is measured. The pressure drop is used to calculate the liquid permeability using single-phase Darcy's law.

Average pore throat radius The pore distribution in the homogeneous core (Figure 8.9) is determined by using an in-house Oxford Instruments GeoSpec2 NMR scanner (Figure 4.4), with the average pore size calculated as 97.8 μm.

This scanner can measure a maximum pore size of $\sim$350 μm before which the bulk relaxivity of the water dominates. The vugs introduced in the core are generally larger than this, therefore we use a theoretical Pittman R_{50} equation [163] (Eq. 8.2) to determine the average pore radius for the vuggy cores.

$$log_{10}\ (R_{50}) = 0.778 + 0.626\ log_{10}\ (k) - 1.205\ log_{10}\ (\phi) \tag{8.2}$$

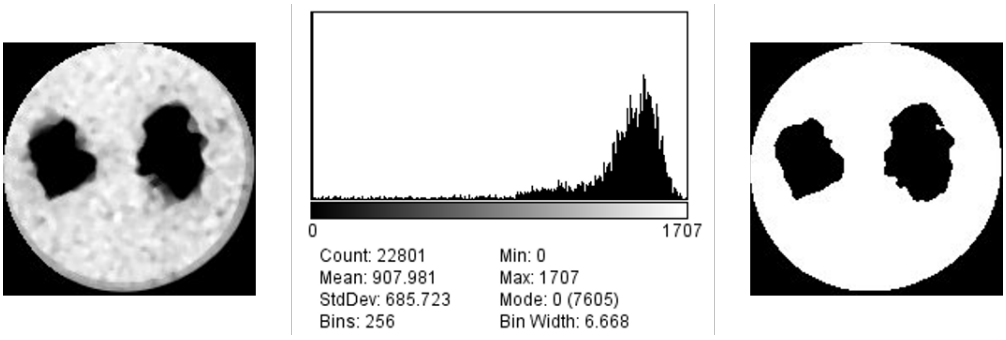

Figure 8.6: Original CT image (left), histogram of the CT image (center) and segmented image (right) using the Otsu method [160] for ADM61 (Resolution = 0.25 mm).

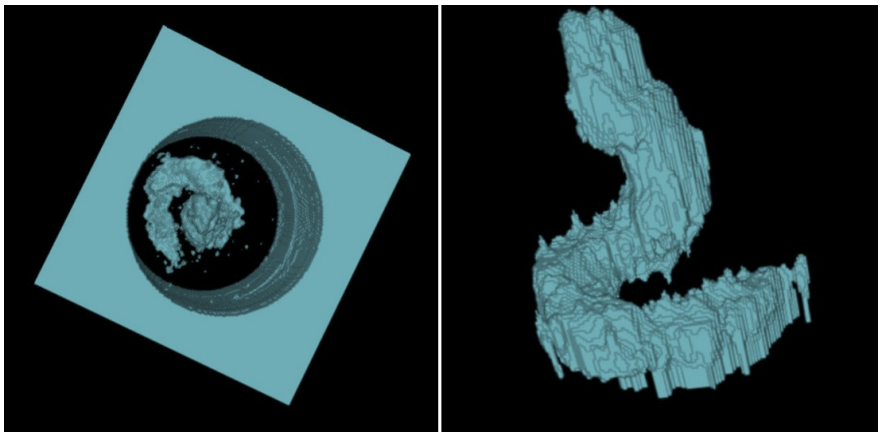

Figure 8.7: 3D visualization of the vug in core (left) and isolated vug (right) for ADM13.

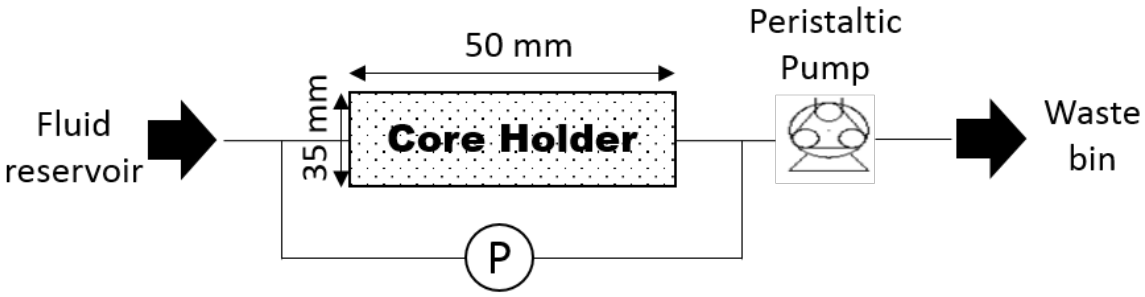

Figure 8.8: Experimental setup for permeability measurement.

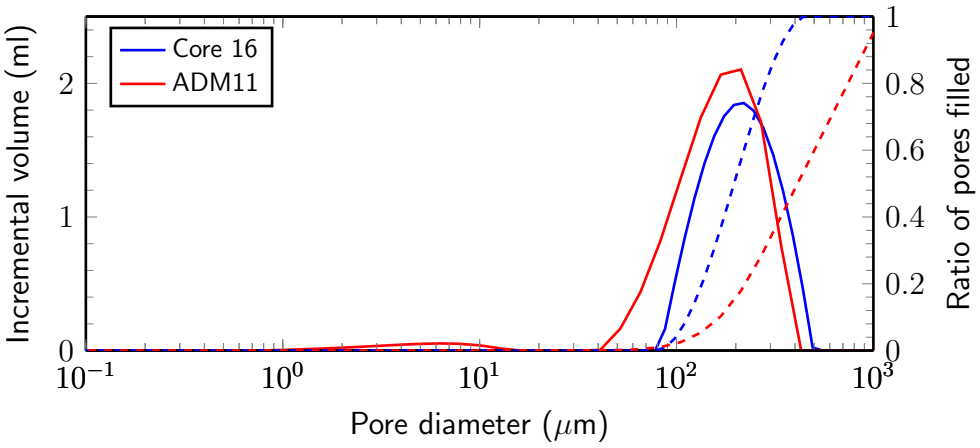

Figure 8.9: NMR for a vuggy core (ADM11) and the homogeneous core (Core 16).

Contact angle Contact angle measurements are made using a static sessile drop contact angle method which uses a goniometer. A goniometer is an optical system which captures the profile of the liquid interface when placed on the measuring medium. The air/water contact angle on a sintered glass bead sheet, generated by placing a sheet of cheese cloth on top of it, was found to vary between 48°– 50°.

Surface tension The surface tension of the air/water system is determined by applying the capillary rise method in fixed diameter tubing. Two tubing, with inner diameter 2.367 mm and 1.605 mm, are vertically placed in a reservoir of DI water, and the capillary rise from the top of the fluid level is measured. The surface tension (Eq. 8.3) for the air-water system is calculated as 0.0512 N/m.

$$\sigma = \frac{\rho g \cdot hR}{2\cos\theta} \tag{8.3}$$

Porosity-permeability crossplot A porosity-permeability crossplot for the vuggy and homogeneous cores is shown in Figure 8.10, along with the k/ϕ ratio contours. The contours trace points with similar flow quality [36] and show three distinct flow units (FU) for the samples. FU-1 (colored blue in Figure 8.10) has the lowest flow quality with a k/ϕ value of 2×10^3, FU-2 (red) has a k/ϕ value of 1.2×10^4, and FU-3 (green) has the best flow quality with a k/ϕ value of 2.5×10^5.

The vug does not seem to impact the flow unit classification of the cores, except when the vug volume fraction is significantly large. Vug volume fraction for FU-1 ranges from 0 to 0.047 while the fraction for FU-2 ranges from 0.014 to 0.049. FU-3 consists of a single value, and has a vug volume fraction larger than 0.1. As expected, the temperature profile used to generate the cores have an impact on the flow unit classification, as it governs the pore size and pore size distribution of the matrix. The vuggy cores present in FU-1 and FU-3 were fabricated with temperature profile I and vuggy cores present in FU-2 were fabricated

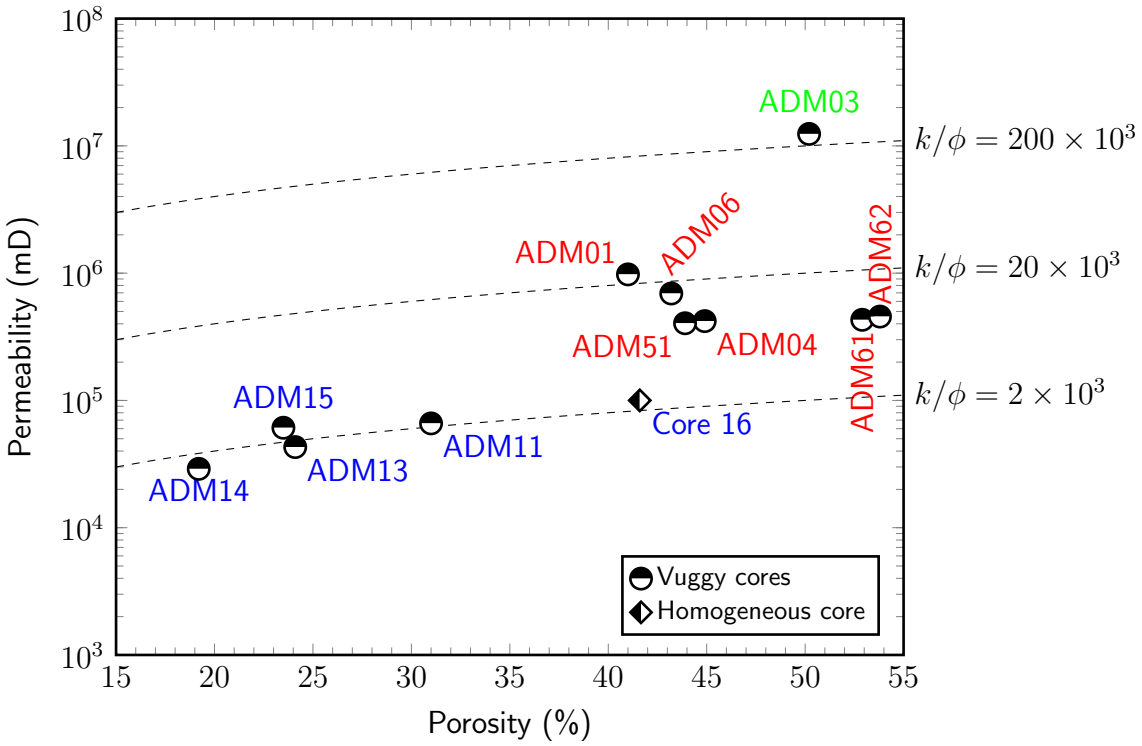

Figure 8.10: Crossplot of experimentally determined permeability and total porosity for each core. k/ϕ contours are superimposed and flow units are identified by the text color (blue – FU-1, red – FU-2, and green – FU-3). The homogeneous core (core 16) is not in a unique flow unit by itself but is associated with the vuggy cores generated using temperature profile II.

with temperature profile II (Figure 8.1). Interestingly the homogeneous core, which has been sintered using temperature profile I (Figure 8.1a), has similar flow characteristics to the vuggy cores fabricated using temperature profile II, which have a lower porosity. The spatial location of the vug does not have any impact on the flow unit classification.

8.3 Capillary rise

8.3.1 Experiment methodology

Capillary rise over time is measured for all the carbonate proxy cores (Figure 8.2): the core is placed in a Petri dish filled with DI water to a height of 10 mm and the water front movement is recorded by continuous optical imaging (Huawei Nexus 6P camera – 12.3 MP Sony Exmor IMX377 with 4K (30 fps) video capture) at a frequency of 120 frames/second. The output video is converted to an image stack and binarized to determine the position of the air-water interface with time.

Three iterations of Core 16 are produced and the capillary rise experiment is performed in each of them. A similar capillary rise profile is observed in all of them. Figure 8.11a can be broken into two segments: a sharp initial increase which lasts for the first 0.15 seconds, followed by a logarithmic decline. The capillary rise is plotted along with the analytical solution for the Washburn equation in a grain pack [73] for the experimentally determined maximum and average pore radii (Figure 8.9). The solution, which assumes a continuous and uniform porous medium bounded on the sides and is not true in this case, is not able to capture the initial sharp fluid rise and ultimately under-predicts the total capillary rise.

Compensating for the initial sharp fluid rise by transposing the solution to the end of that segment (black line in Figure 8.11a) captures the curve nicely and results in a better match with the experimental observations. The capillary rise follows the Lucas–Washburn $\sqrt{t}$ law [202] (Figure 8.11b), which is consistent with previous studies in spontaneous imbibition in homogeneous porous media [78, 79].

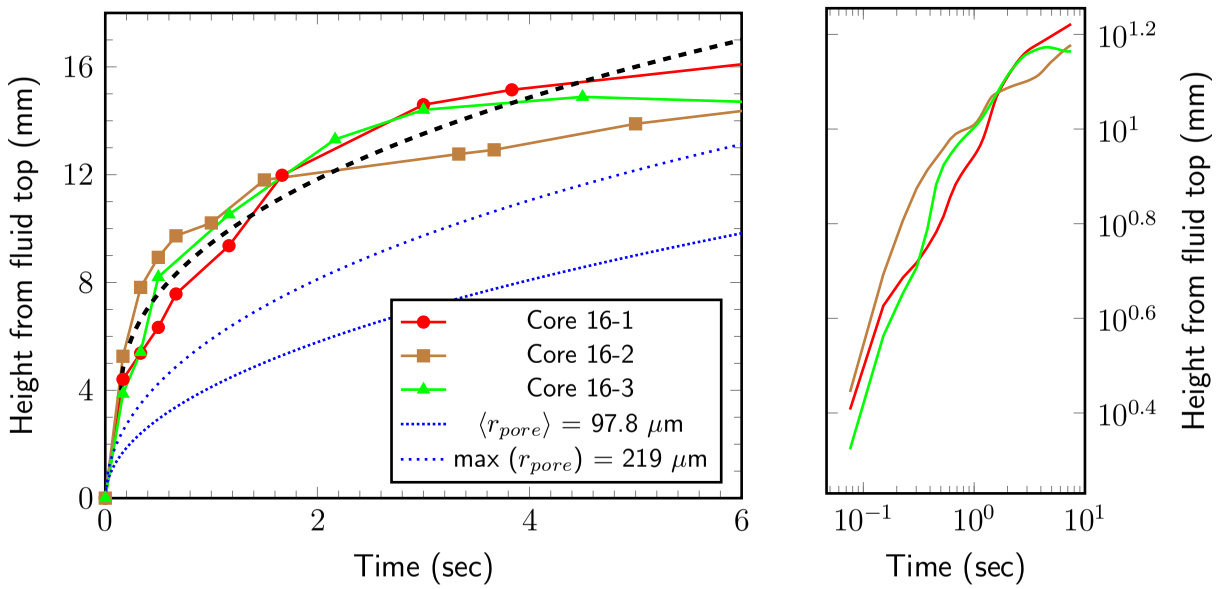

(a) Three replicas of homogeneous core (Core 16) are fabricated and capillary rise experiment is performed with de-ionized water. The experimental data is plotted along with the Fries-Dreyer solution to the Washburn equation for the average and maximum pore radius (Figure 8.9). The black line is a translation of the Washburn solution to the end of the initial sharp rise.

(b) Capillary rise for the three homogeneous cores plotted on the log-log axis results in an average gradient of 0.5.

Figure 8.11: Capillary rise in homogeneous porous medium.

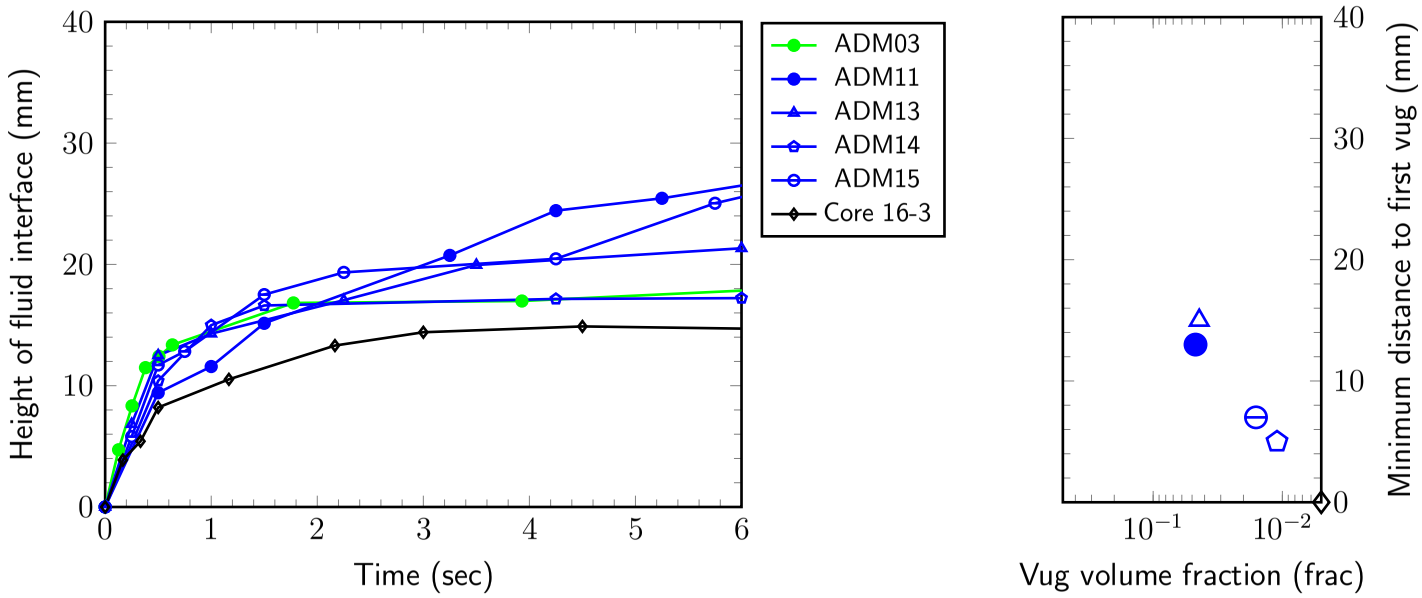

(a) Capillary rise with DI water for all cores, with one iteration of Core 16, is plotted against time. The vuggy cores are colored based on the flow unit they are a part of (Figure 8.10) and the homogeneous core is colored black.

(b) Distance to the bottom of first vug for all cores. Minimum distance to the vug for ADM01 is outside the range for the plot, at 45 mm.

Figure 8.12: Capillary rise in the cores along with the height to first vug for FU-1 and FU-3. The stabilized capillary height does not depend on the height of the first vug.

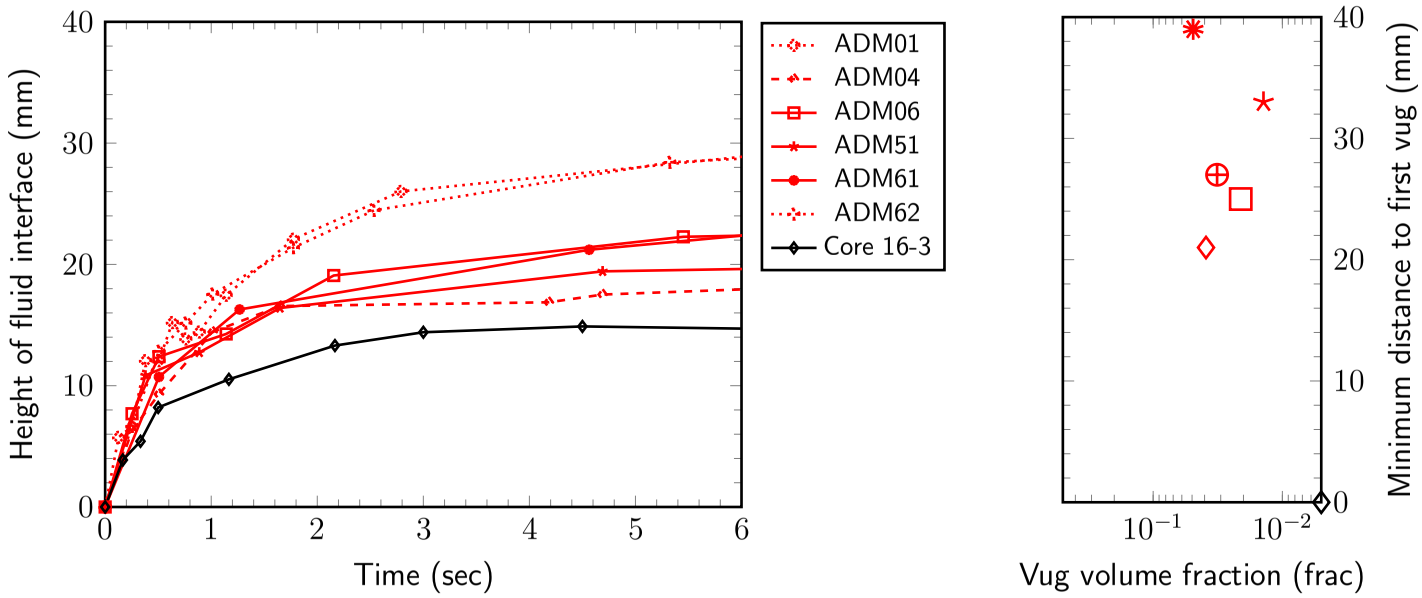

(a) Capillary rise with DI water for all cores, with one iteration of Core 16, is plotted against time. The vuggy cores are colored based on the flow unit they are a part of (Figure 8.10) and the homogeneous core is colored black.

(b) Distance to the bottom of first vug for all cores. Minimum distance to the vug for ADM01 is outside the range for the plot, at 45 mm.

Figure 8.13: Capillary rise in the cores along with the height to first vug for FU-2. The stabilized capillary height does not depend on the height of the first vug.

Capillary rise in all the vuggy cores is plotted in Figure 8.13a along with one iteration of Core 16. The line color denotes the flow unit the core belong to and the marker shape denotes the vug configuration. A large spread in the capillary rise for the vuggy cases is observed; all the vuggy cores result in a higher capillary rise than the homogeneous cores. The capillary rise can also be divided into two segments similar to the homogeneous core: a sharp initial fluid rise, followed by a logarithmic decline. The sharp initial fluid rise has the same gradient as Core 16 and it lasts longer ($\sim$ 0.45 seconds).

Figure 8.13b shows the difference in elevation of the bottom of the first vug from the static water level for all the cores. The experiments show no discernable trend in the the spatial location of the vug (distance from static water level to the start of first vug) and the capillary height at equilibrium. The only observable fact is that the presence of vug results in a higher capillary rise in the porous medium.

8.3.2 Computational fluid dynamics simulation

Capillary rise was modeled by numerically solving the Navier-Stokes equations for two incompressible, isothermal immiscible Newtonian fluid using the InterFOAM solver in OpenFOAM® [1]. We consider two scenarios: (i) two connected tubes of equal diameter (Figure 8.14a); and (ii) two connected tubes of equal diameter till 7 mm above fluid level, and then increasing linearly six-fold at 13 mm above fluid level (Figure 8.14b). The height of the two tubes and the height of fluid above the tube entrance, for both the scenarios, is the same. All tubes are open to the atmosphere and have a constant (atmospheric) pressure boundary. The fluid reservoir is open to the atmosphere, with the top boundary at atmospheric pressure. A high resolution mesh is required to simulate the capillary rise phenomenon. The input parameters are shown in Table 8.2. The surface tension and contact angle at the air-fluid interface is selected based on the experimental measurement (section 8.2.1).

Capillary rise is simulated; the fluid level rises in both tubes and is proportional to the square root of time (Figure 8.15). Fluid preferentially flows in the connected tube (3 mm above

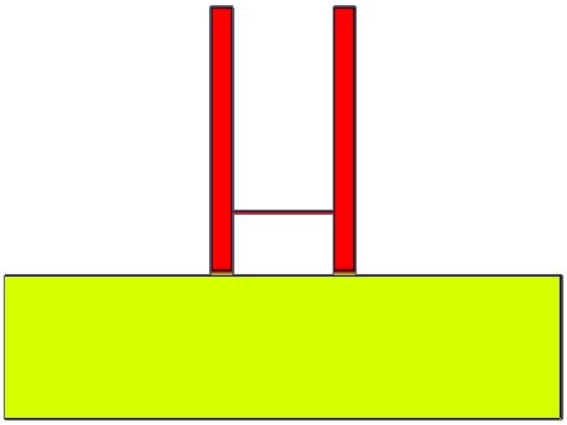

(a) Two-tube model: two tubes of equal diameter (1 mm) connected with a 0.1 mm diameter tubing at a height 3 mm above the static fluid level.

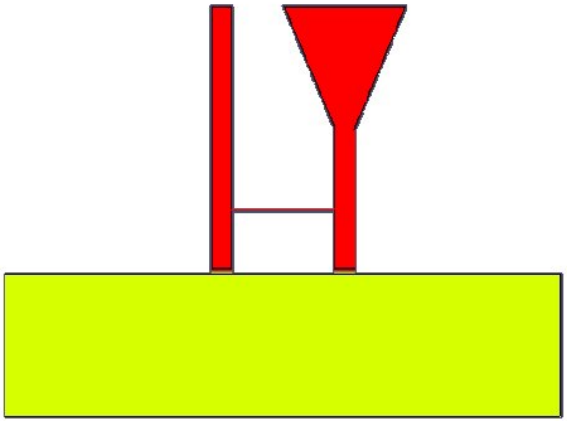

(b) Tube-vug model: two tubes of equal diameter (1 mm) connected with a 0.1 mm diameter tubing at a height 3 mm above the static fluid level. The right tube funnels from 1 mm diameter at 7 mm height to 6 mm diameter at 13 mm above fluid level.

Figure 8.14: Two models being tested: two-tube and tube-vug model, at initial time. The colorbar denotes the ambient fluid saturation (α_{water}), with the fluid reservoir being in blue and the dry tubes being red. The fluid reservoir is significantly larger than the combined volume of the tubes, with the tubes 2 mm below the fluid top.

Table 8.2: OpenFOAM® input parameters.

Input parameter	**Value**
Contact angle	49°
Surface tension	0.0512 N/m
Air density	1 kg/m^3
Air viscosity	$1.48 \times 10^{-}5$ Pa.s
Water density	1000 kg/m^3
Water viscosity	$1 \times 10^{-}3$ Pa.s

static fluid level) until it is filled, which can be observed by the short-duration departure from the proportional relationship at ∼3 mm fluid height. Subsequently, the fluid level continues to increase proportional to the square root of time in both tubes for the two-tube model.

The fluid level in the right tube does not increase after 7 mm (above static fluid level) for the tube-vug model, where the tube diameter starts increasing (Figure 8.16a). On the other hand the fluid level in the constant diameter left tube keeps on increasing with time (Figure 8.16b), keeping the same shape as the two-tube model. Deviation between the two models starts at 1.60 seconds, with the fluid level in the tube-vug model rising quicker (Figure 8.15).

8.3.3 Micro-tomographic imaging

Capillary rise on a homogeneous (Core 16) and a vuggy core (ADM06) is performed inside the in-house x-ray micro-tomography scanner (section 4.1.5). Once the fluid front stabilizes, the cores are scanned at a resolution of 25 μm to get the spatial fluid distribution inside the core (Figure 8.17). The scans are segmented to identify the three components: air (white), water (orange), and solid glass (red), and a 3D volume is reconstructed.

The 3D reconstruction of the air-water interface for Core 16 is shown in Figure 8.17a. The air-water interface, at the boundary of the white and orange colors, is fairly uniform across

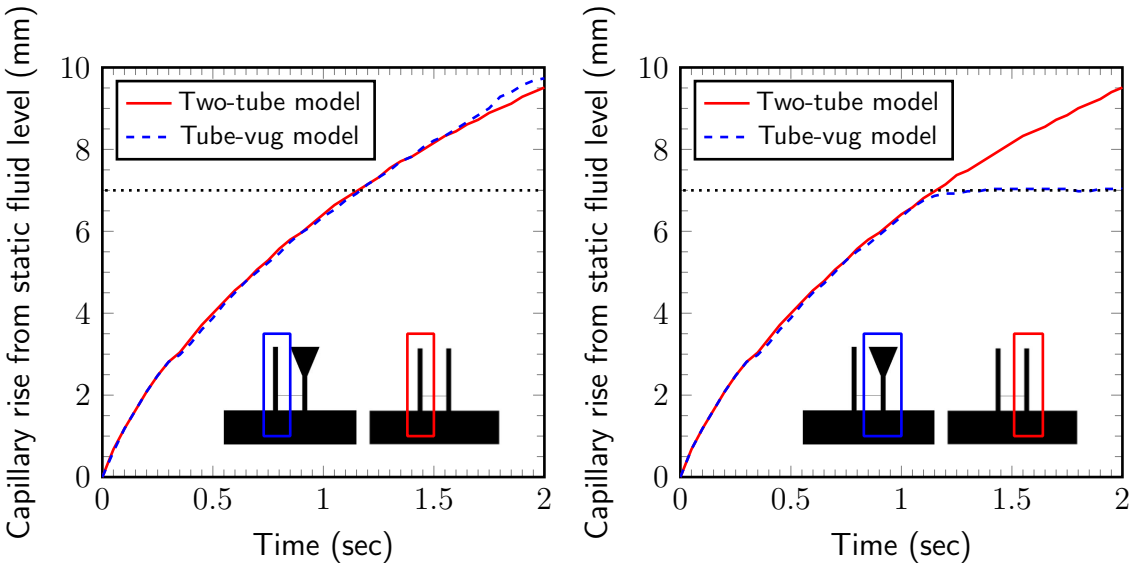

(a) Capillary rise in left tube for both models. (b) Capillary rise in right tube for both models.

Figure 8.15: Capillary rise in the left and right tubes for the two models. The dotted black line represents the height at which the tube diameter changes for the tube-vug model (Figure 8.14b). The tube-vug model shows the air-fluid interface at a greater height in the left tube (Figure 8.16).

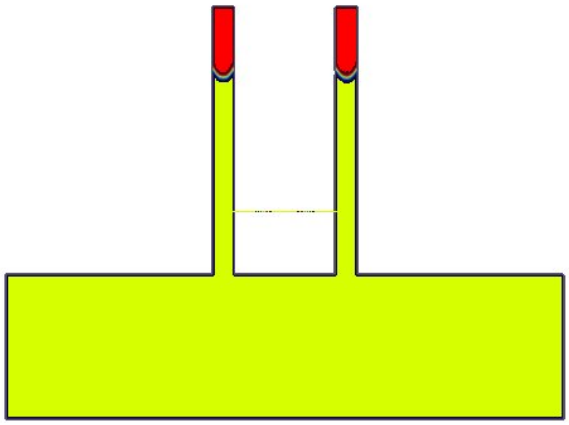

(a) Two-tube model: two tubes of equal diameter (1 mm) connected with a 0.1 mm diameter tubing at a height 3 mm above the static fluid level.

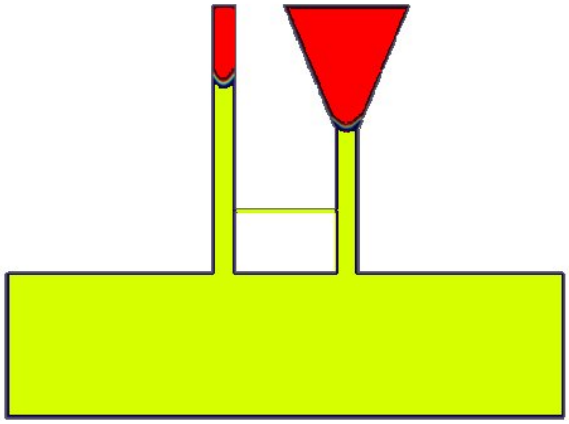

(b) Tube-vug model: two tubes of equal diameter (1 mm) connected with a 0.1 mm diameter tubing at a height 3 mm above the static fluid level. The right tube funnels from 1 mm diameter at 7 mm height to 6 mm diameter at 13 mm above fluid level.

Figure 8.16: Fluid level in the two tubes at the end of the simulation. The fluid level in left tube in the tube-vug model is higher than the fluid level in the left tube in the tube-tube model. The colorbar denotes the ambient fluid saturation (α_{water}), with the fluid reservoir being in blue and the dry tubes being red.

the cross-section with minor variations (less than one bead diameter (1.0 mm)). These variations can be attributed to the local variation in bead packing, and in effect, the pore structure. The air-water interface near the outer surface of the cores has a curvature to it and results in a lower water height at the core boundary.

A similar 3D reconstruction of the air-water interface for the vuggy core (ADM06) is shown in Figure 8.17b; the large white volume within the matrix is the vug. The air-water interface for this core configuration is not uniform across the cross-section with large variations (larger than one bead diameter (1.0 mm)) observed across it. The water level is generally lower near the vug-matrix boundary and the core-atmosphere boundary; the water level increases when it is further away from these boundaries resulting in a higher water level in the matrix with the thicker porous medium. The air-water interface near the outer surface of the core has a curved surface, similar to one observed in Core 16, with the water level lower at the core external boundary.

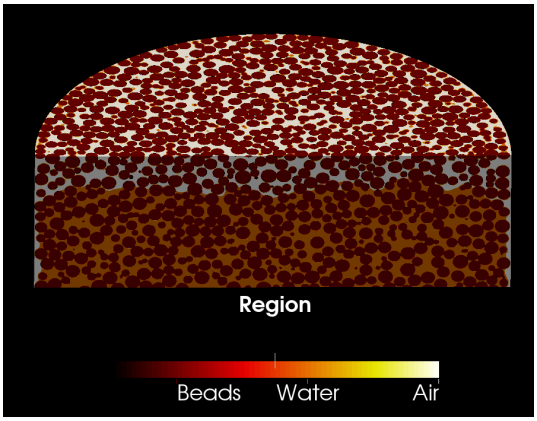

(a) Air-water interface at equilibrium for a continuous glass bead proxy core at a resolution of 24 μm.

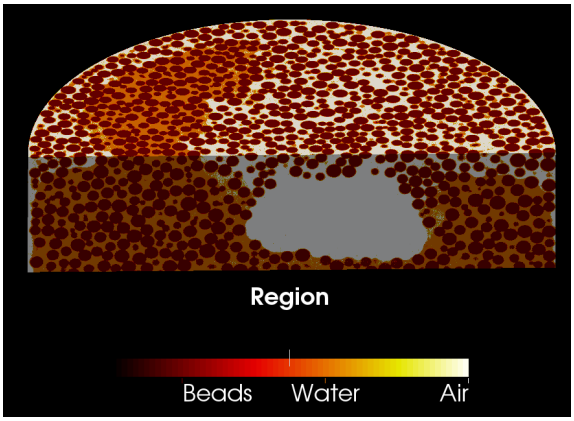

(b) Air-water interface at equilibrium for a vuggy glass bead proxy core at a resolution of 25 μm.

Figure 8.17: False-colored segmented 3D reconstruction of air-water interface in a vuggy and a homogeneous proxy core. Air is colored white, glass beads are colored red and water is colored orange.

8.4 Discussion

Combining the observations from previous sections, we can clearly see that the vugs act as a capillary barrier to the fluid imbibition process and alter the capillary rise behavior in the porous media.

The capillary rise behavior for all the cores can be split into two zones as discussed in Section 8.3.1: (i) an initial quick rise; and (ii) an exponential decay. All the cores agree on the rate of initial capillary rise (Figure 8.18), though the duration for the homogeneous core ($\sim$ 0.15 seconds) is considerably shorter than the average duration for the vuggy cores ($\sim$ 0.45 seconds). The similar rate of increase can be explained by the large permeabilities for all the cores which results in a short degassing time (time for air pressure to reduce from atmospheric pressure to zero in the core), on the order of 1×10^{-3} seconds, which is considerably smaller than the duration of initial rise. The initial rise duration for the vuggy cores can be grouped according to their flow unit classification (Figure 8.10): FU-1 show the longest duration while FU-3 shows the shortest. Permeability difference between the vuggy cores (Table 8.1) explains the difference in initial rise duration; a better flow quality, i.e. FU-3, starts stabilizing quicker and would therefore have the shortest duration.

Capillary rise at equilibrium is not dependent on the flow unit type (Figures 8.18). Two generalization can be made: (i) the presence of vug(s) results in a higher capillary rise at equilibrium conditions; and (ii) the highest capillary rise (ADM01 and ADM62) is in the core with the largest distance to the top of the furthest vug from the bottom. A similar result is also obtained from a CFD simulation (Figure 8.15), where the fluid attains a higher capillary rise in the connected tube-vug model compared to the two-tube model. We deduce that the momentum of the fluid in the vuggy tube (right tube in Figure 8.14b) is transferred to the constant diameter tube (left tube in Figure 8.14a), which pushes the fluid to a greater height and shows the departure from the two-tube model observed in Figure 8.15a. A higher equilibrium height is also observed in μCT scans (Figure 8.17), which also shows the fluid by-passing the vug and preferentially rising on one side (in an uneven manner).

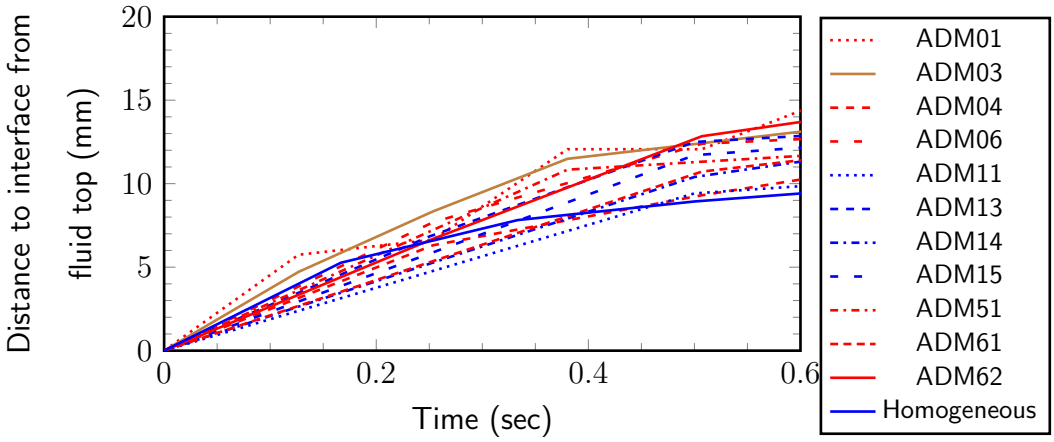

Figure 8.18: Zoomed-in version of Figures 8.12a and 8.13a. The duration of initial capillary rise in different for each flow unit.

A point to take into consideration is that the fluid front is not uniform across the cross-section for vuggy core (Figure 8.19), and for our experiments we have taken the maximum fluid height as the capillary rise value at each timestep. Furthermore, the optical imaging is performed from one side of the core; it is possible that the capillary fluid front might be present at a different height when observed from the backside (Figure 8.17b).

For most cases, vug(s) impact the capillary rise even before the fluid interacts with them (Figure 8.13b). This suggests a feedback mechanism, that transmits information of high permeability ahead, even before the fluid front reaches that point.

Considering the change in matrix cross-sectional area within the presence of the vug when moving up along the length of the core, the fluid velocity will vary in the matrix (Figure 8.20). The converging geometry in the matrix, when moving towards the vug, results a higher fluid velocity which results in a jetting movement of the fluid in the upward direction. As soon as the center of the vug is passed, the geometry becomes divergent and the fluid slows down. If the fluid velocity is large enough when it passes the vug, the fluid can completely encapsulate the vug (Figure 8.21).

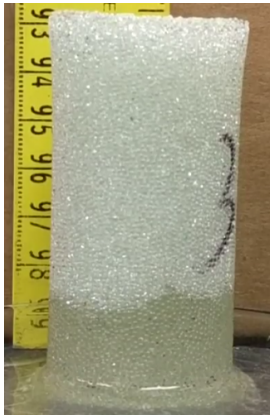

(a) Experimentally observed uneven fluid front in the vuggy core.

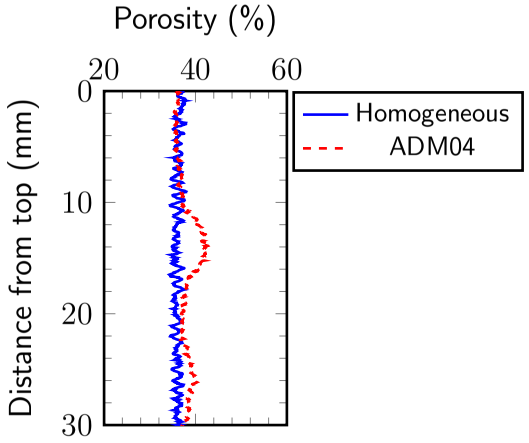

(b) Porosity profile in a section of a vuggy (dashed red) and the homogeneous (solid blue) core determined using μCT scanning at a resolution of 24 μm.

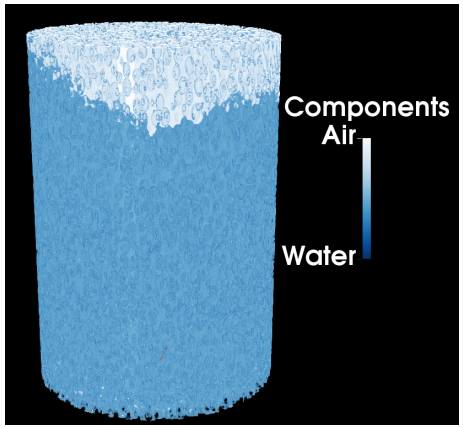

(c) Micro-tomograph of the water front.

Figure 8.19: Presence of a vug results in an non-uniform fluid front across the width of the core, which leads to error in determining the true capillary rise value. The vugs also result in a higher porosity value.

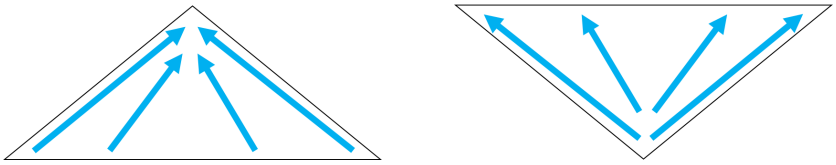

(a) Reduction in the matrix cross-sectional area results in a higher velocity of the fluid, with the jetting action pushing it forward.

(b) Once the vug is passes, the matrix cross-sectional area increases which reduces the velocity of the fluid and slows down the fluid movement.

Figure 8.20: Converging and diverging geometry of the matrix affect the fluid front movement.

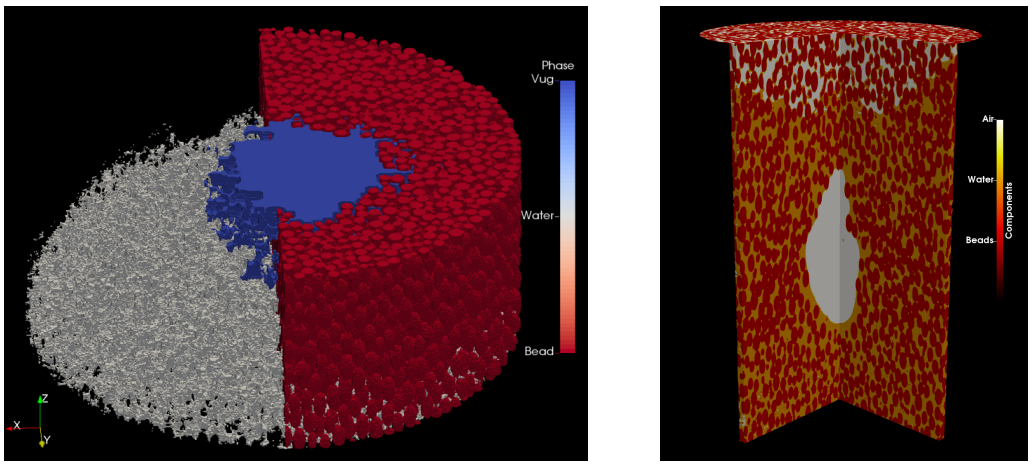

(a) 3D reconstruction of water (white) surrounding and rising around the vug (blue). It does not permeate inside the vug.

(b) The vug is filled with air (white) and is completely encapsulated by the water (orange) phase. The air-water interface is not horizontal, with a higher water level at the edges.

Figure 8.21: The water phase requires a higher capillary pressure to enter the vug, which it does not possess, and therefore rises on the sides of the vug.

8.5 Summary

In sum, our results suggest that for a carbonate rock in the presence of a vug, the fluid (contaminant) penetrates deeper in the porous media compared to a homogeneous porous media. The vugs affect the spontaneous imbibition behavior in a permeable media even before the fluid interacts with them. The vugs are not filled and fluid by-passes them. Vugs affect the spontaneous imbibition behavior in a permeable media even before the fluid interacts with them.

8.6 Acknowledgments

This project started as part of The University of Texas at Austin Hildebrand Department of Petroleum and Geosystems Engineering (UT PGE) Summer Undergraduate Research Internship (SURI) program and continued under support from NSF EAR CAREER Grant 1255622.

Chapter 9: Conclusions and future work

Prior to this work, most studies of particulate transport had been performed in porous and permeable media of uniform pore size, such as sandstones and sandpacks. Carbonates often contain large openings, called vugs, which can significantly affect the flow and transport properties (particle straining) of the porous medium. In this work I experimentally studied the impact of pore heterogeneity, specifically the presence and placement of vugs in carbonates, on particle entrapment by answering three major questions:

1. Can a repeatable rock model be fabricated that is similar to a real carbonate in its pore heterogeneity?
2. What is the effect of pore heterogeneity on straining in vuggy media?
3. What is the effect of vug spatial distribution on straining in vuggy media?

Due to the complexity and high pore heterogeneity in carbonates, experimental studies in carbonates are not repeatable and therefore it is difficult to draw conclusions. Chapter 3: details a workflow for vug characterization based on the high resolution computed tomography (CT) images which shows that vugs of variables shape, size, and spatial distribution are dispersed around the rock. For a repeatable study, I decided to isolate the effect of pore heterogeneity by creating a rock fabrication process that is repeatable and can be used to generate multiple cores with the same porosity and pore size distribution.

The core fabrication process is explained in detail in Chapter 4: where through trial-and-

error I came up with a temperature profile which can be repeated to create glass bead cores with the same porosity and pore size distribution. These core have enough mechanical integrity that they do not collapse on themselves and the glass beads are kept static during the flow experiment. To incorporate the effect of pore heterogeneity, specifically vugs, I introduced dissolvable inclusions in the bead pack prior to sintering which are later dissolved in water/acid. With this process, I now had the capability to generate proxy carbonate cores with the desired porosity, pore size distribution, vug size, vug shape, and vug distribution, and this can be utilized to study the impact of vugs on particle entrapment.

Non-vuggy and single vug cores were fabricated and particle retention experiments were conducted by injecting a bi-modal glass bead suspension in the fabricated core and changes in permeability, effluent solid volume, porosity, and vug volume was determined (Chapter 5:). Prior to the experiment it was expected that the suspension was flow through the vug due to the permeability contrast and the injected particles would be fill up the vug. The results showed that most particles were deposited either right before the entrance of the vug, or on the vug-matrix interface reducing the size of the vug, or at the bottom of the vug. Furthermore higher particle deposition was observed in the vuggy core compared to the homogeneous (non-vuggy) core. No discernible trend was observed with flow rate or injected particle concentration.

Combining the results, I speculate the following developments happening inside the core with time. Fluid converges and preferentially flows through the vug due to the permeability contrast. The injected particles are initially deposited near injection face region of the core, but over time, these particles penetrate deeper inside core. The converging streamlines increase the particle-particle and particle-grain interactions, resulting in particles dropping out near the vug inlet. The particles that enter inside the vug and carried by the flow and gravity to the bottom of the vug where they are deposited. Over time, the deposition near the vug inlet increases resulting in a drop in permeability such that the flow (and particles) starts preferentially entering the vug at a deeper depth (Chapter 7:). This results

in more meandering of the flow stream, ultimately resulting in increased particle-particle and particle-grain interactions, which increases the particle drop out. Particles entering the vug deposit at the vug-matrix interface or are carried with the stream to the bottom of the vug where they are strained when exiting the vug. Over time the particles will deposit around the vug and the vug will be shielded from further deposition. If the suspension is allowed indefinitely, I estimate that the vug will be completely shielded from flow.

The vug system was complicated next by adding another vug, total of two vugs, and similar experimental measurements were performed (Chapter 6:). The two simplistic configurations of dual vugs chosen were two vugs in series and two vugs in parallel with flow. The total vug volume for the two vugs was kept the same as the vug volume of the single vug and the center of mass of the vug system was the same as the single vug. Again, the results showed no discernible trend with flow rate or injected particle concentration. The results showed higher particle deposition in the series configuration, with more deposition at the vug inlet. The parallel vug has a higher deposition in the lower half of the vug.

Combining the results, I speculate the following developments happening inside the core in the series configuration with time. The permeability contrast results in flow converges while entering in the upper vug and starts diverging when exiting the vug. But since the lower vug is not distant enough, the streamlines do not completely diverge, refocus and enter the lower vug at a higher flow concentration. The deposition in the upper vug follows a similar pattern to a single vug: initial deposition near the injection face, subsequent deposition at the vug inlet and vug exit, reduction of permeability near the vug inlet and ultimately vug shielding. The deposition in the lower vug starts along the same lines, with particles depositing near the vug inlet. But since less number of particles are entering in this region and the flow is more focused, less particles would deposit near the vug inlet.

For the parallel vug configuration, the two adjacent vugs compete for flow. Flow near the outside boundary of the core converges towards the vug radial center, but the flow in the radial center of the core (between the two adjacent vugs) is affected by the two vugs and

continues straight along the same trajectory for a longer time and enters the vug at a deeper depth. Therefore a higher particle deposition is observed across the axial center of the vug in the parallel configuration. If the separation between the vugs is larger than the sphere of influence of the individual vug, the vugs act independently to a single vug and do not dictate the deposition of particles.

As a side study, vuggy core fabrication was extended to generate multiple cores with different vug configurations and a capillary rise study was conducted in them (Chapter 8:). Water was spontaneously imbibed in the air saturated proxy core and the air-water interface was continuously tracked using video recording. The results suggest that the presence of a vug causes water to attain a higher capillary height. The vugs are by-passed as fluid does not enter the vug.

9.1 Future work

As discussed in the previous chapter, the core fabrication procedure can be extrapolated to include multiple vugs of different shapes and sizes. The core size can be increased to generate foot-long cores with the availability of a graphite mold of the desired size, and a furnace big enough to fit it. The pore size distributions can be also changed by using smaller, larger, or mixture of sizes of glass beads as the matrix grains. The combination of sizes would result in heterogeneity on a different scale than a vug, and can be used to create low permeability and high permeability layers. Furthermore, the wettability of the system can be changed by chemically modifying the glass beads.

The particle entrapment study can be continued forward by generating a combination of vug sizes and distributions, and conducting experiments in them. The experimental results can be facilitated by conducting the experiments inside a CT machine to get time-lapse particle retention maps and measuring real-time effluent concentrations.

One limitation of the multiple vug configurations is that the vugs have been placed along

one line, which is not the case in reality and the results don't hold while upscaling. The vug configurations can be modified to include an offset vug configuration, which would give a better understanding of the effect of vug distribution on particle deposition.

Furthermore, a numerical CFD-DEM study on particle entrapment in vuggy porous media along the same lines as Mirabolghasemi [144] can aid the explanation of the particle deposition patterns. Finally, machine learning algorithms can be trained based on the temporal CT scans and predict the deposition patterns by changing the input flow parameters. These can significantly improve the simulation time, which currently requires super-computers for a large number of particles.

Appendices

A Data Sheet

Mo-Sci Specialty Products, L.L.C.
A Subsidiary of MO-SCI Corporation
4040 HyPoint North
Rolla, MO 65401
Telephone: 573-364-2338
Fax: 573-364-9589

GL0191
DATA SHEET

Appearance

Solid soda-lime glass beads of various colors.

Chemical Composition (by weight)

Silica (SiO_2)	65~75%
Aluminum oxide (Al_2O_3)	0~5%
Calcium oxide (CaO)	6~15%
Magnesium oxide (MgO)	1~5%
Sodium oxide (Na_2O)	10~20%
Iron Oxide (Fe_2O_3)	<0.8%

Physical Properties

Specific Gravity	2.5 (g/cm^3)
Bulk Density of Dry Beads	1.3 g per cm^3 (77 lbs/ft^3)
pH in water @ 25°C	7.8
Softening Temperature	650°C
Thermal Conductivity	0.9-1.3 W/m.K
Coefficient of Thermal Expansion	$90x10^{-7}$/°C (30-300° C)
Compression Strength	29 kg/mm^2 (39,875 psi)
Vickers Hardness	550 kg/mm^2 (756,250 psi)
Mohs Hardness	6-7
Index of Refraction	1.51(n_D)

Applications

Typical applications of GL0191 glass spheres include: spacer for gauge control, thermal expansion reduction filler for adhesives and polymers.

B Macro for the image processing

```
run("Image Sequence...", "open=[C:/Users/hjk622/Google Drive/Research/3D print/TIF/
pile_HK_Guelph_TD/image_1.tif] convert sort");
selectWindow("pile_HK_Guelph_TD");
run("Scale...", "x=1.0 y=1.0 z=4 width=513 height=513 depth=96 interpolation=
Bicubic average process create");
run("Kuwahara Filter", "sampling=3 stack");
setAutoThreshold("Otsu dark");

//run("Threshold...");
setOption("BlackBackground", true);
run("Convert to Mask", "method=Otsu background=Dark calculate black");
run("Find Connected Regions", "allow_diagonal display_image_for_each display_one_image
display_results regions_for_values_over=100 minimum_number_of_points=100 stop_after=10");
run("Invert", "stack");
run("Find Connected Regions", "allow_diagonal display_image_for_each display_one_image
display_results regions_for_values_over=100 minimum_number_of_points=100 stop_after=10");
selectWindow("Region of value 255 containing 5676 points");

//setTool("hand");
run("3D Viewer");
call("ij3d.ImageJ3DViewer.setCoordinateSystem", "false");
call("ij3d.ImageJ3DViewer.add", "Region of value 255 containing 5676 points", "Green",
"Region of value 255 containing 5676 points", "50", "true", "true", "true", "1", "2");
call("ij3d.ImageJ3DViewer.select", "Region of value 255 containing 5676 points");

call("ij3d.ImageJ3DViewer.exportContent", "STL Binary", "C:/Users/hjk622/Google Drive/
Research/3D print/TIF/largeVug.stl");}
```

C Pressure measurement and processing

The experimental core-flood setup is shown in Figure 5.4a. The particle suspension is injected under gravity in the top-down direction and passes through the sintered proxy core, via the peristaltic pump (which controls the flow) to the waste bin. The core is confined in a heat-shrink tubing with three pressure ports placed equidistantly along the length of the core (Figure C.1). These are connected to OMEGA PX409 differential pressure transducers (range 0-7 kPa with an accuracy of 7 Pa and with an output voltage range of 0-5 Vdc) which are continuously logging the differential pressure data (Figure 8.8) across two of the pressure ports at each time.

Due to the high sensitivity of the pressure transducer, the pressure data is prone to high levels of noise sourced from, including but not limited to, peristaltic pump, stirrer, opening and closing of lab door etc. The raw pressure data therefore is quite noisy (Figure C.2) and needs to be filtered to reduce this noise.

A 4^{th} order low-pass Butterworth filter (Figure C.3) is applied with a cut-off frequency of 0.006. The filtered pressure, and subsequently the permeability (Figure C.4), shows a cleear trend which indicates formation damage occuring in the proxy core. More details about filtering can be found at Khan [105].

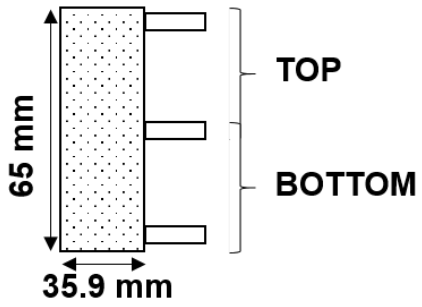

Figure C.1: Three pressure taps are placed equidistantly along the length of the core. The top two pressure ports give the pressure measurement in the top half of the core and the bottom two give the pressure in the bottom half of the core.

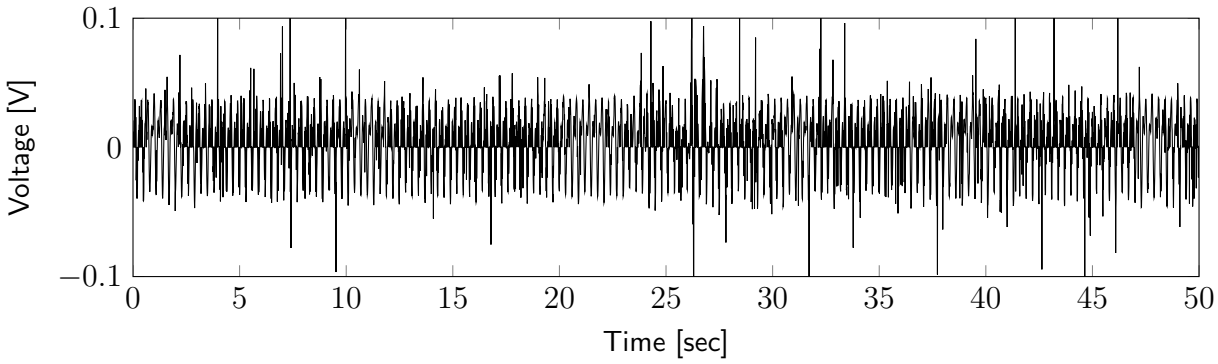

(a) Measured pressure response

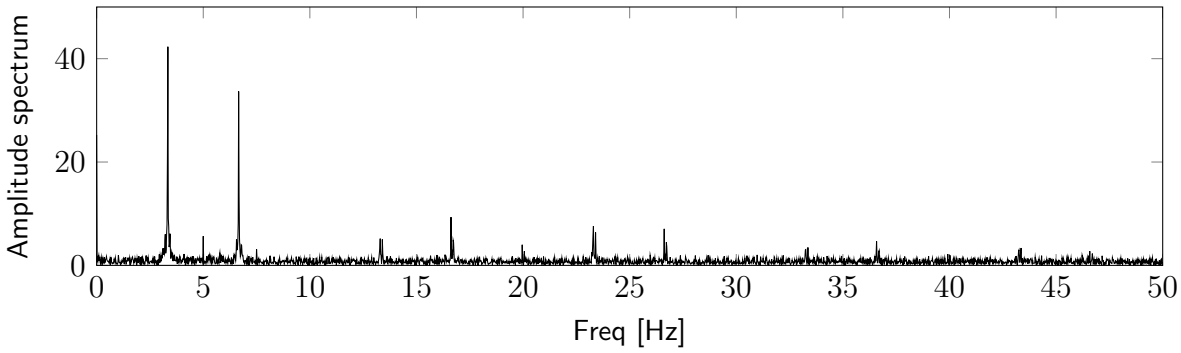

(b) Input signal in frequency domain

Figure C.2: Raw pressure data is very noisy.

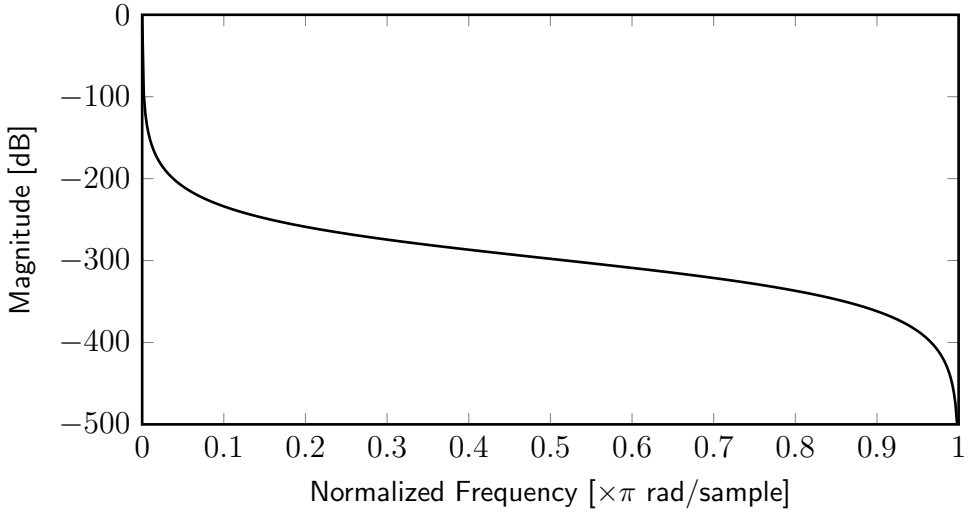

Figure C.3: 4^{th} order Butterworth filter with a cut-off freq of 0.006.

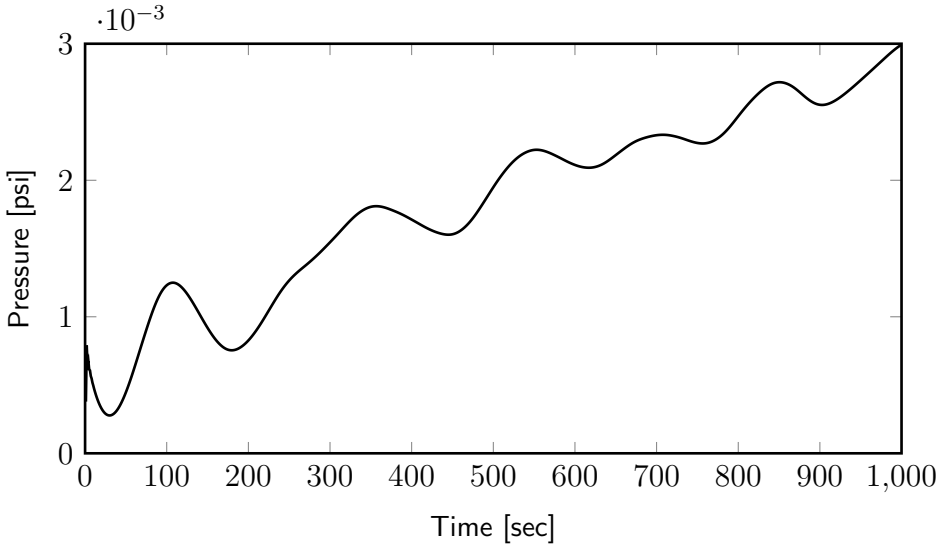

(a) Filtered pressure after applying the 4^{th} order Butterworth filter.

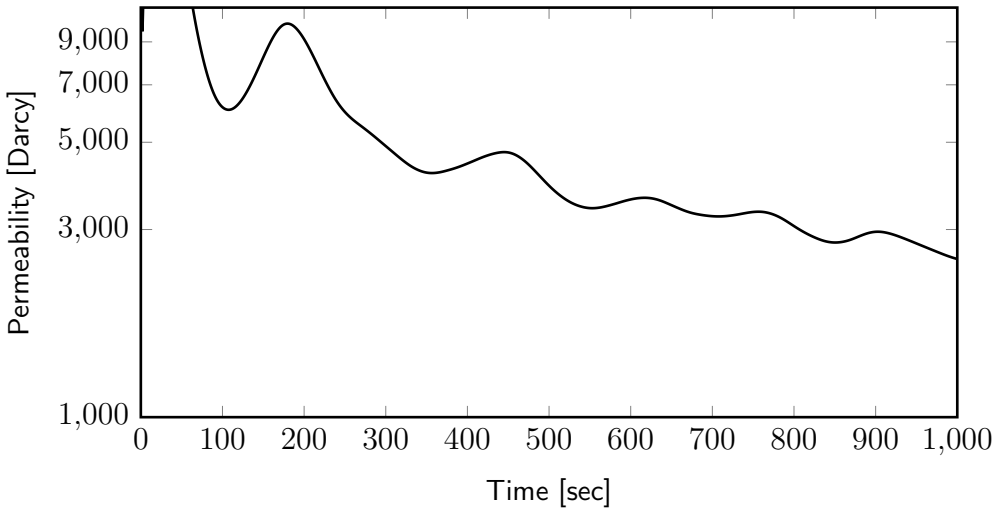

(b) Filtered pressure data converted to permeability of the core.

Figure C.4: Filtered data shows trends in pressure, and therefore, permeability.

D Limitations of the experimental setup

The general experimental schematic and setup are shown in Figure 5.4. The general outline of the experimental procedure is as follows: sinter the glass bead core, wrap it in heat-shrink tubing along with the plastic pipe and attach the three pressure taps, completely saturate the core with de-ionized water, conduct a pre-flood CT scan, connect the suspension reservoir to the core and start injection by operating the peristaltic pump while continuously logging pressure and collecting effluent, and disconnect the 100% water saturated core and install in the CT machine for the post-flood CT scan.

A few processes during these experiments are error prone and can cause erroneous data measurements from the experiments:

Effect of peristaltic pump on pressure measurement The peristaltic pump is a positive-displacement pump that uses rollers to push/control fluid flow in a flexible tubing housed inside the pump casing. For the gravity-dominated flow in these experiments, the peristaltic pump is operating at flowrates of 40 and 60 ml/min, which results in fluid spurts at a frequency of 1 Hz.

This sporadic release of fluid volume results in a non-continuous flow of fluid to the core and ultimately results in a continuous noise in the pressure transducers. The measured pressure data collects noise from other sources including the fluid movement due to stirrer action in the suspension reservoir and mechanical vibrations to the system caused by the continuously rotating stirrer. These noises result in a very messy pressure measurement, which needs to be filtered prior to use in permeability calculations (Appendix C).

Effect of fluid buffer between the reservoir outlet and core injection face A buffer space is present between the suspension reservoir outlet and the core injection face of the core (Figure D.5). This is initially completely filled with water. At the start of the experiment the suspension coming from the reservoir outlet has the desired total injected

particle concentration, but once it interacts with this fluid buffer, it gets diluted before interacting with the core. Therefore the total injected particle concentration observed by the core is not equal to the total injected particle concentration that has been injected from the suspension reservoir. Injecting a higher concentration of the total injected particle concentration would also suffer a similar fate, where the concentration would also get diluted. But on a comparative basis both of the concentrations will be less than that injected but the difference in total injected particle concentration incident on the core would be different for the two cases.

A question that comes up at this point is whether the particles are dropping down on the core as a plume effectively creating an external layer of particles which blocks subsequent particles from penetrating inside the core thereby creating filter cake on top of the injection face? For all the experiments conducted during this study, no external filter cake was observed at the end of the flooding experiment.

Since I am not working with the absolute values of total injected particle concentration but rather the relative difference between the concentrations, the changes in permeability, if they are a function of the total injected particle concentration, should be evident.

Effect of vibration on multi-particle bridging The size of the particles injected (25 & 100 μm) and the pore size distribution (Figure 4.14) suggests that the main mechanism of particle retention would be multi-particle bridging. Multi-particle bridges are formed when multiple particles (smaller than the size of the pore throat) approach the pore throat simultaneously and combine to block up the entrance to the pore. This combination of particles is a weak connection and prone to dislodging based on vibrations in the system.

Multiples avenues of pressure fluctuations are built in the experimental workflow: during the flooding experiment the fluid is pumped using a peristaltic pump which fluctuates the pressure within the core, the core is also moved on and off the CT machine for imaging, and CT machine moves the core up and down during the scanning phase. All of these factors can

Figure D.5: Fluid buffer zone is present above and below the core injection and effluent faces.

contribute to break the multi-particle bridges and release the trapped particles to a deeper depth. The porosity results need to be interpreted with these factors in mind.

Porosity change at outlet end of the core A large porosity change is always observed near the outlet end of the vuggy and non-vuggy core (Figures 5.11 and 6.10). This does not align with the traditional filtration models and experimental observations in homogeneous media where a the porosity loss is reduced with increasing depth. Other zones of high porosity change are the near injection face of the core and the inlet of the vug.

A point to consider here is that at the start of the experiment the whole core, including the vug, is fully saturated with de-ionized water. Their is a fluid buffer between the core and inlet stream and the core and outlet stream (Figure D.5). It can be speculated that a large porosity change is always observed in the zones where the particle suspension comes in contact with the fluid buffer. In essence the effect of the fluid buffer can be reduced by increasing the length of the core or by simply reducing the volume of the fluid present as a buffer.

References

[1] OpenFOAM | The OpenFOAM Foundation. URL https://openfoam.org/.

[2] MATLAB, September 2014.

[3] Ahmed S. Abou-Sayed, Karim S. Zaki, Gary Wang, Manoj Dnyandeo Sarfare, and Martin H. Harris. Produced Water Management Strategy and Water Injection Best Practices: Design, Performance, and Monitoring. *SPE Production & Operations*, 22(01):59–68, February 2007. ISSN 1930-1855. doi: 10.2118/108238-PA. URL https://www.onepetro.org/journal-paper/SPE-108238-PA.

[4] A. Abrams. Mud Design To Minimize Rock Impairment Due To Particle Invasion. *Journal of Petroleum Technology*, 29(05):586–592, May 1977. ISSN 0149-2136. doi: 10.2118/5713-PA. URL http://www.onepetro.org/doi/10.2118/5713-PA.

[5] Wayne M Ahr. *Geology of carbonate reservoirs: the identification, description and characterization of hydrocarbon reservoirs in carbonate rocks*. John Wiley & Sons, 2011.

[6] Wayne M Ahr, David Allen, Austin Boyd, H Nate Bachman, Tony Smithson, EA Clerke, KBM Gzara, JK Hassall, CRK Murty, H Zubari, and others. Confronting the carbonate conundrum. *Oilfield Review*, 17(1):18–29, 2005.

[7] Mahmood Akbar, Badarinadh Vissapragada, Ali H Alghamdi, David Allen, Michael Herron, Andrew Carnegie, Dhruba Dutta, Jean-Rémy Olesen, RD Chourasiya, Dale Logan, Dave Stief, Richard Netherwood, S Duffy Russell, and Kamlesh Saxena. A snapshot of carbonate reservoir evaluation. *Oilfield Review*, 12(4):20–41, 2000.

[8] S. Akin and A. R. Kovscek. Computed tomography in petroleum engineering research. *Geological Society, London, Special Publications*, 215(1):23–38, January 2003. ISSN 0305-8719, 2041-4927. doi: 10.1144/GSL.SP.2003.215.01.03. URL http://sp.lyellcollection.org/content/215/1/23.

[9] F. a. H. Al-Abduwani, A. Shirzadi, W. M. G. T. van den Broek, and P. K. Currie. Formation Damage vs. Solid Particles Deposition Profile during Laboratory Simulated PWRI. Society of Petroleum Engineers, January 2003. ISBN 978-1-55563-963-1. doi: 10.2118/82235-MS. URL https://www.onepetro.org/conference-paper/SPE-82235-MS.

[10] Firas Ali Hassan Al-Abduwani. *Internal filtration and external filter cake build-up in sandstones*. PhD Thesis, TU Delft, Delft University of Technology, 2005.

[11] Ali A. Al-Taq, Mohammed N. Al-Dahlan, and Abdullah A. Alrustum. Maintaining Injectiv-

ity of Disposal Wells: From Water Quality to Formation Permeability. 183743-MS. Society of Petroleum Engineers, March 2017. ISBN 978-1-61399-504-4. doi: 10.2118/183743-MS. URL https://www.onepetro.org/conference-paper/SPE-183743-MS?sort=&start=0&q=183743&from_year=&peer_reviewed=&published_between=&fromSearchResults=true&to_year=&rows=10#.

[12] Ahmed Z. Al-Yaseri, Maxim Lebedev, Sarah J. Vogt, Michael L. Johns, Ahmed Barifcani, and Stefan Iglauer. Pore-scale analysis of formation damage in Bentheimer sandstone with in-situ NMR and micro-computed tomography experiments. *Journal of Petroleum Science and Engineering*, 129:48–57, May 2015. ISSN 0920-4105. doi: 10.1016/j.petrol.2015.01.018. URL http://www.sciencedirect.com/science/article/pii/S0920410515000194.

[13] Stephen T. Solomon Alden J. Martin and Dan J. Hartmann. Characterization of Petrophysical Flow Units in Carbonate Reservoirs. *AAPG Bulletin*, 81(5):734–759, 1997. ISSN 0149-1423. URL http://archives.datapages.com/data/bulletns/1997/05may/0734/0734.htm.

[14] Khaled Aldhayee, Mahmoud T. Ali, and Hisham A. Nasr-El-Din. Acid Wormholing in Multistage Acid Fractured Wells Completed in Tight Naturally Fractured Dolomite Formation: Benefits and Impacts on Acid Fracturing Stimulation Design. Society of Petroleum Engineers, October 2018. ISBN 978-1-61399-622-5. doi: 10.2118/191440-18IHFT-MS. URL https://onepetro.org/conference-paper/SPE-191440-18IHFT-MS?sort=&start=0&q=SPE-191440-18IHFT-MS&from_year=&peer_reviewed=&published_between=&fromSearchResults=true&to_year=&rows=25#.

[15] M. A. Ali and M. R. Islam. The Effect of Asphaltene Precipitation on Carbonate-Rock Permeability: An Experimental and Numerical Approach. *SPE Production & Facilities*, 13(03):178–183, August 1998. ISSN 1064-668X. doi: 10.2118/50963-PA. URL https://www.onepetro.org/journal-paper/SPE-50963-PA.

[16] R. M. Allen and Keith Robinson. Environmental Aspects of Produced Water Disposal. 25549-MS. Society of Petroleum Engineers, January 1993. ISBN 978-1-55563-488-9. doi: 10.2118/25549-MS. URL https://www.onepetro.org/conference-paper/SPE-25549-MS.

[17] Mohand Alyan, Mohamed Al Tamimi, Osama Al Zinati, Dan Calarasu, John Martin, and Drew Irwin. Mitigating Water Injectivity Decline in Tight Carbonates due to Suspended Particles. 183222-MS. Society of Petroleum Engineers, November 2016. ISBN 978-1-61399-503-7. doi: 10.2118/183222-MS. URL https://www.onepetro.org/conference-paper/SPE-183222-MS.

[18] Ignacio Arganda-Carreras, Verena Kaynig, Curtis Rueden, Kevin W Eliceiri, Johannes Schindelin, Albert Cardona, and H Sebastian Seung. Trainable Weka Segmentation: a machine learning tool for

microscopy pixel classification. *Bioinformatics*, 33(15):2424–2426, 2017. doi: https://doi.org/10.1093/bioinformatics/btx180.

[19] David Arthur and Sergei Vassilvitskii. k-means++: The advantages of careful seeding. In *Proceedings of the eighteenth annual ACM-SIAM symposium on Discrete algorithms*, pages 1027–1035. Society for Industrial and Applied Mathematics, 2007.

[20] Maria Auset and Arturo A. Keller. Pore-scale visualization of colloid straining and filtration in saturated porous media using micromodels. *Water Resources Research*, 42(12), 2006. ISSN 1944-7973. doi: 10.1029/2005WR004639. URL https://agupubs.onlinelibrary.wiley.com/doi/abs/10.1029/2005WR004639.

[21] Louise Bailey, E.S. Boek, S.D.M. Jacques, Tony Boassen, O.M. Selle, J.F. Argillier, and D.G. Longeron. Particulate Invasion From Drilling Fluids. *SPE Journal*, 5(04):412–419, December 2000. ISSN 1086-055X. doi: 10.2118/67853-PA. URL http://www.onepetro.org/doi/10.2118/67853-PA.

[22] J.H. Barkman and D.H. Davidson. Measuring Water Quality and Predicting Well Impairment. *Journal of Petroleum Technology*, 24(07):865–873, July 1972. ISSN 0149-2136. doi: 10.2118/3543-PA. URL http://www.onepetro.org/doi/10.2118/3543-PA.

[23] P. Bedrikovetsky, P. Tran, W.M.G.T. Van den Broek, D. Marchesin, E. Rezende, A. Siqueira, A.L. Serra, and F. Shecaira. Damage Characterization of Deep Bed Filtration from Pressure Measurements. Society of Petroleum Engineers, 2002. doi: 10.2118/73788-MS. URL http://www.onepetro.org/doi/10.2118/73788-MS.

[24] L. A. Behrmann, J. K. Pucknell, and S. R. Bishop. Effects of Underbalance and Effective Stress on Perforation Damage in Weak Sandstone: Initial Results. Society of Petroleum Engineers, January 1992. ISBN 978-1-55563-500-8. doi: 10.2118/24770-MS. URL https://www.onepetro.org/conference-paper/SPE-24770-MS.

[25] B. Bennion. Formation Damage-The Impairment of the Invisible, By the Inevitable And Uncontrollable, Resulting In an Indeterminate Reduction of the Unquantifiable! *Journal of Canadian Petroleum Technology*, 38(02), February 1999. ISSN 0021-9487. doi: 10.2118/99-02-DA. URL http://www.onepetro.org/doi/10.2118/99-02-DA.

[26] D. B. Bennion, F. B. Thomas, and D. A. Sheppard. Formation Damage Due to Mineral Alteration and Wettability Changes During Hot Water and Steam Injection in Clay-Bearing Sandstone Reservoirs. Society of Petroleum Engineers, January 1992. ISBN 978-1-55563-515-2. doi: 10.2118/23783-MS. URL https://www.onepetro.org/conference-paper/SPE-23783-MS.

[27] Filippo Bianchi, Marcel Thielmann, Lucilla de Arcangelis, and Hans J. Herrmann. Critical bursts in filtration. *Physical Review Letters*, 120(3), January 2018. ISSN 0031-9007, 1079-7114. doi: 10.1103/PhysRevLett.120.034503. URL http://arxiv.org/abs/1706.02082. arXiv: 1706.02082.

[28] Bichara Adel F. Clogging of Recharge Wells by Suspended Solids. *Journal of Irrigation and Drainage Engineering*, 112(3):210–224, August 1986. doi: 10.1061/(ASCE)0733-9437(1986)112:3(210). URL https://ascelibrary.org/doi/abs/10.1061/(ASCE)0733-9437(1986)112:3(210).

[29] Martin J. Blunt. Flow in porous media — pore-network models and multiphase flow. *Current Opinion in Colloid & Interface Science*, 6(3):197–207, June 2001. ISSN 1359-0294. doi: 10.1016/S1359-0294(01)00084-X. URL http://www.sciencedirect.com/science/article/pii/S135902940100084X.

[30] Martin J. Blunt. *Multiphase Flow in Permeable Media by Martin J. Blunt.* Cambridge University Press, February 2017. ISBN 978-1-316-14509-8. doi: 10.1017/9781316145098. URL /core/books/multiphase-flow-in-permeable-media/455B5CA44AAF69F06A82DE091CD631C7.

[31] Martin J. Blunt, Branko Bijeljic, Hu Dong, Oussama Gharbi, Stefan Iglauer, Peyman Mostaghimi, Adriana Paluszny, and Christopher Pentland. Pore-scale imaging and modelling. *Advances in Water Resources*, 51:197–216, January 2013. ISSN 0309-1708. doi: 10.1016/j.advwatres.2012.03.003. URL http://www.sciencedirect.com/science/article/pii/S0309170812000528.

[32] Edo S. Boek, Christopher Hall, and Philippe M. J. Tardy. Deep Bed Filtration Modelling of Formation Damage Due to Particulate Invasion from Drilling Fluids. *Transport in Porous Media*, 91(2):479–508, September 2011. ISSN 0169-3913, 1573-1634. doi: 10.1007/s11242-011-9856-0. URL http://link.springer.com/article/10.1007/s11242-011-9856-0.

[33] M. Buchgraber, M. Al-Dossary, C. M. Ross, and A. R. Kovscek. Creation of a dual-porosity micromodel for pore-level visualization of multiphase flow. *Journal of Petroleum Science and Engineering*, 86-87:27–38, May 2012. ISSN 0920-4105. doi: 10.1016/j.petrol.2012.03.012. URL http://www.sciencedirect.com/science/article/pii/S0920410512000654.

[34] Vivian K Bust, Joshua U Oletu, Paul F Worthington, and others. The challenges for carbonate petrophysics in petroleum resource estimation. *SPE Reservoir Evaluation & Engineering*, 14(01):25–34, 2011.

[35] John A Chermak and Madeline E Schreiber. Mineralogy and trace element geochemistry of gas shales in the United States: Environmental implications. *International Journal of Coal Geology*, 126:32–44, 2014. doi: https://doi.org/10.1016/j.coal.2013.12.005.

[36] A. K. Chopra, M. H. Stein, and J. C. Ader. Development of Reservoir Descriptions To Aid in Design of EOR Projects. Society of Petroleum Engineers, January 1987. ISBN 978-1-55563-596-1. doi: 10.2118/16370-MS. URL https://www.onepetro.org/conference-paper/SPE-16370-MS.

[37] Philip W. Choquette and Lloyd C. Pray. Geologic Nomenclature and Classification of Porosity in Sedimentary Carbonates. *AAPG Bulletin*, 54(2):207–250, 1970. ISSN 0149-1423. URL http://archives.datapages.com/data/bulletns/1968-70/data/pg/0054/0002/0200/0207.htm.

[38] Fawad A Chuhan, Arild Kjeldstad, Knut Bjørlykke, and Kaare Høeg. Porosity loss in sand by grain crushing—experimental evidence and relevance to reservoir quality. *Marine and Petroleum Geology*, 19(1):39–53, January 2002. ISSN 0264-8172. doi: 10.1016/S0264-8172(01)00049-6. URL http://www.sciencedirect.com/science/article/pii/S0264817201000496.

[39] P. L. Churcher, P. R. French, J. C. Shaw, and L. L. Schramm. Rock Properties of Berea Sandstone, Baker Dolomite, and Indiana Limestone. Society of Petroleum Engineers, January 1991. ISBN 978-1-55563-534-3. doi: 10.2118/21044-MS. URL https://www.onepetro.org/conference-paper/SPE-21044-MS?sort=&start=0&q=21044&from_year=&peer_reviewed=&published_between=&fromSearchResults=true&to_year=&rows=25#.

[40] Lauren Churchwell and David DiCarlo. Measuring Relative Permeability in Cores at Reservoir Pressures Using a Gravity Drainage Method. Society of Petroleum Engineers, April 2018. ISBN 978-1-61399-570-9. doi: 10.2118/190322-MS. URL https://www.onepetro.org/conference-paper/SPE-190322-MS.

[41] F Civan. Predictability of formation damage: an assessment study and generalized models (Final Report). Technical report, US DOE Contract No. DE-AC22-90BC14658, April 1994.

[42] Faruk Civan. *Reservoir formation damage*. Gulf Professional Publishing, Oxford, UK, 2nd edition, September 2015. ISBN 978-0-12-801898-9.

[43] Faruk Civan. Particulate Processes in Porous Media. In *Reservoir Formation Damage*, pages 187–222. Elsevier, 2016. ISBN 978-0-12-801898-9. doi: 10.1016/B978-0-12-801898-9.00008-4. URL https://linkinghub.elsevier.com/retrieve/pii/B9780128018989000084.

[44] Faruk Civan and Vinh Nguyen. Modeling particle migration and deposition in porous media by parallel pathways with exchange, Chap. 11. In Vafai Kambiz, editor, *Handbook of porous media*, volume 2, pages 457–484. Chapman and Hall/CRC, Boca Raton, FL, March 2005. URL https://www.taylorfrancis.com/books/e/9781000006636/chapters/10.1201/9780415876384-14.

[45] C. E. Clark and J. A. Veil. Produced water volumes and management practices in the United States. Technical Report ANL/EVS/R-09-1, Argonne National Lab. (ANL), Argonne, IL (United States), September 2009. URL https://www.osti.gov/biblio/1007397.

[46] CMG. *IMEX User Guide: Three-phase, black-oil reservoir simulator*. Computer Modelling Group Ltd, Calgary, Alberta, Canada, 2015.

[47] Edward B. Coalson, Steven M. Goolsby, and Mark H. Franklin. Subtle Seals and Fluid-flow Barriers in Carbonate Rocks. 1994. URL http://archives.datapages.com/data/rmag/UnconSedSeq1994/coalson_b.htm.

[48] George R Coates, Lizht Xiao, and Manfred G Prammer. NMR Logging Principles and Applications. page 253, 1999.

[49] A Collins. *Geochemistry of oilfield waters*, volume 1. Elsevier, 1975.

[50] Mario Coniglio, Qing Zheng, and Terry R. Carter. Dolomitization and recrystallization of middle Silurian reefs and platformal carbonates of the Guelph Formation, Michigan Basin, southwestern Ontario. *Bulletin of Canadian Petroleum Geology*, 51(2):177–199, June 2003. ISSN 0007-4802. doi: 10.2113/51.2.177. URL https://pubs.geoscienceworld.org/cspg/bcpg/article/51/2/177/57879/dolomitization-and-recrystallization-of-middle.

[51] Peter A Cundall and Otto DL Strack. A discrete numerical model for granular assemblies. *Geotechnique*, 29(1):47–65, 1979.

[52] Kevin J Cunningham, Janine I Carlson, and Neil F Hurley. New method for quantification of vuggy porosity from digital optical borehole images as applied to the karstic Pleistocene limestone of the Biscayne aquifer, southeastern Florida. *Journal of Applied Geophysics*, 55(1):77–90, January 2004. ISSN 0926-9851. doi: 10.1016/j.jappgeo.2003.06.006. URL http://www.sciencedirect.com/science/article/pii/S0926985103000703.

[53] R. A. Cunningham and J. G. Eenink. Laboratory Study of Effect of Overburden, Formation and Mud Column Pressures on Drilling Rate of Permeable Formations. January 1959. URL https://www.onepetro.org/general/SPE-1094-G.

[54] Jérôme Darbon, Alexandre Cunha, Tony F Chan, Stanley Osher, and Grant J Jensen. Fast nonlocal filtering applied to electron cryomicroscopy. In *Biomedical Imaging: From Nano to Macro, 2008. ISBI 2008. 5th IEEE International Symposium on*, pages 1331–1334. IEEE, 2008.

[55] Sanjit K. Das, Robert S. Schechter, and Mukul M. Sharma. The Role of Surface Roughness and

Contact Deformation on the Hydrodynamic Detachment of Particles from Surfaces. *Journal of Colloid and Interface Science*, 164(1):63–77, April 1994. ISSN 0021-9797. doi: 10.1006/jcis.1994.1144. URL http://www.sciencedirect.com/science/article/pii/S0021979784711441.

[56] Yves Delachambre. *Contribution à l'étude de l'écoulement d'une suspension à travers un milieu poreux et du mécanisme de la filtration*. PhD thesis, Faculté des Sciences et Technologies, Nancy, France, 1966.

[57] Hu Dong and Martin J. Blunt. Pore-network extraction from micro-computerized-tomography images. *Physical Review E*, 80(3):036307, September 2009. doi: 10.1103/PhysRevE.80.036307. URL https://link.aps.org/doi/10.1103/PhysRevE.80.036307.

[58] DE Dria, GA Pope, Kamy Sepehrnoori, and others. Three-phase gas/oil/brine relative permeabilities measured under CO2 flooding conditions. *SPE reservoir engineering*, 8(02):143–150, 1993. doi: https://doi.org/10.2118/20184-PA.

[59] F. A. L Dullien, Francis S. Y Lai, and I. F MacDonald. Hydraulic continuity of residual wetting phase in porous media. *Journal of Colloid and Interface Science*, 109(1):201–218, January 1986. ISSN 0021-9797. doi: 10.1016/0021-9797(86)90295-X. URL http://www.sciencedirect.com/science/article/pii/002197978690295X.

[60] Robert J. Dunham. Classification of Carbonate Rocks According to Depositional Textures. 38: 108–121, 1962. URL http://archives.datapages.com/data/specpubs/carbona2/data/a038/a038/0001/0100/0108.htm.

[61] Lon Edelman. Air filtration: Air filter media — an industry evolves. *Filtration & Separation*, 45(9): 24–26, November 2008. ISSN 0015-1882. doi: 10.1016/S0015-1882(08)70368-9. URL http://www.sciencedirect.com/science/article/pii/S0015188208703689.

[62] M Elimelech, J Gregory, X Jia, and RA Williams. Particle Deposition & Aggregation: Measurement, Modelling and Simulation. *Colloid and Surface Engineering, ed. RA Williams*, 1998.

[63] Menachem Elimelech and Charles R. O'Melia. Kinetics of deposition of colloidal particles in porous media. *Environmental Science & Technology*, 24(10):1528–1536, October 1990. ISSN 0013-936X. doi: 10.1021/es00080a012. URL https://doi.org/10.1021/es00080a012.

[64] Brian R. Ellis, Jeffrey P. Fitts, Grant S. Bromhal, Dustin L. McIntyre, Ryan Tappero, and Catherine A. Peters. Dissolution-Driven Permeability Reduction of a Fractured Carbonate Caprock. *Environmental Engineering Science*, 30(4):187–193, March 2013. doi: 10.1089/ees.2012.0337. URL http://online.liebertpub.com/doi/abs/10.1089/ees.2012.0337.

[65] EPA. Profile of the Oil and Gas Extraction Industry. Technical Report EPA/310-R-99-006, U.S. Environmental Protection Agency, October 2000. URL https://archive.epa.gov/sectors/web/pdf/oilgas.pdf.

[66] Darryl H. Fenwick and Martin J. Blunt. Network Modeling of Three-Phase Flow in Porous Media. *SPE Journal*, 3(01):86–96, March 1998. ISSN 1086-055X. doi: 10.2118/38881-PA. URL https://www.onepetro.org/journal-paper/SPE-38881-PA.

[67] Darryl H. Fenwick and Martin J. Blunt. Three-dimensional modeling of three phase imbibition and drainage. *Advances in Water Resources*, 21(2):121–143, March 1998. ISSN 0309-1708. doi: 10.1016/S0309-1708(96)00037-1. URL http://www.sciencedirect.com/science/article/pii/S0309170896000371.

[68] David A. Ferrill, Darrell W. Sims, Deborah J. Waiting, Alan P. Morris, Nathan M. Franklin, and Alvin L. Schultz. Structural framework of the Edwards Aquifer recharge zone in south-central Texas. *GSA Bulletin*, 116(3-4):407–418, March 2004. ISSN 0016-7606. doi: 10.1130/B25174.1. URL https://pubs.geoscienceworld.org/gsa/gsabulletin/article/116/3-4/407/2068/structural-framework-of-the-edwards-aquifer.

[69] Robert L. Folk. Practical Petrographic Classification of Limestones. *AAPG Bulletin*, 43(1):1–38, 1959. ISSN 0149-1423. URL http://archives.datapages.com/data/bulletns/1957-60/data/pg/0043/0001/0000/0001.htm.

[70] Derek Ford and Paul D. Williams. *Karst Hydrogeology and Geomorphology*. John Wiley & Sons, May 2013. ISBN 978-1-118-68499-3. Google-Books-ID: whgNDVXFiqYC.

[71] Gerald M. Friedman. The Making and Unmaking of Limestones or the Downs and Ups of Porosity. *Journal of Sedimentary Research*, 45(2), 1975. ISSN 1527-1404. URL http://archives.datapages.com/data/sepm/journals/v42-46/data/045/045002/0379.htm.

[72] Gerald M Friedman and Syed A Ali. *Diagenesis of carbonate rocks: cement-porosity relationships*. Number 13. Society of Economic Paleontologists and Mineralogists, 1981.

[73] N. Fries and M. Dreyer. An analytic solution of capillary rise restrained by gravity. *Journal of Colloid and Interface Science*, 320(1):259–263, April 2008. ISSN 0021-9797. doi: 10.1016/j.jcis.2008.01.009. URL http://www.sciencedirect.com/science/article/pii/S0021979708000520.

[74] Irene T. Gabardo, Eduardo B. Platte, Antônio S. Araujo, and Fernando H. Pulgatti. Evaluation of Produced Water from Brazilian Offshore Platforms. In Kenneth Lee and Jerry Neff, editors, *Produced Water: Environmental Risks and Advances in Mitigation Technologies*, pages 89–113. Springer New

York, New York, NY, 2011. ISBN 978-1-4614-0046-2. doi: 10.1007/978-1-4614-0046-2_3. URL https://doi.org/10.1007/978-1-4614-0046-2_3.

[75] D. H. Gkay and R. W. Rex. FORMATION DAMAGE IN SANDSTONES CAUSED BY CLAY DISPERSION AND MIGRATION. In S. W. Bailey, editor, *Clays and Clay Minerals*, pages 355–366. Pergamon, January 1966. ISBN 978-0-08-011908-3. doi: 10.1016/B978-0-08-011908-3.50033-5. URL http://www.sciencedirect.com/science/article/pii/B9780080119083500335.

[76] Jose R. A. Godinho, Kuhan Chellappah, Ian Collins, Pei Ng, Megan Smith, and Philip J. Withers. Time-lapse imaging of particle invasion and deposition in porous media using in situ X-ray radiography. *Journal of Petroleum Science and Engineering*, 177:384–391, June 2019. ISSN 0920-4105. doi: 10.1016/j.petrol.2019.02.061. URL http://www.sciencedirect.com/science/article/pii/S0920410519301986.

[77] Jay W. Grate, Marvin G. Warner, Jonathan W. Pittman, Karl J. Dehoff, Thomas W. Wietsma, Changyong Zhang, and Mart Oostrom. Silane modification of glass and silica surfaces to obtain equally oil-wet surfaces in glass-covered silicon micromodel applications. *Water Resources Research*, 49(8):4724–4729, 2013. ISSN 1944-7973. doi: 10.1002/wrcr.20367. URL https://agupubs.onlinelibrary.wiley.com/doi/abs/10.1002/wrcr.20367.

[78] Simon Gruener, Tommy Hofmann, Dirk Wallacher, Andriy V. Kityk, and Patrick Huber. Capillary rise of water in hydrophilic nanopores. *Physical Review E*, 79(6):067301, June 2009. ISSN 1539-3755, 1550-2376. doi: 10.1103/PhysRevE.79.067301. URL https://link.aps.org/doi/10.1103/PhysRevE.79.067301.

[79] Simon Gruener, Zeinab Sadjadi, Helen E. Hermes, Andriy V. Kityk, Klaus Knorr, Stefan U. Egelhaaf, Heiko Rieger, and Patrick Huber. Anomalous front broadening during spontaneous imbibition in a matrix with elongated pores. *Proceedings of the National Academy of Sciences*, 109(26):10245–10250, June 2012. ISSN 0027-8424, 1091-6490. doi: 10.1073/pnas.1119352109. URL https://www.pnas.org/content/109/26/10245.

[80] C. Gruesbeck and R.E. Collins. Entrainment and Deposition of Fine Particles in Porous Media. *Society of Petroleum Engineers Journal*, 22(06):847–856, December 1982. ISSN 0197-7520. doi: 10.2118/8430-PA. URL http://www.onepetro.org/doi/10.2118/8430-PA.

[81] Lara O Haluszczak, Arthur W Rose, and Lee R Kump. Geochemical evaluation of flowback brine from Marcellus gas wells in Pennsylvania, USA. *Applied Geochemistry*, 28:55–61, 2013. doi: https://doi.org/10.1016/j.apgeochem.2012.10.002.

[82] H. C. Hamaker. The London—van der Waals attraction between spherical particles. *Physica*, 4

(10):1058–1072, October 1937. ISSN 0031-8914. doi: 10.1016/S0031-8914(37)80203-7. URL http://www.sciencedirect.com/science/article/pii/S0031891437802037.

[83] A. Hassan, V. Chandra, M. P. Yutkin, T. W. Patzek, and D. N. Espinoza. Improving Pore Network Imaging & Characterization of Microporous Carbonate Rocks Using Multi-Scale Imaging Techniques. Society of Petroleum Engineers, November 2017. ISBN 978-1-61399-563-1. doi: 10.2118/188786-MS. URL https://www.onepetro.org/conference-paper/SPE-188786-MS?sort=&start=0&q=188786&from_year=&peer_reviewed=&published_between=&fromSearchResults=true&to_year=&rows=25#.

[84] D. P. Haughey and G. S. G. Beveridge. Local voidage variation in a randomly packed bed of equal-sized spheres. *Chemical Engineering Science*, 21(10):905–915, October 1966. ISSN 0009-2509. doi: 10.1016/0009-2509(66)85084-4. URL http://www.sciencedirect.com/science/article/pii/0009250966850844.

[85] P.M. Heertjes and C.F. Lerk. The functioning of deep bed bilters, part II: The filtration of flocculated suspensions. *Transactions of the Institution of Chemical Engineers*, 45a:138 – 145, 1967. URL http://archive.icheme.org/cgi-bin/somsid.cgi?record=1045&type=header.

[86] PM Heertjes and CF Lerk. The Functioning of Deep Bed Filters, Part II, The Filtration of Flocculated Suspensions. *Transactions of the Institution of Chemical Engineers*, 45a:138 – 145, 1967. URL http://archive.icheme.org/cgi-bin/somsid.cgi?record=1045&type=header.

[87] J. P. Herzig, D. M. Leclerc, and P. Le. Goff. Flow of Suspensions through Porous Media — Application to Deep Filtration. *Industrial & Engineering Chemistry*, 62(5):8–35, May 1970. ISSN 0019-7866. doi: 10.1021/ie50725a003. URL http://dx.doi.org/10.1021/ie50725a003.

[88] R. Hogg, T. W. Healy, and D. W. Fuerstenau. Mutual coagulation of colloidal dispersions. *Transactions of the Faraday Society*, 62:1638, 1966. ISSN 0014-7672. doi: 10.1039/tf9666201638. URL http://xlink.rsc.org/?DOI=tf9666201638.

[89] IAEA. Nuclear Power Reactors in the World. 2018. URL http://www-pub.iaea.org/books/IAEABooks/13379/Nuclear-Power-Reactors-in-the-World.

[90] International Standard Organization. Geotechnical investigation and testing - Identification and classification of soil - Part 1: Identification and description. Standard ISO 14688-1:2017(E), December 2017. URL http://www.iso.org/cms/render/live/en/sites/isoorg/contents/data/standard/06/63/66345.html.

[91] C. R. Ison and K. J. Ives. Removal mechanisms in deep bed filtration. *Chemical Engineering Science*,

24(4):717–729, April 1969. ISSN 0009-2509. doi: 10.1016/0009-2509(69)80064-3. URL http://www.sciencedirect.com/science/article/pii/0009250969800643.

[92] K. J Ives. Rapid filtration. *Water Research*, 4(3):201–223, March 1970. ISSN 0043-1354. doi: 10.1016/0043-1354(70)90068-0. URL http://www.sciencedirect.com/science/article/pii/0043135470900680.

[93] Kenneth J Ives. Deep filters. *Filtration & Separation*, 4:125–135, 1967.

[94] KJ Ives. Aquifer recharge with waste water. *Effluent and Water Treatment*, pages 184–188, 1964.

[95] K.J. Ives and J. Gregory. Surface forces in filtration. *Proc. Soc. Water Treat. Exam.*, 15(2), 1966.

[96] Tomihisa Iwasaki, J. J. Slade, and Wm. E. Stanley. Some notes on sand filtration [with Discussion]. *Journal (American Water Works Association)*, 29(10):1591–1602, 1937. ISSN 0003-150X. URL http://www.jstor.org/stable/41231759.

[97] V. Jegatheesan and S. Vigneswaran. Deep Bed Filtration: Mathematical Models and Observations. *Critical Reviews in Environmental Science and Technology*, 35(6):515–569, November 2005. ISSN 1064-3389. doi: 10.1080/10643380500326432. URL https://doi.org/10.1080/10643380500326432.

[98] R. Jäger, M. Mendoza, and H. J. Herrmann. Mechanism behind Erosive Bursts In Porous Media. *Physical Review Letters*, 119(12):124501, September 2017. doi: 10.1103/PhysRevLett.119.124501. URL https://link.aps.org/doi/10.1103/PhysRevLett.119.124501.

[99] Ying-Lan Jia, Xiang-Yu Fan, Ren-Shi Nie, Quan-Hua Huang, and Yong-Lu Jia. Flow Modeling of Well Test Analysis for Porous–Vuggy Carbonate Reservoirs. *Transport in Porous Media*, 97(2):253–279, March 2013. ISSN 0169-3913, 1573-1634. doi: 10.1007/s11242-012-0121-y. URL https://link.springer.com/article/10.1007/s11242-012-0121-y.

[100] Di Jiao and M.M. Sharma. Investigation of Dynamic Mud Cake Formation: The Concept of Minimum Overbalance Pressure. Society of Petroleum Engineers, 1993. doi: 10.2118/26323-MS. URL http://www.onepetro.org/doi/10.2118/26323-MS.

[101] S Z Jilani, H Menouar, A A Al-Majed, and M A Khan. Effect of overbalance pressure on formation damage. *Journal of Petroleum Science and Engineering*, page 13, 2002.

[102] Frank O. Jr Jones. Influence of Chemical Composition of Water on Clay Blocking of Permeability. *Journal of Petroleum Technology*, 16(04):441–446, April 1964. ISSN 0149-2136. doi: 10.2118/631-PA. URL https://www.onepetro.org/journal-paper/SPE-631-PA.

[103] Sarkis Kakadjian, Joseph Thompson, Robert Torres, Antonio Pontifes, Amanda Rodriguez, and

Yahia Ait Hamlat. Permian Frac Systems Using Produced Water. 172811-MS. Society of Petroleum Engineers, March 2015. ISBN 978-1-61399-343-9. doi: 10.2118/172811-MS. URL https://www.onepetro.org/conference-paper/SPE-172811-MS.

[104] N. K. Karadimitriou and S. M. Hassanizadeh. A Review of Micromodels and Their Use in Two-Phase Flow Studies. *Vadose Zone Journal*, 11(3), August 2012. ISSN 1539-1663. doi: 10.2136/vzj2011.0072. URL https://pubs.geoscienceworld.org/vzj/article/11/3/vzj2011.0072/111520/a-review-of-micromodels-and-their-use-in-two-phase.

[105] Hasan Khan. *Improved permeability estimation of formation damage through imaged core flooding experiments*. PhD thesis, The University of Texas at Austin, Austin, May 2016. URL http://pge.utexas.edu/images/pdfs/theses16/khan.pdf.

[106] Hasan Khan and Gary Pope. *Guelph dolomite*. Digital Rocks Portal, 2018. doi: 10.17612/P74T1M. URL http://www.digitalrocksportal.org/projects/162.

[107] Hasan Khan, Maryam Mirabolghasemi, Hongtao Yang, Maša Prodanovic, David DiCarlo, Mathew Balhoff, and Kenneth Gray. Comparative Study of Formation Damage due to Straining and Surface Deposition in Porous Media. Society of Petroleum Engineers, February 2016. ISBN 978-1-61399-441-2. doi: 10.2118/178930-MS. URL https://www.onepetro.org/conference-paper/SPE-178930-MS.

[108] Hasan Khan, Maša Prodanović, and David DiCarlo. *Particulate straining in simple porous media*. Digital Rocks Portal, 2016. doi: 10.17612/P7K01C. URL http://www.digitalrocksportal.org/projects/51.

[109] Hasan Khan, Masa Prodanovic, and David Dicarlo. *Particulate straining in carbonate proxy*. Digital Rocks Portal, 2018. doi: 10.17612/P7D96T. URL http://www.digitalrocksportal.org/projects/160.

[110] Hasan Khan, David DiCarlo, and Maša Prodanović. The Effect of Vug Distribution on Particle Straining in Permeable Media. *Journal of Hydrology*, page 124306, November 2019. ISSN 0022-1694. doi: 10.1016/j.jhydrol.2019.124306. URL http://www.sciencedirect.com/science/article/pii/S0022169419310418.

[111] Hasan Khan, Masa Prodanovic, and David DiCarlo. *Particulate straining in series and parallel vuggy configurations*. Digital Rocks Portal, 2019. doi: 10.17612/RJ9P-9438. URL http://www.digitalrocksportal.org/projects/214.

[112] Hasan J. Khan, Maryam S. Mirabolghasemi, Hongtao Yang, Maša Prodanović, David A. DiCarlo, and Matthew T. Balhoff. Study of formation damage caused by retention of bi-dispersed particles using

combined pore-scale simulations and particle flooding experiments. *Journal of Petroleum Science and Engineering*, 158:293–308, September 2017. ISSN 0920-4105. doi: 10.1016/j.petrol.2017.08.061. URL http://www.sciencedirect.com/science/article/pii/S0920410517306873.

[113] Hasan J. Khan, David DiCarlo, and Maša Prodanović. Replicating carbonaceous vug in synthetic porous media. *MethodsX*, 5:808–811, July 2018. ISSN 2215-0161. doi: 10.1016/j.mex.2018.07.018. URL http://www.sciencedirect.com/science/article/pii/S2215016118301250.

[114] Hasan J. Khan, Maša Prodanović, and David A. DiCarlo. The Effect of Vuggy Porosity on Straining in Porous Media. *SPE Journal*, pages SPE–194201–PA, 2019. ISSN 1086-055X. doi: 10.2118/194201-PA. URL http://www.onepetro.org/doi/10.2118/194201-PA.

[115] Kartic C Khilar and H Scott Fogler. *Migrations of fines in porous media*, volume 12. Springer Science & Business Media, 1998.

[116] K.C. Khilar and H.S. Fogler. Colloidally Induced Fines Migration in Porous Media. *Reviews in Chemical Engineering*, 4(1-2):41–108, 2011. ISSN 2191-0235. doi: 10.1515/REVCE.1987.4.1-2.41. URL https://www.degruyter.com/view/j/revce.1987.4.1-2/revce.1987.4.1-2.41/revce.1987.4.1-2.41.xml.

[117] G. Kier, V. Jegatheesan, and S. Vigneswaran. Deep Bed Filtration: Modelling Theory And Practice. In Vigneswaran Saravanamuthu, editor, *Waste Water Treatment Technologies*, volume 8 of *Encyclopedia of Life Support System (EOLSS)*, pages 263–307. EOLSS Publishers, Oxford, 2009. ISBN 978-1-84826-638-4. URL http://hdl.handle.net/10536/DRO/DU:30039565.

[118] N. K. Karadimitriou, P. Nuske, P. J. Kleingeld, S. M. Hassanizadeh, and R. Helmig. Simultaneous thermal and optical imaging of two-phase flow in a micro-model. *Lab on a Chip*, 14(14):2515–2524, 2014. doi: 10.1039/C4LC00321G. URL https://pubs.rsc.org/en/content/articlelanding/2014/lc/c4lc00321g.

[119] Christoph Kloss, Christoph Goniva, Alice Hager, Stefan Amberger, and Stefan Pirker. Models, algorithms and validation for opensource DEM and CFD–DEM. *Progress in Computational Fluid Dynamics, an International Journal*, 12(2-3):140–152, January 2012. ISSN 1468-4349. doi: 10.1504/PCFD.2012.047457. URL http://www.inderscienceonline.com/doi/abs/10.1504/PCFD.2012.047457.

[120] D. W. Knowles and R. G. Boytim. Brine Handling And Disposal By Reinjection. 29763-MS. Society of Petroleum Engineers, January 1995. ISBN 978-1-55563-449-0. doi: 10.2118/29763-MS. URL https://www.onepetro.org/conference-paper/SPE-29763-MS.

[121] Stanley Jr Kolodzie. Analysis Of Pore Throat Size And Use Of The Waxman-Smits Equation To Determine Ooip In Spindle Field, Colorado. Society of Petroleum Engineers, January 1980.

ISBN 978-1-55563-693-7. doi: 10.2118/9382-MS. URL https://www.onepetro.org/conference-paper/SPE-9382-MS.

[122] L. F. Konikow, L. L. August, and C. I. Voss. Effects of Clay Dispersion on Aquifer Storage and Recovery in Coastal Aquifers. *Transport in Porous Media*, 43(1):45–64, April 2001. ISSN 1573-1634. doi: 10.1023/A:1010613525547. URL https://doi.org/10.1023/A:1010613525547.

[123] M. Kuwahara, K. Hachimura, S. Eiho, and M. Kinoshita. Processing of RI-Angiocardiographic Images. In K. Preston and M. Onoe, editors, *Digital Processing of Biomedical Images*, pages 187–202. Springer US, Boston, MA, 1976. ISBN 978-1-4684-0769-3. doi: 10.1007/978-1-4684-0769-3_13. URL https://doi.org/10.1007/978-1-4684-0769-3_13.

[124] Q. Lan, E. Ghanbari, H. Dehghanpour, and R. Hawkes. Water Loss versus Soaking Time: Spontaneous Imbibition in Tight Rocks. Society of Petroleum Engineers, February 2014. ISBN 978-1-61399-294-4. doi: 10.2118/167713-MS. URL https://www.onepetro.org/conference-paper/SPE-167713-MS.

[125] Binhui Li, Xuequn Tan, Fuyong Wang, Peiqing Lian, Wenbin Gao, and Yiqiang Li. Fracture and vug characterization and carbonate rock type automatic classification using X-ray CT images. *Journal of Petroleum Science and Engineering*, 153:88–96, May 2017. ISSN 0920-4105. doi: 10.1016/j.petrol.2017.03.037. URL http://www.sciencedirect.com/science/article/pii/S0920410517303911.

[126] Tianbo Liang, Xiao Luo, Quoc Nguyen, and David A. DiCarlo. Computed-Tomography Measurements of Water Block in Low-Permeability Rocks: Scaling and Remedying Production Impairment. *SPE Journal*, 23(03):762–771, June 2018. ISSN 1086-055X. doi: 10.2118/189445-PA. URL https://www.onepetro.org/journal-paper/SPE-189445-PA.

[127] Mark Longair. "Find Connected Regions" ImageJ PlugIn. URL https://www.longair.net/edinburgh/imagej/find-connected-regions/.

[128] Heinz Adolf Lowenstam. Aragonite needles secreted by algae and some sedimentary implications. *Journal of Sedimentary Research*, 25(4):270–272, December 1955. ISSN 1527-1404. doi: 10.1306/74D7047A-2B21-11D7-8648000102C1865D. URL https://pubs.geoscienceworld.org/sepm/jsedres/article/25/4/270/95184/aragonite-needles-secreted-by-algae-and-some.

[129] F. J. Lucia. Petrophysical Parameters Estimated From Visual Descriptions of Carbonate Rocks: A Field Classification of Carbonate Pore Space. *Journal of Petroleum Technology*, 35(03):629–637, 1983. ISSN 0149-2136. doi: 10.2118/10073-PA. URL https://www.onepetro.org/journal-paper/SPE-10073-PA.

[130] F. Jerry Lucia and Robert G. Loucks. Micropores in Carbonate Mud: Early Development and Petrophysics. 2013. URL http://archives.datapages.com/data/gcags-journal/data/002/002001/pdfs/1.htm.

[131] Jerry Lucia. Rock-Fabric/Petrophysical Classification of Carbonate Pore Space for Reservoir Characterization. *AAPG Bulletin*, 79, 1995. ISSN 0149-1423. doi: 10.1306/7834D4A4-1721-11D7-8645000102C1865D. URL http://search.datapages.com/data/doi/10.1306/7834D4A4-1721-11D7-8645000102C1865D.

[132] V Mackrle, O Dracka, and J Svec. Hydrodynamics of the disposal of low level liquid radioactive wastes in soil. *International Atomic Energy Agency Contract Report*, 98, 1965.

[133] R. W. Maclay and T. A. Small. Hydrostratigraphic subdivisions and fault barriers of the Edwards aquifer, south-central Texas, U.S.A. *Journal of Hydrology*, 61(1):127–146, February 1983. ISSN 0022-1694. doi: 10.1016/0022-1694(83)90239-1. URL http://www.sciencedirect.com/science/article/pii/0022169483902391.

[134] Robert W. Maclay. Geology and hydrology of the Edwards Aquifer in the San Antonio area, Texas. USGS Numbered Series 95-4186, U.S. Geological Survey, Austin, TX, 1995. URL http://pubs.er.usgs.gov/publication/wri954186.

[135] B. J. Mahler, L. Lynch, and P. C. Bennett. Mobile sediment in an urbanizing karst aquifer: implications for contaminant transport. *Environmental Geology*, 39(1):25–38, November 1999. ISSN 1432-0495. doi: 10.1007/s002540050434. URL https://doi.org/10.1007/s002540050434.

[136] Jean Margat, Jac van der Gun, and Jac van der Gun. *Groundwater around the World : A Geographic Synopsis*. CRC Press, March 2013. ISBN 978-0-429-21273-4. doi: 10.1201/b13977. URL https://www.taylorfrancis.com/books/9780429212734.

[137] Alice Maroudas. *Clarification of suspensions: a study of particle deposition in granular filter media*. PhD thesis, Imperial College London, London, 1961. URL http://hdl.handle.net/10044/1/13408.

[138] Alice Maroudas and Paul Eisenklam. Clarification of suspensions: a study of particle deposition in granular media. *Chemical Engineering Science*, 20(10):867–873, October 1965. ISSN 0009-2509. doi: 10.1016/0009-2509(65)80083-5. URL http://www.sciencedirect.com/science/article/pii/0009250965800835.

[139] Nicos S. Martys, S. Torquato, and D. P. Bentz. Universal scaling of fluid permeability for sphere packings. *Physical Review E*, 50(1):403–408, July 1994. doi: 10.1103/PhysRevE.50.403. URL https://link.aps.org/doi/10.1103/PhysRevE.50.403.

[140] David C. Mays and James R. Hunt. Hydrodynamic Aspects of Particle Clogging in Porous Media. *Environmental Science & Technology*, 39(2):577–584, January 2005. ISSN 0013-936X, 1520-5851. doi: 10.1021/es049367k. URL https://pubs.acs.org/doi/10.1021/es049367k.

[141] Laura M. McDowell-Boyer, James R. Hunt, and Nicholas Sitar. Particle transport through porous media. *Water Resources Research*, 22(13):1901–1921, December 1986. ISSN 00431397. doi: 10.1029/WR022i013p01901. URL http://doi.wiley.com/10.1029/WR022i013p01901.

[142] Paul Meakin and Alexandre M. Tartakovsky. Modeling and simulation of pore-scale multiphase fluid flow and reactive transport in fractured and porous media. *Reviews of Geophysics*, 47(3): RG3002, July 2009. ISSN 8755-1209. doi: 10.1029/2008RG000263. URL http://doi.wiley.com/10.1029/2008RG000263.

[143] A. Mehmani, S. Kelly, C. Torres-Verdin, and M. Balhoff. Quantification of Fracture-Matrix Fluid Transport in Unconventional Rocks Using Two-Scale Microfluidic Chips. In *Unconventional Resources Technology Conference, Austin, Texas, 24-26 July 2017*, SEG Global Meeting Abstracts, pages 693–704. Society of Exploration Geophysicists, American Association of Petroleum Geologists, Society of Petroleum Engineers, September 2017. doi: 10.15530/urtec-2017-2669314. URL https://library.seg.org/doi/abs/10.15530/urtec-2017-2669314.

[144] Maryam Mirabolghasemi. *Micro-scale modeling of formation damage*. Thesis, December 2017. URL https://repositories.lib.utexas.edu/handle/2152/62944.

[145] Maryam Mirabolghasemi, Maša Prodanović, David DiCarlo, and Hongyu Ji. Prediction of empirical properties using direct pore-scale simulation of straining through 3d microtomography images of porous media. *Journal of Hydrology*, 529, Part 3:768–778, October 2015. ISSN 0022-1694. doi: 10.1016/j.jhydrol.2015.08.016. URL http://www.sciencedirect.com/science/article/pii/S0022169415005764.

[146] Luis Javier Miranda, Carlos Torres-Verdin, and F. Jerry Lucia. Modeling Mud-Filtrate Invasion Effects on Resistivity Logs to Estimate Permeability of Vuggy and Fractured Carbonate Formations. Society of Petroleum Engineers, January 2009. ISBN 978-1-61399-427-6. doi: 10.2118/121136-MS. URL https://www.onepetro.org/conference-paper/SPE-121136-MS.

[147] J. Moghadasi, M. Jamialahmadi, H. Müller-Steinhagen, A. Sharif, M. R. Izadpanah, E. Motaei, and R. Barati. Formation Damage in Iranian Oil Fields. Society of Petroleum Engineers, January 2002. ISBN 978-1-55563-941-9. doi: 10.2118/73781-MS. URL https://www.onepetro.org/conference-paper/SPE-73781-MS.

[148] Somnath Mondal, Chu-Hsiang Wu, and Mukul M. Sharma. Coupled CFD-DEM simulation of hydro-

dynamic bridging at constrictions. *International Journal of Multiphase Flow*, 84:245–263, September 2016. ISSN 0301-9322. doi: 10.1016/j.ijmultiphaseflow.2016.05.001. URL http://www.sciencedirect.com/science/article/pii/S0301932216302580.

[149] Clyde H Moore and William J Wade. *Carbonate reservoirs: Porosity and diagenesis in a sequence stratigraphic framework*, volume 67. Newnes, 2013.

[150] T.W. Muecke. Formation Fines and Factors Controlling Their Movement in Porous Media. *Journal of Petroleum Technology*, 31(02):144–150, February 1979. ISSN 0149-2136. doi: 10.2118/7007-PA. URL http://www.onepetro.org/doi/10.2118/7007-PA.

[151] Raymond Carl Murray. Origin of porosity in carbonate rocks. *Journal of Sedimentary Research*, 30(1):59–84, March 1960. ISSN 1527-1404. doi: 10.1306/74D709CA-2B21-11D7-8648000102C1865D. URL https://pubs.geoscienceworld.org/sepm/jsedres/article/30/1/59/95474/origin-of-porosity-in-carbonate-rocks.

[152] Narayan Gopinathan Nair. Measurement and modeling of multiscale flow and transport through large-vug Cretaceous carbonates. August 2008. URL https://repositories.lib.utexas.edu/handle/2152/17994.

[153] Rashmi Narayan, José R. Coury, Jacob H. Masliyah, and Murray R. Gray. Particle Capture and Plugging in Packed-Bed Reactors. *Industrial & Engineering Chemistry Research*, 36(11):4620–4627, November 1997. ISSN 0888-5885. doi: 10.1021/ie970101e. URL https://doi.org/10.1021/ie970101e.

[154] H. A. Nasr-El-Din. Permeability Decline Due to Flow of Dilute Suspensions Through Porous Media. In *Suspensions: Fundamentals and Applications in the Petroleum Industry*, volume 251 of *Advances in Chemistry*, pages 289–319. American Chemical Society, May 1996. ISBN 978-0-8412-3136-8. doi: 10.1021/ba-1996-0251.ch006. URL http://dx.doi.org/10.1021/ba-1996-0251.ch006.

[155] Shungo Natsui, Shigeru Ueda, Hiroshi Nogami, Junya Kano, Ryo Inoue, and Tatsuro Ariyama. Gas–solid flow simulation of fines clogging a packed bed using DEM–CFD. *Chemical Engineering Science*, 71:274–282, March 2012. ISSN 0009-2509. doi: 10.1016/j.ces.2011.12.035. URL http://www.sciencedirect.com/science/article/pii/S0009250911008980.

[156] B. M. Newberry, L. M. Grace, and D. O. Stief. Analysis of Carbonate Dual Porosity Systems from Borehole Electrical Images. Society of Petroleum Engineers, January 1996. ISBN 978-1-55563-434-6. doi: 10.2118/35158-MS. URL https://www.onepetro.org/conference-paper/SPE-35158-MS.

[157] Jean Ollion, Julien Cochennec, François Loll, Christophe Escudé, and Thomas Boudier. TANGO: a generic tool for high-throughput 3d image analysis for studying nuclear organization. *Bioinformatics*,

29(14):1840–1841, July 2013. ISSN 1367-4803. doi: 10.1093/bioinformatics/btt276. URL https://academic.oup.com/bioinformatics/article/29/14/1840/231770.

[158] Charles R O'Melia and Werner Stumm. Theory of water filtration. *Journal (American Water Works Association)*, 59(11):1393–1412, 1967. doi: https://doi.org/10.1002/j.1551-8833.1967.tb03469.x.

[159] Stephen P. Opsahl, MaryLynn Musgrove, Barbara J. Mahler, and Rebecca B. Lambert. Water-quality observations of the San Antonio segment of the Edwards aquifer, Texas, with an emphasis on processes influencing nutrient and pesticide geochemistry and factors affecting aquifer vulnerability, 2010–16. USGS Numbered Series 2018-5060, U.S. Geological Survey, Reston, VA, 2018. URL http://pubs.er.usgs.gov/publication/sir20185060. IP-093387.

[160] N. Otsu. A Threshold Selection Method from Gray-Level Histograms. *IEEE Transactions on Systems, Man, and Cybernetics*, 9(1):62–66, January 1979. ISSN 0018-9472. doi: 10.1109/TSMC.1979.4310076.

[161] Owete S. Owete and William E. Brigham. Flow Behavior of Foam: A Porous Micromodel Study. *SPE Reservoir Engineering*, 2(03):315–323, August 1987. ISSN 0885-9248. doi: 10.2118/11349-PA. URL https://www.onepetro.org/journal-paper/SPE-11349-PA.

[162] YAP Perera. *Comparison of performance of radial and upflow filters*. PhD thesis, Asian Institute of Technology, Bangkok, Thailand, 1982.

[163] Edward D. Pittman. Relationship of Porosity and Permeability to Various Parameters Derived from Mercury Injection-Capillary Pressure Curves for Sandstone (1). *AAPG Bulletin*, 76(2):191–198, 1992. ISSN 0149-1423. URL http://archives.datapages.com/data/bulletns/1992-93/data/pg/0076/0002/0000/0191.htm.

[164] Maša Prodanović, M Esteva, M Hanlon, G Nanda, and P Agarwal. *Digital Rocks Portal: A repository for porous media images*. 2015.

[165] Jafar Qajar, Nicolas Francois, and Christoph Hermann Arns. Microtomographic Characterization of Dissolution-Induced Local Porosity Changes Including Fines Migration in Carbonate Rock. *SPE Journal*, 18(03):545–562, February 2013. ISSN 1086-055X. doi: 10.2118/153216-PA. URL https://www.onepetro.org/journal-paper/SPE-153216-PA.

[166] Ali Q. Raeini, Martin J. Blunt, and Branko Bijeljic. Modelling two-phase flow in porous media at the pore scale using the volume-of-fluid method. *Journal of Computational Physics*, 231(17):5653–5668, July 2012. ISSN 00219991. doi: 10.1016/j.jcp.2012.04.011. URL https://linkinghub.elsevier.com/retrieve/pii/S0021999112001830.

[167] R.K. Rajamani, B.K. Mishra, R. Venugopal, and A. Datta. Discrete element analysis of tumbling mills. *Powder Technology*, 109(1-3):105–112, April 2000. ISSN 00325910. doi: 10.1016/S0032-5910(99)00230-2. URL https://linkinghub.elsevier.com/retrieve/pii/S0032591099002302.

[168] K. U. Raju, H. A. Nasr-El-Din, V. V. Hilab, S. Siddiqui, and S. Mehta. Injection of Aquifer Water and GOSP Disposal Water into Tight Carbonate Reservoirs. 87440-MS. Society of Petroleum Engineers, January 2004. ISBN 978-1-55563-985-3. doi: 10.2118/87440-MS. URL https://www.onepetro.org/conference-paper/SPE-87440-MS.

[169] Amir Raoof and S. Majid Hassanizadeh. A New Method for Generating Pore-Network Models of Porous Media. *Transport in Porous Media*, 81(3):391–407, February 2010. ISSN 0169-3913, 1573-1634. doi: 10.1007/s11242-009-9412-3. URL http://link.springer.com/10.1007/s11242-009-9412-3.

[170] P Raveendran and A Amirtharajah. The forces controlling detachment of particles during filter backwashing. In *Joint CSC-ASCE National Conference on Environmental Engineering*, pages 1671–1678, New York, NY, 1993. American Society of Civil Engineers (ASCE).

[171] Palanivel Raveendran and Appiah Amirtharajah. Role of Short-Range Forces in Particle Detachment during Filter Backwashing. *Journal of Environmental Engineering*, 121(12):860–868, December 1995. ISSN 0733-9372, 1943-7870. doi: 10.1061/(ASCE)0733-9372(1995)121:12(860). URL http://ascelibrary.org/doi/10.1061/%28ASCE%290733-9372%281995%29121%3A12%28860%29.

[172] Richard J Reeder. *Carbonates: mineralogy and chemistry*, volume 11 of *Reviews in Mineralogy*. BookCrafters Inc, Washington, 1983. ISBN 0-939950-15-4.

[173] S. D. Rege and H. S. Fogler. A network model for deep bed filtration of solid particles and emulsion drops. *AIChE Journal*, 34(11):1761–1772, November 1988. ISSN 1547-5905. doi: 10.1002/aic.690341102. URL http://onlinelibrary.wiley.com/doi/10.1002/aic.690341102/abstract.

[174] S. Remond. DEM simulation of small particles clogging in the packing of large beads. *Physica A: Statistical Mechanics and its Applications*, 389(21):4485–4496, November 2010. ISSN 0378-4371. doi: 10.1016/j.physa.2010.06.033. URL http://www.sciencedirect.com/science/article/pii/S0378437110005625.

[175] Nima Rezaei, Omidreza Mohammadzadeh, Lesley Anne James, and Ioannis Chatzis. Experimental Investigation of the VAPEX Process in Vuggy Porous Media. *SPE Journal*, 19(01):101–108, February 2014. ISSN 1086-055X. doi: 10.2118/163106-PA. URL http://www.onepetro.org/doi/10.2118/163106-PA.

[176] A. A. Rocha, M. Frydman, S. A. B. da Fontoura, F. F. Rosario, and M. C. M. Bezerra. Numerical Modeling of Salt Precipitation During Produced Water Reinjection. 68336-MS. Society of Petroleum Engineers, January 2001. ISBN 978-1-55563-915-0. doi: 10.2118/68336-MS. URL https://www.onepetro.org/conference-paper/SPE-68336-MS.

[177] Eli Ruckenstein and Dennis C. Prieve. Adsorption and desorption of particles and their chromatographic separation. *AIChE Journal*, 22(2):276–283, March 1976. ISSN 0001-1541, 1547-5905. doi: 10.1002/aic.690220209. URL http://doi.wiley.com/10.1002/aic.690220209.

[178] R. Sakthivadivel. Theory and mechanism of filtration of non-particleal fines through a porous medium. In *HEL 15-5*. Coll. Eng., Univ. California, Berkeley, 1966.

[179] Adrian Scheidegger and others. *The physics of flow through porous media*. University Of Toronto Press: London, 1958.

[180] Johannes Schindelin, Ignacio Arganda-Carreras, Erwin Frise, Verena Kaynig, Mark Longair, Tobias Pietzsch, Stephan Preibisch, Curtis Rueden, Stephan Saalfeld, Benjamin Schmid, Jean-Yves Tinevez, Daniel James White, Volker Hartenstein, Kevin Eliceiri, Pavel Tomancak, and Albert Cardona. Fiji: an open-source platform for biological-image analysis. *Nature Methods*, 9(7):676–682, July 2012. ISSN 1548-7091. doi: 10.1038/nmeth.2019. URL http://www.nature.com/nmeth/journal/v9/n7/full/nmeth.2019.html.

[181] Benjamin Schmid, Johannes Schindelin, Albert Cardona, Mark Longair, and Martin Heisenberg. A high-level 3d visualization API for Java and ImageJ. *BMC bioinformatics*, 11(1):274, 2010.

[182] J. H. Schön. Chapter 1 - Rocks — Their Classification and General Properties. In J. H. Schön, editor, *Handbook of Petroleum Exploration and Production*, volume 8 of *Physical Properties of Rocks*, pages 1–16. Elsevier, January 2011. doi: 10.1016/S1567-8032(11)08001-3. URL http://www.sciencedirect.com/science/article/pii/S1567803211080013.

[183] Caroline A. Schneider, Wayne S. Rasband, and Kevin W. Eliceiri. NIH Image to ImageJ: 25 years of image analysis. *Nature Methods*, 9(7):671–675, July 2012. ISSN 1548-7091. doi: 10.1038/nmeth.2089. URL http://www.nature.com/nmeth/journal/v9/n7/full/nmeth.2089.html.

[184] M. M. Sharma and Y. C. Yortsos. Transport of particulate suspensions in porous media: Model formulation. *AIChE Journal*, 33(10):1636–1643, October 1987. ISSN 1547-5905. doi: 10.1002/aic.690331007. URL http://onlinelibrary.wiley.com/doi/10.1002/aic.690331007/abstract.

[185] John M Sharp Jr and Jay L Banner. The Edwards Aquifer: A resource in conflict. *GSA Today*, 7(8): 1–9, 1997. URL http://www.geo.utexas.edu/faculty/banner/Publications/edwards1997.pdf.

[186] J. C. Shaw, B. Bramhill, N. C. Wardlaw, and J. W. Costerton. Bacterial Fouling in a Model Core System. *Appl. Environ. Microbiol.*, 49(3):693–701, March 1985. ISSN 0099-2240, 1098-5336. URL https://aem.asm.org/content/49/3/693.

[187] Wen Song and Anthony R. Kovscek. Functionalization of micromodels with kaolinite for investigation of low salinity oil-recovery processes. *Lab on a Chip*, 15(16):3314–3325, 2015. doi: 10.1039/C5LC00544B. URL https://pubs.rsc.org/en/content/articlelanding/2015/lc/c5lc00544b.

[188] Yi-Qiao Song, Seungoh Ryu, and Pabitra N Sen. Determining multiple length scales in rocks. *Nature*, 406(6792):178–181, 2000.

[189] Geir Humborstad Sørland, Ketil Djurhuus, Hege C Widerøe, Jan R Lien, and Arne Skauge. Absolute pore size distributions from NMR. *Diffusion Fundamentals*, 5:4–1, 2007.

[190] P Charles Stein. A study of the theory of rapid filtration of water through sand. *D. Sc. Dissertation*, 1940.

[191] R. L. Thomas and C. W. Crowe. Matrix Treatment Employs New Acid System for Stimulation and Control of Fines Migration in Sandstone Formations. *Journal of Petroleum Technology*, 33(08): 1,491–1,500, August 1981. ISSN 0149-2136. doi: 10.2118/7566-PA. URL https://www.onepetro.org/journal-paper/SPE-7566-PA.

[192] A C Todd, J E Somerville, and Graham Scott. The Application of Depth of Formation Damage Measurements in Predicting Water Injectivity Decline. Bakersfield, California, February 1984. doi: doi.org/10.2118/12498-MS.

[193] Eric van Oort, J. F. G. van Velzen, and Klaas Leerlooijer. Impairment by Suspended Solids Invasion: Testing and Prediction. *SPE Production & Facilities*, 8(03):178–184, August 1993. ISSN 1064-668X. doi: 10.2118/23822-PA. URL https://www.onepetro.org/journal-paper/SPE-23822-PA.

[194] Andrea Simone van Overveldt, Hua Guo, Gerard de Blok, Pavel Bedrikovetsky, and Pacelli L.J. Zitha. A CT Scan Study of the Leakoff of Oil-Based Drilling Fluids. Society of Petroleum Engineers, 2012. doi: 10.2118/151856-MS. URL http://www.onepetro.org/doi/10.2118/151856-MS.

[195] Srinivas Veerapaneni. *Formation and morphology of colloidal deposits in porous media.* Thesis, 1996. URL https://scholarship.rice.edu/handle/1911/16966.

[196] John A. Veil. Produced Water Management Options and Technologies. In Kenneth Lee and

Jerry Neff, editors, *Produced Water: Environmental Risks and Advances in Mitigation Technologies*, pages 537–571. Springer New York, New York, NY, 2011. ISBN 978-1-4614-0046-2. doi: 10.1007/978-1-4614-0046-2_29. URL https://doi.org/10.1007/978-1-4614-0046-2_29.

[197] Rodolfo Araujo Victor. *Multiscale, image-based interpretation of well logs acquired in a complex, deepwater carbonate reservoir*. PhD Thesis, University of Texas, Austin, TX, 2017. URL https://repositories.lib.utexas.edu/bitstream/handle/2152/62228/VICTOR-DISSERTATION-2017.pdf.

[198] Jiamin Wan and John L. Wilson. Visualization of the role of the gas-water interface on the fate and transport of colloids in porous media. *Water Resources Research*, 30(1):11–23, January 1994. ISSN 00431397. doi: 10.1029/93WR02403. URL http://doi.wiley.com/10.1029/93WR02403.

[199] Jiamin Wan, Tetsu K. Tokunaga, Chin-Fu Tsang, and Gudmundur S. Bodvarsson. Improved Glass Micromodel Methods for Studies of Flow and Transport in Fractured Porous Media. *Water Resources Research*, 32(7):1955–1964, 1996. ISSN 1944-7973. doi: 10.1029/96WR00755. URL https://agupubs.onlinelibrary.wiley.com/doi/abs/10.1029/96WR00755.

[200] Norman C. Wardlaw. The Effects Of Pore Structure On Displacement Efficiency In Reservoir Rocks And In Glass Micromodels. Society of Petroleum Engineers, January 1980. ISBN 978-1-55563-699-9. doi: 10.2118/8843-MS. URL https://www.onepetro.org/conference-paper/SPE-8843-MS.

[201] Nathaniel R. Warner, Cidney A. Christie, Robert B. Jackson, and Avner Vengosh. Impacts of Shale Gas Wastewater Disposal on Water Quality in Western Pennsylvania. *Environmental Science & Technology*, 47(20):11849–11857, October 2013. ISSN 0013-936X. doi: 10.1021/es402165b. URL http://dx.doi.org/10.1021/es402165b.

[202] Edward W. Washburn. The Dynamics of Capillary Flow. *Physical Review*, 17(3):273–283, March 1921. doi: 10.1103/PhysRev.17.273. URL https://link.aps.org/doi/10.1103/PhysRev.17.273.

[203] Jon N Weber and Peter MJ Woodhead. Carbonate lagoon and beach sediments of Tarawa Atoll, Gilbert Islands. *Atoll Research Bulletin*, 157:1–21, December 1972. doi: 10.5479/si.00775630.157.1.

[204] Hans-Rudolf Wenk, David J Barber, and Richard J Reeder. Microstructures in carbonates. *Reviews in Mineralogy and Geochemistry*, 11(1):301–367, 1983.

[205] Dorthe Wildenschild and Adrian P. Sheppard. X-ray imaging and analysis techniques for quantifying pore-scale structure and processes in subsurface porous medium systems. *Advances in Water Resources*, 51:217–246, January 2013. ISSN 0309-1708. doi: 10.1016/j.advwatres.2012.07.018. URL http://www.sciencedirect.com/science/article/pii/S0309170812002060.

[206] Jessica M. Wilson and Jeanne M. VanBriesen. Oil and Gas Produced Water Management and Surface Drinking Water Sources in Pennsylvania. *Environmental Practice*, 14(4):288–300, December 2012. ISSN 1466-0466, 1466-0474. doi: 10.1017/S1466046612000427. URL https://www.cambridge.org/core/journals/environmental-practice/article/research-article-oil-and-gas-produced-water-management-and-surface-drinking-water-sources-in-pennsylvania/4CD070C0887BBB5406C8F247B8CE1A88.

[207] Qingrong Xiong, Todor G. Baychev, and Andrey P. Jivkov. Review of pore network modelling of porous media: Experimental characterisations, network constructions and applications to reactive transport. *Journal of Contaminant Hydrology*, 192:101–117, September 2016. ISSN 0169-7722. doi: 10.1016/j.jconhyd.2016.07.002. URL http://www.sciencedirect.com/science/article/pii/S016977221630122X.

[208] Chengyuan Xu, Yili Kang, Lijun You, and Zhenjiang You. Lost-Circulation Control for Formation-Damage Prevention in Naturally Fractured Reservoir: Mathematical Model and Experimental Study. *SPE Journal*, 22(05):1,654–1,670, October 2017. ISSN 1086-055X. doi: 10.2118/182266-PA. URL https://www.onepetro.org/journal-paper/SPE-182266-PA.

[209] Chicheng Xu, Zoya Heidari, and Carlos Torres-Verdin. Rock Classification in Carbonate Reservoirs based on Static and Dynamic Petrophysical Properties Estimated from Conventional Well Logs. Society of Petroleum Engineers, January 2012. ISBN 978-1-61399-213-5. doi: 10.2118/159991-MS. URL https://www.onepetro.org/conference-paper/SPE-159991-MS.

[210] Ke Xu, Tianbo Liang, Peixi Zhu, Pengpeng Qi, Jun Lu, Chun Huh, and Matthew Balhoff. A 2.5-D glass micromodel for investigation of multi-phase flow in porous media. *Lab on a Chip*, 17(4):640–646, February 2017. ISSN 1473-0189. doi: 10.1039/C6LC01476C. URL https://pubs.rsc.org/en/content/articlelanding/2017/lc/c6lc01476c.

[211] Hongtao Yang. *Pore-scale modeling of particle filtration in porous media.* Thesis, October 2018. URL https://repositories.lib.utexas.edu/handle/2152/69250.

[212] Hongtao Yang and Matthew T. Balhoff. Pore-network modeling of particle retention in porous media. *AIChE Journal*, 63(7):3118–3131, 2017. ISSN 1547-5905. doi: 10.1002/aic.15593. URL https://onlinelibrary.wiley.com/doi/abs/10.1002/aic.15593.

[213] Ming Yang. Measurement of Oil in Produced Water. In Kenneth Lee and Jerry Neff, editors, *Produced Water: Environmental Risks and Advances in Mitigation Technologies*, pages 57–88. Springer New York, New York, NY, 2011. ISBN 978-1-4614-0046-2. doi: 10.1007/978-1-4614-0046-2_2. URL https://doi.org/10.1007/978-1-4614-0046-2_2.

[214] Ramesh Chandra Yerramilli, P. L. J. Zitha, Sanjay Surya Yerramilli, and Pavel Bedrikovetsky. A Novel Water Injectivity Model and Experimental Validation using CT Scanned Core-Floods. Society of Petroleum Engineers, 2013. doi: 10.2118/165194-MS. URL http://www.onepetro.org/doi/10.2118/165194-MS.

[215] Jianfei Yuan, Fen Xu, Guoshi Deng, Yeqi Tang, and Pengyue Li. Hydrogeochemistry of Shallow Groundwater in a Karst Aquifer System of Bijie City, Guizhou Province. *Water*, 9(8):625, August 2017. doi: 10.3390/w9080625. URL https://www.mdpi.com/2073-4441/9/8/625.

[216] H. Zengin, B. Hu, J. A. Siddiqui, and R. M. Ottenbrite. Surface modification of glass beads with poly(acrylic acid). *Polymers for Advanced Technologies*, 17(5):372–378, 2006. ISSN 1099-1581. doi: 10.1002/pat.721. URL https://www.onlinelibrary.wiley.com/doi/abs/10.1002/pat.721.

[217] Liying Zhang, Steven L. Bryant, James W. Jr Jennings, Todd J. Arbogast, and Ramoj Paruchuri. Multiscale Flow and Transport in Highly Heterogeneous Carbonates. Society of Petroleum Engineers, January 2004. ISBN 978-1-55563-151-2. doi: 10.2118/90336-MS. URL https://www.onepetro.org/conference-paper/SPE-90336-MS.

[218] Qing Zheng. *Carbonate diagenesis and porosity evolution in the Guelph Formation, southwestern Ontario*. PhD thesis, 2000.

[219] Y. G Zhu and G Shaw. Soil contamination with radionuclides and potential remediation. *Chemosphere*, 41(1):121–128, July 2000. ISSN 0045-6535. doi: 10.1016/S0045-6535(99)00398-7. URL http://www.sciencedirect.com/science/article/pii/S0045653599003987.